https://doi.org/10.35662/unine-thesis-3164

University of Neuchâtel, Switzerland

Faculty of Sciences

Centre for Hydrogeology and Geothermics (CHYN)

The Role of Convective Heat and Mass Transfer in the Thermal Response of Karst Conduits

---

Thesis presented for the degree of

Docteur ès sciences

by

Amir Sedaghatkish

Thesis advisors: Prof. Tit. Pierre-Yves Jeannin, SISKA (CH)

Dr. Marc Luetscher, SISKA (CH)

Dr. Frédéric Doumenc, FAST (FR)

Examiners: Prof. Franci Gabrovšek, ZRC SAZU (SI)

Prof. Benoît Valley, University of Neuchâtel (CH)

Defended on the 10th of January 2025

unine
Université de Neuchâtel
Faculté des sciences

Rue Emile-Argand 11
CH-2000 Neuchâtel
doctorat.sciences@unine.ch

IMPRIMATUR POUR THESE DE DOCTORAT

La Faculté des sciences de l'Université de Neuchâtel autorise l'impression de la présente thèse soutenue par

Monsieur Amir SEDAGHATKISH

Titre :

"The Role of Convective Heat and Mass Transfer in the Thermal Response of Karst Conduits"

sur le rapport des membres du jury composé comme suit :

- **Prof. tit. Pierre-Yves Jeannin,** directeur de thèse, Université de Neuchâtel, Suisse
- **Prof. Benoît Valley,** co-directeur de thèse, Université de Neuchâtel, Suisse
- **Dr Marc Luetscher,** ISSKA, Suisse
- **Dr Frédéric Doumenc,** Sorbonne Université, France
- **Prof. Franci Gabrovsek,** ZRC SAZU, Slovénie

Neuchâtel, le 28 janvier 2025

Le Doyen, Prof. P. Brunner

“Perfection is not attainable, but if we chase perfection, we can catch excellence"

Vince Lombardi

Acknowledgements

Completing my PhD has been a journey of growth, challenges, and deep learning, made possible only by the unwavering support and guidance of many individuals.

First and foremost, I extend my deepest gratitude to my supervisors at SISKA (Swiss Institute for Speleology and Karst Studies), Prof. Pierre-Yves Jeannin and Dr. Marc Luetscher. Their invaluable expertise in hydrogeology and karst, combined with their steady guidance, played a pivotal role in shaping the trajectory of this work. Their insightful feedback and thoughtful comments served as a driving force, inspiring and motivating me at every stage of this interdisciplinary project.

I would also like to express my heartfelt thanks to my supervisor Dr. Frédéric Doumenc from FAST (Fluides, Automatique et Systèmes Thermiques). Working under his mentorship has been a great opportunity, offering me not only a wealth of scientific knowledge but also a deeper understanding of what it means to be a researcher. His ability to nurture critical thinking, give supportive advice, and instill the mindset of a scientist helped me shaping the way I approach challenges and ideas.

I extend my sincere gratitude to the members of my thesis committee, Prof. Franci Gabrovšek and Prof. Benoît Valley, for their invaluable time and effort in reviewing this dissertation. This project was funded by Swiss National Science Foundation (SNSF) under grant number 200021_188636.

A special acknowledgment goes to Claudio Pastore, my main collaborator throughout this journey. Claudio has been more than just a colleague. He has also been a close friend, offering much support during both professional and personal moments. His companionship has made this journey not only fruitful but also enjoyable.

My family has been my source of strength and inspiration throughout this journey. My parents, the most important people in my life, endured the difficulties due to my absence during these years. Words cannot fully express my gratitude for their unconditional love and encouragement. Although separated by distance, I have always felt deeply connected to my family, and I hope I can spend more time with them in the rest of my life.

This PhD journey has been more than just an academic pursuit. It has taught me resilience, independence, and a profound appreciation for the relationships and values that truly matter. I am also profoundly thankful to all the members of SISKA and my friends at CHYN. Together, we have shared countless memorable moments over the years, enriching both my professional and personal life.

Abstract

Heat and mass transfer in karst environments are characterized by the complex interactions between geological, hydrological, and atmospheric processes. Karst systems, facilitate unique heat transfer mechanisms through extensive networks of underground fractures, voids and caves representing fragile ecosystems where biogeochemical processes largely depend on temperature. Caves also host unique environmental records whose interpretation closely depends on temperature as well. Achieving a good understanding of the thermal response of karst to atmosphere signals is thus central to quantify dissolution/precipitation rates to interpret geochemical partitioning, to evaluate shallow geothermal extraction efficiency and to determine impacts on organisms living in karst.

Ventilated caves influenced by the chimney effect, where airflow is driven by the density (temperature) contrast between the interior and exterior of the cave, can transmit atmospheric signals to specific distances from entrances—referred to as the convection length—before reaching thermal equilibrium with the surrounding rock. Atmospheric signals consist of different frequencies such as yearly and daily fluctuations with certain amplitudes. The spatial distributions of these amplitudes through cave passages as well as the extent of generated thermal impact on the surrounding rock are investigated in this thesis by developing a thermal model illustrating that the convective length is approximately proportional to the amplitude of the flowrate annual fluctuations divided by the square root of the cave radius. This result is tested against field data from a mine tunnel and two caves.

The real cave passages comprise many obstacles and irregularities increasing the local transfer coefficients and friction compared to the calculated ones from empirical correlations derived for standard pipes. Furthermore, the airflow can transfer water vapor from atmosphere into the cave resulting in local condensation or evaporation. Four thermal scenarios are designed in order to study these complex processes using numerical simulations. The results of one-year field data from monitoring of Longeaigue cave in Switzerland agree with the thermal model results. Finally, an aeraulic-thermal model was developed using the external temperatures and cave aeraulic resistance as inputs calculating air mass flow rate in ventilated caves.

Epikarst located at uppermost layer of karst contributes to the fast transfer of recharge water through fractures by concentrated flow or slow transfer through rock matrix by diffusive flow. A speculative 3D epikarst geometry is built based on the distribution of Discrete Fracture Network (DFN) and a simple thermal model is developed for extreme hydraulic conditions including fully saturated and unsaturated fractures. Although some rainfall intensities are unrealistically high, they can nonetheless be used as extreme hydraulic scenarios during floods. In these cases, convective heat flux in fractures becomes dominant and classical conduction-base models cannot efficiently predict thermal response of underground temperature in epikarst.

Ice-clefts in karstic permafrost region experience temperature variations of atmosphere in the active layer at different time scales. The prediction of melting rate in ice-rich aquifers is essential for their profound impact on their hydrogeological properties, influencing both water availability and the mechanical stability of the ground necessitating a comprehensive understanding of heat transfer mechanisms in this specific medium by developing a fully coupled hydraulic-thermal model. Free convection in meltwater in the ice-clefts occurs due to the anomalous behavior of water between 0 and 4 °C increasing the melting rate by approximately an order of magnitude compared to a model based on purely conduction in stagnant water. The model outcomes are compared qualitatively with field data from Monlesi ice cave in Switzerland and confirm the agreement between real-world observations and the proposed model when free convection is considered.

The results of this thesis provide more detailed insights on different aspects of heat and mass transfer mechanisms in karst systems by considering convective heat flux in ventilated conduits, fractured epikasrt and ice-filled clefts subject to atmospheric temperature variations. Further investigations on this topic can be facilitated by using the current developed models as a basis for the community of geoscience, hydrogeology, and cryosphere.

Keywords

Numerical modelling, convective heat and mass transfer, convection length, ventilated caves, chimney effect, epikarst, DFN, permafrost, free convection, ice melting rate

Résumé

Le transfert de chaleur et de masse dans les environnements karstiques est caractérisé par les interactions complexes entre les processus géologiques, hydrologiques et atmosphériques. Les systèmes karstiques facilitent le transfert de chaleur à travers des réseaux étendus de fractures souterraines, de cavités et de grottes. Ces dernières représentant des écosystèmes fragiles où les processus biogéochimiques dépendent largement de la température. Les grottes abritent également des archives environnementales précieuses dont l'interprétation dépend étroitement de la température. Une bonne compréhension de la réponse thermique du karst aux signaux atmosphériques est donc essentielle pour quantifier les taux de dissolution/précipitation du carbonate, interpréter la distribution géochimique, évaluer l'efficacité de l'extraction géothermique peu profonde et déterminer les impacts sur les organismes vivant dans les karsts.

Les grottes ventilées par l'effet cheminée, où le flux d'air est entraîné par contraste de densité (température) entre l'intérieur et l'extérieur de la grotte, peuvent transférer les signaux atmosphériques à certaines distances des entrées — appelées longueur de convection — avant d'atteindre un équilibre thermique avec la roche environnante. Les signaux atmosphériques consistent en différentes fréquences, telles que les fluctuations annuelles et journalières, avec des amplitudes propres. La distribution spatiale de ces amplitudes à travers les galeries de grottes ainsi que l'étendue de l'impact thermique généré sur la roche environnante sont étudiées dans cette thèse à l'aide d'un modèle thermique démontrant que la longueur de convection est approximativement proportionnelle à l'amplitude des fluctuations annuelles du débit divisé par la racine carrée du rayon de la grotte. Ce résultat est testé avec des données de terrain provenant d'un tunnel de mine et de deux grottes.

Les galeries réelles des grottes comportent de nombreux obstacles et irrégularités augmentant les coefficients de transfert locaux et les frottements par rapport à ceux calculés à partir des corrélations empiriques dérivées pour des tuyaux standard. De plus, le flux d'air peut transporter de la vapeur d'eau, entraînant des phénomènes locaux de condensation ou d'évaporation. Quatre scénarios thermiques sont conçus pour étudier ces processus complexes à l'aide de simulations numériques. Les résultats d'une année de données de terrain issues de la surveillance de la grotte de Longeaigue, en Suisse, concordent avec les résultats du modèle thermique. Enfin, un modèle aéraulique-thermique a été développé en utilisant les températures externes et la résistance aéraulique de la grotte comme entrées pour calculer le débit massique d'air dans les grottes ventilées.

L'épikarst, situé dans la couche superficielle du karst, contribue au transfert rapide de l'eau de recharge à travers les fractures par flux concentré ou au transfert lent à travers la matrice rocheuse par flux diffusif. Une géométrie spéculative en 3D de l'épikarst est construite à partir de la distribution d'un réseau de fractures discrètes (DFN) et un

modèle thermique simple est développé pour des conditions hydrauliques extrêmes incluant des fractures entièrement saturées et non saturées. Bien que certaines intensités de précipitations ne soient pas réalistes, elles peuvent néanmoins être utilisées comme scénarios hydrauliques extrêmes pendant une crue. Dans ces cas, le flux de chaleur convectif dans les fractures devient dominant et les modèles classiques basés sur la conduction ne peuvent pas prédire efficacement la réponse thermique de la température souterraine dans l'épikarst.

Les régions karstiques sujettes au pergélisol subissent des variations de température atmosphérique dans la couche active à différentes échelles temporelles. La prédiction du taux de fonte dans les aquifères riches en glace est essentielle en raison de leur impact profond sur l'hydrogéologie, influençant à la fois la disponibilité en eau et la stabilité mécanique du sol. Une approche complète des mécanismes de transfert thermique dans ce milieu spécifique est proposée au moyen d'un modèle couplant hydraulique et thermique. Dans un réseau de fracture, la convection naturelle dans l'eau de fonte se produit en raison du comportement anormal de l'eau entre 0 et 4 °C, augmentant le taux de fonte d'environ un ordre de grandeur par rapport à un modèle basé uniquement sur la conduction dans l'eau stagnante. Les résultats du modèle sont comparés qualitativement aux données de terrain de la glacière de Monlési en Suisse et confirment l'accord entre les observations réelles et le modèle proposé lorsque la convection naturelle est prise en compte.

Les résultats de cette thèse fournissent des perspectives détaillées sur les différents mécanismes de transfert de chaleur et de masse dans les systèmes karstiques en considérant le flux thermique convectif dans les conduits ventilés, les épikarsts fracturés et les fractures remplies de glace soumises aux variations de température atmosphérique. Des recherches supplémentaires sur ce sujet pourraient être facilitées par l'utilisation de modèles développés comme base pour la communauté des géosciences, de l'hydrogéologie et de la cryosphère.

Mots-clés

Modélisation numérique, transfert de chaleur et de masse convectif, longueur de convection, grottes ventilées, effet cheminée, épikarst, DFN, pergélisol, convection naturelle, taux de fonte des glaces

Table of content

Chapter 1: Introduction

Heat transfer in a karst environment is characterized by the complex interactions between geological, hydrological, and atmospheric processes. In karst systems, heat transfer mechanisms are facilitated by extensive networks of underground fractures, caves, and voids. Water and air flow within karst aquifers act as a significant heat exchange medium, transferring thermal energy between the surface and deeper geological layers. Moreover, the thermal response of karst environments to external temperature fluctuations is modulated by the depth and connectivity of the karst network, making heat transfer in these specific environments a multifaceted and dynamic process influencing the earth's critical zone. This zone is a diverse and dynamic near-surface environment where intricate interactions among rock, soil, water, air and living organisms govern the natural habitat and determine the availability of essential life-sustaining resources (Council et al., 2001).

1.1 Karst landscape

Approximately 20% of the world's land area is covered by karst regions, and around 25% of the global population depends on karst aquifers for their drinking water (Goldscheider et al., 2020). Karst landscapes are characterized by distinctive landforms such as sinkholes, caves, and underground streams, which result from the dissolution of soluble rocks, primarily limestone and dolomite. The formation of conduits and karst networks begins with the infiltration of water into the bedrock through joints, fractures, and bedding planes. Over time, chemical weathering processes enlarge these initial pathways into larger conduits and cave systems (Ford and Williams, 2007; Palmer, 1991). This process is facilitated by carbonic acid formed when water absorbs carbon dioxide from the atmosphere and soil. The chemical reaction between carbonic acid and calcium carbonate in limestone dissolves the rock, enlarging fractures and creating underground cavities. Over tens to hundreds of millennia, continuous dissolution can lead to the development of extensive cave systems and large-scale karst features such as tower karsts and dolines (sinkholes) (Palmer, 1991;Worthington et al., 2000). The flow of water through these systems is influenced by gravity, hydrostatic pressure, and the hydraulic gradient of the region (White, 1988; Ford, 2006). Figure 1 depicts a general schematic of karst landscape which will be elaborated more in next sections.

Airflow also contributes to karstification. It can enhance the evaporation of water, leading to the deposition of minerals such as calcite and the formation of speleothems (stalactites and stalagmites) (Dreybrodt et al., 2005). Additionally, airflow can affect the microclimate within caves, influencing condensation and corrosion processes that further modify the cave environment and contribute to the overall karstification process.

Permafrost and ice-filled clefts significantly influence karst water flow in polar and high-altitude regions. In these environments, the presence of permafrost can inhibit

the infiltration of water, thereby limiting the dissolution processes essential for karstification. Ice-filled fractures can temporarily store water, which, upon melting, can lead to episodic and localized dissolution of the bedrock. This seasonal melting and refreezing can cause physical and chemical weathering, creating unique karst features. The interplay between freezing and thawing cycles results in dynamic karst systems where dissolution is coupled with mechanical breakdown of the rock, often enhancing the development of conduits and cavities (Ford and Williams, 2007; French, 2017; Lauriol and Clark, 1993).

Several factors influence the formation and the rate of evolution of karst landscapes. The solubility of the bedrock, typically limestone or dolomite, is crucial for karst development (Ford and Williams, 2007). The presence of fractures and bedding planes provides pathways for water infiltration and enhances dissolution processes (Goldscheider and Drew, 2007). Climate affects the amount and distribution of precipitation, which in turn influences water availability for karst processes. Humid climates with abundant rainfall promote more extensive karstification compared to arid regions (Groves and Meiman, 2005). The local hydrological conditions, including groundwater flow patterns and the presence of a perched water table, play significant roles in shaping karst systems. Groundwater recharge and discharge areas are often associated with prominent karst features (Ford, 2006; White, 1988). Furthermore, vegetation and soil contribute organic acids to infiltrating water, enhancing its ability to dissolve carbonate rocks. Thick soil cover can also regulate water infiltration rates and protect underlying karst features (Veni et al., 2001). Finally, Anthropogenic activities such as quarrying, land-use changes, and groundwater extraction can impact karst processes. Urbanization and agriculture can alter natural water flow patterns, potentially accelerating or hindering karstification (White, 1988).

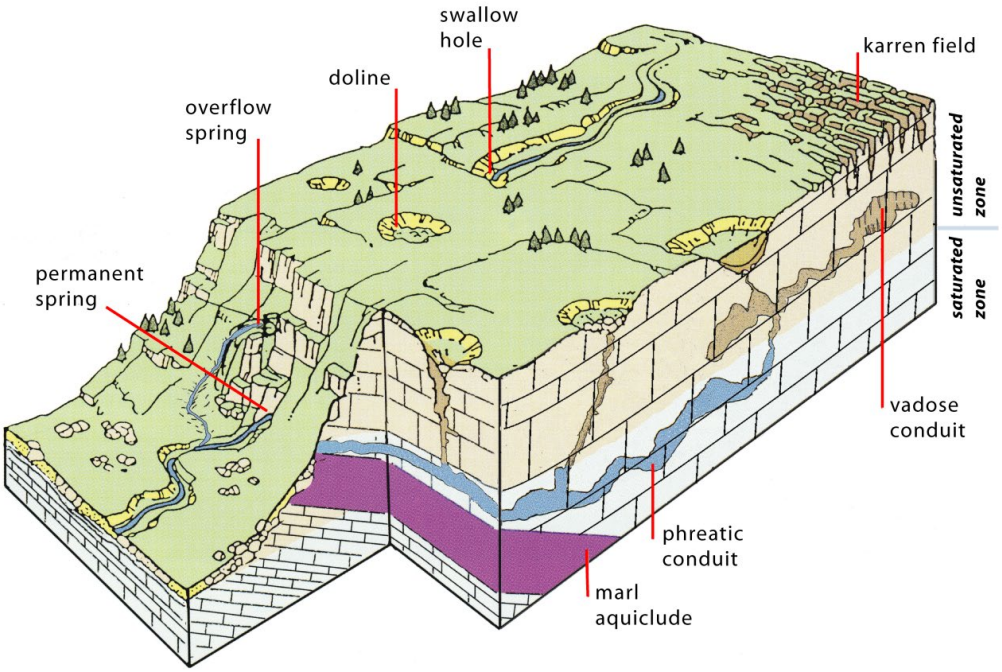

Figure 1. A schematic figure showing karst landscape with some typical surface and underground morphological features (Schaer et al., 1998)

1.2 Thermal configuration of karst (a very general concept)

From a thermal point of view, Luetscher and Jeannin (2004) suggest that karst massifs can be subdivided into two subsystems: the heterothermic and homothermic zones. In heterothermic zone seasonal variations are observed, within the first ~100 meter from the surface. The homothermic zone is situated at greater depths (Fig. 2a), where atmospheric annual temperature variations are almost completely damped. Badino (2018) determines the thickness of the heterothermic zone based on interested time scale. Considering daily or yearly variations results in different thickness of this zone (Fig. 2b). He defines a homothermic layer located under heterothermic zone which the water and rock temperature remains close to the external mean annual temperature and due to water circulation in saturated conduits (shown as horizontal conduit at phreatic zone in Fig. 2-a and blue arrow in Fig. 2-b), geothermal gradient cannot be observed in this layer. The thickness of this layer extends between 50 and 2500 m. In other karst studies, the part of rock massifs (and their caves), where temperature is nearly constant are named differently: "neutral zone" in (Dublyansky and Sockova, 1977; Tikhomirov, 2016) or "isothermal zone" as in (Crestani et al., 1939). A third zone which is called "geothermal layer" is found under the homothermic zone (Badino, 2018) where rock temperature regularly increases with depth, and heat transfer is mainly controlled by conduction of the geothermal heat, as shown in Fig. 2b.

Both the heterothermic and homothermic zones are influenced by the presence of conduits. Heat transfer in the vicinity of these conduits, within the surrounding rock, is predominantly limited to conduction while the effect of convective heat flux is unavoidable within the conduits and fractures. The external surface temperature of

the karst massif results from an energy balance involving different thermal exchanges due to sun radiation, precipitation, evapotranspiration processes, and wind effect on the soil.

The homothermic zone can be unsaturated (vadose) or saturated (phreatic). The former is mainly dominated by ventilated and air-filled conduits but the latter always encloses fully water-saturated conduits (Fig. 2) and exhibits lower temperature gradients compared to the former.

Within the saturated zone, extending to the base of the main conduit network, the temperature gradient approaches zero (Radioti et al., 2017). Below the main conduit system, temperature gradients are predominantly influenced by geothermal heat flux, equivalent to the previously mentioned "geothermal zone" (Luetscher and Jeannin, 2004). Figure 2 shows the thermal interplays between different karst conduits in saturated and unsaturated zones of karst massifs and the corresponding vertical temperature gradients.

In epikarst (the uppermost weathered zone of karst systems), which consists in weathered limestone with tiny fractures and small conduits, heat transfer is influenced by heat conduction from the surface and by the presence of both air and water. It is therefore influenced by the atmosphere temperature variations. The interaction between air, water, and rock in these fractures can lead to localized thermal gradients that impact chemical weathering processes (Williamas, 2008).

The thermal processes taking place in the unsaturated zone of the karst system are poorly understood compared to those of the saturated zone. Highly ventilated caves as well as permafrost active layer in ice-rich karst massifs might be located in unsaturated zones. In this thesis, we focus on the study of their thermal response to external atmospheric temperature variations. Thermal characteristics of ventilated caves and ice-rich karst massifs are introduced in the two following sections.

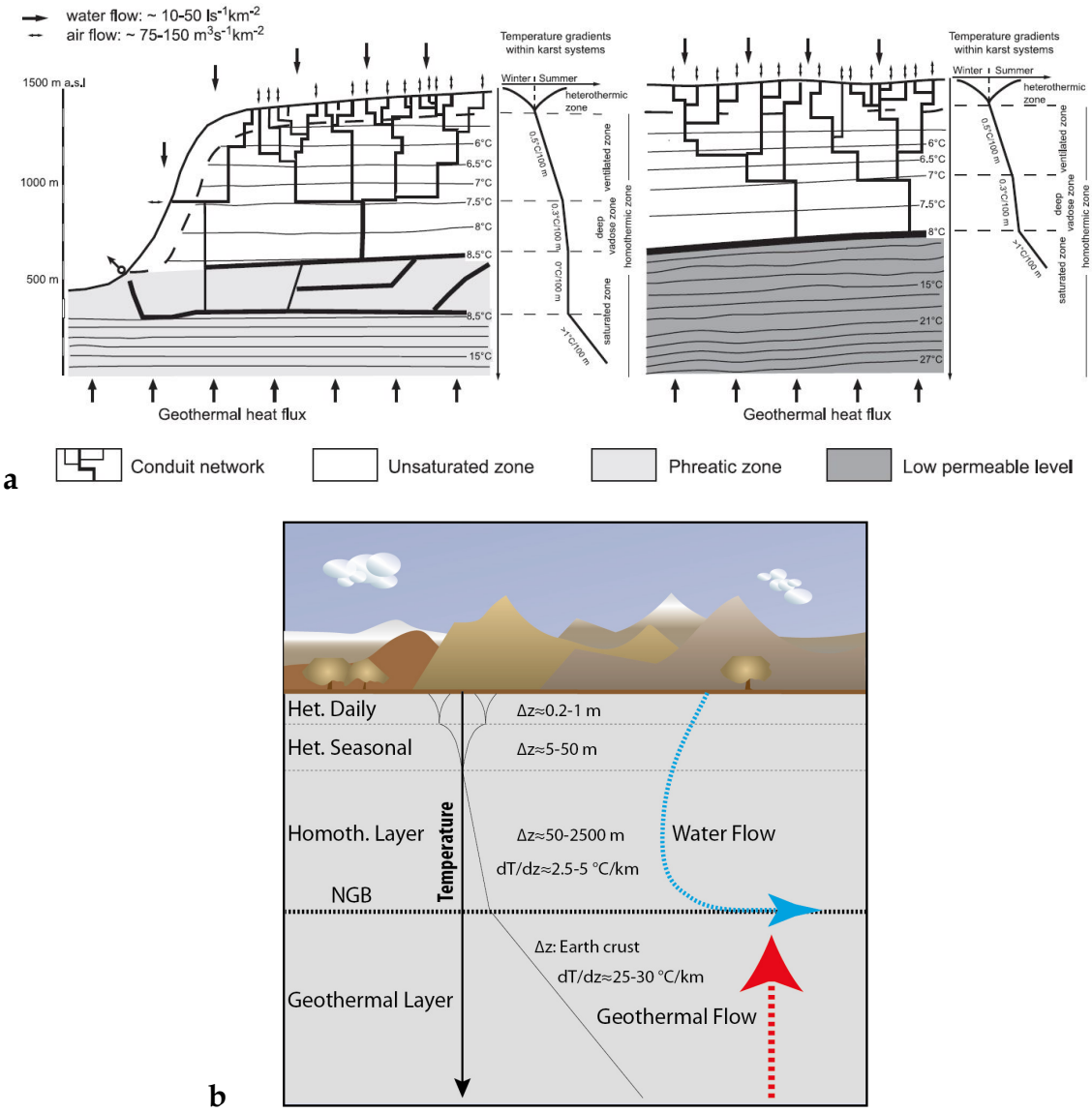

Figure 2. a) temperature gradient at different elevations of karst massifs in the saturated and unsaturated zones (from Luetscher and Jeannin, 2004) b) Heterothermic layers, with daily and seasonal temperature ranges; Homothermic layer with small gradient close to zero; Undisturbed geothermal layer in thermal contact with deep rocks (from Badino, 2018)

1.2.1 Ventilated caves

Ventilated caves are subterranean systems where air circulation plays a significant role in their environmental dynamics. These caves often have multiple entrances or connections to the surface, allowing for the movement of air between different parts of the cave and the outside environment (Hill and Forti, 1997).

Two types of ventilated caves are observed depending on the origin of the driving force inducing the airflow:

1- Caves ventilated by a so-called "chimney effect", where the driving force is due to the density difference between the cave and the outside atmosphere,

2- Caves ventilated by the so-called "barometric effect", where the driving force is due to the pressure difference between the cave and the outside atmosphere.

The barometric effect dominates the caves with a large volume and only a few entrances at the same elevation. Any variation of the atmosphere pressure close to the entrance will induce a volume change of the air in the cave, breathing air in or out of the cave. The pressure variation may be related to changes in atmospheric pressure, wind or local climate changes (Gomell et al., 2021; Perrier et al., 2023). The most common form of ventilation is the density-driven chimney effect which are seen in caves with at least two entrances at different elevations. The air flows in or out of the cave due to a density contrast between the air column inside and outside of the cave. In summer, the atmosphere temperature outside the cave is higher than the air temperature inside leading to a greater air density inside the cave. So, the airflow is downward in summer and upward in winter. Figure 3 shows a sketch of the airflow direction in summer and winter for a cave ventilated under the chimney effect with two entrances at different elevations.

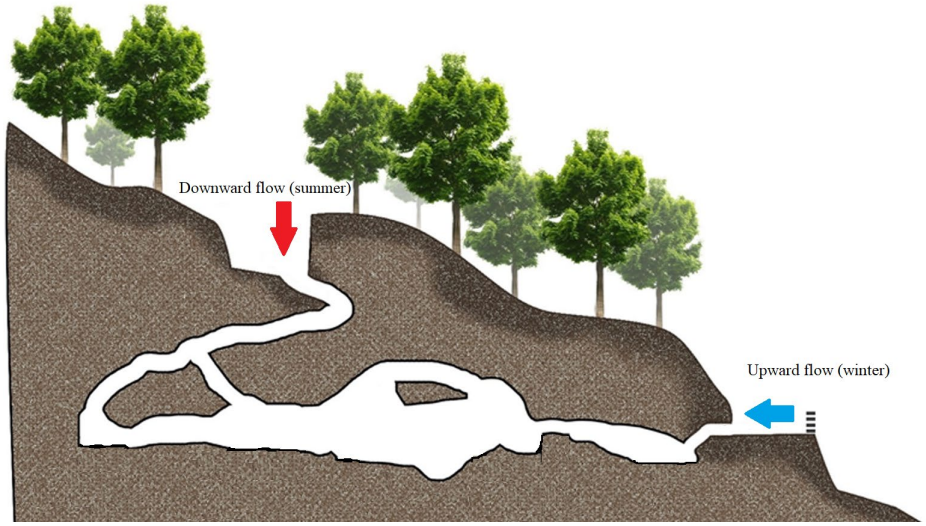

Figure 3. A very simple schematic figure showing the direction of airflow in ventilated caves under chimney effect

It has long been known that, in large cave systems, the convective transport of heat by air currents and streams can propagate thermal perturbations over much larger distances than predicted by a pure conduction model. Cropley (1965) conducted temperature measurements in two West Virginia caves, identifying three distinct zones. Zone I, near the cave entrance, exhibited temperature fluctuations influenced by surface conditions. Zone II was dominated by temperature variations driven by streams and air currents. Zone III maintained a nearly constant temperature, closely aligned with the annual surface mean. Regions where temperature fluctuations were less than 1°F (approximately 0.56°C) around the annual mean were found over 1500-m from the cave entrances. This large distance is mainly due to the cold water entering

the caves during winter recharge. Luetscher and Jeannin, (2004) introduced the concept of the heterothermic vadose zone, the upper part of a karst massif where seasonal temperature gradient inversions occur. In contrast, the homothermic vadose zone features a temperature gradient similar to the lapse rate of humid air (approximately 0.5°C per 100 m). They estimated the distance of heterothermic zone to ground surface is about 100 m in most cases.

One of the key features of ventilated caves is the presence of a "thermal (convection) length". The air entering the cave with a different temperature from that of the rock tends to exchange heat with the surrounding rock and reaches thermal equilibrium after a certain distance. This length from cave entrance to a certain point inside the cave is called thermal (convection) length. This means that the external temperature variations have a thermal impact on the cave until the thermal length. At higher distance from the entrance, air and wall temperatures are the same and remain constant throughout the year. The atmosphere temperature varies according to several modes of frequency such as daily and yearly fluctuations. Of course, smaller frequencies such as centennial and millennial fluctuations also exist with certain amplitudes. The amplitude of these frequencies attenuates differently along the cave passage. The thermal impact of atmosphere temperature variations not only can be seen within the thermal (convection) length along the cave passage but also it is perceptible in the surrounding rock within a certain length which is called "thermal width".

It turns out that distinct microclimates should exist within different sections of the cave system having different thermal responses based on the interested time scale. For instance, areas near entrances may experience more significant temperature and humidity fluctuations compared to deeper parts of the cave, which remain more stable. This variability can influence the life conditions along the cave, but also the rate of mineral deposition and the types of speleothems that form. In ventilated caves, formations such as stalactites and stalagmites tend to grow more rapidly than in non-ventilated caves due to the enhanced evaporation and CO_2 exchange facilitated by air movement (Ford and Williams, 2007).

1.2.2 Ice-rich aquifers

Ice-rich aquifers are subsurface water-bearing formations that contain significant amounts of ice. These aquifers are typical of permafrost regions, where the ground remains frozen for extended periods, often spanning hundreds to thousands of years. The presence of ice within these aquifers has a profound impact on their hydrogeological properties, influencing both water availability and the mechanical stability of the ground (Woo, 2012).

In ice-rich aquifers, the water exists in both liquid and solid phases. During the warmer months, seasonal thawing can lead to the formation of an active layer where the ice melts, increasing the liquid water content and permeability of the soil. This

process creates a dynamic environment where the aquifer's capacity to store and transmit water fluctuates seasonally. The meltwater from these ice-rich layers is crucial for sustaining local ecosystems and providing a water source for human use in arctic and subarctic regions (Hayward et al., 2018; Pelletier et al., 2018). Figure 4 shows some patterns of these ice-rich aquifers in different geological contexts for example in soil (Fig. 4a) and an ice-cleft in alpine karst (Monlesi cave) in Switzerland (Fig. 4b).

Figure 4. Ice-rich aquifers in karst permafrost a) Exposed permafrost along an eroded Arctic coast (https://www.nps.gov/subjects/aknatureandscience/permafrost.htm) b) Monlesi cave (Photo taken by A. Conne)

The thermal dynamics of ice-rich aquifers are complex, as they are influenced by both climate and surface conditions. Changes in air temperature, snow cover, and vegetation can alter the thermal regime of the ground, leading to variations in the thickness and extent of permafrost. For instance, Bartolomé et al., (2023) found that some parts of the Devaux cave located in mountain permafrost are dominated by advective airflow and also heat release by local cave streams increasing the cave air temperature seasonally above 0°C, which in turn affects the amount of meltwater. Or, in arctic karst caves, massive ice blocks the passage. This is due to the condensation of water vapor from warm humid air entering the cave during summer and subsequent freezing in winter (Lauriol and Clark, 1993).

Long-term warming trends associated with climate change are causing permafrost to degrade, thereby affecting the stability and behavior of ice-rich aquifers. As the permafrost thaws, the ground may become more susceptible to subsidence and erosion, potentially impacting infrastructures (Larsen et al., 2008; Cheng, 2005).

Research into ice-rich aquifers is vital for understanding the implications of permafrost thaw on hydrology and water resources. These aquifers act as important reservoirs of freshwater, and their response to climate change can have significant consequences for water availability in cold regions. Studies combining field observations, remote sensing, and modeling are essential to predict the melting rate concerning any changes in these systems and to develop adaptation strategies for

communities and ecosystems reliant on permafrost environments (Walvoord and Kurylyk, 2016).

1.3 Modeling heat transfer in karst

Modeling heat transfer in karst conduits and rock massifs provides information about their thermal response to outside temperature variations. So far, researchers have developed numerous models by employing different assumptions in order to study the thermal response of caves and permafrost to temperature variations in karst environments. These assumptions are based on many simplifications in terms of geometry or governing equations. In this section, we are going to have a brief overview of available models based on the main heat transfer mechanism to study the thermal response of different zones of karst massif.

1.3.1 Conduction

A large part of studies in literature introduces conduction dominating the heat transfer from external atmosphere to underground and infer the convection is limited to the cave entrances in vadose zones (Faimon et al., 2012; Villar et al., 1983; Domínguez-Villar et al., 2013). For instance, Domínguez-Villar et al., (2023) modeled a cave temperature by employing 1D heat conduction equation. The thickness of the bedrock in their model determines the thermal attenuation and the signal delay from the atmosphere temperature. They justified the discrepancy between their model and field data by variability of water content in rock porosity through time leading to different values of thermal diffusivities.

Quindos et al., (1987) conducted a year-long study measuring the monthly mean temperatures within Altamira cave. Their findings indicate that the periodic 1D conduction model accurately predicts both the amplitude and phase shift of the annual temperature fluctuations at the cave roof, where the depth ranges from 3.5 meters to 17.5 meters.

Salmon et al. (2023) developed a model based on purely conduction heat flux in Lascaux cave and they considered that the ground surface and atmosphere temperature are not equal. They computed the surface temperature based on an energy balance of different thermal processes including heat fluxes due to surface convection (related to wind velocity), radiation and soil evapotranspiration. Although there was a good agreement between the temperature measured in the cave and the modeled one, in some locations significant discrepancies were reported. These have been associated to local free convection cells within the cave rooms.

Despite of usefulness of purely conduction models for finding temperature in impermeable solid rock, such thermal models may not be very precise for prediction of the thermal response in shallow caves with negligible ventilation. More realistic model was introduced by Guerrier et al., (2019) considering the coupling of conduction with free convection and radiative heat flux induced by the temperature

difference between cave ceiling and floor . This phenomenon takes place in non-ventilated caves located at shallow depth (<~20 m) as the temperature difference between ceiling and floor triggers free convection. At greater depth, the upper and lower cave walls may be in thermal equilibrium with the air inside the cave.

Concerning ice-rich aquifers, many thermal models were developed for assessing permafrost degradation in heterogenous media. In most models, the temperature distribution of ground layers and water, and its response to climate change is predicted by considering mainly 1D conduction and latent heat fluxes of melting in soil (Malakhova, 2022; Ivanov and Rozhin, 2022; Schuster et al., 2018; Cicoira et al., 2019; Hornum et al., 2020). Even though conventional 1D transient models are not suitable for every context, they offer several advantages including low computational costs and easy implementation to make them widely applied. Pruessner et al., (2021) investigated glacier runoff associated with permafrost degradation in high Alpine catchments. They used two different methods GERM (Huss et al., 2008) and SNOWPACK (Bartelt and Lehning, 2002) which are based on 1D transient conduction considering latent heat of melting, different thermal properties of ground layers constituents and ventilation effects. This distributed model is efficient for calculation of temperature in large domains (catchment scale) but may not efficiently work in particular contexts such as ice-clefts or ice-rich confined aquifers.

1.3.2 Convection and other heat fluxes

In karst, water or airflow concentrates within the conduits generating advective fluxes under different circumstances. “How much does the corresponding advective heat flux impact the conduit temperature and the surrounding rock?” is a key question in this respect.

Many researchers so far developed some models highlighting the effect of air or water-forced convective flux in the karst environment. While the thermal effect of water convection is underlined mainly in saturated (or phreatic) zone of karst conduits, airflow is reported frequently in caves located in the unsaturated (or vadose) zone implicating also the existence of convective heat flux related to air.

Covington et al. (2011) explore various mechanisms influencing heat transport in partially saturated karst aquifers. The study critically examines previous models of heat transport in literature showing a clear lack of validation with field data. By utilizing analytical solutions, the authors assess the relative importance of conduction, convection, and radiation concerning various timescales. They found that conduction through the surrounding rock predominantly governs heat exchange over timescales longer than a week (the conduit wall and water temperatures remain close to each other and vary along the conduits). The study also highlights the significant role of radiative heat flux in open channel conduits. The developed numerical model, validated against field observations from two distinct karst settings, demonstrates its applicability in accurately simulating thermal responses in partially saturated karst

systems. The findings underscore the necessity of coupling conduction-convection into heat transport models for realistic simulations. In a more recent study, Luo et al. (2023) investigated the thermal responses of groundwater in karst springs in South China, aiming at understanding the heat exchange mechanisms between recharge water and surrounding rock formations. Using an analytical solution for heat transfer in karst conduits, the research simulates the temperature variations in four karst springs with circulation depths ranging from 60 to 820 meters. The study finds that the hydraulic diameter, flow velocity, input temperature, and circulation depth are crucial factors influencing thermal equilibrium depth and heat exchange efficiency. In shallow aquifers, insufficient heat exchange leads to distinct temperature peaks and troughs corresponding to seasonal changes, while deeper aquifers reach thermal equilibrium, resulting in stable temperatures. Although these models are very useful for conduits filled or partially filled with water, they are not applicable for ventilated conduits as the effect of airflow reversal and latent heat flux (evapo-condensation) is not taken into account.

Some other studies can be seen in references (Qaddah et al., 2023; Qaddah et al., 2022; Guerrier et al., 2019) implicating that in closed shallow caves with negligible ventilation other mechanisms such as wall radiation and free convection heat fluxes can be of significance for determining cave temperature. On the other hand, in ventilated caves, Kukuljan et al. (2021) believe that "Advection is the main driving force of spatial and temporal variations in atmospheric parameters in the karst vadose zone".

One of the premier and first study about the airflow in karst conduits and the modelling of the conjugated convective and latent heat flux was proposed by Wigley and Brown (1971) who calculated the temperature and moisture content profiles in the air as a function of the distance from the entrance. They used a 1D model based on the energy and water mass conservation in the airflow. The convective heat transfer coefficient between the air and the wall was estimated using an empirical correlation valid for forced convection in smooth pipes. The model assumes prescribed uniform wall temperature, a major simplification that allows to obtain simple closed-form expressions for the temperature and moisture profiles. De Freitas and Littlejohn (1987) used the model of Wigley and Brown to describe the latent heat flux within caves. Considering the cave's boundary conditions and environmental inputs in their model, they provided some insights into the spatial and temporal distribution of condensation and evaporation processes. However, this approach assumes that the heat flux through the cave wall is convection-limited and that the rock mass does not contribute to heat transfer.

Lismonde (2002) pointed out that the airflow modifies the rock temperature, therefore it changes the air temperature profile in the cave. This author developed a model to predict heat transfer in a straight inclined pipe of constant diameter included in a rock massif. The model couples 1D radial conduction in the rock mass with convective

transfer in the air, using a sinusoidal function of time as inlet temperature. The airflow rate was predicted by considering the interaction between the temperature field inside and outside the conduit through the buoyancy term in the momentum balance equation. This model reproduced qualitatively some field observations, e.g. the thermal anomaly in the entrance areas. Recently, Gabrovšek (2023) studied the airflow patterns in karst caves, focusing on the chimney effect driven airflow in ventilated caves. The research presents a numerical model of airflow in a passage thermally coupled to the surrounding rock mass, examining how passage geometry influences airflow. Key findings include the role of airflow velocity in determining relaxation length and the impact of non-uniform passage profiles, such as L-shaped or V-shaped outlines, on airflow patterns. Seasonal asymmetry in airflow rate is noted, with distinct differences in ventilation during warm and cold periods. The study also highlights how snow and ice accumulation can alter airflow patterns, leading to the formation of ice caves. Although these studies provide helpful information and basic formulations for building thermal models in ventilated caves, their model results were hardly validated by field data. Additionally, these models did not consider the effect of evaporation cooling and condensation warming which is an obvious phenomenon in ventilated caves.

1.4 Relevance of heat and mass transfer in karst environment

The unique characteristics of karst landscapes, which include features such as fractures, caves, sinkholes, and underground streams, make them particularly sensitive to thermal dynamics. Understanding heat transfer mechanisms within these systems is essential for multiple questions, from environmental monitoring to water resources management.

In the saturated zone, water temperature acts as a non-conservative tracer in the environment. As water travels through the rock, its heat is exchanged (mitigated and delayed) with the surrounding rock (Luhmann et al., 2012) providing information about the volume and geometry of conduits, recharge mode and aquifer depth (Birk et al., 2006; Long and Gilcrease, 2009; Liedl et al., 1998).

In the unsaturated zone, also known as the vadose zone, caves are located above the water table where air and water interact within the rock. This zone recharges karst aquifers as it allows for the infiltration of rainwater, in partially filled conduits through the unsaturated zone, from ground surface to the phreatic zone, flowing mainly vertically downwards. Cave ventilation in the vadose zone is variably intense leading to various microclimates, which affect the development of speleothems (Ford and Williams, 2007). According to De Freitas and Schmekal (2003), as the exchange of heat between the cave atmosphere and the external environment can significantly influence the speleothem growth. Additionally, airflow can transport heat over long distances within cave systems, leading to temperature variations that impact the growth of speleothems as well as biological communities and chemical reactions within the cave environment (Lismonde, 2002).

Mass transfer through condensation and evaporation also plays a vital role in the formation of speleothems which are carbonate cave deposits that form as the result of precipitation from flowing or dripping groundwater (Elias, 2013) and are mainly referred to as stalagmites, stalactites and flowstone (Sinha et al., 2010). The rate and nature of speleothem formation provide valuable information about past climatic conditions. Research by Fairchild and Baker (2012) highlights that variations in speleothem growth rates can be correlated with historical climate data, offering insights into paleoclimate reconstructions.

Moreover, the processes of condensation and evaporation influence the humidity levels and temperature within the cave, which are critical for maintaining the delicate equilibrium of the cave environment. According to a study by De Freitas and Littlejohn (1987), the microclimate of a cave, including temperature and humidity variations, can significantly impact both geological formations and biological communities. High humidity, resulting from condensation, can promote the growth of microbial mats and cave flora, which in turn can affect the cave's nutrient cycles and energy flow. Dublyansky and Spötl (2015) further note that condensation corrosion, a process where condensed water dissolves rock surfaces, significantly alters cave morphology over time. This can result in the deterioration of speleothems and other cave features. Besides that, condensation could be even a source of water for karst aquifers.

Additionally, understanding these processes is essential for cave conservation and management. Prehistorical painted caves such as Lascaux cave is under the danger of vermiculation process (thin, irregular and discontinuous deposits of incoherent materials commonly found on the walls of caves as defined by Bini et al., (1978)). The humidity, temperature changes and the chemical compound of the water film on the cave wall are important factors for triggering vermiculation (Freydier et al., 2021). Human activities, such as tourism and mining, can alter the cave's natural ventilation and humidity levels, leading to accelerated evaporation rates or changes in condensation patterns (Baker and Genty, 1998). For instance, Cigna (1993) discusses how changes in air circulation and humidity caused by human interference can lead to the desiccation of cave formations and the disruption of the cave's ecological balance. Further research by Lario and Soler (2010) indicates that even minor modifications to cave environments can result in significant changes to speleothem growth and preservation.

In summary, the study of heat and mass transfer processes within caves is fundamental for paleoclimate reconstruction, for maintaining cave microclimates, and for ensuring the conservation of these unique environments. Ongoing research in this field continues to shed light on the intricate interactions between geological, hydrological, and biological processes within cave systems.

1.5 Research motivation

As previously mentioned, most researches to date have focused on the thermal response of the saturated zone of karst systems. However, there are a few studies describing the thermal response of the unsaturated zone within highly ventilated conduits or the effect of (water) convection on permafrost thawing in ice-rich aquifers (or ice-clefts).

Considering only conduction, which is typical in many available thermal models, causes a very shorter length scale for perfect attenuation of external signals in karst conduits (which is called diffusion length) compared to convection length. The diffusion length is proportional to the square root of the fluctuation period multiplied by the thermal diffusivity of the rock. Although Lismonde (2002) and Gabrovšek (2023) developed preliminary thermal models for ventilated conduits highlighting the impact of airflow, there still remains a gap in detailed understanding of the effects of convection and latent heat flux in ventilated caves subject to the chimney effect. The concept of convection length — the distance from a cave entrance to a location inside the cave where the temperature is influenced by external climatic variations — has not yet been correlated with certain geometrical and flow characteristic parameters for different amplitudes of external fluctuations. Airflow convection not only affects the cave passage temperature but also generates a thermal field within the surrounding rock. Due to the lack of systematic comparison between model results and field data, it is difficult to evaluate the efficiency of existing models. Moreover, a comprehensive thermal model that simultaneously considers convection, conduction, and latent heat flux has not yet been developed. Such a model would require the incorporation of mass transport equations to determine water vapor concentration spatially and temporally.

Additionally, in mountain permafrost or arctic karst caves, these external climatic variations can melt the ice-filled clefts distributed in rock massif. The accumulated meltwater at the top of the ice can experience temperatures above zero due to daily warming. Building thermal models considering the effect of water free convection on the melting rate of permafrost thawing has not been already examined. This convection may accelerate the melting rate of ice-rich aquifers (ice-clefts) due to the anomalous behavior of water density between 0 and 4°C.

These concerns regarding the impact of "**convection**" motivate us to develop novel thermal models that incorporate this mechanism of heat transfer. These models will enable more accurate predictions of the thermal response of the unsaturated zone of karst and their original contributions are twofold: (1) the derivation of a quantitative scaling law for the convection length; (2) comprehensive comparisons between numerical simulations and field data to test the capabilities and limitations of the model which cannot be seen in the literature. Therefore, this thesis aims to fill this gap by using the principles of fluid dynamics, heat and mass transfer, providing a more

realistic model and analysis for the community of geoscience, hydrogeology, and cryosphere.

1.6 Research strategy / Structure of the thesis

This thesis focuses on modeling heat transfer in the unsaturated zone of karst systems. This includes the effect of convection heat transfer in "ventilated caves (conduits)" and "ice-rich aquifers (ice-filled clefts)" in active layer of permafrost for karst areas situated in polar regions or high altitudes. The content of this thesis is divided into five main chapters which are briefly described as follows:

1.6.1 Chapter 2: Modeling heat transfer for assessing the convection length in ventilated caves (published paper)

In this chapter, a very general thermal model is developed for ventilated caves with a simplified geometry. The external temperature consists of only yearly average and yearly amplitude of fluctuations and the corresponding mass flow rate is estimated with a straightforward assumption. The heat transfer equation for dry air is derived from coupling convection inside a 1D conduit with constant diameter and conduction in a 2D-axisymmetric rock domain. The main strategies used in this chapter can de listed as following:

1- Determining the main controlling variables (dimensionless numbers) quantifying the thermal response of ventilated caves
2- Estimation of a lower and upper bound of heat transfer coefficient using Gnielinski empirical correlation and infinite heat transfer coefficient, respectively.
3- Using Fourier series for reaching a periodic regime avoiding high computational costs produced by using time integration

The main outcomes of this chapter are as follows:

1- The quantitative definition of the convection length as a distance between cave entrance and a point inside the cave where the cave temperature is no more under the influence of external temperature variations. This will be elaborated in detail in chapter 2,
2- Characterization of the convection length as a function of dimensionless numbers after testing different parametric studies and finally introducing a general formula for expressing the order of magnitude of the convection length in ventilated caves,
3- Comparing the developed formula with the field data from three ventilated conduits in order to assess the efficiency of the developed model.

1.6.2 Chapter 3: Thermal modelling of caves ventilated by chimney effect (paper under review)

In the third chapter, we try to modify the model developed in the first chapter by employing more realistic assumptions. A systematic comparison between the field data from Longeaigue cave in Switzerland and the modelling results with different scenarios is given in this part. The main strategies used in this chapter are listed as follows:

1- Modifying the model developed previously by imposing different assumptions such as variable cave diameter and measured mass flow rate as well as external upper and lower entrance atmosphere temperature from field data (including daily fluctuations),
2- Adding mass transfer equation considering humid air and the corresponding latent heat flux in the energy balance between cave wall and air,
3- Introducing four different scenarios including dry and humid air associated to finite and infinite heat transfer coefficients as four possible scenarios in the thermal study of ventilated caves.

The main outcome of this chapter is the evaluation of the thermal performance of the four scenarios in comparison with field data in Longeaigue cave. The annual mean temperature, annual and daily temperature fluctuations along the cave passage are compared with field data. Other issues such as the discrepancy between the field data and the model results due to the effect of boundary condition at the external ground surface on thermal history of rock massif, potential difference between sensor temperature and air/wall temperatures as well as the amount of water produced by condensation or consumed due to evaporation along the cave are discussed to illustrate the weakness and capabilities of the developed model.

1.6.3 Chapter 4: Developing an aeraulic-thermal model for ventilated caves with known cave resistance (unpublished)

In this chapter, an aeraulic-thermal model is developed in order to calculate the resulting mass flow rate from the chimney effect using only external temperatures and cave resistance as the model inputs. Finding the cave aeraulic resistance is a prerequisite input of this model. The momentum equation is coupled with the energy balance leading to more complexity of governing equations. This chapter is complementary to the previous chapter using the same variables and parameters.

1.6.4 Chapter 5: Modeling the thermal response in epikarst (unpublished)

A purely qualitative thermal analysis in epikarst including 3D Discrete Fracture Network (DFN) and impermeable rock is developed for extreme hydraulic scenarios corresponding to fully saturated and unsaturated fractures. The rapid infiltration of rainfall water may lead to significant convective heat flux inside the fractures which consequently penetrates to surrounding impermeable rock by conduction.

This chapter provides some insights into the relative significance of convective heat flux in air and water compared to conduction in the fracture network in epikarst.

1.6.5 Chapter 6: Modeling the effect of free convection on permafrost melting-rates in frozen rock-clefts (published paper)

In this chapter, the effect of liquid water free convection is examined on melting rate of ice-clefts in active layer of permafrost under daily atmosphere warming. The model is based on incompressible Navier-Stoke equations assuming Boussinesq approximation for modelling free convection. The heat transfer equation uses the apparent heat capacity approach in order to model the latent heat of melting inside a 2D initially filled ice-cleft surrounded by rock massif. The main outcomes of this chapter are mentioned as follows:

1- The free convection of liquid water resulting from abnormal behavior of water density between 0 and 4°C may increase the melting rate by about one order of magnitude compared to stagnant liquid water in the absence of free convection;
2- The liquid water temperature on top of ice-clefts remains between 0 and 1°C due to the mixing and circulation of water;
3- The aperture size is an important geometrical parameter determining the intensity of free convection on the melting rate. The effect of free convection on ice-clefts with lower aperture size will be reduced gradually and finally, within a certain height of meltwater, the impact of free convection disappears;
4- The melting rate of an ice-cleft in Monlesi cave in Switzerland was monitored for four days and was compared with the results of the developed model considering free convection.

Chapter 2: Modeling heat transfer for assessing the convection length in ventilated caves (published paper)

Sedaghatkish, A., Pastore, C., Doumenc, F., Jeannin, P.-Y., & Luetscher, M. (2024). Modeling heat transfer for assessing the convection length in ventilated caves. *Journal of Geophysical Research: Earth Surface*, 129, e2024JF007646. https://doi.org/10.1029/2024JF007646

Abstract

The present study focuses on heat transfer in ventilated caves for which the airflow is driven by the temperature contrast between the cave and the external atmosphere. We use a numerical model that couples the convective heat transfer due to the airflow in a single karst conduit with the conductive heat transfer in the rock mass. Assuming dry air and a simplified geometry, we investigate the propagation of thermal perturbations inside the karst massif. We perform a parametric study to identify general trends regarding the effect of the air flowrate and conduit size on the amplitude and spatial extent of thermal perturbations. Numerical results support the partition of a cave into three regions: (1) a short (few meters) diffusive region, where heat mainly propagates from the external atmosphere by conduction in the rock mass; (2) a convective region where heat is mainly transported by the air flow; (3) a deep karst region characterized by quasi-constant temperatures throughout the year. Numerical simulations show that the length of the convective region is approximately proportional to the amplitude of the flowrate annual fluctuations divided by the square root of the cave radius. This result is tested against field data from a mine tunnel and two caves. Our study provides first estimates to identify climate sensitive regions for speleothem science and/or ecosystemic studies.

1. Introduction

Understanding heat transfer in karst systems is a key issue for underground biota (Mammola et al., 2019), preservation of cave art (Bourges et al., 2014), speleothem growth rates (Spötl et al., 2005; Banner et al., 2007), or paleoclimate reconstruction (Borsato et al., 2016; Casteel and Banner, 2015; Domínguez-Villar et al., 2021). However, heat transfer in karst results from an intricate coupling between several mechanisms, including heat conduction in the rock mass (Quindos et al., 1987), convection due to water or air flow in caves (Cropley, 1965), or radiative transfer between cave walls (Guerrier et al., 2019). Latent heat exchanges are also present because of evaporation and condensation on cave walls (Dreybrodt et al., 2005) or ice formation and permafrost (Luetscher et al., 2008). A key issue for the understanding of heat transfer in karst is to determine the processes that dominate in a given configuration, and those that can be neglected.

The simplest heat transfer model of a vadose karst assumes 1D conduction heat transfer in a rock mass of infinite depth with periodic temperature fluctuations at the

ground surface (Villar et al. 1983; Domínguez-Villar et al. 2023; Salmon et al., 2023). This model predicts that the depth corresponding to 99% attenuation of the temperature fluctuations at the ground surface is a few tens of centimeters for the daily fluctuations and approximately 10 m for the annual fluctuations. Quindos and co-workers (Villar et al., 1983; Quindos et al., 1987) measured the monthly mean temperatures in Altamira Cave during a year. They found that the periodic 1D conduction model correctly predicts the amplitude and the phase shift of the annual fluctuations at the cave roof whose depth varied from 3.5 m to 17.5 m. In contrast, the floor temperature was much closer to the roof temperature than expected from a 1D conduction model. The authors attributed this effect to the homogenization of the temperature field by radiative transfer between roofs and floors. Guerrier et al. (2019) and Qaddah et al. (2023) confirmed by numerical simulations the significance of radiative transfer inside weakly ventilated shallow caves, and showed that turbulent free convection also had to be considered. Both heat transfer mechanisms contribute to the homogenization of the wall temperature and the deformation of the temperature field in the rock matrix around the cave.

The situation is different when forced convection is present. It has long been known that, in large cave systems, the convective transport of heat by air currents and streams can propagate thermal perturbations over much larger distances than predicted by a pure conduction model. Cropley (1965) found that temperature measurements performed in two caves in West Virginia supported the definition of three zones: zone I immediately adjacent to the cave entrance, where the cave temperature follows the surface temperature fluctuations; zone II where the cave temperature is driven by streams and air currents; zone III where the temperature is approximately constant and close to the annual mean temperature at the surface. Areas where the amplitude of temperature fluctuations was lower than 1°F (*ca.* 0.56°C) around the annual mean temperature were located at more than 1500 m from the cave entrances. This long distance was mainly due to cold water carried into the caves by winter water recharge. Luetscher and Jeannin (2004) defined the heterothermic vadose zone as the surficial part of a karst massif showing seasonal inversions of the temperature gradient, in contrast with the homothermic vadose zone characterized by a temperature gradient close to the lapse rate of humid air (*ca.* 0.5°C 100 m^{-1}). These authors estimated the depth of the heterothermic zone at about 100 m in most cases.

Considerable work has been undertaken to simulate heat transfer by forced convection due to water flow in the vadose and phreatic zones of karst (Gong et al., 2019; Long and Gilcrease, 2009; Sinokrot and Stefan, 1993). Covington et al. (2011) showed that the relative significance of different heat fluxes including convection and conduction are timescale dependent. Conduction through the rock surrounding a conduit determines heat flux at times of the order of weeks and longer. Coupling convection in water with conduction in rock is thus necessary to get a realistic model valid at all time scales.

Forced convection due to airflow must be considered when a network of karst conduits has at least two entrances. In this configuration, several mechanisms can contribute to the production of airflow through the cave, resulting in significant convective heat transfer between the cave and the external atmosphere. Potential driving forces are barometric fluctuations (Gomell et al., 2021), dynamic pressure effect due to external winds (Kukuljan et al., 2021), diphasic flow due to water circulation (Atkinson, 1977), or the buoyancy due to the density contrast between the air inside and outside of the cave (Gabrovšek, 2023). The latter mechanism is likely the most significant in most cases. The air density depends on moisture content, CO_2 concentration and temperature. In temperate climates, temperature fluctuations are the main cause of density variations (Gabrovšek, 2023). Therefore, the flow direction is upward when the temperature inside the cave is warmer (or downward when inside the cave is colder) than the external atmosphere. Because of the thermal inertia of the massif, a lower entrance operates as an inlet of cold external air during most of the winter, whereas it acts as an outlet during most of the summer. In the latter case, the air cooled down when crossing the massif before getting out the lower entrance. The lower entrance thus receives in summer an airflow colder than the external temperature. Because of this seasonal asymmetry, the annual mean temperature is shifted to colder values at lower entrances (cold thermal anomaly). The same mechanism produces a shift of the annual mean temperature to hotter values at upper entrances (hot thermal anomaly) (Lismonde, 2002). In alpine ice caves, where this ventilation pattern represents the normal unless the cave is clogged with sediments, these thermal anomalies usually extend over a few hundred meters from the cave entrances (Luetscher et al., 2008).

Wigley and Brown (1971) calculated the temperature and moisture content profiles in the air as a function of the distance from the entrance. They used a 1D model based on the energy and water mass conservation in the airflow. The convective heat transfer coefficient between the air and the wall was estimated using an empirical correlation valid for forced convection in smooth pipes. The model assumes prescribed uniform wall temperature, a major simplification that allows to obtain simple closed-form expressions for the temperature and moisture profiles. However, this approach implicitly assumes that the heat flux through the cave wall is convection-limited, and that the rock mass does not play any role. Lismonde (2002) pointed out that the airflow modifies the rock temperature, which in turn changes the air temperature profile in the cave. This author developed a model to predict heat transfer in a straight inclined duct of constant diameter included in a rock massif. The model coupled 1D radial conduction in the rock mass with convective transfer in the gas, using a sinusoidal function of time as inlet temperature. The airflow rate was predicted by considering the interaction between the temperature field in the gas and the airflow through the buoyancy term in the momentum balance equation of the gas. This model reproduced qualitatively some field observations, e.g. the hysteresis of the flow rate or the thermal anomaly in the entrance areas. Gabrovšek (2023) used a similar model to investigate

by numerical simulations the effect of conduit shape on the airflow pattern in ventilated caves.

The present study focuses on the numerical simulation of heat transfer in ventilated caves for which the airflow is driven by the temperature contrast between the cave and the external atmosphere. Our objective is to go beyond the qualitative results obtained from previous numerical studies available in the literature. We aim at assessing orders of magnitudes of the spatial extent of the karst region where the airflow induces significant thermal perturbations. We use for that a numerical model close to that already developed by Lismonde (2002) or Gabrovšek (2023), and we apply it to the simplest possible configuration in order to quantify general trends common to most ventilated caves. The convective heat transfer due to dry airflow in a single horizontal karst conduit of constant diameter is coupled with the conductive heat transfer in the impermeable rock mass.

This article contains a first theoretical part (sections 2-5) dedicated to numerical simulations based on a model including many simplifying assumptions. The relevance of these assumptions to achieve our objective, which consists in the assessment of general orders of magnitude, is evaluated in a second part (section 6) by comparison with the field data obtained from three sites, a mine tunnel and two caves.

2. Model definition

2.1 Cave geometry and computational domain

We consider the idealized ventilated cave displayed in Figure 1, located in a rock massif of infinite extent in both vertical directions. The cave consists of a vertical conduit connected by two horizontal conduits to two entrances at different elevations. The rock mass is assumed impermeable. The horizontal conduits are supposed long enough for the vertical conduit to be fully included in the homothermic area where the temperature gradient reduces to the adiabatic lapse rate. The aeraulic and thermal problems are uncoupled in this simplified configuration, since the temperature field in the horizontal conduits have no effect on buoyancy. The air flowrate thus only depends on the temperature contrast between the temperature in the vertical conduit, independent of time, and the temperature of the atmosphere outside the cave, a known function of time.

Another source of simplification is that the thermal problems in the regions of upper and lower entrances are uncoupled. They can thus be treated separately. We arbitrarily focus on the upper entrance, but all the results can be easily translated to a lower entrance (the only difference is that the air flows through the upper entrance inward during summer and outward during winter, and vice-versa through the lower entrance).

The computational domain is a cylinder of length L_{dom} and outer radius R_{dom} displayed in red in Figure 1. It contains a conduit of same axis and length and constant radius $R \ll R_{dom}$, inside which the air circulates. The length L_{dom} and outer radius R_{dom} are set so that the computational domain includes the whole thermal perturbation induced in the rock mass by the airflow. Practically, in a given configuration, L_{dom} and R_{dom} are increased until they no longer influence the results.

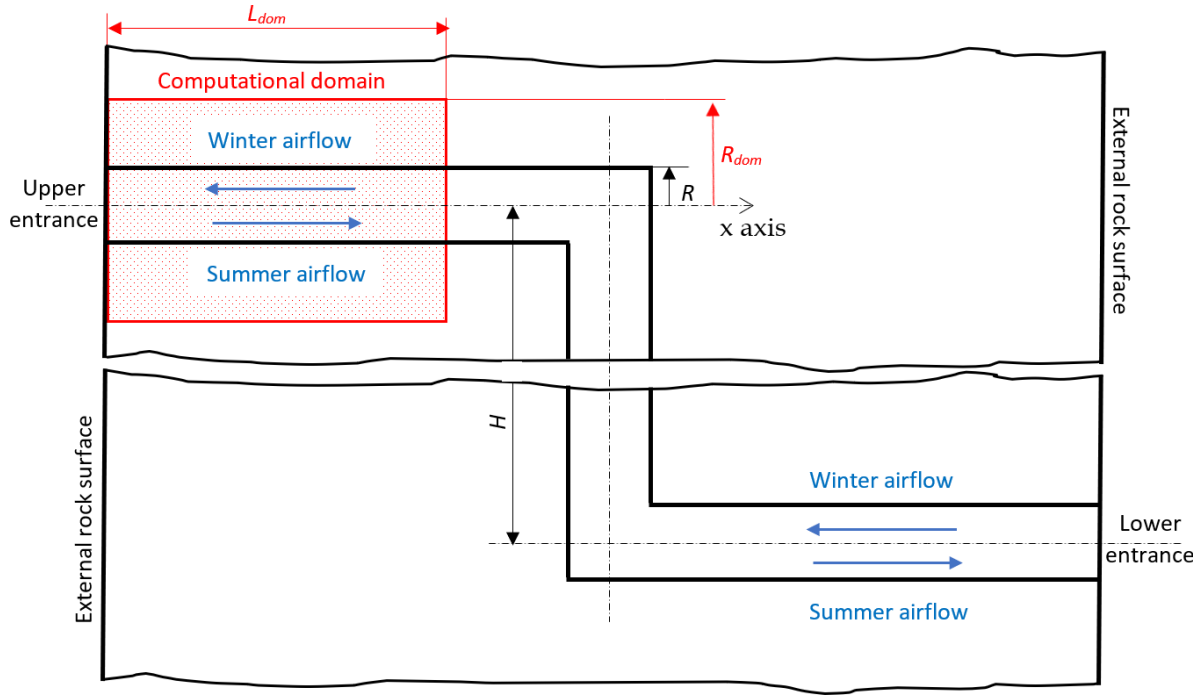

Figure 1. Cave geometry (the computational domain is displayed in red). The rock massif is assumed infinite in both vertical directions.

2.2 Atmosphere temperature and mass flow rate

For the sake of simplification, only the annual fluctuation of the atmosphere temperature T_{atm} is considered. It is thus assumed that $T_{atm}(t)$ follows the simple law:

$$T_{atm}(t) = T_m + \Delta T_y \sin\left(2\pi \frac{t}{\tau_y}\right) \quad (1)$$

where T_m and ΔT_y are the annual mean temperature (AMT) and the amplitude of the annual temperature fluctuation (ATF), respectively, in the external atmosphere at the elevation of the upper entrance. The corresponding period is $\tau_y = 1$ year.

The air mass flow rate $\dot{m}$ is deduced from the momentum balance applied to the air inside the cave. Assuming negligible inertia, the balance between friction and buoyancy yields (Lismonde, 2002):

$$K\, \dot{m}\, |\dot{m}\,| = -(\bar{\rho}_{atm} - \bar{\rho}_m) g H\,, \quad (2)$$

where H is the length of the vertical conduit and g the gravitational acceleration. The cave aeraulic resistance K can be assumed constant in the turbulent regime.

$\bar{\rho}_{atm}$ and $\bar{\rho}_m$ are the densities of the air outside the cave and inside the homothermic zone, respectively, averaged over the cave height. Assuming that: (1) the difference of densities depends only on the temperature drop between the external atmosphere and the homothermic zone, (2) the temperature field in the vertical conduit follows the AMT in the external atmosphere, we get after linearization:

$$\bar{\rho}_{atm}(t) - \bar{\rho}_m = -\frac{M_a\, P_{atm}}{R_g\, T_m^2}\,(T_{atm}(t) - T_m) \tag{3}$$

where P_{atm} is the atmospheric pressure, M_a the molar mass of air and R_g the ideal gas constant. Eqs. (2) and (3) show that the air flowrate is proportional to the square root of the temperature drop $(T_{atm} - T_m)$. Injecting Eqs. (1) and (3) in Eq. (2) yields

$$\dot{m}(t) = S\,\Delta\dot{m}\,\sqrt{\left|\sin\left(\frac{2\pi}{\tau_y}t\right)\right|} \tag{4}$$

where S=-1 for $T_{atm} < T_m$ (wintertime, upward flow) and S=1 for $T_{atm} > T_m$ (summertime, downward flow). The positive constant $\Delta\dot{m}$ is the amplitude of the annual fluctuation of the flow rate. It is an input of the model.

2.3 Governing equations

The air temperature verifies the energy balance

$$\dot{m}\, c_{p,a}\,\frac{\partial T_a}{\partial x} = \varphi_w P \tag{5}$$

where $c_{p,a}$ is the air heat capacity at constant pressure, T_a is the mixing temperature of the air inside the conduit, x the distance from the external rock surface, P the conduit perimeter ($P = 2\pi R$ for a circular cross-section) and φ_w the conductive flux at the conduit wall, positive when going from the rock to the air. Equation (5) is a balance between the energy advected by the air flow (LHS) and the conduction flux at the conduit wall (RHS). The air thermal inertia has been neglected compared to advection (quasi-steady approximation). Equation (5) requires a single boundary condition at the conduit inlet located at x=*0* for downward flow (S=*1*) or at $x=L_{dom}$ for upward flow (S=*-1*). We thus impose the boundary condition

$$T_a(x = 0, t) = T_{atm}(t) \;\; \textit{for S=1} \quad \textit{or} \quad T_a(x = L_{dom}, t) = T_m \;\; \textit{for S=-1} \tag{6}$$

The conductive flux φ_w is required to solve Eq. (5). The conduction equation must therefore be solved in the impermeable rock matrix around the cave. The transient 2D axisymmetric conduction equation reads

$$\frac{1}{r}\frac{\partial}{\partial r}\left(r\frac{\partial T_r}{\partial r}\right) + \frac{\partial^2 T_r}{\partial x^2} = \frac{1}{\alpha_r}\frac{\partial T_r}{\partial t} \tag{7}$$

where $T_r(x,r,t)$ is the rock temperature, α_r the rock thermal diffusivity, and r the distance from the cave axis. The boundary conditions are as follows. The atmosphere temperature is imposed on the external rock surface:

$$T_r(x=0,r,t) = T_{atm}(t) \text{ for } R < r < R_{dom} \quad (8)$$

The boundary at $r=R_{dom}$ can be assumed adiabatic because the temperature field only depends on x far from the cave (i.e., for a large value of R_{dom}), and the radial component of the temperature gradient is thus close to zero. The boundary condition at $x=L_{dom}$ is also adiabatic, because this boundary is located in the homothermic zone. We get

$$\frac{\partial T_r}{\partial r}(x,R_{dom},t) = 0 \text{ for } 0 < x < L_{dom} \text{ and } \frac{\partial T_r}{\partial x}(L_{dom},r,t) = 0 \text{ for } R < r < R_{dom} \quad (9)$$

The last boundary condition is at the conduit wall. It is given by Newton's law of cooling and the heat flux continuity at the conduit wall:

$$\varphi_w = \lambda_r \frac{\partial T_r}{\partial r}(x,R,t) = h_{th}(t)\big(T_r(x,R,t) - T_a(x,t)\big) \quad (10)$$

where λ_r is the rock thermal conductivity, $T_r(x,R,t) = T_w(x,t)$ is the temperature of the conduit wall and h_{th} the heat transfer coefficient. The latter is time-dependent since it depends on the air flowrate $\dot{m}(t)$. All the conditions at the boundaries of the rock domain are displayed in Figure 2. No initial condition is required because we are looking for the periodic regime, i.e., the solution asymptotically reached by the model at infinite time.

2.4 Determination of the heat transfer coefficient

The heat transfer coefficient h_{th} in Eq. (10) is a key parameter. The estimation of h_{th} must therefore be performed with great care to get a reliable model. Assuming forced convection in conduits, Wigley and Brown (1971) and Gabrovšek (2023) used a correlation close to the Colburn correlation (Bergman et al., 2017), valid for fully developed turbulent flow in smooth pipes. Lismonde (2002) pointed out that a cave cannot be considered as a smooth pipe, and multiplied by two the numerical prefactor of the Colburn correlation to account for the effect of wall roughness. Covington et al (2011) used the Gnielinski correlation (Bergman et al., 2017), which explicitly considers the effect of wall roughness.

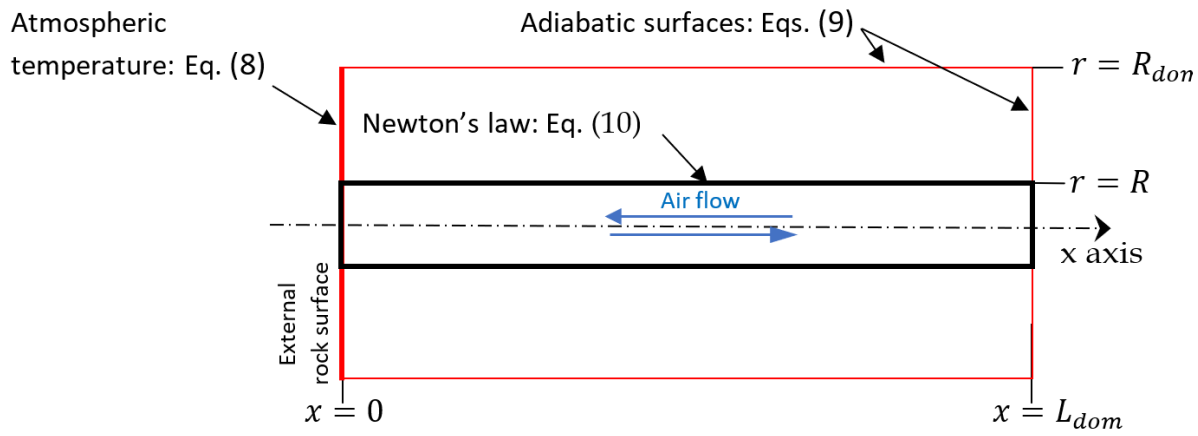

Figure 2. Rock domain with the boundary conditions of the heat conduction equation (7).

However, it is unlikely that a cave can be considered as a rough pipe. Indeed, caves can have complicated shapes, ranging from sub-circular conduits with several meters in diameter to complex cave passages associated with the collapse of the host-rock. A succession of bends, conduit contractions or enlargements, or obstacles of any kind are expected to increase the transfer of heat between the air and the wall. Indeed, all of these singularities not only increase the heat exchange surface between the wall and the fluid, but also enhance the heat transfer coefficient by generating secondary flows and by increasing the turbulence level. It is well known that heat exchanger performance can be improved by the insertion of twisted tapes, longitudinal fins or helical ribs inside the tubes (Bergman et al., 2017). For instance, spirally corrugated tubes can increase the heat transfer coefficient by a factor 3 (Promthaisong et al., 2016; Pethkool et al., 2011). However, although empirical correlations exist to predict heat transfer coefficient for a wide range of well-defined geometries used in heat exchangers, no correlation is available for the irregular and tortuous geometries commonly encountered in caves.

To get around this difficulty, two distinct cases will be considered. In the first case (case A in the following), correlations for forced convection and fully developed flow in pipes will be used to estimate the heat transfer coefficient. This approach is expected to give a lower bound of the heat transfer coefficient, and thus a lower bound of the heat flux at the conduit wall. In the second case (case B in the following), a higher bound of the wall heat flux will be obtained assuming infinite heat transfer coefficient. Reality must lie between these two limiting cases.

Case A: forced convection and fully developed flow.

The Nusselt number $Nu = \frac{h_{th}\, D_h}{k_a}$ used for the estimation of h_{th} is displayed in Figure 3 as a function of the Reynolds number $Re_t = \frac{V(t)\, D_h}{\nu_a}$, for three values of the relative roughness ε (ratio of the wall roughness over D_h). k_a and ν_a are the conductivity and the kinematic viscosity of the air, V is the mean air velocity at time t, D_h=$4A/P$ is the

hydraulic diameter with A and P the cross-sectional area and the perimeter of the conduit. Nu is computed as follows:

$$Nu = \max(Nu_L, Nu_T) \tag{11}$$

where $Nu_L = 3.66$ is the Nusselt number in the laminar regime (independent of the roughness) and Nu_T is given by the Gnielinski correlation (Bergman et al., 2017), which takes into account the effect of the wall roughness expected in the turbulent regime:

$$Nu_T = \frac{\left(\frac{f_d}{8}\right)(Re_t - 1000)\,Pr}{1 + 12.7\left(\frac{f_d}{8}\right)^{0.5}(Pr^{2/3} - 1)} \tag{12}$$

where Pr is the air Prandtl number (Pr=0.71). f_d is the Darcy friction factor which depends on the Reynolds number and the wall relative roughness ε. f_d was estimated using the Haaland correlation (Haaland, 1983):

$$\frac{1}{\sqrt{f_d}} = -1.8\,log\left[\left(\frac{\varepsilon}{3.7}\right)^{1.11} + \frac{6.9}{Re_t}\right] \tag{13}$$

All the simulations of case A were done using $\varepsilon = 0.01$ as a lower bound of the relative roughness in a cave (red curve in Figure 3).

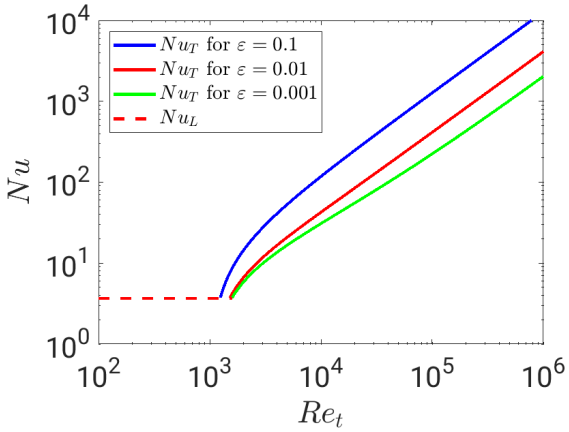

Figure 3. Nusselt number as a function of the Reynolds number (Prandtl number: Pr=0.71). The red curve was used for the simulations of case A.

Case B: Infinite heat transfer coefficient

In this case, the conduit wall temperature is equal to the bulk air temperature and Eq.(10) thus reduces to

$$\varphi_w = \lambda_r \frac{\partial T_r}{\partial r}(x, R, t) \quad \text{and} \quad T_r(x, R, t) = T_a(x, t) \tag{14}$$

2.5 Physical properties

All the physical properties are gathered in Table 1. They are assumed constant and estimated at the temperature T_m= 12°C.

Table 1 : Thermophysical properties (estimated at temperature T_m=285 K = 12°C and atmospheric pressure $p_{ref} = 101325\ Pa$).

properties	Value and unit	Reference
Conduit relative roughness	$\varepsilon = 0.01$	(see section 2.4)
Rock density	$\rho_r = 2320 \frac{kg}{m^3}$	(Covington et al., 2011)
Rock heat capacity	$c_{p,r} = 810 \frac{J}{kgK}$	(Covington et al., 2011)
Rock thermal conductivity	$k_r = 1.656 \frac{W}{m.K}$	(Guerrier et al., 2019)
Rock thermal diffusivity	$\alpha_r = \frac{k_r}{\rho_r c_{p,r}} = 8.81 \times 10^{-7} \frac{m^2}{s}$	-
Air dynamic viscosity	$\mu_a = 1.77 \times 10^{-5} Pa.s$	(Bergman et al., 2017)
Air density	$\rho_a = 1.23 \frac{kg}{m^3}$	(Bergman et al., 2017)
Air kinematic viscosity	$\nu_a = \frac{\mu_a}{\rho_a} = 1.43 \times 10^{-5}\ m^2/s$	-
Air thermal conductivity	$k_a = 0.0251\ \frac{W}{m.K}$	(Bergman et al., 2017)
Air Prandtl number	$Pr = \frac{\nu_a}{\alpha_a} = 0.71$	-
Molar mass of air	$M_a = 28.97 \frac{g}{mol}$	-
Ideal gas constant	$R_g = 8.314 \frac{J}{molK}$	-

2.6 Dimensionless equations

We define the dimensionless temperatures $\theta_a = (T_a - T_m)/\Delta T_y$ and $\theta_r = (T_r - T_m)/\Delta T_y$ in the air and the rock, respectively. The dimensionless temperature 0 thus corresponds to the external annual mean temperature and 1 is the amplitude of the external annual fluctuations. We take the period $\tau_y = 1$ year as the unit of time and the diffusion length $L_{dif} = \sqrt{\alpha_r \tau_y} \approx 5.3$ m as the unit of length. The dimensionless atmospheric temperature θ_{atm} and air flowrate μ are deduced from Eqs.(1) and (4):

$$\theta_{atm}(\tilde{t}) = \sin(2\pi\tilde{t}) \tag{15}$$

$$\mu(\tilde{t}) = \frac{\dot{m}(t)}{\Delta\dot{m}} = S\sqrt{|\sin(2\pi\tilde{t})|} \tag{16}$$

The dimensionless counterparts of Eqs. (5)-(10) read

$$\mu(\tilde{t})\, Re\, \frac{\partial \theta_a}{\partial \tilde{x}} = \left(4 \frac{k_r}{k_a} Pr^{-1}\right) \tilde{\varphi}_w \,, \tag{17}$$

$$\theta_a(\tilde{x}=0,t) = \sin(2\pi\, \tilde{t}) \quad \text{for } S{=}1 \quad \text{or} \quad \theta_a\left(\tilde{x}=\tilde{L}_{dom},\tilde{t}\right) = 0 \quad \text{for } S{=}{-}1, \tag{18}$$

$$\frac{1}{\tilde{r}} \frac{\partial}{\partial \tilde{r}} \left(\tilde{r} \frac{\partial \theta_r}{\partial \tilde{r}}\right) + \frac{\partial^2 \theta_r}{\partial \tilde{x}^2} = \frac{\partial \theta_r}{\partial \tilde{t}} \,, \tag{19}$$

$$\theta_r(\tilde{x}=0,\tilde{r},\tilde{t}) = \sin(2\pi\, \tilde{t}) \;\text{ for }\; \tilde{R} < \tilde{r} < \tilde{R}_{dom} \,, \tag{20}$$

$$\begin{aligned} &\frac{\partial \theta_r}{\partial \tilde{r}}\left(\tilde{x}, \tilde{R}_{dom}, \tilde{t}\right) = 0 \text{ for } 0 < \tilde{x} < \tilde{L}_{dom} \text{ and} \\ &\frac{\partial \theta_r}{\partial \tilde{x}}\left(\tilde{L}_{dom}, \tilde{r}, \tilde{t}\right) = 0 \text{ for } \tilde{R} < \tilde{r} < \tilde{R}_{dom}, \end{aligned} \tag{21}$$

$$\tilde{\varphi}_w = \frac{\partial \theta_r}{\partial \tilde{r}}\left(\tilde{x}, \tilde{R}, \tilde{t}\right) \;=\; \eta(\tilde{t})\, Bi\, \left(\theta_r\left(\tilde{x}, \tilde{R}, \tilde{t}\right) - \theta_a(\tilde{x}, \tilde{t})\right), \tag{22}$$

where the tilde (~) indicates dimensionless time or lengths. $\eta(\tilde{t}) = \frac{h_{th}(t)}{H_{th}}$ is the heat transfer coefficient scaled by H_{th}, its maximum value reached for $\dot{m} = \Delta\dot{m}$. The Reynolds number $Re = \frac{4\,\Delta\dot{m}}{P \mu_a}$ (with μ_a the air dynamic viscosity) and the Biot number $Bi = \frac{H_{th}\, \sqrt{\alpha_r \tau_y}}{k_r}$ are based on the maximum values $\Delta\dot{m}$ and H_{th}, respectively. $\mu(\tilde{t})Re$ and $\eta(\tilde{t})Bi$ are the Reynolds and Biot numbers at a given time $\tilde{t}$. In a given configuration, $\tilde{R}_{dom}$ and $\tilde{L}_{dom}$ that define the size of the computational domain are increased until they do not modify the results, as stated in section 2.1.

With the constant physical properties defined in Table 1, a configuration is well-defined if only two dimensionless numbers are known: the dimensionless conduit radius $\tilde{R}$ and the Reynolds number *Re*. In case A, i.e., when fully developed forced convection is assumed for the estimation of the heat transfer coefficient, the Biot number in Eq. (22) is related to the Nusselt number by the simple relation $\eta(\tilde{t})Bi = \frac{Nu}{\tilde{R}} \left(\frac{k_a}{2\, k_r}\right)$, where *Nu* depends on $Re_{\tilde{t}} = \mu(\tilde{t})Re$ through Eqs.(11)-(12). In case B, the Biot number is infinite, i.e., $\eta(\tilde{t})Bi \to \infty$. Eq. (22) thus reduces to

$$\tilde{\varphi}_w = \frac{\partial \theta_r}{\partial \tilde{r}}\left(\tilde{x}, \tilde{R}, \tilde{t}\right) \quad \text{and} \quad \theta_r\left(\tilde{x}, \tilde{R}, \tilde{t}\right) = \theta_a(\tilde{x}, \tilde{t}) \tag{23}$$

3. Method of resolution

We are looking for the periodic solution of the mathematical model defined in section 2.6. The periodic regime could be obtained by time integration starting from an arbitrary initial condition, after simulating a number of cycles large enough to get a good approximation of the solution at infinite time. However, the slow convergence of this method can generate large computational times. We thus prefer to use another method, based on Fourier series. All time-varying variables, including the temperatures in the rock and in the air, are approximated by truncated Fourier series and inserted in the mathematical model of section 2.6. This yields a set of coupled

partial differential equations (PDE), which does not include the time. The numerical resolution by the Galerkin method of this set of PDE gives the spatial distribution of the amplitude and phase of the Fourier modes. The temporal evolution of the dependent variables is then recovered from Fourier series. This method is detailed in supplemental material. The validation by comparison with a standard time integration method is presented in the same appendix. All the numerical simulations were performed with the commercial software Comsol Multiphysics, version 6.1.

The method of resolution based on Fourier series used in this work is particularly relevant for the simplified time variation of the external temperature considered in Eq.(1). Considering all the Fourier modes included in real times series of the external temperature would clearly increase both the complexity of the method implementation and the computational resources required for the simulations. In that case, only the most significant modes of the input temperature should be considered. In contrast, using Fourier series to simulate the complex geometry of real caves would not cause any particular problem.

4. Characterization of the thermal perturbation

Figure 4 displays the wall and air temperatures inside the cave at different distances from the entrance, for case A with $\tilde{R} = 0.189$ and $Re = 1.8 \times 10^5$. Figure 4a shows the amplitude of the Fourier modes that stems directly from the numerical simulation. The mode k refers to the dimensionless period $1/k$. The amplitudes of the modes k=0 and k=1 are thus the annual mean temperature (AMT) and the amplitude of the annual temperature fluctuation (ATF), respectively. The modes k=2, k=3, and so on, refer to the periods 6 months, 4 months, etc. Although the external temperature imposed at $\tilde{x} = 0$ contains the single mode k=1 (since it reduces to Eq. (15)), the coupling between modes due to convection results in the existence of other modes than k=1 in cave temperatures (modes k=0 to 18 were considered in the simulations, see supplemental material). Figure 4b displays the periodic time series built from the Fourier series. The amplitude of the temperature fluctuations decreases when the distance from the entrance increases, as expected. The hot thermal anomaly expected at the vicinity of an upper entrance is also observed. Indeed, for $\tilde{x} = 10$ to 10^3, the dimensionless temperature is positive throughout the year, which means that it is always higher than the external AMT, even in winter.

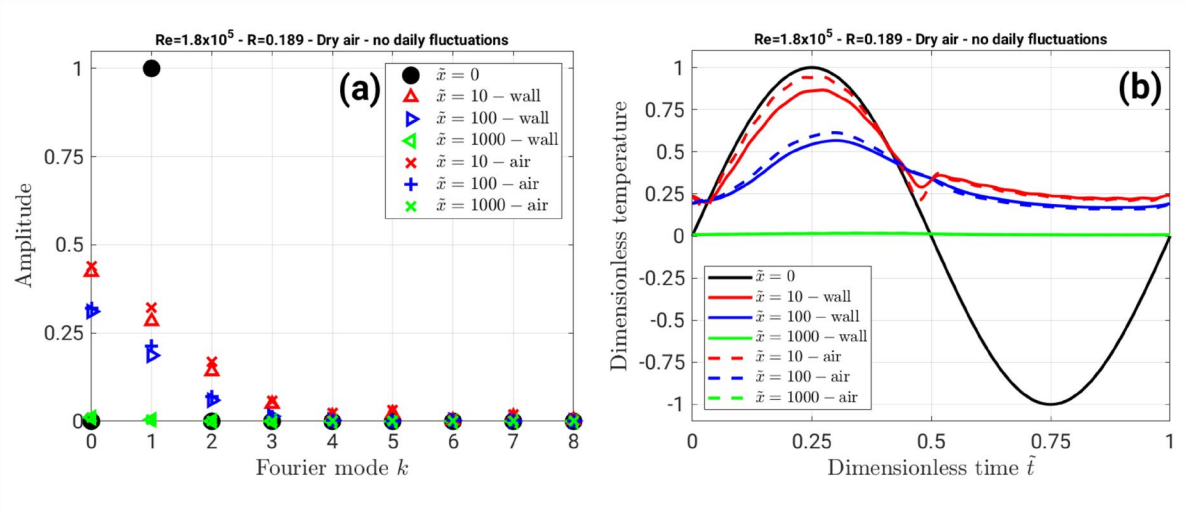

Figure 4. Wall and air temperatures at different distances $\tilde{x}$ from the entrance (case A with $\tilde{R}$=0.189 and *Re*=1.8×10⁵). (a) Amplitude of the Fourier modes. (b) Time series.

Figure 5a displays the temperature profiles in the air and at the cave wall at times t =0, 0.25, 0.5 and 0.75, corresponding to the external temperatures 0, 1, 0 and -1, respectively. Following an approach similar to that of Cropley (1965), we split the cave into three zones.

1- A first zone, from $\tilde{x} = 0$ to $\tilde{x} \approx 1$ (the diffusion length), where the cave temperature follows the fluctuations of the external temperature. More precisely, the sign of the temperature gradient changes in summer and winter (see the inset in Figure 5a). This first zone is dominated by the temperature fluctuations of the external wall, propagating inside the rock mass by heat conduction. It will be called diffusive region in the following.

2- A second zone characterized by a positive dimensionless temperature and reduced but significant fluctuations. In the specific case of Figure 5a, it approximately extends from $\tilde{x} \approx 1$ to 10^3. In this zone, heat diffusion from the external wall is negligible compared to convection. It will be called convective region in the following. Because of the seasonal flow reversals, the inlet temperature of the air flow is 1 in summer (inward flow) and 0 in winter (outward flow, coming from the deep karst). As a consequence, this zone does not "feel" the negative winter temperatures. This results in: (1) a shift of the AMT to positive values, the so-called thermal anomaly, (2) a reduction of the amplitude of the fluctuations, because the temperature oscillates between 0 and 1 whereas the external temperature fluctuates between -1 and 1.

3- A third zone, called deep karst in the following, where the dimensionless temperature is approximately constant and close to zero (the external AMT).

These three regions appear clearly on the amplitude of the Fourier modes plotted in Figure 5b as a function of the distance from the entrance $\tilde{x}$. The amplitude of the mode k=1 (i.e. the ATF) decreases in two steps. It first drops down from 1 to 0.3 in the diffusive region (from $\tilde{x} = 0$ to $\tilde{x} \approx 1$), then slowly decreases in the convective region, over a distance much longer than 1 (of the order of 10^3 in the specific case of Figure 5). The amplitude of the mode k=0 (i.e. the AMT) increases in the diffusive region until it reaches a quasi-plateau. Then it slowly decreases in the convective region, over a distance of the same order as for the mode k=1. The modes such that $k \gtrsim 2$ follow qualitatively the behavior of mode k=0, with a lower amplitude and a shorter attenuation length. In the following, we will focus on both modes with the highest amplitude, k=0 and k=1, as representative of the AMT (the thermal anomaly) and the ATF, respectively.

In all the simulations we did, the transition between the diffusive and convective regions always take place at a distance from the entrance of the order of 1, as expected. Conversely, the characteristics of the convective domain (amplitude of the thermal perturbation and its spatial extent) depend on the model parameters: the Reynolds number *Re* (containing the air flow rate) and the cave radius $\tilde{R}$. This dependence will be systematically investigated in the parametric study of the next section. In order to facilitate the interpretation of the results, we define a small number of relevant parameters characterizing the perturbation of the cave temperature field by the air flow. The magnitude of the perturbation is characterized by the AMT and the ATF at the beginning of the convective region, where the impact of convection is maximum, and the effect of thermal conduction from the external wall negligible. We define $\Delta\theta_w$ as the maximum amplitude of the mode k=1 in the convective region, for the wall temperature. Practically, it is evaluated at the change of slope noticed on the solid blue line in the inset of Figure 5b. Similarly, $\bar{\theta}_w$ is the maximum amplitude reached by the mode k=0 for the wall temperature (maximum of the red solid line in the inset of Figure 5b). The corresponding amplitudes for the air temperature, $\Delta\theta_a$ and $\bar{\theta}_a$, are estimated at the same location as $\Delta\theta_w$ and $\bar{\theta}_w$, respectively. For example, in the specific case of Figure 5, we get $\Delta\theta_w \approx 0.30$ and $\Delta\theta_a \approx 0.34$ (maximum ATF), $\bar{\theta}_w \approx 0.425$ and $\bar{\theta}_a \approx 0.44$ (maximum AMT).

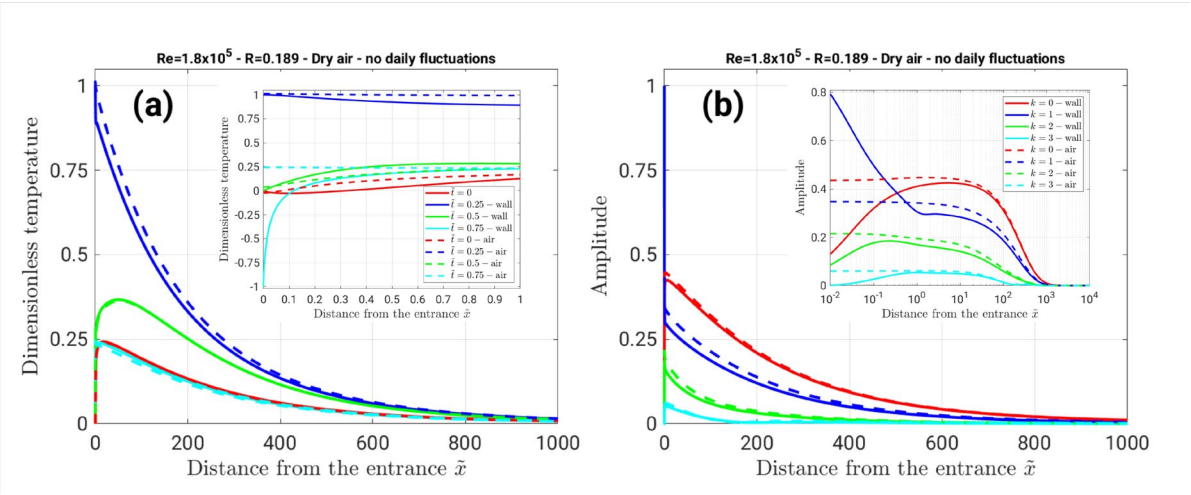

Figure 5. Wall (solid lines) and air (dashed lines) temperatures as a function of the distance $\tilde{x}$ from the entrance (case A with $\tilde{R}$=0.189 and Re=1.8×10^5). (a) Temperature profiles at various times (Inset: zoom in the diffusive region). (b) Amplitude of the Fourier modes k=0 to 3 (Inset: log scale on the $\tilde{x}$-axis).

The four parameters $\bar{\theta}_w$, $\bar{\theta}_a$, $\Delta\theta_w$ and $\Delta\theta_a$ represent the maximum amplitudes of the perturbation in the convective region. These amplitudes decrease with the distance from the entrance, as the heat transported by the air flow is gradually dissipated by conduction in the rock mass. We arbitrarily assume that a Fourier mode has been damped when its amplitude has been divided by 10. Figure 6a shows the thermal perturbation in a rock massif with the black solid lines corresponding to an AMT equal to $\bar{\theta}_w/10 = 0.0425$. The rock domain thus defined can be characterized by the length $\tilde{L}_0$ along the cave axis and the maximum width $\tilde{W}_0$ along the radial direction. Note that this maximum width is observed at a certain distance from the external wall because of the competition between radial diffusion from the cave which transports the thermal anomaly through the massif, and axial diffusion from the external wall which reduces it. Similarly, the black solid lines in Figure 6b correspond to an ATF equal to $\Delta\theta_w/10 = 0.030$. The size of the corresponding domain is characterized by its length $\tilde{L}_1$ and its width $\tilde{W}_1$. The latter is taken close to the entrance, but out of the diffusive region. The lengths $\tilde{L}_0$ and $\tilde{L}_1$ can also be estimated from the air temperature (length such that the amplitude of AMT and ATF in the air are equal to $\bar{\theta}_a/10$ and $\Delta\theta_a/10$, respectively).

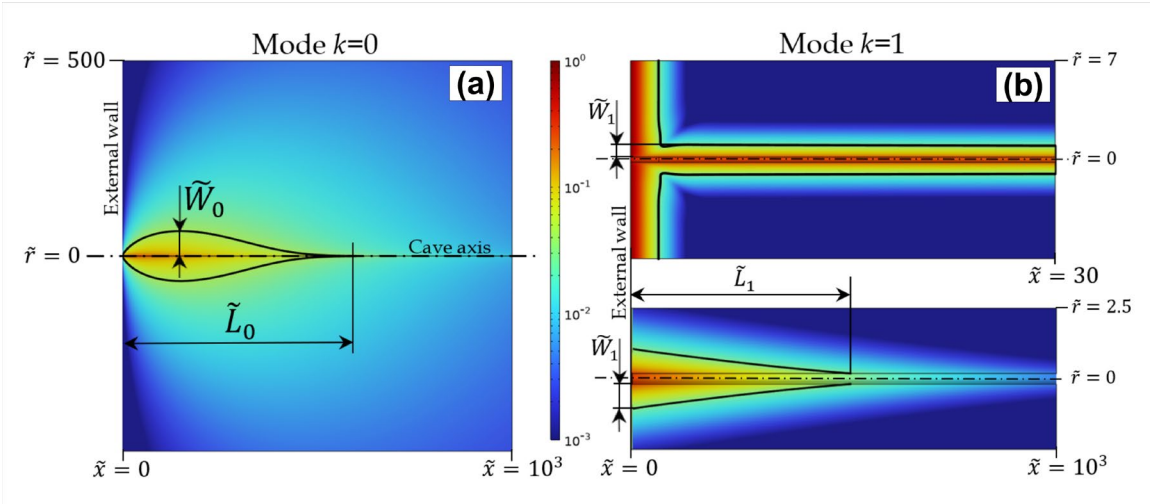

Figure 6. Amplitude contour of the thermal perturbation in a symmetry plane of the rock massif (case A with $\tilde{R}$=0.189 and Re=1.8×10^5). (a) Mode k=0; the black solid lines correspond to the amplitude $\bar{\theta}_w/10 = 0.0425$ (n.b.: at the scale of the figure, the cave reduces to a line). (b) Mode k=1; the black solid lines correspond to the amplitude $\Delta\bar{\theta}_w/10 = 0.030$ (n.b.: the top view focuses on the entrance region; the bottom view has been plotted with different scales on $\tilde{x}$ and $\tilde{r}$ to display the whole perturbed region).

5. Parametric study

5.1 Amplitude of the thermal perturbation induced by the air flow

Figure 7 displays the AMT ($\bar{\theta}_w$ and $\bar{\theta}_a$) and the ATF ($\Delta\theta_w$ and $\Delta\theta_a$) at the beginning of the convective region. Cases A and B yield close values of $\bar{\theta}_a$, which is also little sensitive to the model parameters Re and $\tilde{R}$. Indeed, $\bar{\theta}_a$ varies only from 0.25 to 0.6 when Re and $\tilde{R}$ are increased by three and two orders of magnitude, respectively. With the exception of small conduits ($\tilde{R} = 0.2$) at small Reynolds number ($Re \lesssim 3 \times 10^3$), a similar remark can be made on $\Delta\theta_a$.

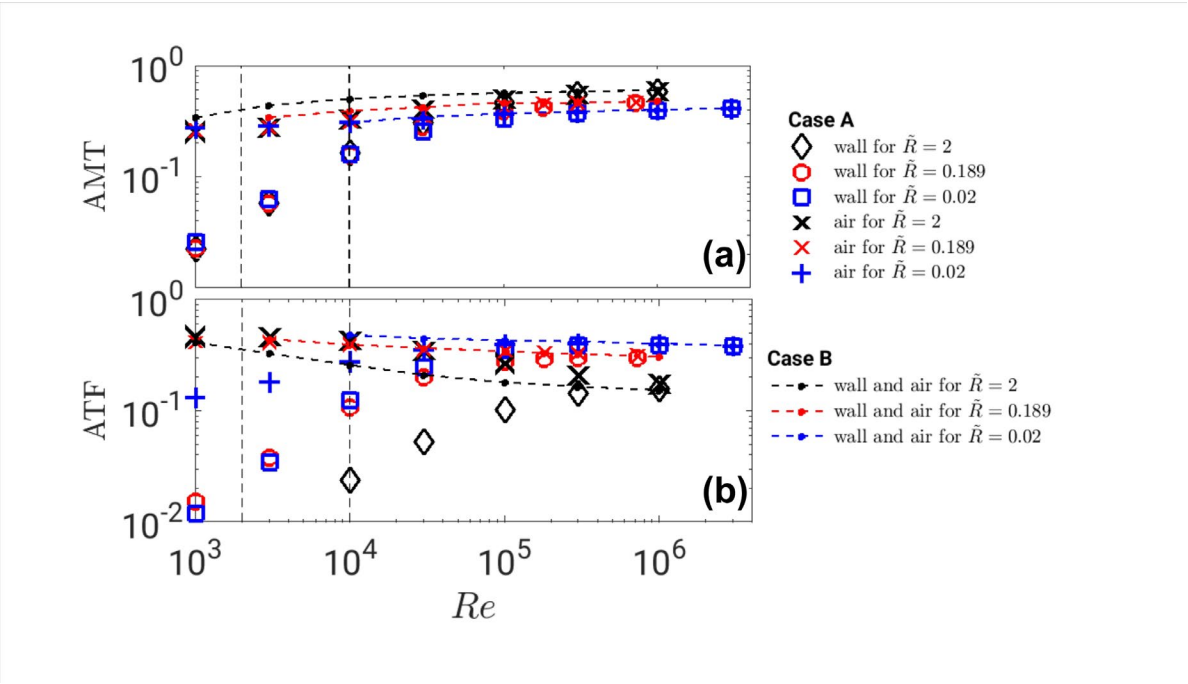

Figure 7. Maximum thermal perturbation at the beginning of the convective region for cases A (Biot number estimated from forced convection correlations) and B (infinite Biot number). (a) Maximum AMT ($\bar{\theta}_w$ and $\bar{\theta}_a$ for the wall and the air, resp.). (b) Maximum ATF ($\Delta\theta_w$ and $\Delta\theta_a$ for the wall and the air, resp.). The vertical dashed lines correspond to the limits of the laminar and turbulent regimes.

The evolution of the wall temperature is more intricate. In case B, the assumption of infinite Biot number imposes $\bar{\theta}_w = \bar{\theta}_a$ and $\Delta\theta_w = \Delta\theta_a$ (since the air and wall temperatures are equal). Assuming that Case A provides a lower bound of the actual Biot number in a cave, Eq.(14) allows to estimate the consequences of an error in the determination of the Biot number on the estimation of the wall temperature at the beginning of the convective region. At high Reynolds number ($Re \gtrsim 3 \times 10^5$), no accurate estimation of the relation of the function *Nu(Re)* is required because the heat transfer is completely driven by heat conduction in the rock massif. Conversely, the relation *Nu*(*Re*) is a key information for convection-limited heat transfer at small Reynolds number ($Re \lesssim 10^4$). At intermediate *Re*, an accurate estimation of *Nu* is required to get the ATF of the wall in a cave with a large radius ($\tilde{R} \gtrsim 1$).

5.2 Spatial extent of the thermal perturbation induced by the air flow

The characteristic lengths $\tilde{L}_0$ and $\tilde{L}_1$ for the damping of the AMT and ATF along the cave axis are displayed in Figure 8. The values of $\tilde{L}_0$ computed in case B (infinite Biot number) support the simple relation obtained from curve fitting:

$$\tilde{L}_0 \approx 3.1 \times 10^{-3}\, Re^{1.06}\, \tilde{R}^{0.61} \qquad (24)$$

In case A, estimating $\tilde{L}_0$ from the air or the wall temperatures give the same results (the lengths required to get $\bar{\theta}_a$ or $\bar{\theta}_w$ divided by 10 are the same, even when $\bar{\theta}_a$ and $\bar{\theta}_w$ are different). At high Reynolds number, $\tilde{L}_0$ estimated from case A follows Eq.(24)

derived for case B, as expected when heat transfer is conduction-limited. When *Re* is decreased, using the forced convection correlations of case A reduces the heat flux at the cave wall compared to the infinite Biot number of case B, leading to larger values of $\tilde{L}_0$ than predicted by Eq. (24).

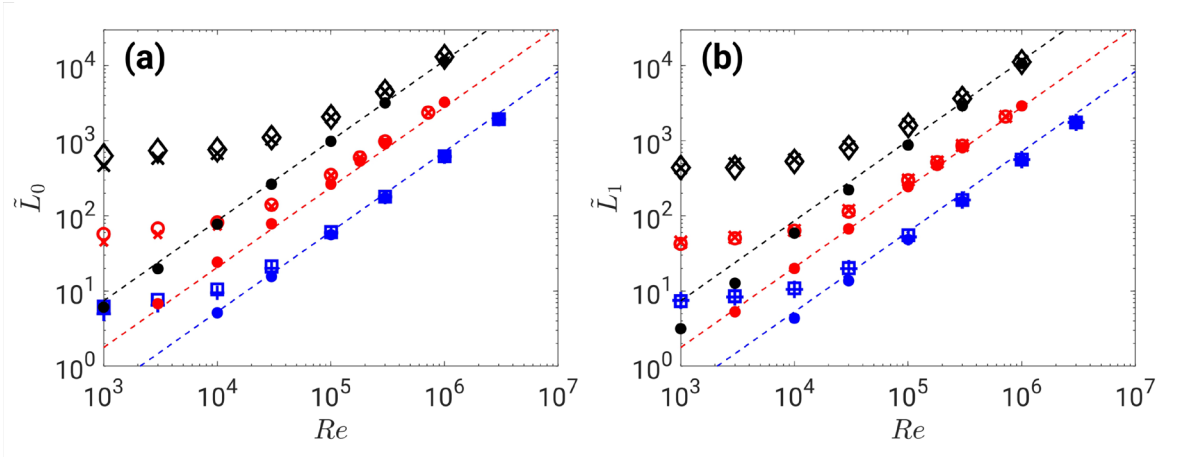

Figure 8. Characteristic lengths $\tilde{L}_0$ (a) and $\tilde{L}_1$ (b) as a function of the Reynolds number *Re* for various radius $\tilde{R}$, computed from wall or gas temperatures. The dashed lines correspond to Eq.(24). Symbols: same legend as in Figure 7.

$\tilde{L}_1$, the distance corresponding to the damping of the ATF, is nearly equal to $\tilde{L}_0$, with the exception of slight differences at low Reynolds number for $\tilde{R}$=2 (see Figure 8b). The length of the convective region (called convection length in the following) can thus be indifferently determined from the damping of the AMT or ATF, based on the wall or the air temperatures. A higher bound of the convection length is provided by case A, while case B provides a lower bound. We can see in Figure 8 that the uncertainty on the convection length increases when the Reynolds number *Re* is decreased and when the cave diameter $\tilde{R}$ is increased.

The width $\tilde{W}_0$ corresponding to the damping of the AMT in radial directions inside the rock mass is displayed in Figure 9. It is approximately proportional to $\tilde{L}_0$ and an order of magnitude smaller.

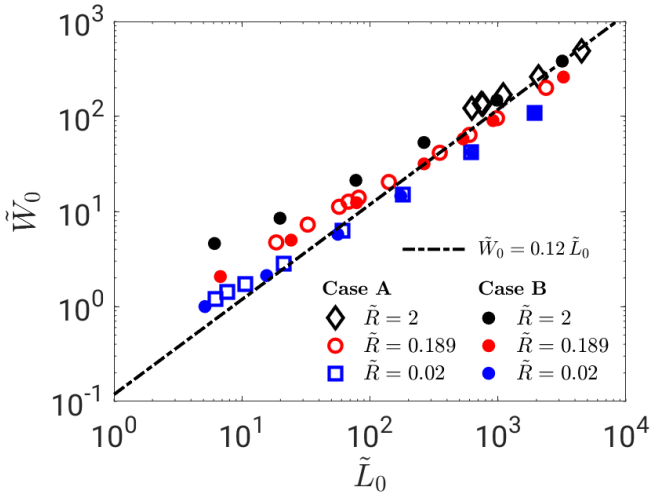

Figure 9. Width $\widetilde{W}_0$ corresponding to the damping of the AMT in the radial directions inside the rock mass

6. Comparison with field data

6.1 Baulmes mine (Switzerland)

The Baulmes mine (46°47'33"N, 6°31'35"E, 655 m a.s.l.) is located in western Switzerland. This mine comprises a network of 11 sub horizontal levels with a cumulated length of about 17 km (Figure 10). The difference in elevation between the uppermost and lowest entrances is 90 m, ensuring a strong chimney effect. The sub horizontal conduits at intermediate elevations between the lower and upper entrances, connected by shafts, lead to dead ends in the horizontal directions (for more information about Baulmes mine, see Bourret et al. (2007)). The temperature delivered by Mathod weather station (46°44'13"N, 6°34'4"E, 435 m a.s.l., at 7 km SW from the study site) is used as an estimation of the external atmosphere temperature. A correction has been applied to account for the difference of elevation with the mine entrance, using the vertical thermal gradient -5.2°C/km (mean value from the network of swiss meteorological stations for the time range 1991-2020). The resulting external temperature is displayed in Figure 11 for one year from July 1st 2022 at 0h00 (this date is taken as time $t = 0$ for all the data from Baulmes mine). The sampling period was 1 hour. The Fast Fourier Transform (FFT) of the external atmosphere temperature yielded $T_m = 10.4$°C (after correction) and $\Delta T_y = 9.4$°C for the external AMT and ATF, respectively.

The 360 m long tunnel #10 is connected horizontally to the lower entrance with no connection to other branches. This is the zone of interest of study. It is indicated by the yellow shading in Figure 10. This conduit has a typical horseshoe cross section. The geometrical characteristics of this conduit, including the mean perimeter and cross-sectional area, their standard deviation as well as its total length are summarized in Table 2. We instrumented this tunnel with seven temperature probes at different distances from the entrance. They are listed in Table 3. The first six temperature probes

are Reefnet (Sensus Ultra) with ±0.3 °C accuracy. The last one located at 360 m from entrance is HOBO (u22-001) with ±0.2 °C accuracy. The temperature inside the conduit was recorded by these seven probes from February 3rd 2023 ($t = 0.596$ year) to July 7th 2023 ($t = 1.017$ year). This time range is displayed by the horizontal arrow in Figure 11. The sampling period was 1 hour.

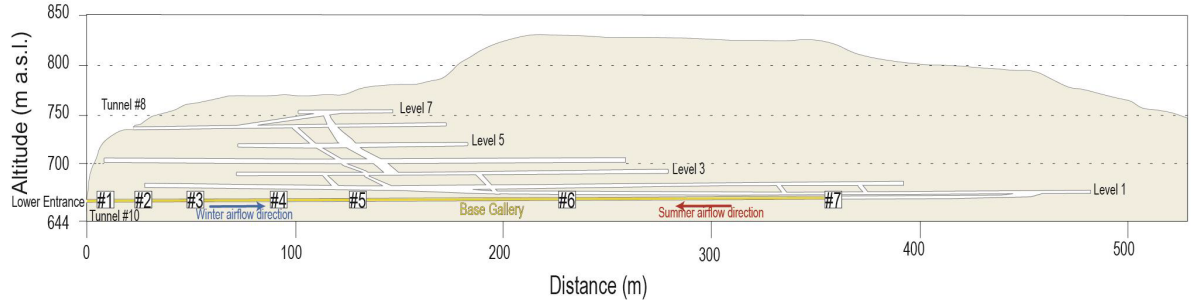

Figure 10. Map of Baulmes mine (vertical section).

Table 2: Geometrical characteristics of the instrumented conduit of Baulmes mine (length L_c, mean value and standard deviation of the perimeter P and the cross-sectional area A from the survey of 28 cross-sections).

L_c (m)	P (m)		A (m²)	
	Mean	std	Mean	std
360	9.7	1.1	6.6	1.5

Table 3: location of the seven temperature probes inside the instrumented conduit of Baulmes mine. x is the distance from the lower entrance.

Probe	#1	#2	#3	#4	#5	#6	#7
x (m)	10	26	50	90	128	220	360
$\tilde{x} = x/L_{dif}$	1.9	4.9	9.4	17	24	42	68

The air mass flow rate was measured sporadically with a manual hot wire anemometer (Testo425 with an accuracy of 0.03 m/s ±5% of the measured value). The measurements were carried out at the four dates listed in Table 4 and displayed by vertical red bars in Figure 11. There are two dates in winter and two in summer. The mean flowrates in winter and summer are 2.4 kg/s and 5.0 kg/s, respectively. In the following, we consider $\Delta\dot{m} \sim (2.4 + 5.0)/2 \sim 4$ kg/s as a rough estimation of the annual amplitude of the air flowrate. With the mean conduit perimeter P=9.7 m from Table 2 and the air viscosity $\mu_a \approx 1.77 \times 10^{-5}$ Pa.s from Table 1, we get the order of magnitude of the Reynolds number $Re = \frac{4\,\Delta\dot{m}}{P\mu_a} \sim 10^5$. The airflow is thus in the turbulent regime most of the time. The conduit radius reads $R = P/(2\,\pi) \approx 1.5$ m that yields the scaled value $\tilde{R} = R/L_{dif} \approx 0.3$. The conduit is thus close to the configuration displayed in Figure 4 and Figure 5 corresponding to $Re = 1.8 \times 10^5$ and $\tilde{R} = 0.189$. In this configuration, cases A and B yield approximately the same results. The heat transfer is thus limited by conduction in the rock rather than convection. Therefore, Eq.(24), for which conduction-limited heat transfer is assumed, is expected to provide a fair estimation of the convection length, and not only a lower bound. We get $\tilde{L}_0 \approx$

$\tilde{L}_1 \sim 3 \times 10^2$. The theory thus predicts a convection length significantly larger than the conduit length $\tilde{L}_c = L_c/L_{dif} \approx 68$.

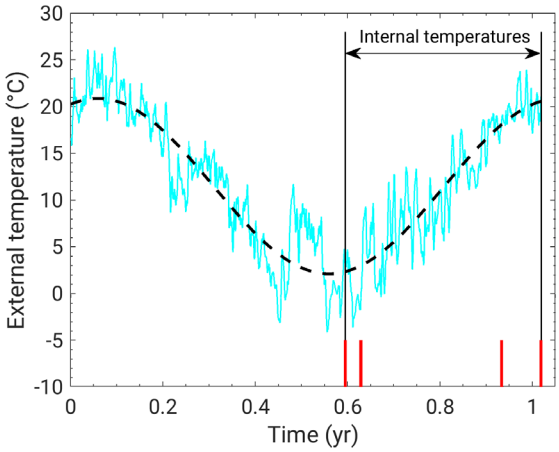

Figure 11. External atmosphere temperature estimated at Baulmes mine (daily averaged data). The horizontal arrow displays the time range during which the temperature inside the cave was measured by the sensors listed in Table 3. The vertical red bars correspond to the dates of the air flowrate measurements listed in Table 4. The black dashed line displays the mode k=0 and k=1 of the external temperature.

Table 4: air mass flow rate measured in winter and summer.

	Winter (upward flow)		**Summer (downward flow)**	
Date	02/02/2023	02/15/2023	06/06/2023	7/7/2023
$\tilde{t} = t/\tau_y$	0.595	0.628	0.933	1.018
$\dot{m}$ (kg/s)	1.9	2.8	4.5	5.4

The time series of the external atmosphere temperature and the temperatures inside the conduit have been plotted in Figure 12a. The dimensionless temperatures inside the conduit are always negative (i.e., lower than the external AMT), even in summer. This is the cold thermal anomaly expected at a lower entrance.

In the following, we assume that the temperature profiles $\theta_w(\tilde{x})$ at time $\tilde{t} = 0.611$ and $\theta_s(\tilde{x})$ at time $\tilde{t} = 1.016$ give an assessment of the coldest and hottest temperatures reached inside the conduit in winter and summer, respectively. These two times are displayed by vertical bars in Figure 12a, and the corresponding profiles are plotted in Figure 12b (the temperature at $\tilde{x} = 0$ is the external atmosphere temperature). In winter, the dimensionless temperature continuously increases from -1.6 at the inlet ($\tilde{x} = 0$) to -0.56 at the end of the conduit ($\tilde{x} = 68$). Spatial temperature variations are thus significant over the entire length of the conduit. This suggests that the convection length should be larger than the conduit length. In summer, the reverse flow direction yields a different temperature profile. The temperature at the end of the conduit ($\tilde{x} = 68$) is -0.06, close to the external AMT. When getting closer to the entrance, the temperature decreases to -0.16 at the first probe ($\tilde{x} = 1.9$). The temperature then suddenly increases within the diffusive region, from -0.16 at the first probe ($\tilde{x} = 1.9$) to the positive value 0.78 at the entrance ($\tilde{x} = 0$).

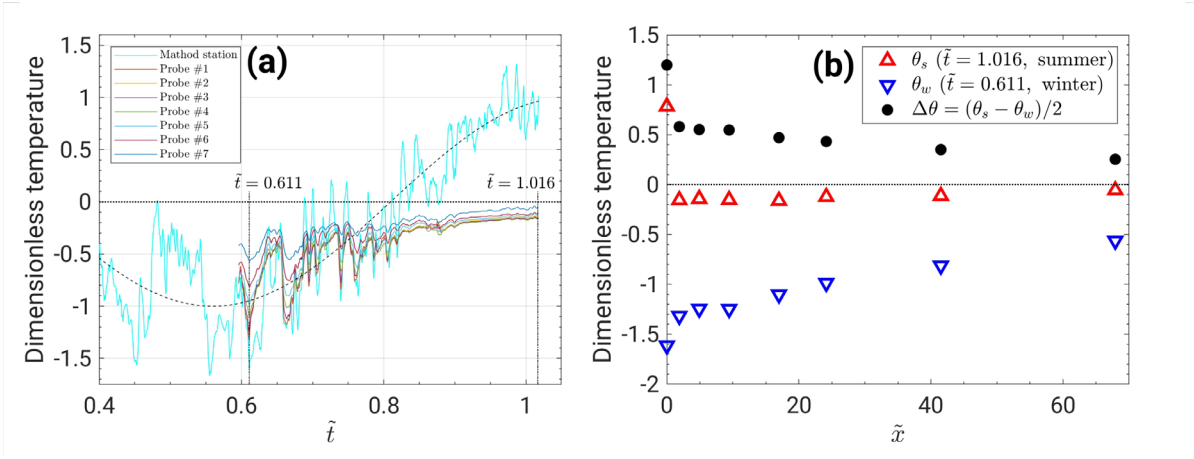

Figure 12. Temperatures in Baulmes conduit. (a) Daily averaged temperatures as a function of time (the temperature at $\tilde{x} = 0$ is the external atmosphere temperature measured at Mathod weather station). (b) Temperature profiles $\theta_s(\tilde{x})$ and $\theta_w(\tilde{x})$ measured respectively in summer and winter, and amplitude of the annual variation $\Delta\theta = (\theta_s - \theta_w)/2$. Dimensionless temperatures defined as $\theta = (T - T_m)/\Delta T_y$.

The difference $\Delta\theta = (\theta_s - \theta_w)/2$ between summer and winter profiles yields an assessment of the amplitude of the ATF in the conduit. $\Delta\theta$ drops from 1.2 to 0.58 between the entrance ($\tilde{x} = 0$) and the first probe ($\tilde{x} = 1.9$). This sudden decrease takes place in the diffusive region. $\Delta\theta$ then smoothly decreases from 0.58 (first probe at $\tilde{x} = 1.9$) to 0.25 at the end of the conduit ($\tilde{x} = 68$). Assuming that the first sensor yields the temperature at the beginning of the convective region, the amplitude of the temperature fluctuation is thus divided by approximately 2.3 in the convective domain of the conduit. This confirms that the conduit length is significantly shorter than the convection length, defined as the distance required to divide by 10 the ATF measured at the beginning of the convective region (see section 4).

6.2 D7.1 Cave (Sieben Hengste, Switzerland)

D7.1 cave is located in the Sieben Hengste karst area (46°45'43"N, 7°49'51"E, 1750 m a.s.l). It is part of a large ventilated cave system (>160 km of cumulated length) subject to chimney effect (see the map in Figure 13). Field observations reveal a seasonal airflow consistent most of the time with an upper entrance of the cave system (i.e., air inflow during the summer season). The ingress of warm external air during summer is marked by some condensation within the first 20 m of the meander, drained as a streamlet at the base of the meander. Otherwise, the cave passage remains remarkably dry. Unexpectedly, temperature and flow rate measurements show periods of time in winter during which the cave sporadically behaves as a lower entrance, with cold air inflow. The explanation of these unexpected flow reversals is still being searched.

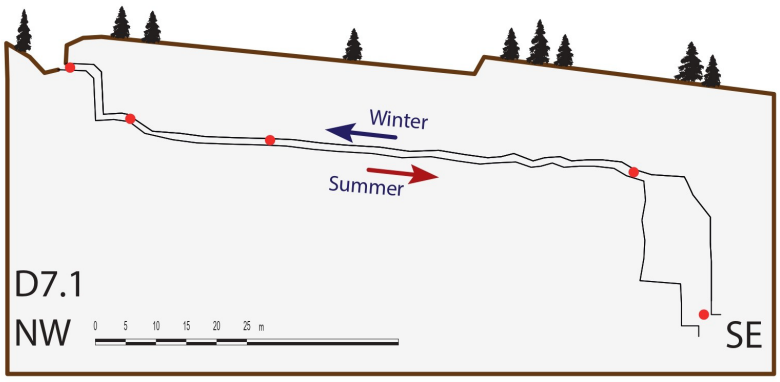

Figure 13. Map of D7.1 Cave. The red circles indicate temperature sensors.

External air temperatures displayed in Figure 14a are provided by an automatic weather station located at 1850 m elevation (SLF), approximately 2 km SE of our study site (sampling period: 1 hour). The external atmosphere temperature was corrected from the elevation as in section 6.1. The FFT yielded $T_m = 5.0°C$ (after correction) and $\Delta T_y = 7.1°C$ for the external AMT and ATF, respectively.

The *ca.* 100 m-long entrance meander of D7.1 Cave has a simple geometry with an average hydraulic diameter of *ca.* 1 m, despite local variations in the cross-sectional area and perimeter. The perimeter $P \approx 3$ m and the scaled radius $\tilde{R} \approx 0.1$ will be considered in the calculations. The meander was instrumented for temperature and airflow measurements between 25/08/2021 and 10/08/2022. Five temperature probes were installed along the main conduit at distances from the cave entrance listed in Table 5. Probes #1 to #4 are Reefnets Sensus Ultra with ±0.3 °C accuracy (sampling period: 30 min). Probe #5 is a HOBO U22-001 with ±0.2 °C accuracy (sampling period: 2 hours). It is located at the base of a 20 m shaft following the entrance meander. Time series from the five probes are displayed in Figure 14b.

Table 5: location of the five temperature probes inside the instrumented conduit of D7.1 Cave. x is the distance from the entrance.

Probe	**#1**	**#2**	**#3**	**#4**	**#5**
x (m)	2	11	33	93	125
$\tilde{x} = x/L_{dif}$	0.38	2.1	6.2	18	24

The cave airflow was measured using a low pressure drop flowmeter (Sensirion SFM 3000 with accuracy of 5% and 20% when velocity is higher and lower than 0.3 m/s, respectively; 50 m from cave entrance) and validated with independent flow measurements (CO_2 gauging) on 10/08/2022. The FFT of the air flow yields the order of magnitude $\Delta\dot{m} \sim 0.1$ kg/s rate (red dashed line in Figure 14a), which results in $Re \sim 7 \times 10^3$. The cave is thus most of the time in the transition between laminar and turbulent regimes. Eq.(24) yields the theoretical convection length $\tilde{L}_0 \approx \tilde{L}_1 \sim 10$. It is important to note that this value must be considered as a lower bound of the convection length. Indeed, Eq.(24) stands for case B (infinite Biot number). At $Re \sim 7 \times 10^3$, case A (finite Biot number) yields a convection length significantly larger than case B (see Figure 8).

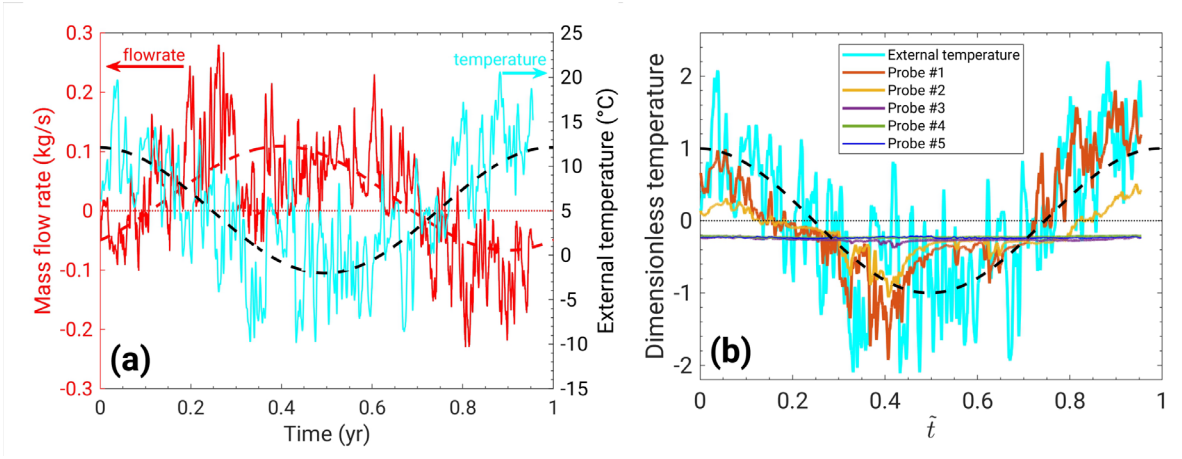

Figure 14. Field data from D7.1 cave (all the data are daily averaged). (a) External temperature and mass flow rate; black and red dashed lines represent the modes k=0 and k=1 computed from the FFT of the external atmosphere temperature and the air flow rate, respectively. (b) Dimensionless temperatures outside and inside the cave ($\theta = (T - T_m)/\Delta T_y$).

The AMT inside D7.1 Cave is displayed in Figure 17a. It decreases to reach a negative quasi-plateau in the range from -0.26 to -0.23 in between probes #3 ($\tilde{x} = 6.2$), and #5 ($\tilde{x} = 24$). This is not the behavior expected for an upper entrance, for which the AMT is supposed to be positive in the convective region before decreasing to zero at some distance from the entrance. Sporadic flow reversals in winter can contribute to this negative AMT (an instance of such an event can be observed around time $\tilde{t} \approx 0.33$ in Figure 14). Moreover, the cave entrance is in a topographic low, resulting in local cold air trapping during winter. In addition, snow is likely to accumulate near the cave entrance. Both may induce local free convection cells in the entrance zone in winter resulting in the cooling of the cave below the external AMT.

If we assess $\tilde{L}_0$ from the distance over which the AMT significantly varies inside the cave, it would range between $\tilde{x} = 2.1$ (probe #2) and $\tilde{x} = 6.2$ (probe #3). This estimation is confirmed by the variation of the ATF with the distance from the entrance (Figure 17b). The ATF at probe #1 ($\tilde{x} = 0.38$), located in the diffusive region, is close to 1. Then it decreases to 0.36 at probe #2 ($\tilde{x} = 2.1$), the first probe in the convective region, and drops down to 0.02 at probe #3 ($\tilde{x} = 6.2$). The ATF being reduced by a factor larger than 10 between probes #2 and #3, $\tilde{L}_1$ should be in between these two probes. It is worthwhile to note that this estimation is consistent with the limit of condensation, which falls in between probes #2 and #3 (20 m corresponds to $\tilde{x} \approx 4$). The convection length of D7.1 Cave is thus in the range from 2.1 to 6.2.

6.3 Bärenhöhle Cave (Austria)

The cave is located in Vorarlberg, Austria (47°22'17''N, 9°52'52''E, 901 m asl). The external atmosphere temperature is obtained from the weather station located at Saint Gallen (47°25'31.7094"N, 9°23'54.7008"E, 776 m a.s.l.), Switzerland about 37 km WNW of our study site (the closer Schopernau station (47°19' N, 10°1'E, 835 m a.s.l.; ZAMG

2012) is subject to thermal inversions during the winter season and thus considered as being less representative). The temperature measured at Saint Gallen has been corrected from the elevation as in section 6.1. It is displayed in Figure 16a. The FFT yielded $T_m = 8.7°C$ (after correction) and $\Delta T_y = 7.6°C$ for the external AMT and ATF, respectively.

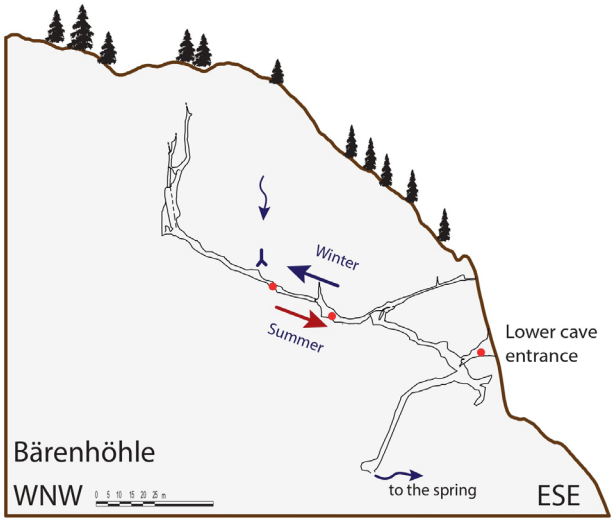

Figure 15. Map of Bärenhöhle. The red circles indicate temperature sensors.

Chimney effect drives the airflow in the cave which behaves as a lower entrance (air inflow in winter, see Figure 15). The difference in elevation between the lower and upper entrances is *ca.* 130 m for a conduit length along the main air passage approximating 240 m (Perkmann and Luetscher, 2013). The average hydraulic diameter is assessed to about 1 m, so that $P \approx 3$ m and $\tilde{R} \approx 0.1$. Air temperature was recorded at 1h interval using three HOBO (U22-001) temperature probes at distances from the entrance listed in Table 6. The corresponding time series are displayed in Figure 16b.

Table 6: location of the three temperature probes inside Bärenhöhle. x is the distance from the lower entrance.

Probe	#1	#2	#3
x (m)	5	85	120
$\tilde{x} = x/L_{dif}$	0.95	16	23

Air flow was recorded between 16/04/2013 and 16/04/2014 at the lower entrance using a thermo-anemometer calibrated to ±0.1 m/s. The FFT of the air flow rate (red dashed line in Figure 16a) yields the orders of magnitude $\Delta\dot{m} \sim 0.6$ kg/s and $Re \sim 5 \times 10^4$. The cave is thus in the turbulent regime most of the time. In this configuration ($\tilde{R} \approx 0.1$ and $Re \sim 5 \times 10^4$), cases A and B predict approximately the same theoretical convection length (see Figure 8). Eq.(24) yields $\tilde{L}_0 \approx \tilde{L}_1 \sim 70$.

The AMT of Bärenhöhle Cave is displayed in Figure 17a. Negative values are consistent with a lower entrance. The lowest AMT (-0.27) is measured at probe #2 ($\tilde{x} = 16$). It increases slightly between probe #2 and the last probe #3. The ATF displayed

in Figure 17b decreases over the whole instrumented conduit, from 1 outside the cave to 0.11 at the last probe ($\tilde{x} = 23$). These two pieces of information suggest that the convection length should be longer than 23, the cave length.

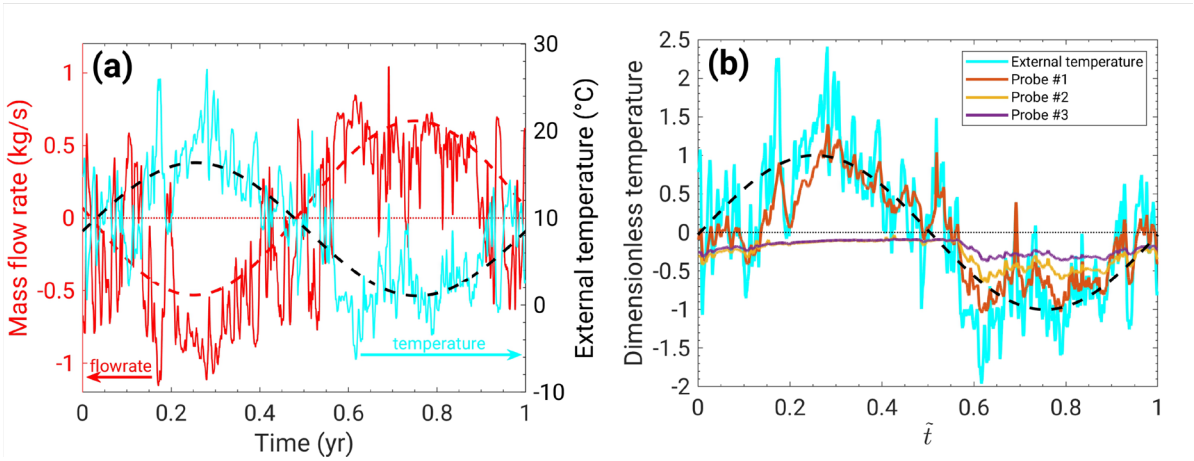

Figure 16. Field data of Bärenhöhle Cave (all the data are daily averaged). (a) External temperature and mass flow rate; black and red dashed lines represent the modes k=0 and k=1 computed from the FFT of the external atmosphere temperature and the air flow rate, respectively. (b) Dimensionless temperatures outside and inside the cave ($\theta = (T - T_m)/\Delta T_y$).

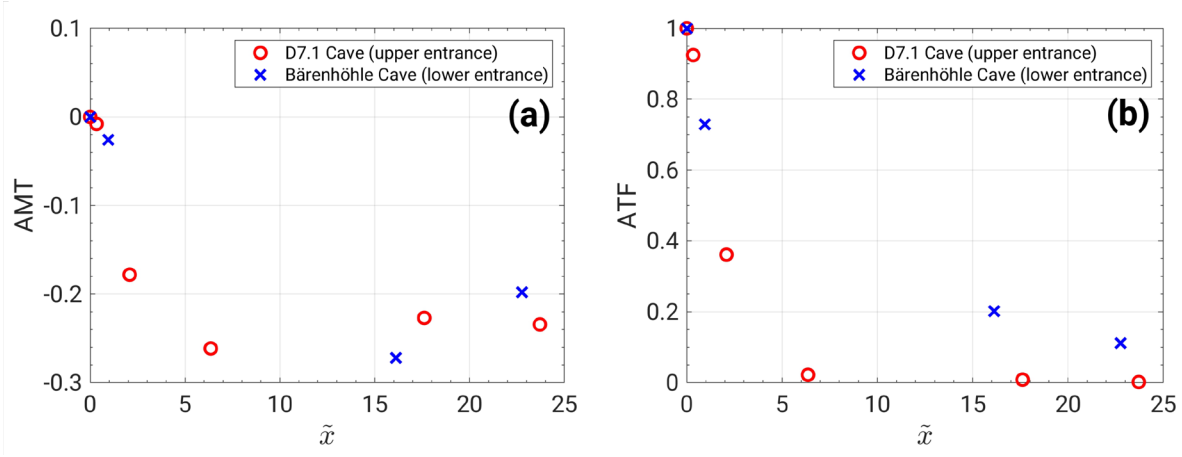

Figure 17. AMT (a) and ATF (b) in D7.1 and Bärenhöhle Caves.

7. Discussion

The main results from the three investigated sites are summarized in Table 7. For two sites (Baulmes mine and Bärenhöhle Cave), we do not observe any contradiction between the model and the field data since both yield a convection length larger than the instrumented conduit (a hundred meters for Bärenhöhle, a few hundreds of meters for Baulmes). In D7.1 Cave, the field data suggest a shorter convection length, in the range from 10 m to 30 m, whereas the theoretical prediction yields a lower bound of 50 m. Although the theoretical order of magnitude is correct, the theory overestimates the convection length. In a cave with a small Reynolds number and a short convection length, local effects in the entrance region, not considered in the model, could

overcome the effect of the mean flow generated by the chimney effect. In the case of D7.1 Cave, cold air ingress in winter might cool down the cave passage more than considered in the model, thus producing an actual shorter thermal length.

Table 7 : Summary table of the three investigated sites (R: cave radius in meters,$\tilde{R}$: dimensionless cave radius; $\Delta\dot{m}$: amplitude of the air flow rate in kg/s; Re: Reynolds number; $\tilde{L}_0$ and $\tilde{L}_1$: dimensionless convection lengths deduced from the AMT and the ATF, respectively; L_0 and L_1: same variables in meters.

		Baulmes mine	**D7.1 Cave**	**Bärenhöhle Cave**
R		1.5 m	0.5 m	0.5 m
$\tilde{R}$		0.3	0.1	0.1
$\Delta\dot{m}$		4 kg/s	0.1 kg/s	0.6 kg/s
Re		10^5	7×10^3	5×10^4
$\tilde{L}_0 \approx \tilde{L}_1$	Field data	>68	[2.1 , 6.2]	> 23
	Theory	$\sim 3 \times 10^2$	> 10	~ 70
$L_0 \approx L_1$	Field data	> 360 m	[10 m , 30 m]	> 120 m
	Theory	$\sim 2 \times 10^3$ m	> 50 m	$\sim 4 \times 10^2$ m

Using a theoretical approach, we defined the characteristic lengths $\tilde{L}_0$ and $\tilde{L}_1$ from the damping in the convective region of the AMT (mode k=0) and ATF (mode k=1), respectively. $\tilde{L}_0$ and $\tilde{L}_1$ are close to each other, and similar results are obtained if the estimation of these lengths is based on the wall temperature or that of the air (see Figure 8). A single convection length is thus sufficient to characterize the extent of the AMT and the ATF along the cave axis. The case B (infinite Biot number) provides a lower bound of the convection length through the simple expression (24). If the Reynolds number is large enough (typically, if $Re > 3 \times 10^4$ for a conduit with a radius of 1 m, see Figure 8), the approximation of infinite Biot number is valid and Eq. (24) is expected to give a right estimation of the convection length. Turning this relation into unscaled variables yields

$$L_0 \approx L_1 \approx 4.0 \times 10^2 \, \frac{\Delta\dot{m}^{1.06}}{R^{0.45}} \tag{25}$$

where L_0, L_1 and R are in meters and $\Delta\dot{m}$ in kg/s. Eq.(25) gives the convection length resulting from the balance between heat advection by the air flow and heat conduction in the rock mass, in the conduction-limited regime. In this case, the convection length is approximately proportional to the amplitude of the flowrate annual fluctuations $\Delta\dot{m}$ divided by the square root of the cave radius R. Ventilated conduits with R of the order of 1 m traversed by an airflow with $\Delta\dot{m}$ ranging from 0.1 kg/s to 1 kg/s are commonly encountered in mines and caves (see the case studies of section 6). For such conduits, Eq.(25) yields a convection length along the conduit axis between a few tens and a few hundreds of meters. Thermal perturbations also propagate in the radial direction, i.e., along the directions perpendicular to the conduit. As expected, the amplitude of the annual fluctuations vanishes over the diffusion length, i.e., a few meters. Conversely, the thermal anomaly (defined as the shift of the annual mean

temperature), propagates along distances of the order of $L_0/10$ (see Figure 9), i.e., over distances of the order of a few meters to a few tens of meters. It is worthwhile to note that in some cases, the extent of the thermal perturbation might be much larger than mentioned above. Luetscher and Jeannin (2004) measured air flow rates around 10 kg/s in Hölloch Cave (Switzerland) and La Diau (France). Recently, airflow rates around 40 kg/s were measured in Shpella Shtares Cave, in Albania (42.31766° N, 19.85403° E, 1427 m a.s.l, see Ref. (Pastore et al., 2019) for more details about this cave). Taking a couple of meters as a rough estimation of the conduit radius in Shpella Shtares, the thermal perturbation should extend over kilometers and hundreds of meters in the axial and radial directions, respectively.

Assessing the thermal penetration length at different time-scales is fundamental to quantify bio-geochemical processes in karst systems. Our study demonstrates that seasonal temperature fluctuations propagate from a few tens of meters up to several thousands of meters into a karst system, depending on ventilation rate and conduit geometry. By way of illustration, let us cite the large ice caves in Austria which host perennial ice formations over several hundreds of meters in the lower entrance zone of ventilated cave systems (e.g. Eisriesenwelt; (Obleitner and Spötl, 2011)). However, it is the advent of speleothems as precisely and accurately dated paleoclimate archives which rises the significance of our study. Stalagmites and flowstones are commonly used to reconstruct climate fluctuations based on their isotope (oxygen and carbon) and trace element concentrations (Fairchild and Baker, 2012). In both cases, the proxy partitioning depends strongly on the cave temperature. While it is commonly assumed that the cave temperature at depth is constant, this is only true beyond the convection length which strongly depends on the time-scale of interest.

Because the temperature-dependent oxygen isotope fractionation between water and calcite ranges between -0.18 and -0.21 ‰/°C (Kim and O'Neil, 1997)(Tremaine et al., 2011), seasonal temperature changes >0.5°C represent a significant source of uncertainty in the speleothem-proxy interpretation and it might be of interest to sample beyond the convective region. Meanwhile, it can be strategic to focus speleothem research on the convective region associated with decadal to millennial cycles, as this area will respond sensitively to outside climate changes without picking up short-term temperature fluctuations.

8. Conclusion

We developed a model coupling buoyancy-induced convection (chimney effect) in a single karst conduit with conduction in the rock mass. We used this model to investigate the propagation of thermal perturbations inside a karst massif. Assuming dry air and a simplified geometry, and reducing the time variations of the external temperature to the annual fluctuations, we performed a parametric study to identify general trends regarding the effect of the air flowrate and conduit size on the amplitude and relaxation length of the thermal perturbations induced by the air flow. The thermal anomaly (defined as a shift in the annual mean temperature) and the

annual temperature fluctuations both propagate over the same distances from the entrance. We call this distance the convection length and we show that at high Reynolds number, it is approximately proportional to the air flow rate divided by the square root of the cave radius. The order of magnitude of the theoretical convection length seem to compare satisfactorily with field data obtained from a mine and two caves. Convection lengths of a few tens to a few hundreds of meters should be commonly encountered in ventilated caves. In extreme cases, it could go up to kilometers.

Acknowledgements

This research was funded in whole or in part by the Swiss National Science Foundation (SNSF) [200021_188636]. The data from Bärenhöhle were acquired in the frame of an APART-fellowship from the Austrian Academy of Science granted to ML.

Open Research

Text files including the numerical results plotted in Figures 4-9 are available in https://doi.org/10.5281/zenodo.10953068 cited as Sedaghatkish and Doumenc (2024). The Comsol Multiphysics file containing the data and results related to the reference case of Figures 4-6 is also available, but a license of Comsol Multiphysics software is necessary to use it. All the field data (including the three instrumented sites) can be found in https://doi.org/10.5281/zenodo.10514555 associated to Sedaghatkish et al.

References

Atkinson, T. C.: Carbon dioxide in the atmosphere of the unsaturated zone: an important control of groundwater hardness in limestones, J. Hydrol., 35, 111–123, 1977.

Banner, J. L., Guilfoyle, A., James, E. W., Stern, L. A., and Musgrove, M.: Seasonal variations in modern speleothem calcite growth in central Texas, USA, J. Sediment. Res., 77, 615–622, 2007.

Bergman, T. L., Lavine, A. S., Incropera, F. P., and DeWitt, D. P.: Fundamentals of Heat and Mass Transfer, Wiley, 2017.

Borsato, A., Johnston, V. E., Frisia, S., Miorandi, R., and Corradini, F.: Temperature and altitudinal influence on karst dripwater chemistry: Implications for regional-scale palaeoclimate reconstructions from speleothems, Geochim. Cosmochim. Acta, 177, 275–297, 2016.

Bourges, F., Genthon, P., Genty, D., Lorblanchet, M., Mauduit, E., and d'Hulst, D.: Conservation of prehistoric caves and stability of their inner climate: lessons from Chauvet and other French caves, Sci. Total Environ., 493, 79–91, 2014.

Bourret, F., Jeannin, P.-Y., Lalou, J.-C., Lambelet, J., Pauli, C., Spring, D., and Thévoz, P.-Y.: Inventaire spéléologique de la suisse, Tome v, Nord vaudois, La Commission de Spéléologie de l'Académie suisse des sciences naturelles, 2007.

Casteel, R. C. and Banner, J. L.: Temperature-driven seasonal calcite growth and drip water trace element variations in a well-ventilated Texas cave: Implications for speleothem paleoclimate studies, Chem. Geol., 392, 43–58, 2015.

Covington, M. D., Luhmann, A. J., Gabrovšek, F., Saar, M. O., and Wicks, C. M.: Mechanisms of heat exchange between water and rock in karst conduits, Water Resour. Res., 47, 2011.

Cropley, J. B.: Influence of surface conditions on temperatures in large cave systems, Bull. Natl. Speleol. Soc., 27, 1–10, 1965.

Domínguez-Villar, D., Krklec, K., López-Sáez, J. A., and Sierro, F. J.: Thermal impact of Heinrich stadials in cave temperature and speleothem oxygen isotope records, Quat. Res., 101, 1–14, 2021.

Domínguez-Villar, D., Krklec, K., and Sierro, F. J.: Thermal conduction in karst terrains dominating cave atmosphere temperatures: Quantification of thermal diffusivity, Int. J. Therm. Sci., 189, 108282, 2023.

Dreybrodt, W., Gabrovšek, F., and Perne, M.: Condensation corrosion: a theoretical approach, Acta carsologica, 34, 2005.

Fairchild, I. J. and Baker, A.: Speleothem science: from process to past environments, John Wiley & Sons, 2012.

Gabrovšek, F.: How do caves breathe: The airflow patterns in karst underground, PLoS One, 18, e0283767, 2023.

Gomell, A., Austin, D., Ohms, M., and Pflitsch, A.: Air pressure propagation through Wind Cave and Jewel Cave: How do pressure waves travel through barometric caves?, Int. J. Speleol., 50, 263–273, https://doi.org/10.5038/1827-806x.50.3.2393, 2021.

Gong, X., Yang, X., Luo, Q., and Tang, L.: Effects of convective heat transport in modelling the early evolution of conduits in limestone aquifers, Geothermics, 77, 383–394, 2019.

Guerrier, B., Doumenc, F., Roux, A., Mergui, S., and Jeannin, P.-Y.: Climatology in shallow caves with negligible ventilation: Heat and mass transfer, Int. J. Therm. Sci., 146, 106066, 2019.

Haaland, S. E.: Simple and explicit formulas for the friction factor in turbulent pipe flow, 1983.

Kim, S.-T. and O'Neil, J. R.: Equilibrium and nonequilibrium oxygen isotope effects in synthetic carbonates, Geochim. Cosmochim. Acta, 61, 3461–3475, 1997.

Kukuljan, L., Gabrovsek, F., and Covington, M.: The relative importance of wind-driven and chimney effect cave ventilation: Observations in Postojna Cave (Slovenia), Int. J. Speleol., 50, 275–288, https://doi.org/10.5038/1827-806x.50.3.2392, 2021.

Lismonde, B.: Climatologie du monde souterrain; Tome 2-Aérologie des systèmes karstiques, Persée-Portail des revues scientifiques en SHS, 2002.

Long, A. J. and Gilcrease, P. C.: A one-dimensional heat-transport model for conduit flow in karst aquifers, J. Hydrol., 378, 230–239, 2009.

Luetscher, M. and Jeannin, P.: Temperature distribution in karst systems: the role of air and water fluxes, Terra Nov., 16, 344–350, 2004.

Luetscher, M., Lismonde, B., and Jeannin, P.: Heat exchanges in the heterothermic zone of a karst system: Monlesi cave, Swiss Jura Mountains, J. Geophys. Res. Earth Surf., 113, 2008.

Mammola, S., Piano, E., Cardoso, P., Vernon, P., Domínguez-Villar, D., Culver, D. C., Pipan, T., and Isaia, M.: Climate change going deep: the effects of global climatic alterations on cave ecosystems, Anthr. Rev., 6, 98–116, 2019.

Obleitner, F. and Spötl, C.: The mass and energy balance of ice within the Eisriesenwelt cave, Austria, Cryosph., 5, 245–257, 2011.

Pastore, C., Pastore, M., Marraffa, M., Marraffa, A., Romano, R., Crespo, S., Fabbri, I., and Santagata, T.: Albania – Tra le (R)Rughe albanesi. Racconti di esplorazioni condivise, Speleologia, 80, 38–45, 2019.

Perkmann, L. and Luetscher, M.: Vermessung und hydrogeologische Untersuchung des Bärenhöhlensystems, Bregenzerwald, Vorarlberg, 64, 32–44, 2013.

Pethkool, S., Eiamsa-Ard, S., Kwankaomeng, S., and Promvonge, P.: Turbulent heat transfer enhancement in a heat exchanger using helically corrugated tube, Int. Commun. Heat Mass Transf., 38, 340–347, 2011.

Promthaisong, P., Jedsadaratanachai, W., and Eiamsa-Ard, S.: 3D Numerical study on the flow topology and heat transfer characteristics of turbulent forced convection in spirally corrugated tube, Numer. Heat Transf. Part A Appl., 69, 607–629, 2016.

Qaddah, B., Soucasse, L., Doumenc, F., Mergui, S., Rivière, P., and Soufiani, A.: Coupled heat and mass transfer in shallow caves: interactions between turbulent convection, gas radiative transfer and moisture transport, Int. J. Therm. Sci., 194, 108556, 2023.

Quindos, L. S., Bonet, A., Diaz-Caneja, N., Fernandez, P. L., Gutierrez, I., Solana, J. R., Soto, J., and Villar, E.: Study of the environmental variables affecting the natural

preservation of the Altamira Cave paintings located at Santillana del Mar, Spain, Atmos. Environ., 21, 551–560, 1987.

Salmon, F., Lacanette, D., Lharti, H., and Sirieix, C.: Heat transfer in rock masses: Application to the Lascaux Cave (France), Int. J. Heat Mass Transf., 207, 124029, 2023.

Sedaghatkish, A. and Doumenc, F.: Software file and numerical results of Modelling heat transfer for assessing the convection length in ventilated caves, April 2024, [Software]. Zenodo. https://doi.org/10.5281/zenodo.10953068

Sedaghatkish, A., Pastore, C., Doumenc, F., Jeannin, P.-Y., and Luetscher, M.: field data for Modelling heat transfer for assessing the convection length in ventilated caves, 2024, [Dataset]. Zenodo. https://doi.org/10.5281/zenodo.10514555

Sinokrot, B. A. and Stefan, H. G.: Stream temperature dynamics: measurements and modeling, Water Resour. Res., 29, 2299–2312, 1993.

Spötl, C., Fairchild, I. J., and Tooth, A. F.: Cave air control on dripwater geochemistry, Obir Caves (Austria): Implications for speleothem deposition in dynamically ventilated caves, Geochim. Cosmochim. Acta, 69, 2451–2468, 2005.

Tremaine, D. M., Froelich, P. N., and Wang, Y.: Speleothem calcite farmed in situ: Modern calibration of δ18O and δ13C paleoclimate proxies in a continuously-monitored natural cave system, Geochim. Cosmochim. Acta, 75, 4929–4950, 2011.

Villar, E., Fernández, P. L., Quindos, L. S., Solana, J. R., and Soto, J.: Temperature of rock surfaces in Altamira Cave (Spain), Trans. Br. Cave Res. Assoc., 10, 165–170, 1983.

Wigley, T. M. L. and Brown, C.: Geophysical applications of heat and mass transfer in turbulent pipe flow, Boundary-layer Meteorol., 1, 300–320, 1971.

Supporting Information

Introduction

Text S1 describes the method based on Fourier series to compute the time-periodic solution of the mathematical model defined in section 2.6. The numerical validation of the method is displayed in Text S2 (including Figs. **S1** to **S3**). A brief comparison between Fourier series (FS) and the resolution of the transient problem by time integration (TI) is presented in Text S3 (including Figs. **S4** to **S6**).

Text S1

The resolution by Fourier series requires a slight modification of the model defined in section 2.6. Eq. (17) resulting from the air energy balance is of order 1 in space, so that only 1 boundary condition must be imposed, the air temperature at the inlet. Since the position of the inlet changes at each flow reversal, the boundary condition has to be applied alternatively on each side of the conduit. This is possible when the problem is solved by time integration, but difficult to implement with Fourier series. This difficulty is overcome by adding a dispersion term in the air energy balance which turns to second order in space, making it possible to apply Dirichlet boundary conditions on both sides of the conduit whatever the flow direction. Eqs. (17-18) turn to:

$$\mu\left(\tilde{t}\right) Re \frac{\partial \theta_a}{\partial \tilde{x}} = \left(4 \frac{k_r}{k_a} Pr^{-1} \right) \tilde{\varphi}_w + RePe^{-1} \frac{\partial^2 \theta_a}{\partial \tilde{x}^2} \tag{S1}$$

$$\theta_a\left(\tilde{x}=0,\tilde{t}\right) = \sin\left(2\pi\tilde{t}\right) \text{ and } \theta_a\left(\tilde{x}=\tilde{L}_{dom},\tilde{t}\right) = 0 \tag{S2}$$

It is important to note that the new dispersion term in Eq. (S1) is a numerical trick with no physical sense. If the Peclet number Pe is large enough, the addition of the dispersion term in Eq. (S1) does not significantly modify the model output. An exception is the outlet region, where the dispersion term induces the air temperature to fit the external temperature at the end of the conduit. This change in the air temperature field takes place over a distance from the outlet of the order of Pe^{-1}, which can be arbitrarily small if Pe is large enough. The constant value $Pe = 10^5$ was set in all the simulations. We checked on a few cases that imposing $Pe = 10^6$ did not change the results.

In a second step, all the functions of time are approximated by truncated Fourier series and inserted in the mathematical model. These functions of time include:

- Two model inputs: the reduced air flowrate $\mu\left(\tilde{t}\right)$ and heat transfer coefficient $\eta\left(\tilde{t}\right)$.
- Two model outputs: the rock and air temperatures, respectively $\theta_r\left(\tilde{x},\tilde{r},\tilde{t}\right)$ and $\theta_a\left(\tilde{x},\tilde{t}\right)$.

We begin with the model inputs. The exact expression of $\mu(\tilde{t})$ and $\eta(\tilde{t})$ are known *a priori* (see section 2.6). Considering that $\mu(\tilde{t})$ is an odd function of time and $\eta(\tilde{t})$ an even function of time, their approximations by truncated Fourier series read:

$$\mu(\tilde{t}) = \sum_{k=1}^{N_\mu} \mu_k \sin(2\pi k\tilde{t}) \quad \text{and} \quad \eta(\tilde{t}) = \eta_0 + \sum_{k=1}^{N_\eta} \eta_k \cos(2\pi k\tilde{t}) \tag{S3}$$

Where μ_k and η_k are real coefficients deduced from the exact expressions of $\mu(\tilde{t})$ and $\eta(\tilde{t})$, respectively. N_μ and N_η are the number of modes taken into account. Increasing N_μ and N_η improves the accuracy of the approximated relations (S3), but requires morecomputational resources.

We now focus on the model outputs. The temperatures fields in the rock $\theta_r(\tilde{x},\tilde{r},\tilde{t})$ and in the air $\theta_a(\tilde{x},\tilde{t})$ are approximated by the truncated Fourier series:

$$\begin{aligned}\theta_r(\tilde{x},\tilde{r},\tilde{t}) &= \theta_{r,0}(\tilde{x},\tilde{r}) + \sum_{k=1}^{N_\theta} \theta_{r,k}(\tilde{x},\tilde{r})\cos\left(2\pi k\tilde{t} + \varphi_{r,k}(\tilde{x},\tilde{r})\right) \\ &= \sum_{-N_\theta}^{N_\theta} \Theta_{r,k}(\tilde{x},\tilde{r})\exp(2\pi jk\tilde{t})\end{aligned} \tag{S4}$$

$$\begin{aligned}\theta_a(\tilde{x},\tilde{t}) &= \theta_{a,0}(\tilde{x}) + \sum_{k=1}^{N_\theta} \theta_{a,k}(\tilde{x})\cos\left(2\pi k\tilde{t} + \varphi_{a,k}(\tilde{x})\right) \\ &= \sum_{-N_\theta}^{N_\theta} \Theta_{a,k}(\tilde{x})\exp(2\pi jk\tilde{t})\end{aligned} \tag{S5}$$

Where the same number of modes N_θ is considered for the rock and air temperatures. The complex coefficients $\Theta_{r,k}$ are such that $\Theta_{r,-k}$ is the conjugate of $\Theta_{r,k}$. They are related to the real amplitudes ($\theta_{r,k}$ and $\theta_{a,k}$) and phase shifts ($\varphi_{r,k}$ and $\varphi_{a,k}$) through the standard relations:

$$\theta_{r,0} = \Theta_{r,0} \quad \text{and} \quad \theta_{a,0} = \Theta_{a,0} \tag{S6}$$

$$\theta_{r,k} = 2\sqrt{\Theta_{r,k}\Theta_{r,-k}} \quad \text{and} \quad \theta_{a,k} = 2\sqrt{\Theta_{a,k}\Theta_{a,-k}} \quad \text{for } k > 0 \tag{S7}$$

$$\tan\varphi_{r,k} = -\frac{j\left(\Theta_{r,k} - \Theta_{r,-k}\right)}{\Theta_{r,k} + \Theta_{r,-k}} \quad \text{and} \quad \tan\varphi_{a,k} = -\frac{j\left(\Theta_{a,k} - \Theta_{a,-k}\right)}{\Theta_{a,k} + \Theta_{a,-k}} \quad \text{for } k > 0 \tag{S8}$$

Injecting Eqs. (S3-S5) in the mathematical model of section 2.6 yields the equations:

$$\frac{Re}{2j}\sum_{m=1,3,\ldots}^{N_\mu} \mu_m\left(\frac{d\Theta_{a,k-m}}{d\tilde{x}} - \frac{d\Theta_{a,k+m}}{d\tilde{x}}\right) = \left(4\frac{k_r}{k_a}Pr^{-1}\right)\tilde{\Phi}_{w,k} + RePe^{-1}\frac{d^2\Theta_{a,k}}{d\tilde{x}^2} \tag{S9}$$

$$\Theta_{a,k}(\tilde{x}=0) = \frac{1}{2j} \text{ for } k=1, \ \Theta_{a,k}(\tilde{x}=0) = 0 \text{ for } k \neq 1 \tag{S10}$$

$$\Theta_{a,k}(\tilde{x}=\tilde{L}_{dom})=0, \tag{S11}$$

$$2\pi jk\Theta_{r,k}=\frac{1}{\tilde{r}}\frac{\partial}{\partial\tilde{r}}\left(\tilde{r}\frac{\partial\Theta_{r,k}}{\partial\tilde{r}}\right)+\frac{\partial^2\Theta_{r,k}}{\partial\tilde{x}^2} \tag{S12}$$

$$\Theta_{r,k}(0,\tilde{r})=\frac{1}{2j}\ \text{ for }\ k=1,\ \Theta_{r,k}(0,\tilde{r})=0\ \text{ for }\ k\neq 1 \tag{S13}$$

$$\frac{\partial\Theta_{r,k}}{\partial\tilde{x}}(\tilde{x}=\tilde{L}_{dom},\tilde{r})=0\ \text{ and }\ \frac{\partial\Theta_{r,k}}{\partial\tilde{r}}(\tilde{x},\tilde{r}=\tilde{R}_{dom})=0 \tag{S14}$$

$$\begin{aligned}&\text{Case A}: \tilde{\Phi}_{w,k}=\frac{\partial\Theta_{r,k}}{\partial\tilde{r}}(\tilde{x},\tilde{R})\\&=Bi\sum_{n=0,2,\ldots}^{N_\eta}\frac{\eta_n}{2}\left[\Theta_{r,k-n}(\tilde{x},\tilde{R})-\Theta_{a,k-n}(\tilde{x})+\Theta_{r,k+n}(\tilde{x},\tilde{R})-\Theta_{a,k+n}(\tilde{x})\right]\end{aligned} \tag{S15}$$

$$\text{Case B}:\ \tilde{\Phi}_{w,k}=\frac{\partial\Theta_{r,k}}{\partial\tilde{r}}(\tilde{x},\tilde{R})\ \text{ and }\ \Theta_{a,k}(\tilde{x})=\Theta_{r,k}(\tilde{x}) \tag{S16}$$

Where $j=\sqrt{-1}$ and k is an integer varying from 0 to N_θ. Eqs. (S9) and (S12) thus define a set of $2(N_\theta+1)$ coupled partial differential equations (PDE) with boundary conditions (S10-S11, S13-S16). This set of PDE, which does not include the time variable $\tilde{t}$, is solved numerically by finite elements (Galerkin method with quadratic Lagrangian elements, Comsol Multiphysics software). The resolution yields the complex coefficients $\Theta_{r,k}(\tilde{x},\tilde{r})$ and $\Theta_{a,k}(\tilde{x})$. The real amplitudes and phase shifts are deduced from relations (S7-S8) and the temperatures as a function of time from relations (S4-S5).

Text S2

The choice of N_μ, N_η and N_θ results from a compromise between the accuracy of the results on one hand, the difficulty of the implementation and the available computational resources on the other hand. The sensitivity of the simulation results to N_θ, N_μ and N_η is investigated below for case A with $\tilde{R}=0.2$ and Re = 7.2 × 10^5.

We first set N_η = 0 and N_μ = 1 and we investigate the effect of N_θ. Figure **S1** displays the effect of N_θ on the time series of the wall temperature at $\tilde{x}=10$ and $\tilde{x}=100$. The general shape of the curve is little modified for $N_\theta \geq 6$, but the description of the rapid oscillations around $\tilde{t}\simeq 0.05$ and $\tilde{t}\simeq 0.45$ requires a larger number of modes. The same approach is used to investigate the effect of N_η and N_μ. Figure **S2** shows that these parameters have little effect on the results for the selected configuration. In all the simulations, we imposed N_θ = 18, N_η = 6 and N_μ = 7 which happened to be a reasonable compromise between accuracy and complexity. We checked on a few configurations that increasing the number of modes above the selected values did not significantly changed the results.

In order to confirm its validity, the numerical solution based on Fourier series was compared with the solution obtained by time integration (Galerkin method with quadratic Lagrangian elements, time discretization using implicit Backward Differentiation Formula, Comsol Multiphysics software). The TI simulation was done over 28 cycles (i.e., from time $\tilde{t}=0$ to $\tilde{t}=28$) taking as the initial condition the solution obtained from Fourier series at $\tilde{t}=0$. The comparison between TI (last cycle, from time $\tilde{t}=27$ to 28) and FS is displayed in Fig. **S3**. Small discrepancies are observed during the rapid oscillations around times $\tilde{t}\simeq 27.05$ and $\tilde{t}\simeq 27.45$ for $\tilde{x}=10$ and $\tilde{x}=100$, but the overall agreement is excellent.

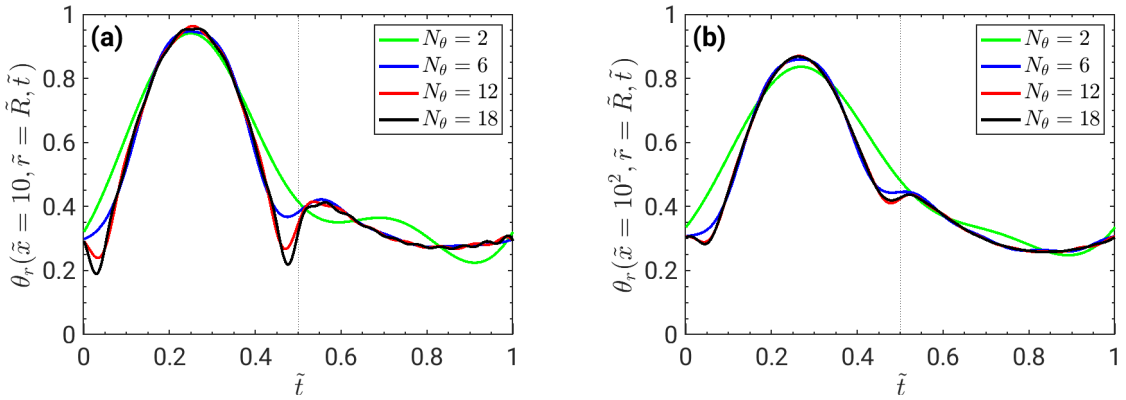

Figure S1. Time evolution of the wall temperature at $\tilde{x}=10$ (a) and $\tilde{x}=100$ (b) for N_η = 0, N_μ = 1 and different values of N_θ. Case A with $\tilde{R}=0.2$ and Re = 7.2 × 10^5.

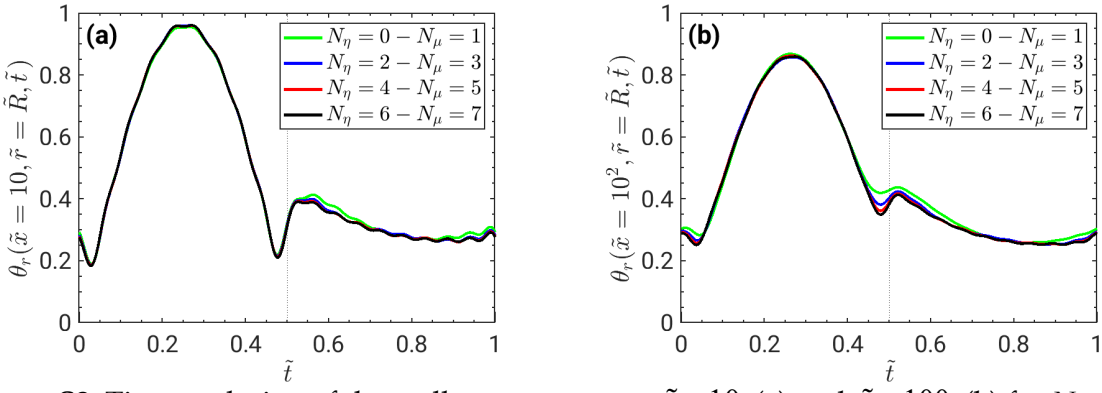

Figure S2. Time evolution of the wall temperature at $\tilde{x}=10$ (a) and $\tilde{x}=100$ (b) for N_θ =18 and different values of N_η and N_μ. Case A with $\tilde{R}=0.2$ and Re = 7.2 × 10^5.

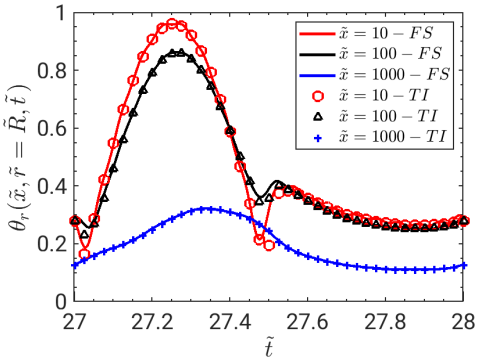

Figure S3. Time evolution of the conduit wall temperature calculated using Fourier series (FS) or time integration (TI), at different distances from the entrance $\tilde{x}$. FS solution at $\tilde{t} = 0$ used as the initial condition of TI simulation. Case A with $\tilde{R} = 0.2$ and $Re = 7.2 \times 10^5$.

Text S3

A standard approach, not used in this study, would consist in solving the time-dependent problem by TI starting from an arbitrary initial condition (e.g., $\theta_r(\tilde{x}, \tilde{r}, \tilde{t} = 0) = \theta_a(\tilde{x}, \tilde{t} = 0) = 0$). The time-dependent solution converges to the periodic regime at infinite time. A good approximation can thus be obtained if the simulated time is long enough. Figures (**S4-S6**) display the parameters defined in Section 4 calculated from TI as a function of time or FS, for case A with $\tilde{R} = 0.189$ and $Re = 1.8 \times 10^5$. With the exception of $\tilde{W}_1$, TI results converge slowly to the periodic regime. Taking FS as a reference, TI yields errors at time $\tilde{t} = 50$ in the range from 10% to 30% for $\overline{\theta}_w$, $\Delta\theta_w$, $\tilde{L}_0$ and $\tilde{L}_1$. These errors are acceptable if rough estimates are required. In contrast, TI underestimates $\tilde{W}_0$ by an order of magnitude. To get a correct estimate of this parameter and improve the accuracy of others, TI would require to simulate a time of the order of the diffusion time $\tilde{W}_0^2 \simeq 64^2 \sim 4 \times 10^3$, i.e. thousands of years. Such simulations would require computational times hardly compatible with current computer resources.

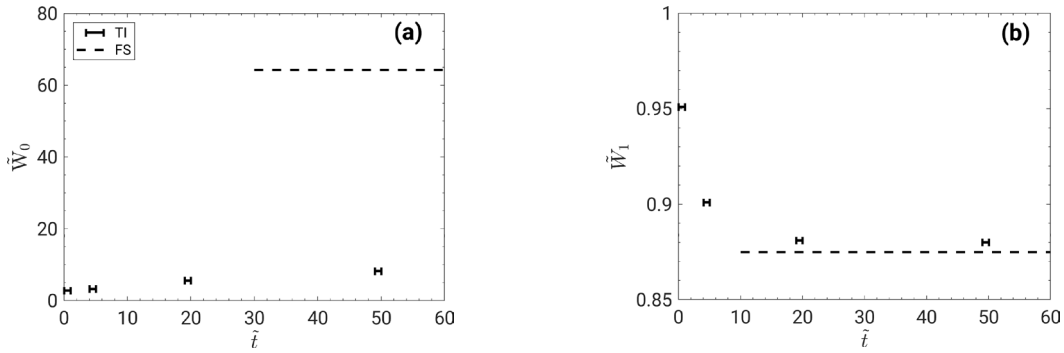

Figure S4. $\tilde{W}_0$ (a) and $\tilde{W}_1$ (b) estimated from Fourier series (FS) or time integration (TI). Initial conditions in TI simulations set to zero. Case A with $\tilde{R} = 0.189$ and $Re = 1.8 \times 10^5$.

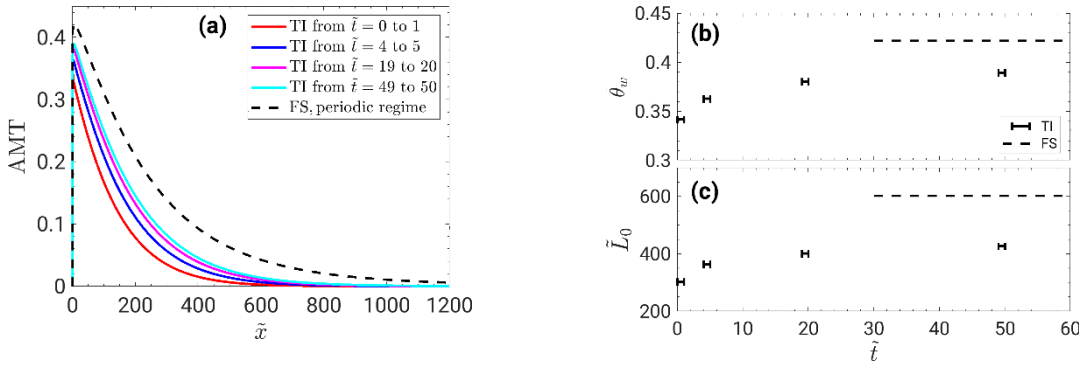

Figure S5. AMT of the conduit wall (a), $\overline{\theta}_w$ (b) and $\tilde{L}_0$ (c) estimated from Fourier series (FS) or time integration (TI). Initial conditions in TI simulations set to zero. Case A with $\tilde{R}=0.189$ and $Re = 1.8 \times 10^5$.

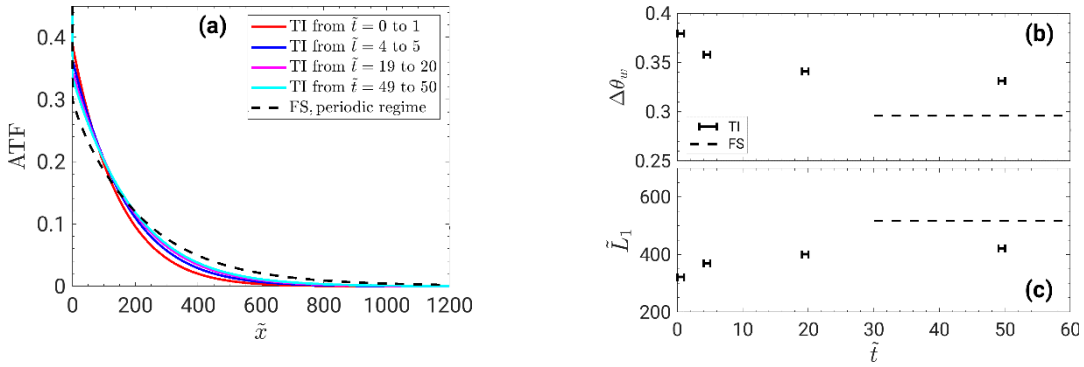

Figure S6. ATF of the conduit wall (a), $\Delta\theta_w$ (b) and $\tilde{L}_1$ (c) estimated from Fourier series (FS) or time integration (TI). Initial conditions in TI simulations set to zero. Case A with $\tilde{R}=0.189$ and $Re = 1.8 \times 10^5$.

Chapter 3: Thermal modelling of caves ventilated by chimney effect (published paper)

Amir Sedaghatkish, Claudio Pastore, Frédéric Doumenc, Pierre-Yves Jeannin, Marc Luetscher, Thermal modeling of caves ventilated by chimney effect, *International Journal of Thermal Sciences*, Volume 212, 2025, 109757, https://doi.org/10.1016/j.ijthermalsci.2025.109757

Abstract

Cave ventilation significantly increases the depth of natural thermal oscillations and decreases the time of propagation compared to heat conduction in the rock mass. This makes it necessary to develop and test thermal models for the prediction of temperature fields in ventilated karst massifs. Here, we develop a thermal model of a single conduit ventilated by chimney effect. The model is based on the diffusion equation in the rock mass coupled to the conservation of energy and water vapor mass in the airflow. The effect of the latent heat of evaporation and condensation is considered. In parallel, the main conduit of a ventilated cave has been equipped with a flowmeter and several temperature sensors. The model is tested against field data collected during a complete year. The relevance of the model assumptions (geometry simplification, initial and boundary conditions, use of transfer coefficients to couple the air and the conduit wall) is thoroughly analyzed. The model correctly predicts the temperature fluctuations at daily and yearly scale, but underestimates the mean annual temperatures inside the cave. A biased assessment of the ground temperature seems to explain this discrepancy. The effect of condensation and evaporation on the cave climate turns out to be low on cave temperature, but significant on air humidity with consequences for ecology or paleoclimatology. This study is a first step towards the elaboration and validation of models providing a quantitative assessment of caves' thermal response at any location and time scale.

1. Introduction

Extensive cave networks in karst massifs are traversed by airflows that considerably enhance heat and mass transfer between the bedrock and the external environment (Lismonde, 2002). The impact of airflow must be considered in a wide range of areas including paleoclimatology and ecological issues. Indeed, isotope fractionation that occurs during calcite precipitation is temperature dependent. Airflow also controls evaporation and condensation of water, the transport of carbon dioxide, and their consequences on precipitation and dissolution rates of calcite (Kukuljan et al., 2021a; Kowalczk and Froelich, 2010). A good understanding of heat and mass transfer associated with airflow is thus requested for paleoclimate reconstructions (Cuthbert et al., 2014; Rau et al., 2015). It is also relevant for the study of subterranean fauna and flora (Culver and Pipan, 2019). Indeed, caves are home to many temperature sensitive species, including bats, beetles, or thysanurans (Braack, 1989). These subterranean ecosystems and their biodiversity are particularly vulnerable to climate change (Castaño-Sánchez et al., 2020). For instance, Rizzo et al. (2015) observed that the

survival rate of Pyrenean beetles over 7 days was 100% at 6-20°C, and collapsed to 0% at 23-25°C. This example illustrates the need for reliable thermal model for predicting the consequences of global warming on the temperature field in karst massifs.

The fluctuations of the external pressure can play a role in cave ventilation (Gomell et al., 2021). Large caves with a single narrow entrance are ventilated by barometric effect (Borsato et al., 2024), and wind pressure may be the dominant driving force in caves with multiple entrances at similar heights (Kukuljan et al., 2021b). In caves with multiple entrances at different heights, the most significant cause of ventilation is the chimney effect resulting from the density contrast between the air inside and outside the cave (Lismonde, 2002). In temperate climates, this density contrast is mainly due to temperature (Gabrovšek, 2023). Because of the high thermal inertia of the massif, the airflow direction is upward during most of the winter, when the temperature inside the cave is warmer than the atmospheric temperature. Conversely, the air flows downward during most of the summer. A noticeable consequence of this seasonal inversion of the airflow is the thermal anomalies observed in the entrance regions (Lismonde, 2002). In lower entrance areas, the annual mean temperature is shifted to a lower value than outside because this part of the cave receives cold air at the atmospheric temperature in winter and air cooled down after circulating in the massif in summer. The same mechanism produces a warm anomaly in upper entrance areas.

Airflow modifies the rock temperature in the cave, which in turn changes the air temperature profile inside the cave. Therefore, both the air and the rock mass must be considered in a model aiming at predicting the climate of a ventilated cave. Lismonde (2002) and Gabrovšek (2023) developed such models based on the 1D energy balance in the airflow and the heat conduction equation in the rock mass. Both equations were coupled by the Newton's law of cooling, which states that the local heat flux through the cave wall is proportional to the difference between the wall temperature and the mixing temperature of the air. The coefficient of proportionality, the so-called heat transfer coefficient, depends on the conduit geometry, the fluid properties, the wall roughness and the fluid velocity. It was assessed using standard correlations for fully developed forced convection in pipes (see for instance Bergman et al., 2017). This approach allowed Lismonde (2002) and Gabrovšek (2023) to reproduce qualitatively in numerical simulations some field observations as for instance the seasonal hysteresis of the flow rate or the thermal anomaly in the entrance areas.

Recently, we used similar models to investigate the propagation of thermal perturbations by the airflow inside a karst massif in a quantitative way (Sedaghatkish et al., 2024). We considered the simple geometry of a straight horizontal conduit of constant circular cross-section. Numerical simulations showed that turbulent airflow, very common in ventilated caves, significantly modifies the rock temperature. Numerical simulations supported the partition of the cave into three regions as first proposed by Cropley (1965): (a) a short diffusive region, where heat mainly propagates from the atmosphere by conduction in the rock mass; (b) a convective

region where heat is mainly transported by the air flow; (c) a deep karst region characterized by quasi-constant temperatures throughout the year. The length of the diffusive region is of the order of a few meters, whatever the values of the air flowrate and conduit diameter. The length of the convective region, defined as the convection length, corresponds to both the extent of the thermal anomaly and the distance of propagation of the annual temperature fluctuations. Numerical simulations showed that the convection length can commonly reach a few tens to a few hundreds of meters. It is approximately proportional to the amplitude of the flowrate annual fluctuations divided by the square root of the cave radius (Sedaghatkish et al., 2024). The orders of magnitude predicted by the model were consistent with field data from a mine tunnel and two caves.

In the present paper, we want to go beyond orders of magnitude by carrying out detailed and systematic comparisons between numerical simulations and field data. Indeed, numerical simulation of ventilated cave climate is still a challenge. To our knowledge, direct and quantitative comparisons between models and field data are still lacking. The present article provides such a comparison, with the aim of testing the validity of the physical assumptions included in the model. We focused on the following issues.

- A cave is a succession of bends, conduit contractions or enlargements, and obstacles of any kind. The first of the problems posed by this complex geometry is the level of accuracy required for its description. More specifically, is it necessary to consider a full 3D problem, or can we define an equivalent 2D geometry to save computational resources?

- The irregular geometry of caves also has important consequences on the assessment of the heat transfer coefficient. Correlations commonly used in thermal models are valid for straight rough pipes of uniform cross-section (Bergman et al., 2017). Geometrical singularities are expected to increase the turbulence level, which in turn can significantly enhance the heat transfer coefficient. Some corrections exist to take into account the effect of the well-defined singularities commonly found in heat exchangers (Rohsenow et al., 1998). However, they can hardly be used for the tortuous geometries typically encountered in caves.

- Numerical simulations are based on mathematical models that require initial and boundary conditions. Ideally, the temperature field at any point of the massif should be known at the initial time, which is never the case. Another issue is the boundary condition at the external surface (i.e., the interface between the massif and the atmosphere). The simplest choice is to assume that the external surface temperature is equal to the atmospheric temperature (Gabrovšek, 2023; Sedaghatkish et al., 2024). However, the earth surface does not only interact with the surrounding air. Its temperature results from an energy balance including convection with the air, solar irradiation (short

wavelength), radiative exchange with the surrounding environment and the sky (long wavelength), latent heat due to evaporation or condensation, and conduction inside the rock (Salmon et al., 2023). This raises the question of the most relevant boundary condition at the external surface.

- Condensation and evaporation of water are commonly observed on the walls of ventilated caves (De Freitas and Schmekal, 2005; Fernandez-Cortes et al., 2013; Gázquez et al., 2022). Since the latent heat of evaporation or condensation induces cooling or warming, its contribution to cave climate must be evaluated.

With the aim of addressing these issues, flowrate and temperatures in the ventilated cave of Longeaigue (Switzerland) have been recorded during a complete year. In parallel, we developed a thermal model of the cave, for which results have been tested against the field data collected in the cave.

2. Field data

2.1. Study site

The "Baume de Longeaigue" displayed in Fig. 1 is located in the Swiss Jura Mountains (Val-de-Travers; Upper entrance: 46°52′22″ N 6°31′09″ E, 917 m a.s.l.; Lower entrance: 46°52′18″ N 6°31′09″ E, 820 m a.s.l.). The difference of elevation between both entrances is 97 m. This induces an intense buoyancy-driven airflow inside the conduit that connects both entrances. A secondary conduit (blue arrow on Fig. 1), likely connecting the cave to the atmosphere through a network of fractures, intersects the main conduit at approximately 16 m from the upper entrance. The possibility of a leak through this secondary conduit cannot be excluded.

The total length of the main conduit of Longeaigue cave is 311 m. Its shape and size are highly variable. The cross-sectional area A and perimeter P are displayed in Fig. 2 as a function of x, the distance from the upper entrance following the conduit axis. Both values were obtained using a laser-scanner with a 10^{-2} m resolution every 10 m along the cave. Fig. 3 displays the angle $\theta(x)$ between the upward vertical direction and the velocity vector of the air when flowing from the upper to the lower entrance.

The lower entrance is a temporary spring acting as an overflow of the "Raies" hydrogeological system, whose catchment area is approximately 60 to 80 km^2. The maximum water discharge-rate at Longeaigue entrance does probably reach approximately 5 m^3/s (Jeannin, 2018). A perennial lake has formed in the lower part of the main conduit (see Fig. 1). During flood events, the rise of the water level is sufficient to close the conduit, interrupting the airflow. This is an important feature of Longeaigue Cave that must be considered in the thermal model.

Since August 2020, several stations monitor the cave temperature as well as the airflow along the main conduit of the cave (red symbols in Fig. 1).

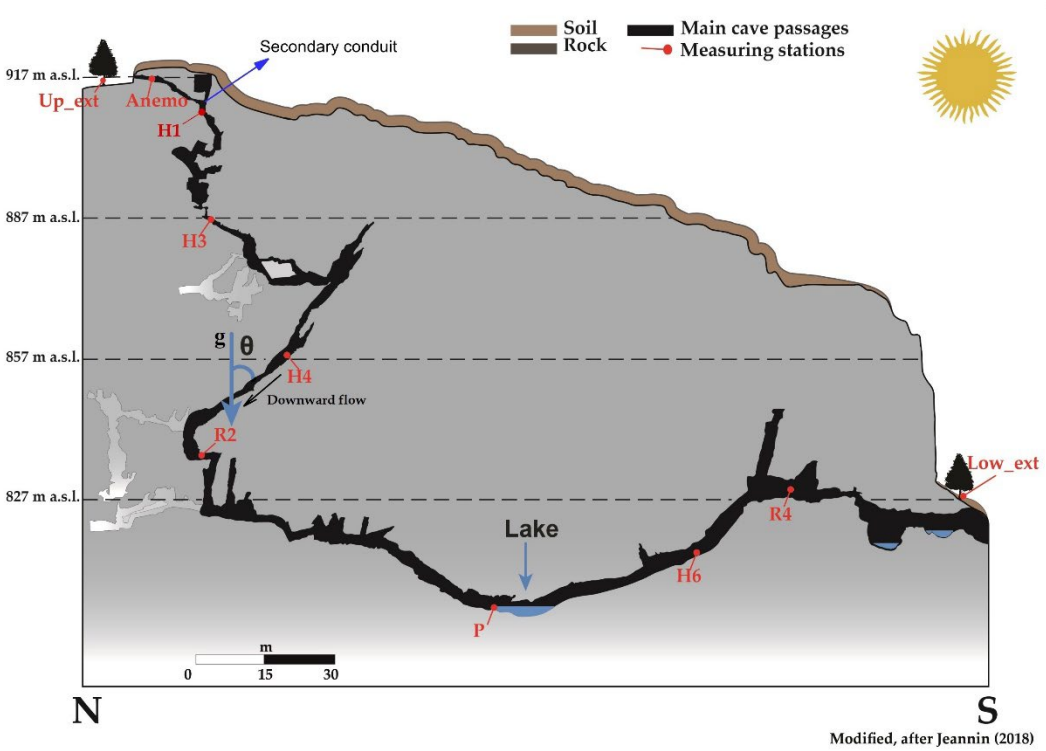

Fig 1. Longeaigue cave topography (developed vertical profile; main conduit in black, sensor locations in red).

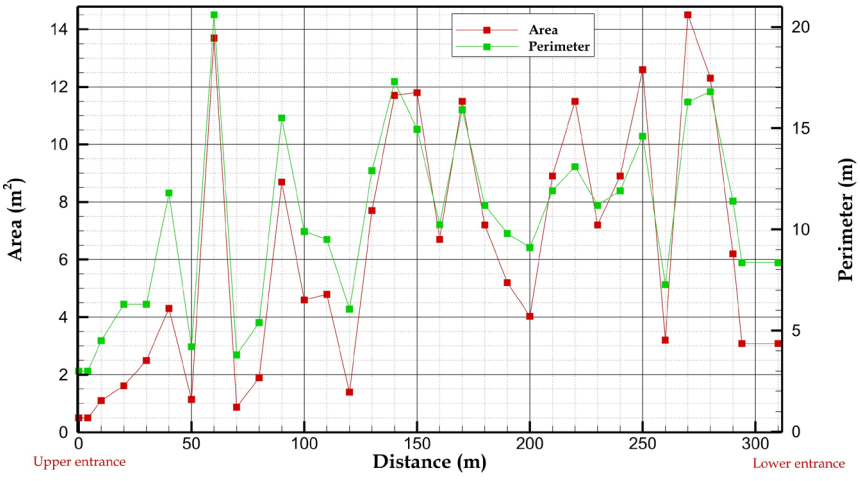

Fig 2. Variation of the cross-sectional area A and perimeter P as a function of the distance x from the upper entrance.

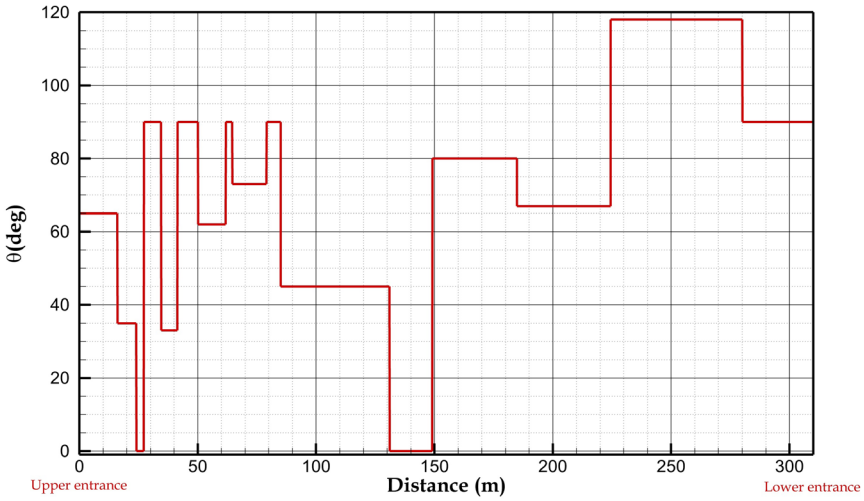

Fig 3. Angle θ between the gravity vector and the velocity vector of the air when flowing from the upper to lower entrance as a function of the distance x from the upper entrance (θ is larger than 90°C in the conduit segment between P and R4 stations, see Fig. 1).

2.2. Temperature measurements

The temperature data logging stations indicated by H in Fig. 1 were equipped with Hobo Water Temperature Pro v2 (sensor type U22-01, accuracy ±0.21 °C, resolution 0.02 °C). Reefnet Sensus Ultra temperature (accuracy ±0.3 °C, resolution 0.01 °C) were deployed at the stations indicated by R. Two additional Reefnet sensors were used to monitor the atmospheric temperature close to the upper and lower entrances. Another temperature sensor was installed in Anemo station close to the upper entrance (sensor type MS8607 (Adafruit), accuracy ±1 °C, resolution 0.01 °C). The distance of each station from the upper (and lower) entrance are listed in Table 1. To make the conduit open enough for the commuting of cavers, all the sensors were located close to the wall, at a distance ranging from 2 to 4 cm.

With the exception of H1, the temperatures used in this paper were recorded from 13/08/2020 to 13/08/2021, which is exactly one year. The Hobo water probe installed in H1 at a few centimeters from the wall was complemented with a Pt100 sensor (TMC1-HD from Hobo Company, resolution: 0.02°C, accuracy: 0.1) suspended approximately at the center of the cross-section. The temperature of these two probes were recorded for approximately one month, from 11/10/2022 to 06/11/2022 (sampling rate for all temperature measurements: one measuring point per hour).

Table 1. Location of measuring stations

Station	Distance from the upper (lower) entrance
Up_ext	Outside, near the upper entrance
Anemo	4 m (307 m)
H1	16 m (295 m)
H3	55 m (256 m)
H4	97 m (214 m)
R2	140 m (171 m)
P	216 m (95 m)
H6	269 m (42 m)
R4	294 m (17 m)
Low_ext	Outside, near the lower entrance

External upper and lower temperatures are displayed in Fig. 4a. The dashed lines represent the function:

$$T_{atm}(t) = T_m - \Delta T \, sin\left[\frac{2\pi}{\tau}(t - t_0)\right] \quad (1)$$

where $\tau = 1$ year, t_0 is a parameter that accounts for the origin of time, T_m is the annual mean temperature (AMT) and ΔT the amplitude of the annual temperature fluctuations (ATF). t_0, T_m and ΔT are deduced from the Fast Fourier Transform (FFT) of the atmospheric temperatures displayed in Fig. 4b, which also provides the amplitude of all other modes, including that of the daily temperature fluctuations (DTF). As expected, the modes showing the highest amplitudes are the ATF and the DTF. The ATF amplitudes at the upper and lower entrances (respectively 8.34 and 8.28°C) are very close to each other. The amplitudes of the DTF differ a little more (3.4°C and 2.4°C at the upper and lower entrances, respectively). The AMT is higher at the upper entrance (7.38°C) than at the lower entrance (6.75°C). The mean vertical thermal gradient between both entrances is thus 6.5 °C/km.

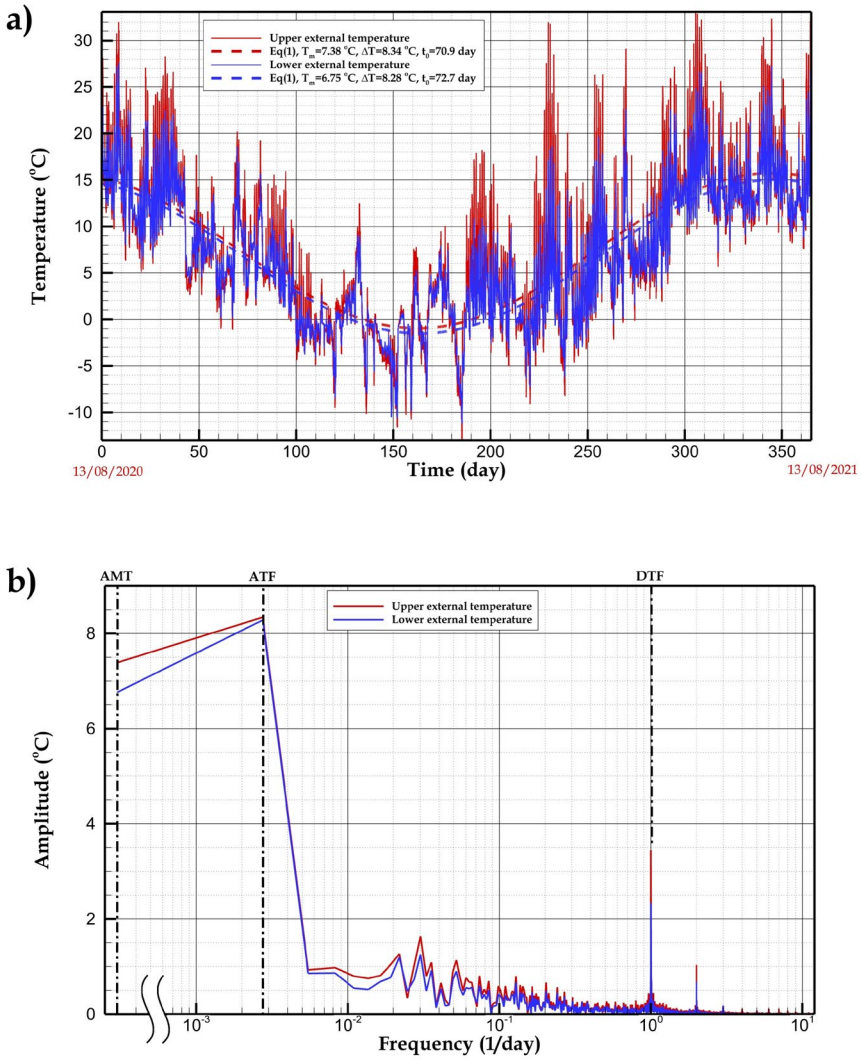

Fig 4. Atmospheric temperature close to the upper and lower entrances. a) Time series; b) Amplitude as a function of frequency deduced from FFT (due to the logarithmic scale the AMT, which corresponds to zero frequency, is located at an arbitrary origin).

2.3. Airflow measurements

The Sensirion SFM3003-300-CE (from now on SFM) is a digital bidirectional mass flowmeter installed at Anemo station, at 4 m from the upper entrance (Fig. 1). The device is compact and robust. It shows a high data resolution (up to 16 bit) and low power requirement (typically 3.3 V and 3.8 mA). Furthermore, the bidirectional cave airflow is well recognized by the device which records the flow direction as negative or positive values. The device measures the flowrate that passes through a tube with an inner diameter of 20 mm. This flowrate is then converted in local air velocity through appropriate calibration with an accuracy of ±5% for speeds higher than 0.30 m/s and ±26% for speeds in the range from 0.15 to 0.30 m/s (Pastore et al., 2024). The flowrate through the conduit is obtained by multiplying this local velocity by the cross-sectional area. The main cause of uncertainty is the non-uniform velocity field

over the cross-section. Complementary measurements performed by other means (including manual measurements with an anemometer, CO_2 gauging, comparison with other SFM) suggest that: (a) the flowrate measured at Anemo station is certainly underestimated, (b) the ratio of the real flowrate over the measured flowrate cannot be larger than 1.5.

The air mass flowrate was recorded simultaneously with the temperatures using the same sampling rate (see Fig. 5a). It varies approximately in the range from -1.5 $kg.s^{-1}$ in winter to 1 $kg.s^{-1}$ in summer (positive values correspond to airflow direction from the upper to the lower entrance). The sporadic interruptions of airflow when the lake completely fills the lower part of the conduit are clearly observed in Fig. 5a. A pressure sensor has been installed in point P (see Fig. 1 and Table 1) to measure the lake level. It provides the time ranges during which the main conduit is blocked by the lake (called "cave closures" in the following). Fig. 5a shows that the flowrate measured at Anemo station during these cave closures is not always zero. This can be due to the existence of a leakage rate through the secondary conduit (see Section. 2.1 and Fig. 1), or to sporadic free convection cells developing from the upper entrance, inducing local velocities recorded by the SFM. Conversely, it can happen that no airflow is measured whereas the pressure sensor indicates that the cave is open (e.g., for time ranging from 196 and 213 days). This happens when the flowrate is too small to be detected by the SFM, or because of an uncertainty on the lake level corresponding to cave closures. During the monitoring year, the cave was closed for 203 days (56% of the time). The airflow was directed from the upper to the lower entrance for 66 days and in the reverse direction for 95 days (respectively 18% and 26% of the time).

The FFT of the mass flowrate is displayed in Fig. 5b. In contrast with the temperature spectrum that was dominated by the annual and daily fluctuations, many other modes emerge with amplitudes comparable or even higher than the annual flowrate fluctuations (AFF) or daily flowrate fluctuations (DFF). These modes with intermediate frequencies originate from the intermittent lake closures. Moreover, the annual mean flowrate (AMF) is strictly positive, and equal to half the AFF. This seasonal asymmetry is due to the highest flowrates reached in winter. The dashed lines in Fig. 5a represent the same sine function as in Eq. (1) after substituting temperatures for mass flowrates.

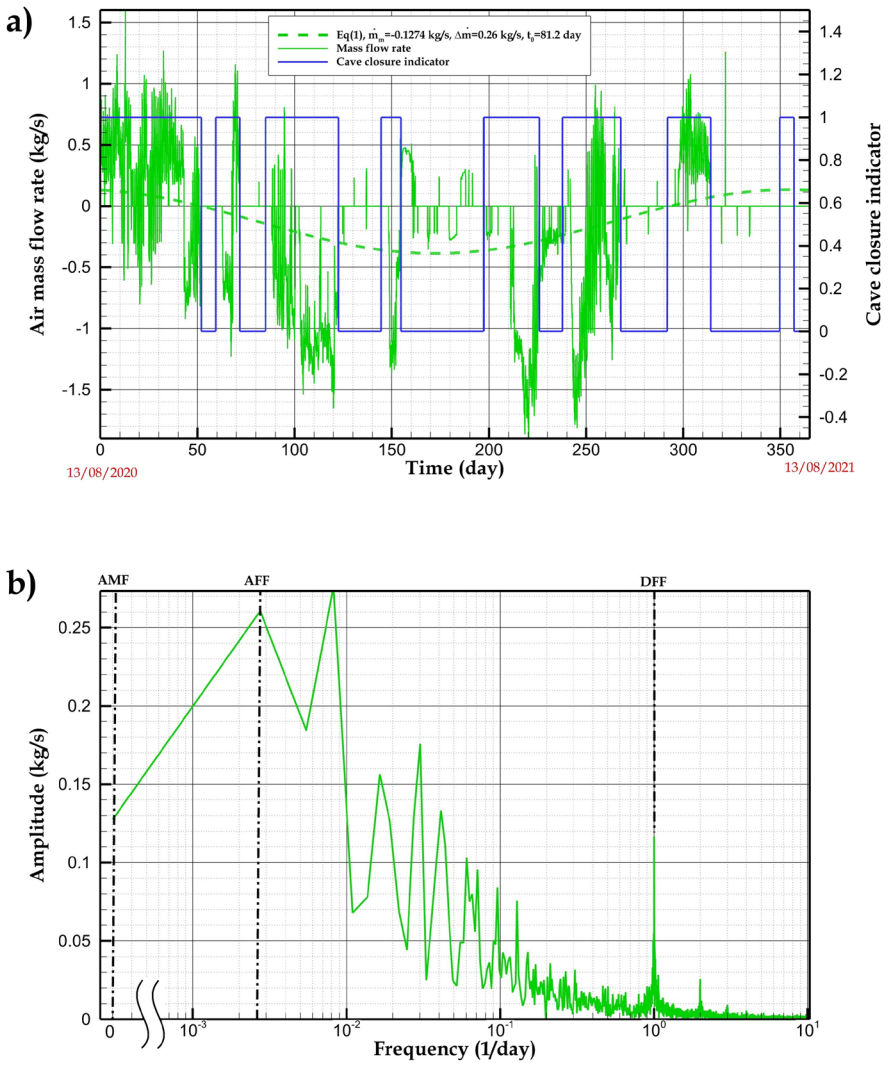

Fig 5. Air mass flowrate measured at Anemo station; a) Time series (dashed line corresponds to Eq. (1) where T_m and ΔT are replaced by the AMF $\dot{m}_m$ and the AFF $\Delta\dot{m}$, respectively). The cave closure periods are shown by blue solid line determining if the cave is open (one) or closed (zero). b) Amplitudes versus frequency deduced from FFT (due to the logarithmic scale, the AMF, which corresponds to zero frequency, is located at an arbitrary origin).

3. Numerical simulations

3.1. Simplifying assumptions

Only the main conduit connecting the upper to the lower entrance is considered in the numerical simulations (see Fig. 1). For the sake of simplification, it has been "unfolded" to yield a rectilinear conduit of the same length L_{cave} as the real cave (see Fig. 6). A circular cross-section of variable diameter $D_p(x)$ is assumed. $D_p(x)$ is set to get the same perimeter $P(x)$ as the true conduit (i.e., $D_p(x) = P(x)/\pi$, where the perimeter $P(x)$ is known from the cave survey, see Fig. 2). The sensitivity study presented in Appendix A suggests that this choice, which preserves the exchange

surface between the air and the rock, is a good approximation in most cases. The conduit is located in an impermeable rock domain of outer radius R_{dom} where conduction is the only heat transfer process. The outer radius must be large enough to ensure that the corresponding domain boundary is not significantly influenced by the airflow in the conduit and is thus approximately adiabatic. These simplifications allow to consider a 2D axisymmetric conduction problem in the rock mass, resulting in a significant reduction in the computational resources compared to the real 3D geometry. Moreover, we assume that the temperature of the external surface is equal to the measured atmospheric temperature. This boundary condition offers the advantage of simplicity, but neglects the effect of radiative transfer and evaporation or condensation on the temperature of the external surface.

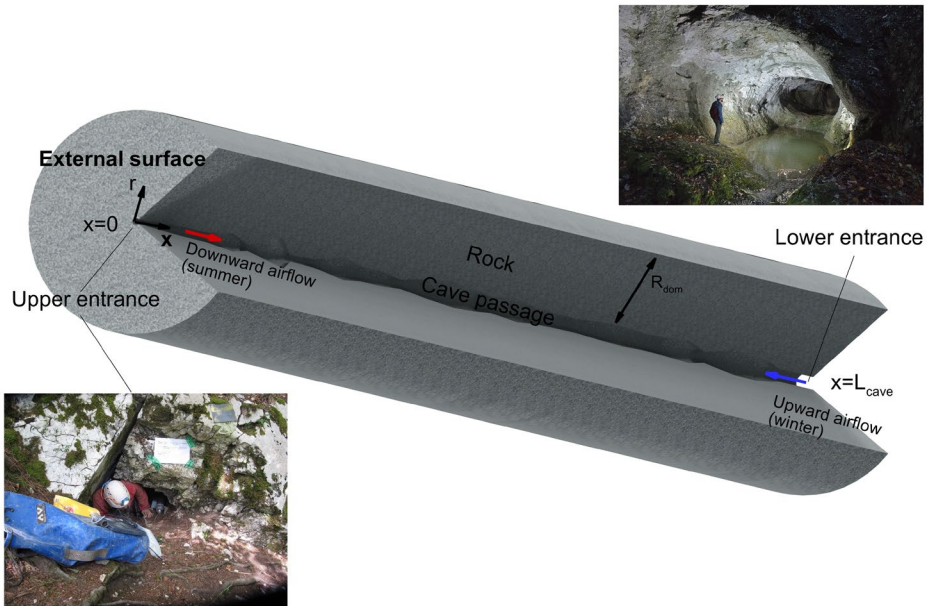

Fig 6. The simplified geometry of the ventilated cave with a single conduit and two entrances at different elevations

The need for an aeraulic model is avoided by using the air flowrate measured by the SFM. During cave closure periods, we assume that the air only circulates in the part of the conduit between the upper entrance and the junction with the secondary conduit (at 16 m from the upper entrance). We impose zero flowrate in the rest of the conduit (i.e., between the junction with the secondary conduit and the lower entrance). Although the conduit is assumed rectilinear, the variation of potential energy with the altitude will be considered in the air energy balance using the conduit tilt angle $\theta(x)$ displayed in Fig. 3.

The effect of the latent heat of evaporation or condensation inside the cave is an important issue that must be evaluated. A difficulty is that the cave walls might be covered with a water film or completely dry, depending on the season and the weather conditions. To avoid the complicated task of defining a model predicting the amount of water lying on the walls, we define two simple limiting cases representing a lower and an upper bound of the latent heat effects.

- Case 1: evaporation and condensation are disregarded (no latent heat effect).
- Case 2: a permanent thin film of water covers all the cave walls, so that evaporation cannot be interrupted by the lack of water on the walls. In addition, the water film is assumed thin enough to neglect its thermal resistance compared to that due to conduction in the rock or convection. Condensation in the gas phase is disregarded. We assume that it only takes place on the conduit wall (same assumptions as in Qaddah et al., (2023)).

The advection of heat by water flowing down the conduit is disregarded. This assumption seems reasonable when the water flow reduces to a thin liquid film due to condensation or percolation through the rock porosity. In contrast, it is questionable during cave flooding induced by intense water recharge. This point is discussed in Section 4.2.

The heat flux through the conduit wall, which couples the energy balance in the air to the conduction equation in the rock mass, is estimated using the Newton's law of cooling based on a heat transfer coefficient. When condensation and evaporation are considered, the mass balance of the water vapor transported by the humid air is also included in the model. This equation contains a mass transfer coefficient for the assessment of the evaporation/condensation fluxes at the cave wall. The Lewis analogy (Cussler and Cussler, 2009) states that the heat and mass transfer coefficients follow the same physical laws. To overcome the difficulty that arises from the complex geometry of a cave, we adopt the same method as in our previous work (Sedaghatkish et al., 2024). We perform two distinct set of simulations to assess a lower bound and a higher bound of the heat and vapor fluxes through the cave wall. In a first set, the transfer coefficients are estimated from standard correlations valid for forced convection and fully developed flow in pipes, which is expected to yield a lower bound. In a second set of simulations, an upper bound of these fluxes is obtained assuming infinite transfer coefficients. Combining dry or humid air along with finite or infinite transfer coefficients yields the four limiting cases listed in Table 2.

Table 2. Abbreviated names of the four cases considered in the numerical simulations. The estimation of the transfer coefficients required for DA and HA models is detailed in Appendix B.

	Transfer coefficients	
	Finite	Infinite
1- Dry air	**DA**	**DA**$_\infty$
2- Humid air	**HA**	**HA**$_\infty$

3.2. Governing equations

We first detail the complete set of equations for the **HA** case (humid air and finite transfer coefficients), which is the most general. Then we give the simplifications for the simulation of dry air or infinite transfer coefficients.

3.2.1. Rock mass

The temperature field in the impermeable rock mass follows the heat conduction equation in the cylindrical coordinates system:

$$\frac{1}{r}\frac{\partial}{\partial r}\left(r\frac{\partial T_r}{\partial r}\right)+\frac{\partial^2 T_r}{\partial x^2}=\frac{1}{\alpha_r}\frac{\partial T_r}{\partial t} \tag{2}$$

$T_r(x,r)$ is the rock temperature at distances x from the upper entrance and r from the conduit axis. α_r is the thermal diffusivity of the rock.

Defining right boundary condition at the external ground surface is challenging. For the sake of simplicity, the atmospheric temperature is imposed at the external surfaces located at $x=0$ and $x=L_{cave}$:

$$T_r(0,r,t)=T_{atmU}(t) \qquad \text{for } R_p(0)\le r\le R_{dom}\,, \tag{3}$$

$$T_r(L_{cave},r,t)=T_{atmL}(t) \quad \text{for } R_p(L_{cave})\le r\le R_{dom}\,, \tag{4}$$

where $R_p(x)=D_p\,(x)/2$ is the cave radius that yields the perimeter obtained from the cave survey (Fig. 2). T_{atmL} and T_{atmU} are the atmospheric temperatures measured in the vicinity of the lower and upper entrances, respectively (Fig. 4). The impact of the boundary conditions defined in Eqs. (3,4) will be analyzed in detail in section 5.1.

Assuming an adiabatic boundary at $r=R_{dom}$ yields

$$\frac{\partial T_r}{\partial r}(x,R_{dom},t)=0 \text{ for } 0\le x\le L_{cave} \tag{5}$$

The energy conservation at the conduit wall reads:

$$k_r\frac{\partial T_r}{\partial r}\big(x,R_p,t\big)=\varphi_c+L_v\,J_w \tag{6}$$

where k_r is the thermal conductivity of the rock, φ_c is the convective heat flux at the conduit wall (positive when directed from the rock to the air), L_v is the molar latent heat of evaporation (J.mol^{-1}) and J_w is the molar flux at the conduit wall (mol.m^{-2}.s^{-1}), positive for evaporation, negative for condensation. Eq. (6) states that the sum of the convective and latent heat fluxes is equal to the conductive heat flux leaving the rock mass. This equation couples the rock mass with the airflow.

3.2.2. Airflow

Since the water vapor is always dilute (its mass fraction in the humid air never exceeds 2%), the heat capacity of the water vapor can be neglected against that of the air. With this assumption, the energy balance in the air reduces to:

$$\rho_a c_{v,a} A(x)\frac{\partial \bar{T}_a}{\partial t}+\dot{m}\left(c_{p,a}\frac{\partial \bar{T}_a}{\partial x}-g\cos\big(\theta(x)\big)\right)=P(x)\varphi_c, \tag{7}$$

where $\bar{T}_a(x)$ is the mixing temperature of the air, i.e., the air temperature averaged over the conduit cross-section (Bergman et al., 2017):

$$\bar{T}_a(x) = \frac{1}{\dot{m}} \iint T_a(x,r)\rho_a u(x,r) dA \tag{8}$$

where $T_a(x,r)$ is the local air temperature and $u(x,r)$ the axial component of the local velocity vector. $A(x)$ and $P(x)$ are the cross-sectional area and perimeter obtained from the cave survey and displayed in Fig. 2. $\dot{m}$ is the air mass flowrate measured by the SFM-device and displayed in Fig. 5 (positive when the air enters through the upper entrance). ρ_a, $c_{v,a}$ and $c_{p,a}$ are the air density, specific heat at constant volume and specific heat at constant pressure.

The first term in the left-hand side (LHS) of Eq. (7) is an approximate expression of the rate of variation of the air internal energy. This term is necessary to regularize the solution when rapid fluctuations occur during flow reversals. Most of the time, it is negligible compared to the other terms. Therefore, Eq. (7) mainly expresses a balance between the energy transported by the fluid (thermal and gravitational potential energy in the second term of the LHS) and the heat transferred to the conduit wall, in the right-hand side (RHS).

The inlet temperature is equal to the atmospheric temperature T_{atmL} or T_{atmU} according to the direction of the flow:

$$\bar{T}_a(0,t) = T_{atmU}(t) \qquad \text{for } \dot{m} > 0 \tag{9}$$

$$\bar{T}_a(L_{cave},t) = T_{atmL}(t) \quad \text{for } \dot{m} < 0 \tag{10}$$

The water vapor balance in the humid air and its associated boundary conditions are similar to Eqs. (7-10):

$$A(x)\frac{\partial \bar{c}_v}{\partial t} + \frac{\dot{m}}{\rho_a}\frac{\partial \bar{c}_v}{\partial x} = P(x)J_w \tag{11}$$

$$\bar{c}_v(0,t) = \phi_{ext} c_{s,atmU} \quad \text{for } \dot{m} > 0 \tag{12}$$

$$\bar{c}_v(L_{cave},t) = \phi_{ext} c_{s,atmL} \text{ for } \dot{m} < 0 \tag{13}$$

$\bar{c}_v$ is the water vapor molar concentration (mol.m^{-3}) averaged over the cross-section similarly to the temperature in Eq. (8). Index "s" indicates saturated condition defined as:

$$c_s = \frac{p_{sat}(T)}{RT} \tag{14}$$

where p_{sat} is the saturated water vapor pressure at temperature T (Lide, 2004). R is the ideal gas constant. Thus, $c_{s,atmU}$ and $c_{s,atmL}$ are the saturated water vapor concentrations based on the atmospheric temperature close to the upper and lower entrances, respectively. ϕ_{ext} is the atmospheric relative humidity. The same constant value of 75% is assumed at the lower and upper entrances.

3.2.3. Heat and vapor fluxes at the conduit wall

The Newton's law of cooling is a general law that applies to any convection process (Bergman et al., 2017). This law states that the heat flux transferred from the wall to a flowing fluid is proportional to the temperature difference between the wall and the fluid:

$$\varphi_c(x,t) = h_t\big(T_w(x,t) - \bar{T}_a(x,t)\big) \quad \text{for } 0 \le x \le L_{cave}, \tag{15}$$

where $T_w(x,t) = T_r\big(x, R_p, t\big)$ is the wall temperature and $\bar{T}_a(x,t)$ the air mixing temperature defined in Eq.(8). The heat and mass transfer analogy provide the same kind of relation for the water vapor flux:

$$J_w(x,t) = h_m\big(c_{sw}(x,t) - \bar{c}_v(x,t)\big) \text{ for } 0 \le x \le L_{cave}, \tag{16}$$

where c_{sw} is the saturated water vapor concentration obtained by substituting T for T_w in Eq. (14). h_t and h_m are the heat and mass transfer coefficients, respectively. In a pipe flow, they depend on the physical properties of air (Table 3) and the conduit geometry defined by the cross-section $A(x)$ and the perimeter $P(x)$ (Fig. 2). In the turbulent regime, they also depend on the air flowrate $\dot{m}$ (Fig. 5) and the wall relative roughness ε, defined as the ratio of the roughness over the hydraulic diameter $D_h(x) = 4A(x)/P(x)$. We set $\varepsilon = 0.01$ in all simulations.

Assessing the heat and mass transfer coefficients requires the evaluation of the Reynolds number Re that characterizes the ratio of inertia to viscous friction in the airflow:

$$Re(x) = \frac{\rho_a\, |\bar{u}(x)|\, D_h(x)}{\mu_a} = \frac{4\,|\dot{m}|}{P(x)\,\mu_a} \tag{17}$$

where $\bar{u} = \frac{\dot{m}}{(\rho_a\, A)}$ is the mean velocity over the cross-section and μ_a the dynamic viscosity of the air. At fixed air flowrate, the Reynolds number is inversely proportional to the conduit perimeter $P(x)$. At the maximum mass flowrate (of the order of 1 kg.s^{-1}, see Fig. 5) Re ranges from 10^4 (in the largest parts of the conduit) to 10^5 (in the narrowest parts) denoting turbulent flow throughout the cave. The method used to estimate the transfer coefficients from standard correlations for fully developed flow in pipes in the laminar and turbulent regimes is detailed in Appendix B.

3.2.4. Infinite transfer coefficient and/or dry air

Eqs. (2-16) assume humid air and finite transfer coefficients (**HA**). In the limiting case of infinite heat transfer coefficients (**HA**$_\infty$), the conditions at the conduit wall Eqs. (15-16) are replaced by

$$T_a(x,t) = T_w(x,t) \text{ for } 0 \le x \le L_{cave}, \tag{18}$$

$$c_v(x,t) = c_{sw}(x,t) \text{ for } 0 \le x \le L_{cave}. \tag{19}$$

Injecting Eqs. (18-19) in Eqs. (7) and (11) provides the relations for φ_w and J_w required by Eq. (6). A noticeable consequence of Eqs. (18-19) is that the humid air inside the cave is saturated at the wall temperature all over the conduit.

In the case of dry air with finite transfer coefficients (**DA**), Eqs. (11-14) and (16) are ignored and we impose $J_w = 0$ in Eq. (6). When, in addition, the heat transfer coefficient is infinite ($\mathbf{DA}_\infty$), Eq. (15) is replaced by Eq. (18).

3.2.5. Initial condition

The initial condition required for solving Eq. (2) is the temperature field at any point of the rock mass at the beginning of the cave monitoring (i.e., on August 13, 2020). Obviously, this information is not directly available, since the temperature is only known at a few locations where sensors have been installed. Because of the thermal inertia of the massif, the initial temperature field depends in a non-trivial way on the history of the atmospheric temperature and the air flowrate.

Interestingly enough, the upper entrance of Longeaigue was enlarged by cavers in 1982. This artificial modification likely induced a significant increase of the air flowrate through the main conduit. Although it is unlikely that the air flowrate before the opening was strictly equal to zero, it was certainly much lower than after the opening. We thus do the approximation that the main conduit was closed before this date, and the air flowrate insignificant. Considering this specific feature of Longeaigue Cave, an approximate initial temperature field was assessed assuming a simplified history consisting of two steps. We first assume no airflow in the conduit, resulting in an adiabatic conduit wall. More precisely, we solved the pure conduction problem defined by Eqs. (2-6), with $\varphi_c = 0$ and $J_w = 0$ in Eq. (6). The atmospheric temperatures in Eqs. (3,4) were approximated by Eq. (1) (displayed by the dashed lines in Fig. 4a), which only considers the annual fluctuations. Starting from an arbitrary uniform initial temperature field, the simulations of this 1D conduction problem was carried out over 200 years, a time long enough to reach the periodic regime. In a second step, we used this result as the initial temperature field to simulate the 38 years between the opening of the conduit in 1982 and the beginning of the monitoring in 2020. The full **HA** model defined in Section 3.2 was used with the simplified atmospheric temperatures of Eq. (1) as in the first step, along with the same kind of simplified function for the air flowrate (dashed line in Fig. 5a). The resulting temperature field was used as the initial condition for the numerical simulation of the year during which the cave was monitored.

3.3. Physical properties

The physical properties used in the numerical simulations are assumed constant. They are listed in Table 3. The saturated vapor pressure of water as a function of temperature was interpolated from data in (Lide, 2004).

Table 3. Physical properties used in the numerical simulations (reference temperature: 12°C)

Properties	Value and unit	Reference
Rock density	$\rho_r = 2325 \frac{kg}{m^3}$	(Tiwari et al., 2020)
Rock heat capacity	$c_{p,r} = 841.09 \frac{J}{kgK}$	(Tiwari et al., 2020)
Rock thermal conductivity	$k_r = 2.302 \frac{W}{m.K}$	(Tiwari et al., 2020)
Rock thermal diffusivity	$\alpha_r = 1.177 \times 10^{-6} \frac{m^2}{s}$	(Tiwari et al., 2020)
Air dynamic viscosity	$\mu_a = 1.77 \times 10^{-5} Pa.s$	(Bergman et al., 2017)
Air density	$\rho_a = 1.23 \frac{kg}{m^3}$	(Bergman et al., 2017)
Air kinematic viscosity	$\upsilon = \frac{\mu_a}{\rho_a} = 1.44 \times 10^{-5} \frac{m^2}{s}$	-
Air heat capacity at constant pressure	$c_{p,a} = 1007 \frac{J}{kgK}$	(Bergman et al., 2017)
Air heat capacity at constant volume	$c_{v,a} = 719.29 \frac{J}{kgK}$	-
Air thermal conductivity	$k_a = 0.0251 \frac{W}{m.K}$	(Bergman et al., 2017)
Air thermal diffusivity	$\alpha_a = 2.02 \times 10^{-5} \frac{m^2}{s}$	-
Ideal gas constant	$R = 8.314 \frac{J}{molK}$	-
Molar mass of water vapor	$M_w = 18.015 \frac{g}{mol}$	-
Diffusion coefficient of water vapor in air	$D_w = 2.43 \times 10^{-5} \frac{m^2}{s}$	(Cussler and Cussler, 2009)
Molar specific vaporization latent heat	$L_v = 44.55 \frac{kJ}{mol}$	(Riddick et al., 1986)
Prandtl number	$Pr = \frac{\upsilon}{\alpha_a} = 0.71$	-
Schmidt number	$Sc = \frac{\upsilon}{D_w} = 0.59$	-

3.4. Numerical methods

All the numerical simulations were performed with the commercial software Comsol Multiphysics, version 6.1. This software solves partial differential equations by finite elements (Galerkin method). Time discretization was based on implicit backward differentiation formula. The mesh was made of Lagrangian quadratic elements, including 12600 2D elements in the rock mass (mapped mesh) and 200 1D elements in the air. The hyperbolic Eqs. (7) and (11) required the implementation of the stabilization techniques detailed in Appendix C.

4. Results

4.1. Field data

The AMT, ATF and DTF deduced from the FFT of the field data are displayed by black symbols in Figs. 7a to 7c. Thermal anomalies are clearly visible in Fig. 7a. Indeed, the AMT passes through a local maximum at ~9.5°C at H3 station located at 55 m from the upper entrance (warm anomaly). Conversely, a local minimum at ~5.7°C is observed at R4 station at 20 m from the lower entrance (cold anomaly). The warm anomaly is more pronounced than the cold one (approximately +2°C and -1°C relative to the outside temperatures at the upper and lower entrances, respectively). Between these two extrema (i.e., between H3 and R4 stations), the AMT continuously decreases with increasing x. The absence of plateau in the temperature profile suggests that the convection length is larger than half the cave length, and that there is no deep karst region in Longeaigue Cave.

Fig. 7b displays the ATF. A sharp decrease is observed close to the entrances, as expected in diffusive regions (Sedaghatkish et al., 2024). The ATF then gradually declines in the convective region to reach a minimum nearby the middle of the conduit.

The DTF is displayed in Fig. 7c. A sharp decrease is observed close to the entrances, similarly to the ATF. However, in the convective region, the DTF decreases over a much shorter distance than the ATF. It becomes hardly measurable beyond a few tens of meters from the entrances. This suggests that the distance of propagation of a thermal perturbation advected by the airflow should depend on the frequency.

The time series of field data from three selected stations are displayed by solid black lines in Fig. 8. Station H3 (Fig. 8a) is close to the upper entrance, station R2 (Fig. 8b) is approximately in the middle of the cave, and station R4 (Fig. 8c) is close to the lower entrance. Comparisons with the atmospheric temperatures displayed in Fig. 4a confirms the strong damping of the daily temperature fluctuations. In contrast, the impact of cave closures on the temperatures is clearly observed at all stations displayed in Fig. 8 (see for instance the time range from 120 to 196 days).

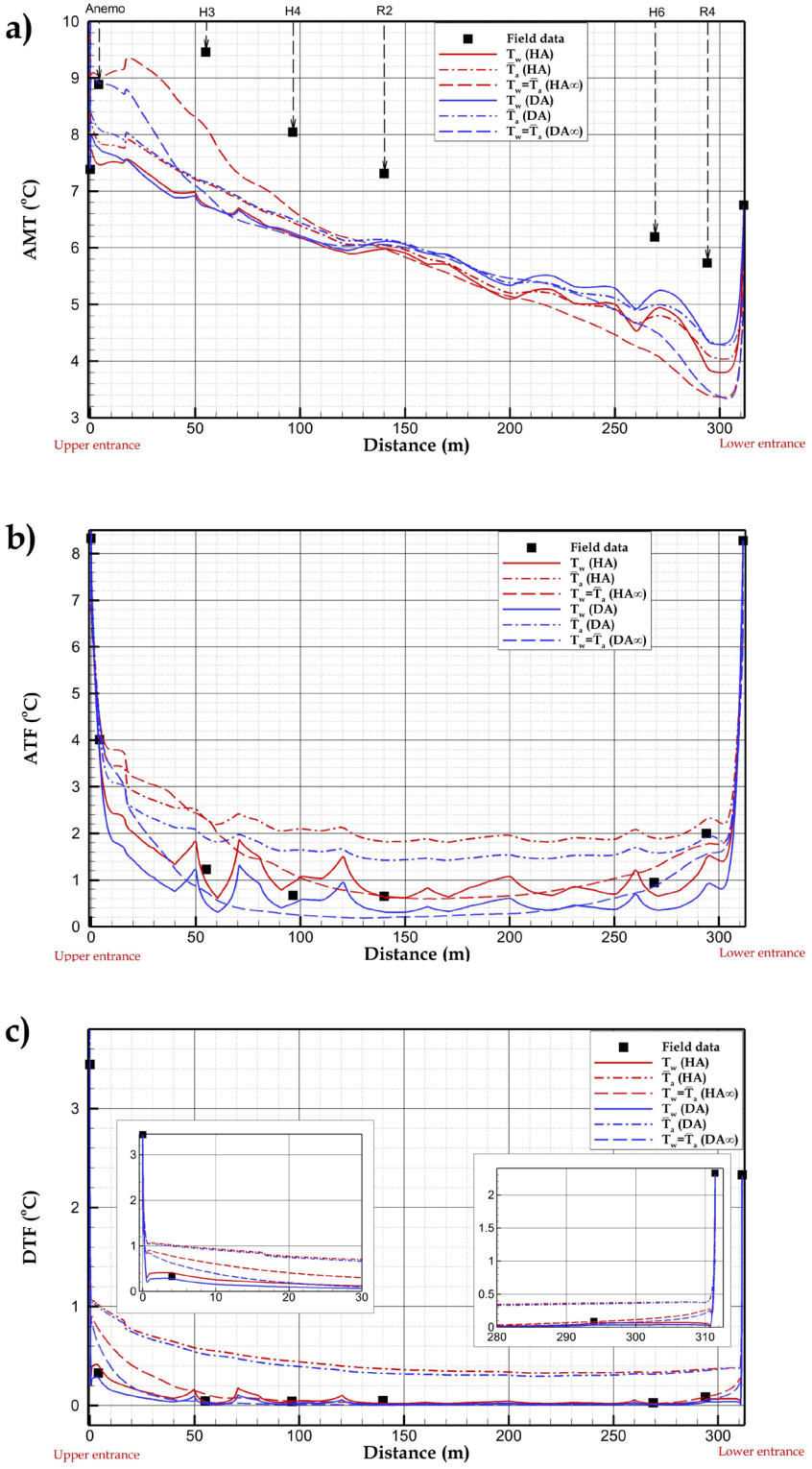

Fig 7. AMT(a), ATF (b) and DTF (c) from the field data and the numerical simulations. Data at $x = 0$ and $x = L_{cave} = 311$ m correspond to the atmospheric temperature close to the upper and the lower entrances, respectively.

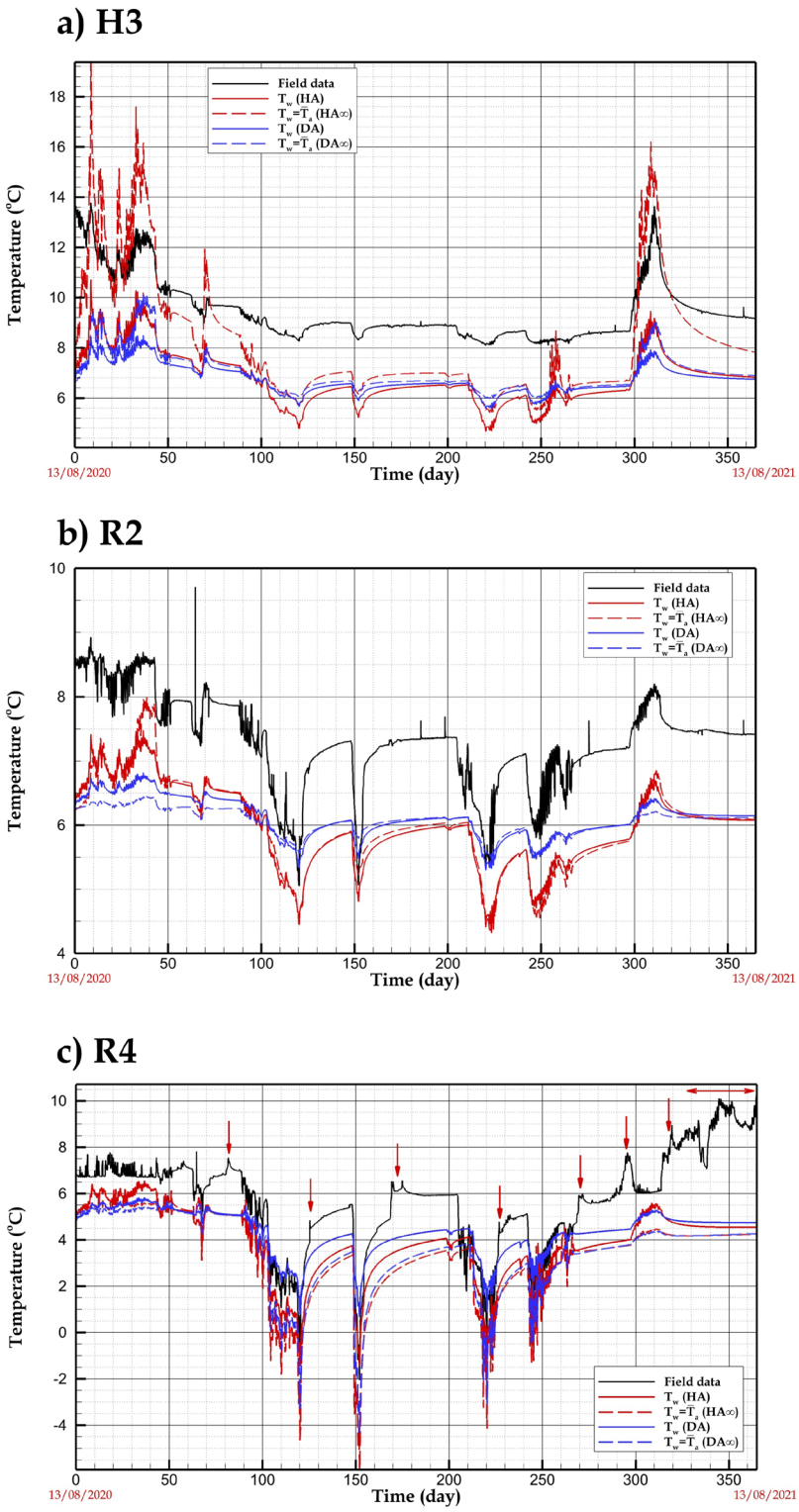

Fig 8. Temperature time series in three stations inside the cave a) H3 (x=55 m); b) R2 (x=140 m); c) R4 (x=294 m), red arrows indicates temperature peaks in the field data not predicted by the model.

4.2. Numerical simulations

Fig. 7a displays the AMT of the conduit wall and the air as a function of the distance from the upper entrance, for the four models defined in Table 2 (notice that in $\mathbf{DA}_\infty$ and $\mathbf{HA}_\infty$ models, wall and air temperatures are equal). All models significantly underestimate the AMT computed from the field data (approximately by 1 or 2°C). $\mathbf{DA}_\infty$ and $\mathbf{HA}_\infty$ predict larger thermal anomalies compared to **DA** and **HA**. $\mathbf{HA}_\infty$ seems to better reproduce the shape of the field data close to the upper entrance.

Regarding the ATF (Fig. 7b), the four models reproduce qualitatively the main trends observed in the field data. All of them predict a sharp decrease over the first few meters from the entrances (i.e., in the diffusive regions) followed by a more gradual decline. $\mathbf{DA}_\infty$ globally underestimates the field ATF. $\mathbf{HA}_\infty$ is in good agreement with the field data in the lower half of the cave, but overestimates the ATF at $x = 55$ m (by approximately 1°C). The air and wall temperatures predicted by **DA** or **HA** models significantly differ from each other. The simulated air temperatures of both models overestimate the field data by approximately 1°C all over the cave. A significantly better agreement is obtained with the simulated wall temperatures. **HA** model shows a maximum error of approximately half a degree at H4 station, at 20 m from the lower entrance.

Similar comments apply to the DTF displayed in Fig. 7c. $\mathbf{DA}_\infty$ and $\mathbf{HA}_\infty$ slightly overestimate the field data close to the upper entrance. The best fit is obtained for the wall temperature with **DA** and **HA**, whereas the air DTF predicted by these models is significantly above the field data. This is confirmed by the time series at R4 station, at 20 m from the lower entrance (Fig. 9). This station is close enough to the lower entrance to get a significant DTF when the lower entrance operates as an inlet. Compared to the field data, the wall temperature predicted by the **HA** model is shifted to lower values, with comparable (slightly lower) amplitudes. In contrast, the model predicts that the air temperature fluctuates with a much larger amplitude than the field temperatures.

The comparison between the simulated wall temperature and the field temperatures is completed by the time series displayed in Figs. 8a to 8c. At H3 ($x = 55$ m) and R2 ($x = 140$ m) stations, the simulated wall temperatures follow most of the time the field temperatures with a quasi-constant shift to lower values, in agreement with the difference between the simulated and field AMT observed in Fig. 7a. An exception is the first 30 days of the monitoring period. During this time range, the field temperatures globally decrease, whereas all models predict increasing temperatures. This discrepancy is due to the approximated initial condition used in the simulations. The actual history of the atmospheric temperature before the initial time, different from the periodic function assumed in the simulations (see Section 3.2.5), results in significant errors during the first month. This time lapse is short compared to the duration of the monitoring (1 year).

The behavior observed in Fig. 8c at R4 station ($x = 294$ m), located in the lower part of the cave, is different from H3 and R2. The evolution of simulated and measured temperatures not only differs during the first month of the simulated time range, but the field temperature also shows several peaks not predicted by the simulations. They are indicated by red arrows in Fig. 8c. The most significant event is not localized at a specific time, but extends over approximately two months, from time $t = 310$ days to the end of the monitoring period (see Fig. 8c). The same behavior has been observed at station H6 (figure not shown). These events are correlated with the lake level. During floods, H6 and R4 stations, both located in the lower part of the cave, are submerged, or very close to the water stream which modifies the temperature field in the cave. Because of thermal anomalies, a downward water flow induces heat transfer from the warmer upper part of the cave to the colder lower part (compare for instance the time series of the field temperatures at stations H3 (x=55 m) in Fig. 8a and R4 (x=294 m) in Fig. 8c). This explains that, in the lower part of the cave, floods always result in temperature increases. In Longeaigue cave, the rise of the atmospheric temperature with the altitude (see Section 2.2) might also play a role.

As stated in Section 3.1, heat advection by water flow is not considered in our models. Taking into account this effect would require the development of a hydraulic model, an intricate task beyond the scope of this article. However, comparisons between field and simulated temperatures reveal that the effect of water flow is only perceptible in the lower part of the conduit. At higher elevation, the climate is controlled by the airflow coupled to heat conduction in the rock mass. This is likely a general pattern in case of diffuse recharge through the epikarst. At the top of the massif, water infiltration is distributed all over the catchment area inducing low water velocity and thus negligible advection compared to heat conduction in the rock mass. When flowing downward, water concentrates in specific conduits until it reaches the spring where the water velocity, and thus the advection of heat, are maximum. The situation would be different in case of concentrated recharge (swallowing stream), as described by (Covington et al., 2011; Luhmann et al., 2012; Birk et al., 2006). In this case, the effect of water advection on the temperature field would be significant throughout the conduit, including its upper part.

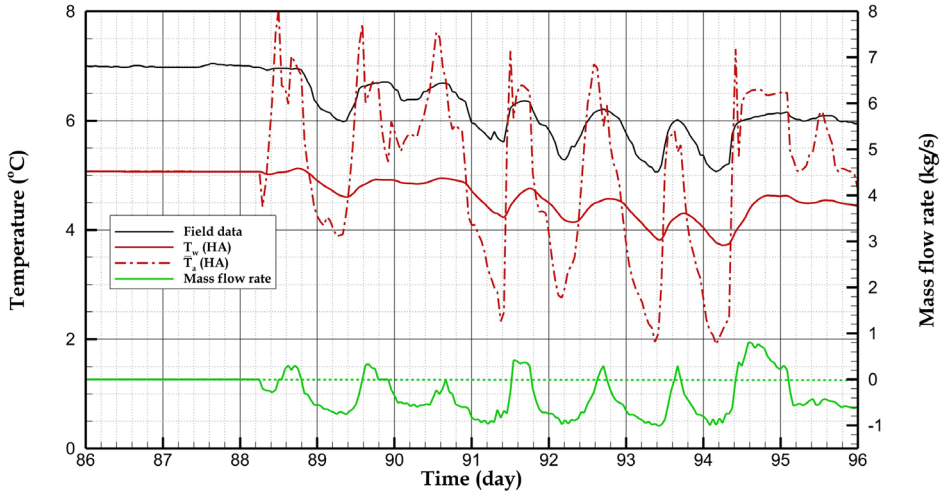

Fig 9. Temperature time series from field data and HA model at R4 station, at 17 meters from the lower entrance. Positive airflow indicates that the air enters through the upper entrance (origin of time: 13/08/2020).

The effect of the uncertainty on the airflow rate has been investigated by recalculating the outputs of **DA** and **HA** models after multiplying the airflow rate by 1.5 (see Appendix D). Although non-negligible, the impact on the results during the monitoring year is limited, and does not modify the observations drawn from the comparisons between the simulated and field temperatures. However, these observations raise issues requiring in-depth analyses developed in the next section:

1) Models systematically underestimate the annual mean temperatures obtained from field data;

2) Although the temperature sensors are located in the air, the amplitude measured in the field are much closer to temperature simulated for the cave walls than for the air;

3) Models with finite or infinite transfer coefficients yields significantly different results. What is the most relevant assumption?

5. Discussion

5.1. Annual mean temperatures

As pointed out in Section 4.2, the numerical simulations underestimate by approximately 1 or 2°C the AMT obtained from the field data (see fig. 7a). The predominant cause of this discrepancy, which is the main weakness of the model, must be sought in the boundary conditions at the external surfaces (i.e., the interfaces between the rock mass and the atmosphere, see Fig. 6). Indeed, Eqs. (3-4) impose that the external surface temperature is equal to the atmospheric temperature. However, several effects may induce a significant gap between these temperatures. The energy balance at an external surface reads (Salmon et al., 2023):

$$\left(-k_r.\vec{\nabla}T_r\right)\cdot\vec{n} = \varphi_{conv} + \varphi_{rad,lw} - \varphi_{rad,sw} + \varphi_{evap}. \quad (20)$$

This equation states that the conduction flux leaving the rock (LHS) is the sum of all the thermal fluxes transferred from the external surface to the external environment (RHS). $\vec{n}$ is the normal unit vector pointing to the atmosphere, φ_{conv} the convective heat flux from the rock to the atmosphere, $\varphi_{rad,lw}$ the net radiative flux lost by the rock in the long wave-length range, $\varphi_{rad,sw}$ the sun irradiation (short wave-length range) and φ_{evap} the latent heat flux (positive for evaporation). Some of these terms tend to increase the soil temperature (e.g., the sun irradiation), others to decrease it (e.g., the latent heat of evaporation). Molnar (2022) analyzed the atmosphere and soil AMT from 212 sites throughout the world. He concluded that the soil temperature is generally warmer than the atmosphere. The difference between the AMT of the soil and the atmosphere mainly depends on the land surface cover. It approximately ranges from 1°C in wetlands and forests to 3-5°C or more in arid or cold regions. Fig. 10a displays the values measured at different weather stations located in Switzerland. Most data are included in the range from 0 to 2°C, with significant variations from year to year.

The sensitivity of the conduit temperature to the temperature of the external surfaces was assessed from additional numerical simulations. Fig. 10b displays the AMT of the conduit wall obtained from the **HA** model in two cases: (a) equal atmospheric and wall temperatures, as specified by Eqs. (3-4) (blue curves), (b) external surface temperatures increased by $\Delta T = 2$°C compared to the atmospheric temperatures (red curves). In the latter case, the boundary conditions

$$T_r(0,r,t) = T_{atmU}(t) + \Delta T \qquad \text{for } R_p(0) \le r \le R_{dom}\,, \quad (21)$$

$$T_r(L_{cave},r,t) = T_{atmL}(t) + \Delta T \quad \text{for } R_p(L_{cave}) \le r \le R_{dom}\,, \quad (22)$$

have been used instead of Eqs. (3-4). Setting $\Delta T = 2$°C is a rough approximation since the actual difference between the atmospheric and external surface temperatures is unknown and may vary with time and space. However, this is relevant for a sensitivity analysis. To simulate a large time range (200 years) with a reasonable computational time, we used the simplified atmospheric temperatures of Eq. (1) and the same kind of simplified function for the air flowrate (dashed line in Fig. 5a). The initial condition was determined using the method detailed in Section 3.2.5. Fig. 10b shows that increasing the external surface temperatures by 2°C results in a similar temperature raise throughout the conduit wall, over the entire time range considered in the simulations (200 years). This result strongly suggests that the main source of discrepancy between the field and simulated AMT at the conduit wall may be the boundary conditions at the external surfaces.

Improving the accuracy of the model thus necessitates to replace Eqs. (3-4) with more realistic boundary conditions, based for instance on the energy balance Eq. (20). This would require appropriate models for assessing the various terms included in this equation (see for instance Larwa, 2018), and thus the monitoring of additional input

data (e.g., the wind velocity for the assessment of φ_{conv} or the sky temperature for $\varphi_{rad,lw}$). An alternative could be to disseminate temperature sensors at a few tens of centimeters below the external surface and use the measured temperatures in Eqs. (3-4) instead of the atmospheric temperature.

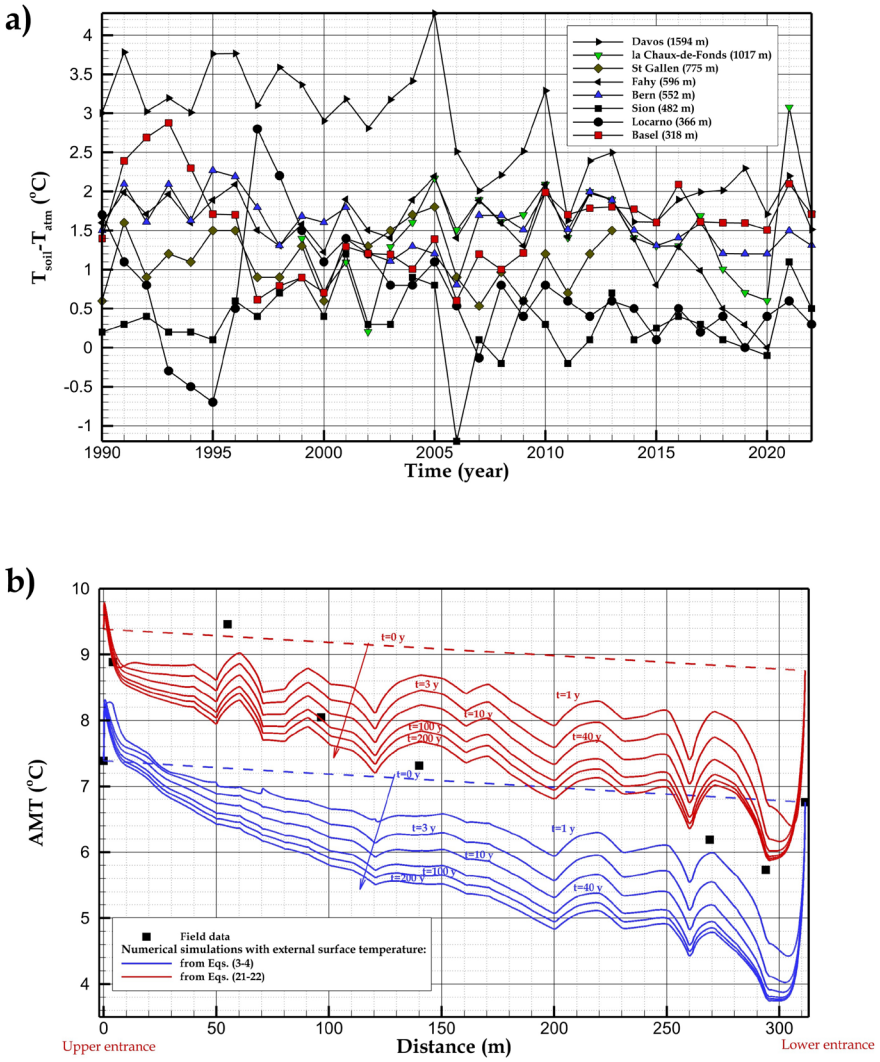

Fig 10. a) Mean annual temperature difference between the soil and the atmosphere (T_{soil} -T_{atm}) for some different weather stations in Switzerland (from Federal Office for Meteorology and Climatology of Switzerland (2024)). The soil temperature is measured at 5 cm depth, the atmospheric temperature at 2 m above the ground. b) Effect of the external surface temperatures on the AMT of the conduit wall (numerical simulations with simplified time functions for the air flowrate and the atmospheric temperature, HA model). Blue curves: external surface temperature equal to the atmospheric temperature (Eqs. (3-4)). Red curves: external surface temperatures increased by ΔT =2°C (Eqs. (21-22)). Dashed lines: initial conditions obtained by solving the diffusion problem. The arrows point to increasing times

5.2. Temperature fluctuations

The ATF and DTF of the air predicted by **DA** and **HA** models show significant discrepancies with field data (see Figs. 7b and 7c). $\mathbf{DA}_\infty$ and $\mathbf{HA}_\infty$ better fit the measured values, but are slightly less accurate than the wall temperatures yielded by **DA** and **HA** models. This is unexpected since the temperature sensors are located in the airflow, not in the rock. There are two possible explanations for this: (1) **DA** and **HA** models fail in predicting the air temperature, $\mathbf{DA}_\infty$ and $\mathbf{HA}_\infty$ models based on infinite transfer coefficients and equal temperatures in the air and the wall are closer to reality; (2) The wall temperature from **DA** and **HA** models fit well the field temperatures because the temperature sensors measure the wall temperature rather than the air temperature. Although counterintuitive, the latter explanation is the most likely. A first point is that the local air temperature T_a varies within the cross-section, and reaches the rock temperature at the conduit wall. Incidentally, the mixing temperature of the air $\bar{T}_a$ provided by the numerical simulations is a cross-sectional averaged temperature. Considering its definition in Eq. (8), we expect $\bar{T}_a$ to be quite close to the local temperature in the center of the conduit, where the local velocity is maximum. A second point to be considered is that a temperature sensor always measures its own temperature (Lundström and Mattsson, 2020), which might differ from the temperature of the surrounding fluid.

Fig. 11 displays the temperatures measured in the air at H1 station (at 16 m from the upper entrance) during approximately a month. Two temperature sensors were installed, a Hobo Water Pro v2 at a few centimeters from the wall (similar to the other probes used in this study) and a Pt100 sensor suspended approximately in the center of the conduit. Fig. 11 shows that the amplitude of the daily oscillations measured by the Pt100 is two or three times larger than that measured by the Hobo Water sensor.

As pointed out by Lundström and Mattsson (2020), a sensor immersed in a transparent fluid (the air in the present case) receives a convective flux from the fluid and a net radiative flux from the conduit wall. Therefore, its temperature is a weighted average of the air and wall temperatures. A simple model based on the energy conservation yields the following expression for the sensor temperature (Lundström and Mattsson, 2020):

$$T_{sensor} = \frac{h_{conv}}{h_{conv} + h_{rad}} T_a + \frac{h_{rad}}{h_{conv} + h_{rad}} T_w \tag{21}$$

where h_{conv} and h_{rad} are the convective and radiative transfer coefficients at the sensor surface. Eq. (21) qualitatively explains the results displayed in Fig. 11. A temperature sensor measures the air temperature if convection prevails over radiation (i.e., if $h_{conv} \gg h_{rad}$). Otherwise, it measures a temperature in between the wall and air temperatures, or even the wall temperature if $h_{conv} \ll h_{rad}$. h_{conv} is an increasing function of the air velocity and a decreasing function of the sensor size. h_{rad} is proportional to the emissivity of the sensor surface. Compared to the Pt100 sensor, the Hobo Water sensor is larger (30 mm against 5 mm) and has a higher emissivity

(polypropylene sheath against metallic sheath). In addition, the Hobo Water sensor is located closer to the wall, where the air flows with a smaller local velocity and a local temperature T_a closer to the wall temperature T_w. All of these effects bring the Hobo Water sensor nearer the wall temperature. This sensor thus yields a better estimate of the wall temperature T_w than the air mixing temperature $\overline{T}_a$. In contrast, the temperature of the Pt100 sensor yields a better estimate of the air temperature in the center of the conduit. This interpretation, consistent with the results displayed in Fig. 11, explains the good agreement between the field data and the wall temperature predicted by **DA** and **HA** models, and the discrepancy with the air temperature. Indeed, the configuration of all sensors used in this work is similar to that of the Hobo Water sensor used in the comparison displayed in Fig. 11.

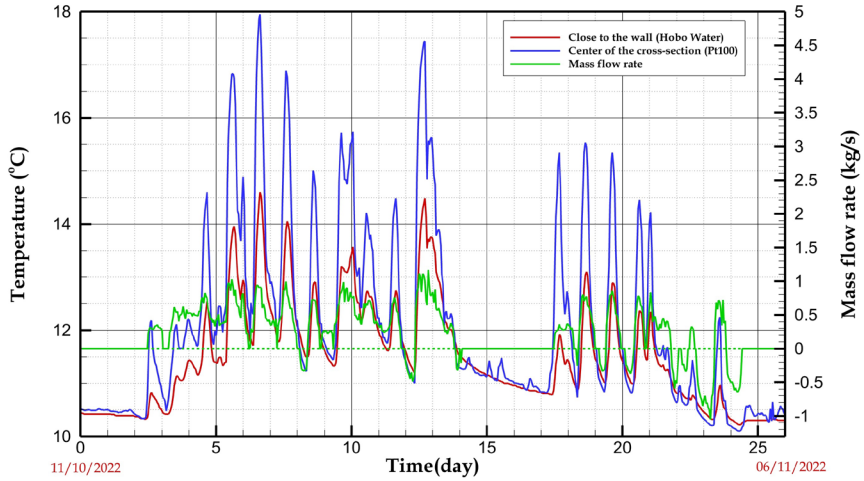

Fig 11. Temperature measured by a Hobo Water sensor at a few centimeters from the conduit wall and a Pt100 sensor in the center of the conduit. Test section H1 located at 16 m from the upper entrance. Positive flowrate indicates airflow entering through the upper entrance.

5.3. Finite versus infinite transfer coefficients

As pointed out in the introduction, assessing relevant values of the transfer coefficients in the complex geometry of a cave is a difficult task. However, the impact of transfer coefficients on the prediction of cave climate can be more or less significant depending on whether heat transfer is convection-limited or conduction-limited. In a previous work (Sedaghatkish et al., 2024), we showed from numerical simulations that no accurate estimation of the heat transfer coefficient is required when the Reynolds number corresponding to the maximum mass flowrate is larger than 3×10^5 (conduction-limited regime). Conversely, the heat transfer coefficient is a key information when the maximum Reynolds number is lower than 10^4 (convection-limited regime).

The maximum Reynolds number in Longeaigue Cave ranges from 10^4 to 10^5, depending on the cave section (see Section 3.2.3). Longeaigue Cave is thus in the

intermediate regime, in which both convection in the air and conduction in the rock mass should be considered. Consequently, the temperature fields predicted by **DA** and **HA** (finite transfer coefficients) or by $\mathbf{DA}_\infty$ and $\mathbf{HA}_\infty$ (infinite transfer coefficients) are significantly different. If we assume that:

(1) the temperature sensors better estimate the wall temperatures than the air temperatures (see Section 5.2),

(2) the general underestimation of the AMT by all models is mainly due to the initial and boundary conditions (see Section 5.1),

then **DA** and **HA** models yield more accurate results compared to $\mathbf{DA}_\infty$ and $\mathbf{HA}_\infty$ (see Fig. 7). With this in mind, the fact that $\mathbf{DA}_\infty$ and $\mathbf{HA}_\infty$ better reproduce the measured AMT in the upper part of the cave (see Fig. 7a) is likely a coincidence resulting from error compensation. In line with this, Fig. 7b shows that, in the same region of the cave, the ATF is underestimated by $\mathbf{DA}_\infty$ and overestimated by $\mathbf{HA}_\infty$.

As pointed out in Section 3.1, **DA** and **HA** models are two limiting cases (no latent heat effect in the former case, permanent water film on the cave walls in the latter case). Comparisons between the outputs of both models suggest that the effect of the latent heat on the cave climate is rather weak (see Figs. 7 and 8). Considering the uncertainties on the airflow rate and the temperature measurements, the accuracy of **DA** or **HA** models for the prediction of the temperature fields are approximately equivalent.

6. Condensation and evaporation

6.1. Vapor transfer rate and consequences on paleoclimatology

Fig. 12a displays the mass fluxes of water vapor at the conduit wall (positive and negative for evaporation and condensation, respectively) at two selected times corresponding to high air flowrates (**HA** model). Both mass fluxes are close to the maximum values reached during the year, one in summer ($t = 32.6$ days, $\dot{m} = 1.26$ kg.s^{-1}, air intake from the upper entrance), the other in winter ($t = 220.3$ days, $\dot{m} = -1.92$ kg.s^{-1}, air intake from the lower entrance).

In summer, evaporation is only observed in areas very close to the entrances: less than a meter from the upper entrance, a few meters from the lower entrance. Evaporation at the upper entrance arises from the need to increase the relative humidity from 75% (the atmospheric humidity) to 100% before condensation starts. At the lower entrance, evaporation results from the increase in the wall temperature in the diffusive region. With the exception of these two short regions, condensation takes place everywhere over the conduit wall. As expected, the condensation rate is maximum close to the inlet (the upper entrance), where the temperature contrast between the air and the wall is greatest. However, the condensation rate does not decrease monotonically with increasing distance from the upper entrance. Oscillations are correlated with conduit size variations (compare Fig. 12a with the conduit perimeter displayed in Fig.

2). We demonstrate in Appendix B that, in the turbulent regime and for a given air flowrate, the transfer coefficients are inversely proportional to the product of the conduit perimeter by the hydraulic diameter. This quadratic dependence results in a strong effect of the conduit size on the vapor transfer rate, with highest values in the narrowest parts of the conduit.

In winter, condensation is limited to a few meters from the upper entrance (the air outlet in winter). Condensation in this short region results from the decrease in the conduit wall temperature in the diffusive region. Evaporation takes place anywhere else. As expected, the evaporation rate is maximum close to the inlet (the lower entrance). Despite the higher air flowrate in winter, the evaporation rate is lower than the condensation rate in summer, for two reasons: (a) lower temperatures in winter (especially near the inlets) resulting in lower saturated vapor pressure and thus lower vapor concentration in the air; (b) larger conduit size in the lower part of the cave compared to the upper part (see Fig. 2), resulting in lower transfer coefficients. The total amount of condensation and evaporation is assessed and discussed in Section 6.2.

A quantitative estimate of a cave's thermal response to the outside environment is essential for the interpretation of paleoclimate records from speleothems (Lyu et al., 2024). Although variations in the drip water composition largely control the proxy partitioning in speleothems (Fairchild and Baker, 2012), trace elements and oxygen isotope fractionation during $CaCO_3$ precipitation are also temperature-dependent (Tremaine et al., 2011; Wassenburg et al., 2020) and become significant for temperature amplitudes exceeding ±0.5°C. The model developed in this study is capable of calculating this amplitude on daily and yearly scale at any location within the cave and illustrates the temperature sensitivity in the convection zone. Moreover, Fig. 12a (red line) reveals that, in winter, evaporation is present all along the cave at significant rates but, in particular, close to the lower cave entrance. There, the evaporation flux may reach 2×10^{-3} g.m^{-2}.s^{-1} during intense upward air flow ($t = 220.3$ days; $\dot{m} = -1.92$ kg.s^{-1}). Whilst this rate is still significantly lower than the potential evaporation rate considered in geochemical models (Dreybrodt and Deininger, 2014), it may become locally important at very low drip rates feeding speleothems. Results from the highly ventilated Longeaigue cave thus suggest that the role of evaporation on the isotope proxy record can often be neglected in hydrologically active caves but must be considered in semi-arid environments with only sporadic drips

6.2. Role of condensation in water production

Evaporation and condensation produce and consume water inside the cave. Fig. 12b displays the evaporation rate integrated throughout the conduit wall as a function of time (**HA** model, negative values refer to condensation). Condensation takes place during approximately two months in summer. The total amounts of condensed and evaporated water during the year were -8.8×10^3 and 16.7×10^3 kg respectively. The mass of evaporated water throughout the year is twice the mass of condensed

water. These values are low (<0.1%) compared to the water flow-through in the groundwater catchment of Raies/Longeaigue system. Nonetheless, our model also shows that condensation may happen, preferentially at the upper entrance, during downward ventilation regimes. Whilst the total amount of condensed water during the 2020-21 annual cycle reached 8800 kg, it is still negligible with respect to the hydrological mass balance of Longeaigue cave. In arid environments, this amount may nonetheless be sufficient to maintain a moist atmosphere in the upper entrance zone of a cave system and thus support the local ecosystem. Because cave-adapted species may be sensitive to even small changes in the subsurface environment (Medina et al., 2023; Jegla and Poulson, 1970), prediction of the amplitude and frequency of temperature changes might be crucial for cave conservation issues.

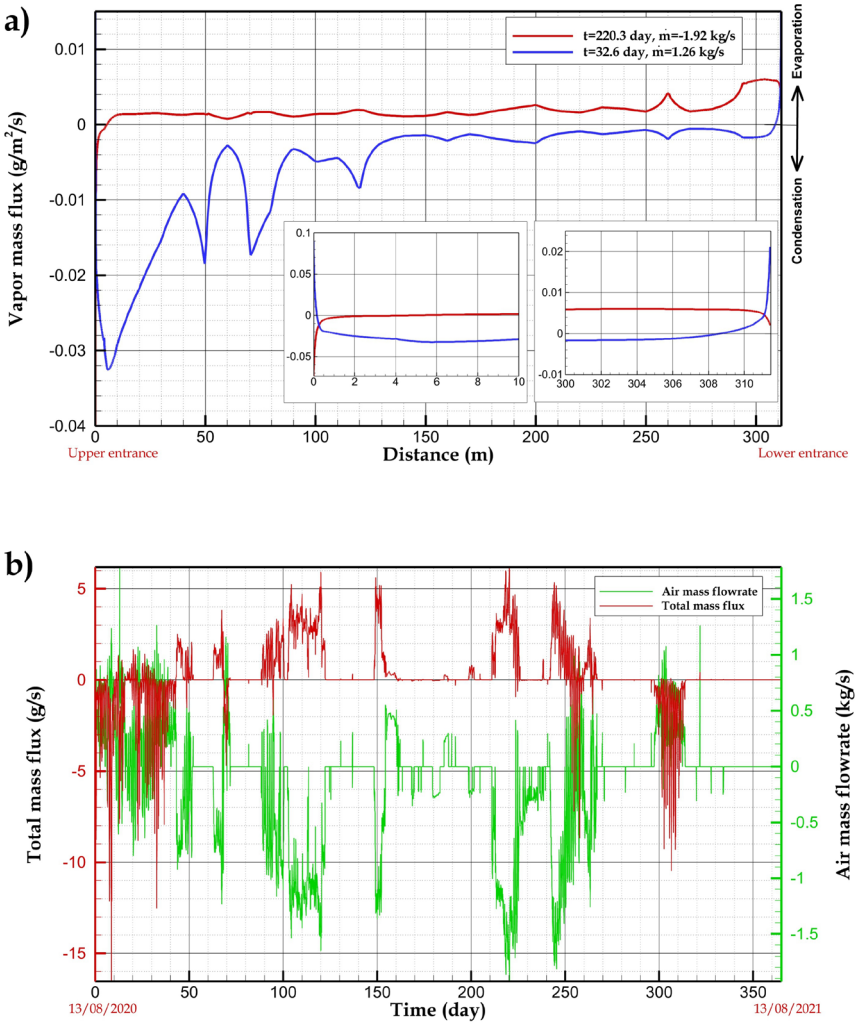

Fig 12. a) Vapor mass flux at the conduit wall corresponding to high air flowrate events in summer (t = 32.6 days) and winter (t = 220.3 days); insets: zooms in the first 10 meters from the entrances b) Evaporation flux integrated over the conduit wall as a function of time. In both figures, positive and negative values denote evaporation and condensation, respectively (HA model).

7. Conclusion

The main conduit of Longeaigue cave is ventilated by a strong airflow driven by chimney effect. In order to predict the temperature field in this conduit, we developed a thermal model based on the diffusion equation in the rock mass along with the conservation of energy and vapor mass in the airflow. The conduit wall and the air are coupled by transfer coefficients assessed from standard correlations for fully developed forced convection in pipes. The model has been tested against the field data collected in the cave during a complete year.

The complex geometry of a cave is a serious difficulty for thermal modeling. A major simplification was done by assuming a rectilinear conduit of circular cross-section with variable diameter. In this context, the conduction problem in the rock mass is 2D axisymmetric, and only two independent parameters are required to characterize the conduit cross-section: the effective diameter D_p based on the conduit perimeter and the hydraulic diameter D_h. Using D_p in the conservation equations preserves the exchange surface between the air and the rock, while D_h is the relevant geometrical characteristic to be used in the estimation of the transfer coefficients.

The numerical results underestimate by 1 or 2°C the mean annual temperatures obtained from field data. This is the most significant weakness of the model. This discrepancy is mainly due to the assumption of equal rock and atmospheric temperatures at the external surface of the massif. More realistic boundary conditions are proposed.

In contrast, the model accurately predicts the temperature fluctuations from daily to yearly time scales, which includes in the specific case of Longeaigue Cave the temperature fluctuations generated by intermittent cave closures. The impact of the initial condition assessed from a simplified history is limited to the first month after the beginning of the simulation. Moreover, comparisons between field and simulated temperatures reveal that the effect of water flow due to diffuse water recharge is only perceptible in the lower part of the cave. At higher elevation, the temperature field is controlled by the airflow coupled to heat conduction in the rock mass. The latent heat effect of evaporation and condensation seems to play a minor role on the cave climate. However, predicting the order of magnitude of condensation or evaporation rate is valuable for applications related to ecology or paleoclimatology. In arid environments, maintaining moist atmosphere in the upper part of caves might be crucial for the ecosystems. The order of magnitude of evaporation rates also show that, in temperate European caves, the role of evaporation on the isotope proxy record can often be neglected.

Compared to heat diffusion in a rock mass, cave ventilation significantly increases the depth of natural thermal oscillations and decreases the time of propagation. This makes it necessary to develop and test thermal models for the prediction of temperature fields in ventilated karst massifs. We provided and discussed simplifying

assumptions that allow the accurate prediction of the temperature field in a ventilated cave from daily to yearly time scale. However, extrapolating the results of this study to larger time horizons (centuries or more) must be undertaken with great caution. The long-term impact of geometry simplifications, or initial and boundary conditions, will require further research. This study is a first step towards the elaboration and validation of models capable of tackling these issues. Our model opens the way for a quantitative assessment of the cave's thermal response at any location, providing a well-known cave geometry.

The thermal model presented in this article is applied to caves naturally ventilated by chimney effect. However, some issues raised in this article are relevant to engineering applications with artificial ventilation, as mines (Yu et al., 2013; Parra et al., 2006) and tunnels (Lv et al., 2020). Defining the right boundary conditions or convection model also matters in these configurations. More specifically, there is a growing interest for the recovery of geothermal energy from tunnels (Dornberger et al., 2022). Taking into account the advection of heat by the airflow and the coupling between convection and conduction in the rock mass should improve performance predictions for these complex geotechnical structures.

Appendix A. Effect of the cross-sectional shape on wall temperature and heat flux

The numerical simulation of 3D geometries requires a large amount of computational resources. The objective of this appendix is to test whether a 2D (axisymmetric) circular cross-section can be substituted for the 3D geometry of a real conduit with an acceptable loss of accuracy. To address this issue, we computed the temperature field in the rock mass surrounding the conduits displayed in Fig. A1. Three cases are considered: (a) the circular shape, (b) the triangular shape as an instance of simple 3D geometry, (c) a more complicated shape obtained from a survey in a real cave. The conduit perimeter P is expected to be an important parameter since it imposes the exchange surface between the rock and the air (see Eqs. 7 and 11). Therefore, all the comparisons between the different shapes displayed in Fig. A1 will be done between conduits of equal perimeter P.

The transient conduction equation is solved in the cross-sectional plane assuming uniform temperature in the direction parallel to the conduit. The temperature of the dry air inside the conduit follows a sinusoidal function of time. The heat flux at the conduit wall is deduced from the Newton's law of cooling, assuming uniform heat transfer coefficient all along the conduit circumference.

The problem variables are the coordinates x and y, the time t, the temperature in the rock mass T_r, and the temperature of the air $\bar{T}_a$. The corresponding dimensionless variables read:

$$X = \frac{x}{L_d}, Y = \frac{y}{L_d}, t^* = \frac{t}{\tau}, \theta_r = \frac{T_r - T_m}{\Delta T}, \theta_a = \frac{\bar{T}_a - T_m}{\Delta T} \quad \text{(A1)}$$

where T_m is the mean temperature of the air and ΔT the amplitude of the temperature fluctuations of period τ. $L_d = \sqrt{\alpha_r \tau}$ is the diffusion length in the rock mass. $P^* = \frac{P}{L_d}$ and $D_p^* = \frac{D_p}{L_d} = \frac{P}{\pi L_d}$ are the dimensionless perimeter and perimeter-based diameter of the conduit, respectively.

The diffusion equation reads:

$$\frac{\partial^2 \theta_r}{\partial X^2} + \frac{\partial^2 \theta_r}{\partial Y^2} = \frac{\partial \theta_r}{\partial t^*} \quad \text{(A2)}$$

The Newton's law of cooling yields the boundary condition at the conduit wall:

$$\left(-\vec{\nabla}\theta_r\right) \cdot \vec{n} = Bi(\theta_r - \theta_a) \quad \text{with } \theta_a = \sin(2\pi t^*) \quad \text{(A3)}$$

where the Biot number $Bi = \frac{h_t L_d}{k_r}$ is the dimensionless heat transfer coefficient. $\vec{n}$ is the outward unit normal vector. From air mass flowrate measurements and correlations in Appendix B, the maximum heat transfer coefficient in Longeaigue is of the order of 20 W.m^{-2}.K^{-1}. Therefore, Bi can be as high as 3 for the daily fluctuations (τ=1 day and $L_d = 0.32$ m) and 50 for the annual fluctuations (τ=1 year and $L_d = 6.1$ m). The computational domain is sufficiently large to make the external boundaries adiabatic. The simulation time is increased until the periodic regime is reached.

Fig. A2 shows the amplitude of the local temperature fluctuation along the conduit circumference. The 3D shape of the triangular and real cross sections results in non-uniform fluctuations, lower in the corners and larger in the tips. However, the amplitudes averaged over the conduit circumference are close from each other (less than 4% difference). Therefore, if we just need the mean temperatures, the circular cross-section (a) with the same perimeter as the 3D shapes (b) and (c) yields satisfying results.

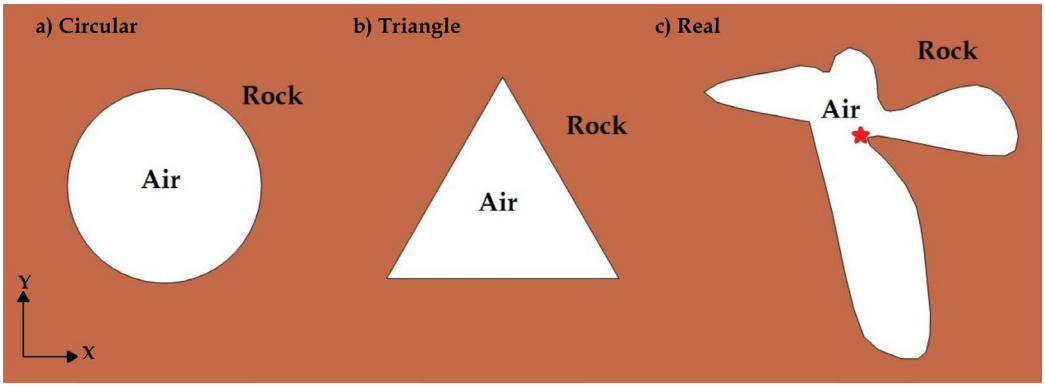

Fig A1: Three different conduit shapes (the figures are not scaled). Cross-section (c) was surveyed at 47.7 m from the entrance of D7.1 Cave located in Sieben Hengste, Switzerland (Sedaghatkish et al., 2024).

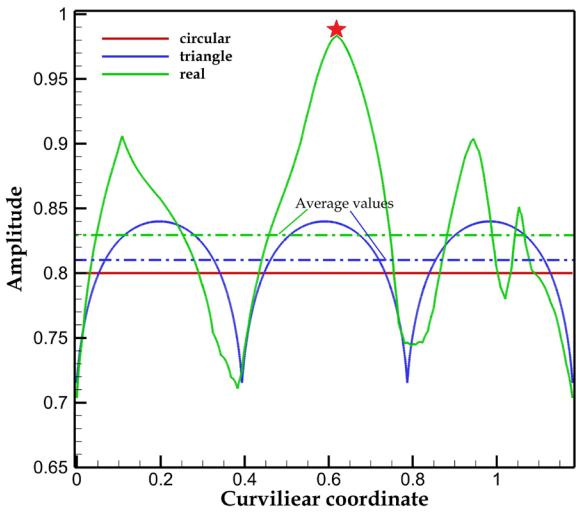

Fig A2. Amplitude of the temperature fluctuations along the conduit circumference (solid lines) and corresponding averaged values (dashed-dotted lines), for $Bi = 15.9$ and $D_p^* = P^*/\pi = 0.378$. For case (b), the origin of the curvilinear coordinate is taken in a corner of the triangle. For case (c), the position of the maximum is indicated by a star in Fig. A1c.

We performed a systematic parametric study varying the Biot number Bi and the perimeter-based diameter D_p^*. The amplitude of the wall temperature variations is displayed in Fig. A3. The maximum difference between circular and 3D cross sections is less than 20 %. We are also interested in the heat flux through the conduit wall integrated over the conduit perimeter $\Phi = \int_p Bi(\theta_r - \theta_a)\, d\hat{l}$ (where $\hat{l}$ is the curvilinear coordinate over the conduit circumference). Fig. A4 compares the values obtained for the three cross-sectional shapes. The difference between the circular cross section and the other ones increases with Biot number. It never exceeds 25%.

This simple study suggests that substituting a conduit with a circular cross-sectional shape to the real 3D geometry results in a reasonable loss of accuracy, if we content ourselves with the temperatures and heat fluxes averaged over the conduit circumference.

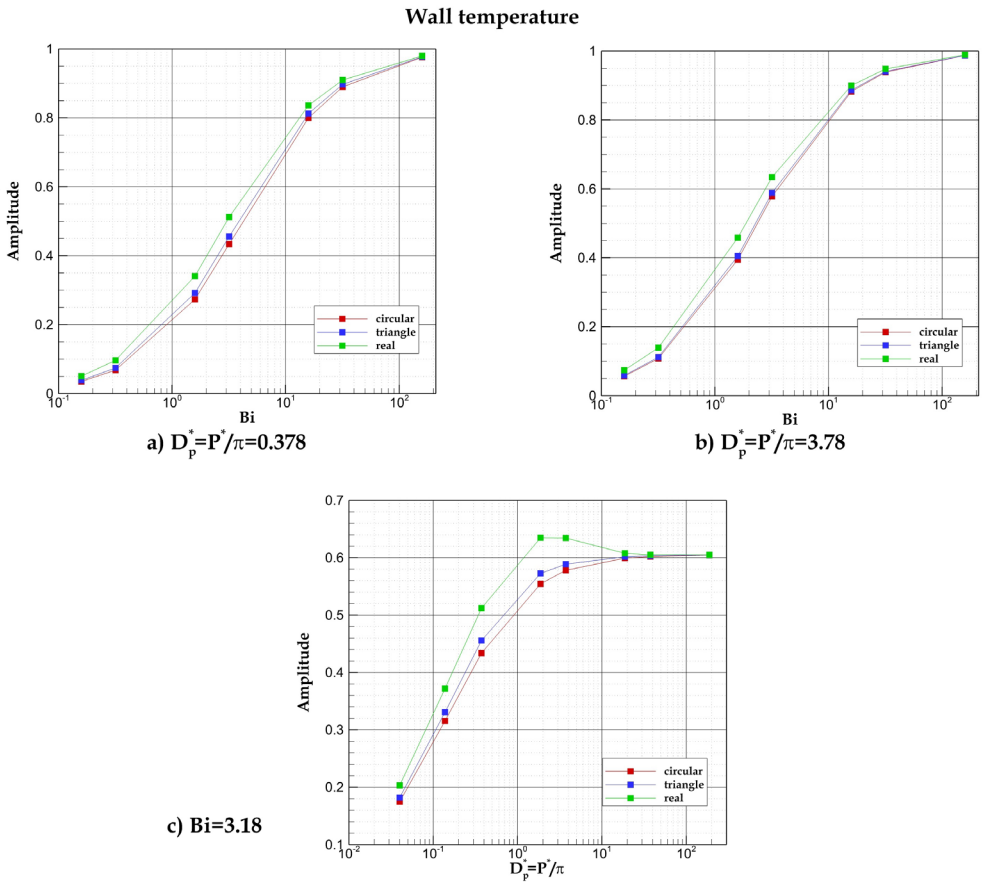

Fig A3. Amplitude of the temperature fluctuations averaged over the conduit perimeter, for different values of the perimeter-based diameter $D_p^* = P^*/\pi$ and the Biot number Bi.

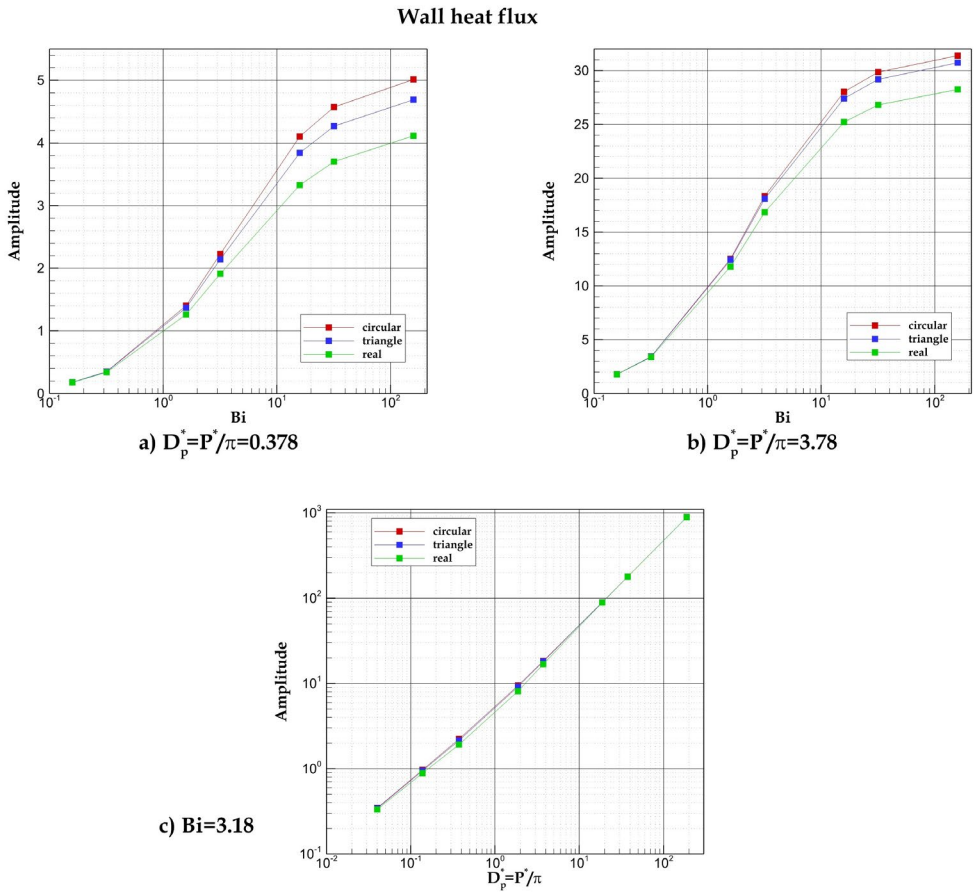

Fig A4. Fluctuation amplitude of the wall heat flux integrated over the conduit circumference, for different values of the perimeter-based diameter $D_p^* = P^*/\pi$ and the Biot number Bi.

Appendix B. Estimation of heat and mass transfer coefficients at the conduit wall

In the turbulent regime, the heat transfer coefficient is obtained from correlations between the Reynolds (Eq. 17), Prandtl and Nusselt numbers, respectively defined as:

$$Pr = \frac{c_{p,a}\mu_a}{k_a} \quad \text{and} \quad Nu = \frac{h_t D_h}{k_a} \tag{B1}$$

Nu and *Re* are based on the hydraulic diameter D_h to account for the specific shape of the conduit. The Gnielinski correlation (Gnielinski, 1975) has the advantage to take into account the wall roughness. This correlation reads:

$$Nu = \frac{\left(\frac{f_d}{8}\right)(Re - 1000)Pr}{1 + 12.7(\frac{f_d}{8})^{0.5}(Pr^{2/3} - 1)} \quad \text{for } Re \geq 4000 \tag{B2}$$

The Darcy friction factor f_d, which depends on the wall relative roughness ε and the Reynolds number, was estimated from the Haaland correlation (Haaland, 1983):

$$\frac{1}{\sqrt{f_d}} = -1.8\, log\left[(\frac{\varepsilon}{3.7})^{1.11} + \frac{6.9}{Re}\right] \tag{B3}$$

In the laminar regime, the Nusselt number is equal to a constant that depends on the conduit shape. For a circular cross-section, we get:

$$Nu = 3.66 \quad Re \leq 2000 \tag{B4}$$

We did not try to adapt the value of the constant to the actual shape of the conduit. Indeed, the heat transfer coefficient in the laminar regime is small. It is thus not expected to have significant effect on the results.

In all simulations, the Prandtl number was set to $Pr = 0.71$ (from Table 3), and the wall relative roughness to $\varepsilon = 0.01$. The resulting function $Nu = f(Re)$ is displayed in Fig. B1. A "smooth" transition between the laminar and turbulent regimes was achieved using the step function of Comsol Multiphysics for $2000 < Re < 4000$.

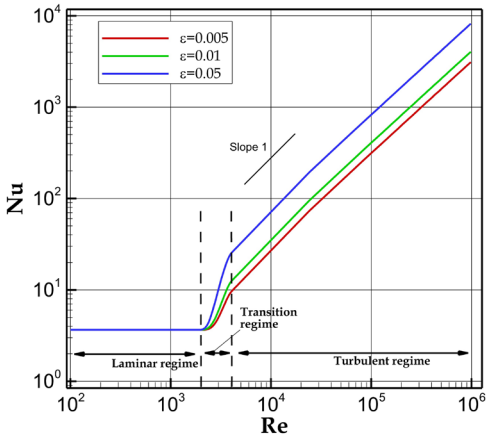

Fig B1. Nusselt number as a function of the Reynolds number for three different relative wall roughness and $Pr = 0.71$.

Using the Lewis analogy (Cussler and Cussler, 2009), the mass transfer coefficient h_m is obtained by substituting the Sherwood number $Sh = \frac{h_m D_h}{D_w}$ and the Schmidt number $Sc = \frac{\upsilon}{D_w}$ for Nu and Pr in Eqs. (B2) and (B4). It is worth noting that gases verify $Sc \approx Pr$ (from Table 3, $Sc \approx 0.59$ and $Pr \approx 0.71$). The Sherwood number Sh used in the simulations is thus close to the Nusselt number Nu displayed in Fig. B1.

A simple relation between transfer coefficients on one hand and the air flowrate and the conduit geometry on the other hand can be easily deduced from Fig. B1. This figure shows that, in the turbulent regime (i.e., for $Re \geq 4000$) and for a rough tube, the Nusselt number is approximately proportional to the Reynolds number (these results can also be deduced from Eqs. (B2-3)). The definitions of the Nusselt and Reynolds numbers yields:

$$h_t \propto \frac{\dot{m}}{P\, D_h} \tag{B.5}$$

The same relation can be inferred for h_m using the Lewis analogy. The heat and mass transfer coefficients are thus proportional to the air flowrate and inversely proportional to the product of the perimeter by the hydraulic diameter.

Appendix C. Solver stabilization

The Galerkin method used in Comsol Multiphysics is numerically unstable for the hyperbolic partial differential Eqs. (7) and (11). Classically, stabilization is achieved by adding in the equations a minor amount of artificial diffusion.

The general 1D advection-diffusion equation for the arbitrary variable S reads:

$$\frac{\partial S}{\partial t} + u\frac{\partial S}{\partial x} = c\frac{\partial^2 S}{\partial x^2} + F \tag{C1}$$

u and c are the velocity and diffusivity, respectively. F is a source term. It has been mathematically proven that the Galerkin method is numerically stable if the cell Peclet number Pe is lower than a critical value Pe_c (Kuzmin and Hämäläinen, 2015):

$$Pe = \frac{|u|h}{c} < Pe_c \tag{C2}$$

where h is the mesh element size and $Pe_c = 2$. Obviously, Eqs. (7) and (11) cannot satisfy Eq. (C2) since, in these equations, $c = 0$ results in $Pe \to \infty$.

This problem is solved by adding in Eqs. (7) and (11) an artificial diffusion term (equivalent to the first term in the RHS of Eq. C1), with a variable diffusivity set to satisfy the condition in Eq. (C2):

$$c = \max\left(c_{min}, \frac{u\,h}{Pe_c}\right) \tag{C3}$$

where c_{min} is a lower bound of the virtual diffusivity, set to the air thermal diffusivity in Eq. (7) and the water vapor diffusivity in Eq. (11).

Eq. (C3) insures the numerical stability of the Galerkin method, but we must check that the artificial diffusion introduced in the equations does not significantly affect the results. The virtual diffusivity c is a decreasing function of the mesh size. The final test for the regularization validity consists in reducing the mesh size until it has no significant effect on the results.

Appendix D. Impact of the air flowrate uncertainty on the model outputs

Figs. D1a to D1c display the impact of the air flowrate uncertainty on the conduit wall and air temperatures obtained from HA and DA models. We assume that the actual air flowrate is in the range from the measured value to this value multiplied by 1.5.

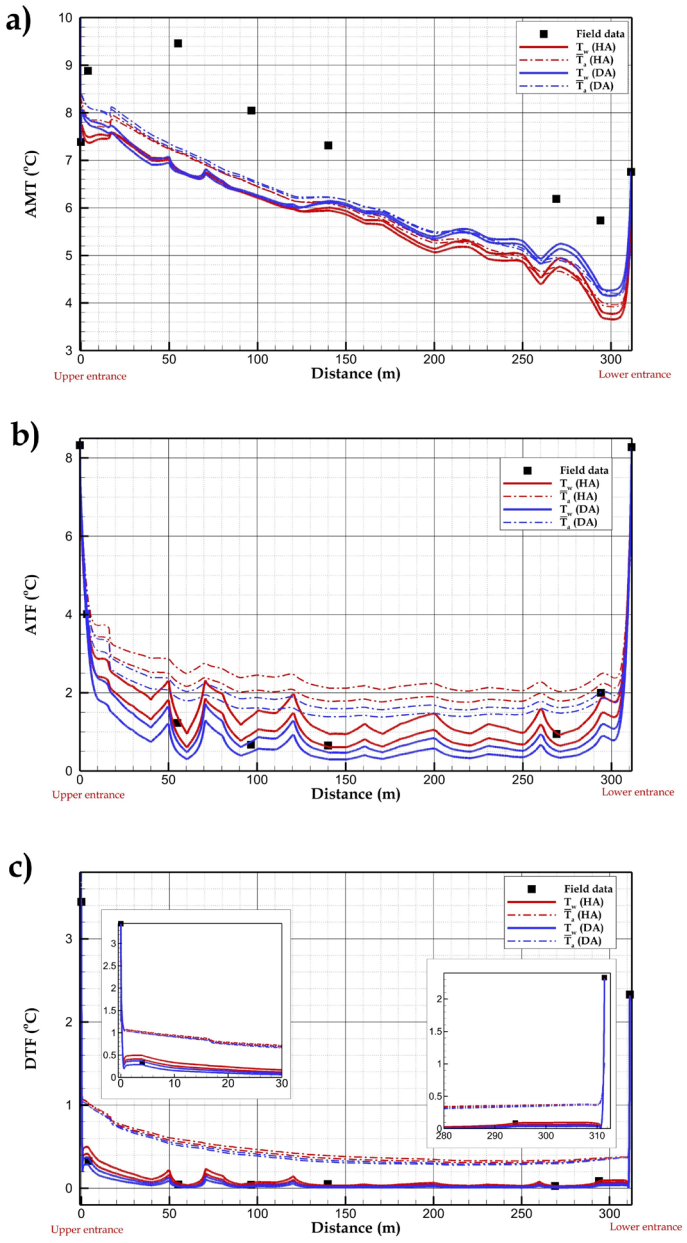

Fig D1. Impact of the air flowrate uncertainty on the model outputs, (a) AMT, (b) ATF, (c) DTF. The solid and dash-dotted lines delineate the uncertainty ranges for the conduit wall and the air temperatures, respectively.

CRediT authorship contribution statement

Amir Sedaghatkish: Conceptualization, Investigation, Methodology, Software, Visualization, Writing – original draft. **Claudio Pastore:** Data curation, Methodology, Investigation. **Frédéric Doumenc:** Conceptualization, Methodology, Writing – review & editing, Validation, Supervision. **Pierre-Yves Jeannin:** Project administration, Supervision, Writing – review & editing. **Marc Luetscher:** Conceptualization, Supervision, Writing – review & editing.

Declaration of competing interest

The authors declare that they have no known competing financial interests or personal relationships that could have appeared to influence the work reported in this paper.

Data availability

The Comsol Multiphysics file for HA scenario (humid air with finite heat transfer) is available in https://doi.org/10.5281/zenodo.14535340 associated with (Sedaghatkish, 2024) but a license of the software is necessary to use it.

Acknowledgements

This project was supported by the Swiss National Science Foundation (project no. 200021_188636). Open access funding is provided by university of Neuchâtel. We would like to thank Sven Friedel for his support and providing the COMSOL Multiphysics license for the Thermokarst project.

References

Federal Office for Meteorology and Climatology of Switzerland: www.meteoswiss.admin.ch, last access: 1 March 2024.

Bergman, T. L., Lavine, A. S., Incropera, F. P., and DeWitt, D. P.: Fundamentals of Heat and Mass Transfer, Wiley, 2017.

Birk, S., Liedl, R., and Sauter, M.: Karst spring responses examined by process-based modeling, Groundwater, 44, 832–836, 2006.

Borsato, A., Samadelli, M., Martimucci, V., and Manzi, G.: Temperature fluctuations and ventilation dynamics induced by atmospheric pressure variations in Lamalunga Cave (Apulia, Italy) and their influences on speleothem growth, Quat. Res., 118, 100–115, 2024.

Braack, L. E. O.: Arthropod inhabitants of a tropical cave 'island'environment provisioned by bats, Biol. Conserv., 48, 77–84, 1989.

Castaño-Sánchez, A., Hose, G. C., and Reboleira, A. S. P. S.: Ecotoxicological effects of anthropogenic stressors in subterranean organisms: A review, Chemosphere, 244, 125422, 2020.

Covington, M. D., Luhmann, A. J., Gabrovšek, F., Saar, M. O., and Wicks, C. M.: Mechanisms of heat exchange between water and rock in karst conduits, Water Resour. Res., 47, 2011.

Cropley, J. B.: Influence of surface conditions on temperatures in large cave systems, Bull. Natl. Speleol. Soc., 27, 1–10, 1965.

Culver, D. C. and Pipan, T.: The biology of caves and other subterranean habitats, Oxford University Press, 2019.

Cussler, E. L. and Cussler, E. L.: Diffusion: mass transfer in fluid systems, Cambridge university press, 2009.

Cuthbert, M. O., Rau, G. C., Andersen, M. S., Roshan, H., Rutlidge, H., Marjo, C. E., Markowska, M., Jex, C. N., Graham, P. W., and Mariethoz, G.: Evaporative cooling of speleothem drip water, Sci. Rep., 4, 5162, 2014.

Dornberger, S. C., Loria, A. F. R., Zhang, M., Bu, L., Epard, J.-L., and Turberg, P.: Heat exchange potential of energy tunnels for different internal airflow characteristics, Geomech. Energy Environ., 30, 100229, 2022.

Dreybrodt, W. and Deininger, M.: The impact of evaporation to the isotope composition of DIC in calcite precipitating water films in equilibrium and kinetic fractionation models, Geochim. Cosmochim. Acta, 125, 433–439, 2014.

Fairchild, I. J. and Baker, A.: Speleothem science: from process to past environments, John Wiley & Sons, 2012.

Fernandez-Cortes, A., Benavente, D., Cuezva, S., Cañaveras, J. C., Álvarez-Gallego, M., Garcia-Anton, E., Soler, V., and Sanchez-Moral, S.: Effect of water vapour condensation on the radon content in subsurface air in a hypogeal inactive-volcanic environment in Galdar cave, Spain, Atmos. Environ., 75, 15–23, 2013.

De Freitas, C. R. and Schmekal, A.: Prediction of condensation in caves, Speleogenes. Evol. Karst Aquifers, 3, 2005.

Gabrovšek, F.: How do caves breathe: The airflow patterns in karst underground, PLoS One, 18, e0283767, 2023.

Gázquez, F., Quindós, L., Rábago, D., Fuente, I., Celaya, S., and Sainz, C.: The role of cave ventilation in the triple oxygen and hydrogen isotope composition of condensation waters in Altamira Cave, northern Spain, J. Hydrol., 606, 127416, 2022.

Gnielinski, V.: Neue Gleichungen für den Wärme- und den Stoffübergang in turbulent durchströmten Rohren und Kanälen, Forsch. im Ingenieurwes. A, 41, 8–16, 1975.

Gomell, A., Austin, D., Ohms, M., and Pflitsch, A.: Air pressure propagation through Wind Cave and Jewel Cave: How do pressure waves travel through barometric caves?, Int. J. Speleol., 50, 263–273, https://doi.org/10.5038/1827-806x.50.3.2393, 2021.

Haaland, S. E.: Simple and explicit formulas for the friction factor in turbulent pipe flow, 1983.

Jeannin, P.-Y.: La Baume de Longeaigue, 30 ans de silence. Cavernes., 2018.

Jegla, T. C. and Poulson, T. L.: Circanian rhythms—I. Reproduction in the cave crayfish, Orconectes pellucidus inermis, Comp. Biochem. Physiol., 33, 347–355, 1970.

Kowalczk, A. J. and Froelich, P. N.: Cave air ventilation and CO2 outgassing by radon-222 modeling: how fast do caves breathe?, Earth Planet. Sci. Lett., 289, 209–219, 2010.

Kukuljan, L., Gabrovšek, F., Covington, M. D., and Johnston, V. E.: CO2 dynamics and heterogeneity in a cave atmosphere: role of ventilation patterns and airflow pathways, Theor. Appl. Climatol., 146, 91–109, 2021a.

Kukuljan, L., Gabrovsek, F., and Covington, M.: The relative importance of wind-driven and chimney effect cave ventilation: Observations in Postojna Cave (Slovenia), Int. J. Speleol., 50, 275–288, https://doi.org/10.5038/1827-806x.50.3.2392, 2021b.

Kuzmin, D. and Hämäläinen, J.: Finite element methods for computational fluid dynamics: a practical guide, SIAM Rev, 57, 642, 2015.

Larwa, B.: Heat transfer model to predict temperature distribution in the ground, Energies, 12, 25, 2018.

Lide, D. R.: CRC handbook of chemistry and physics, CRC press, 2004.

Lismonde, B.: Climatologie du monde souterrain; Tome 2-Aérologie des systèmes karstiques, Persée-Portail des revues scientifiques en SHS, 2002.

Luhmann, A. J., Covington, M. D., Alexander, S. C., Chai, S. Y., Schwartz, B. F., Groten, J. T., and Alexander Jr, E. C.: Comparing conservative and nonconservative tracers in karst and using them to estimate flow path geometry, J. Hydrol., 448, 201–211, 2012.

Lundström, H. and Mattsson, M.: Radiation influence on indoor air temperature sensors: Experimental evaluation of measurement errors and improvement methods, Exp. Therm. Fluid Sci., 115, 110082, 2020.

Lv, Y., Jiang, Y., Hu, W., Cao, M., and Mao, Y.: A review of the effects of tunnel excavation on the hydrology, ecology, and environment in karst areas: Current status, challenges, and perspectives, J. Hydrol., 586, 124891, 2020.

Lyu, Y., Luo, W., Zeng, G., Wang, Y., Chen, J., and Wang, S.: The effect of cave ventilation on carbon and oxygen isotopic fractionation between calcite and drip water, Sci. Total Environ., 915, 169967, 2024.

Medina, M. J., Antić, D., Borges, P. A. V, Borko, Š., Fišer, C., Lauritzen, S.-E., Martín, J. L., Oromí, P., Pavlek, M., and Premate, E.: Temperature variation in caves and its significance for subterranean ecosystems, Sci. Rep., 13, 20735, 2023.

Molnar, P.: Differences between soil and air temperatures: Implications for geological reconstructions of past climate, Geosphere, 18, 800–824, 2022.

Parra, M. T., Villafruela, J. M., Castro, F., and Mendez, C.: Numerical and experimental analysis of different ventilation systems in deep mines, Build. Environ., 41, 87–93, 2006.

Pastore, C., Sedaghatkish, A., Weber, E., Schmid, N., Jeannin, P.-Y., and Luetscher, M.: Monitoring air fluxes in caves using digital flow metres, Int. J. Speleol., 53, 7, 2024.

Qaddah, B., Soucasse, L., Doumenc, F., Mergui, S., Rivière, P., and Soufiani, A.: Coupled heat and mass transfer in shallow caves: interactions between turbulent convection, gas radiative transfer and moisture transport, Int. J. Therm. Sci., 194, 108556, 2023.

Rau, G. C., Cuthbert, M. O., Andersen, M. S., Baker, A., Rutlidge, H., Markowska, M., Roshan, H., Marjo, C. E., Graham, P. W., and Acworth, R. I.: Controls on cave drip water temperature and implications for speleothem-based paleoclimate reconstructions, Quat. Sci. Rev., 127, 19–36, 2015.

Riddick, J. A., Bunger, W. B., and Sakano, T. K.: Organic solvents: physical properties and methods of purification, 1986.

Rizzo, V., Sánchez-Fernández, D., Fresneda, J., Cieslak, A., and Ribera, I.: Lack of evolutionary adjustment to ambient temperature in highly specialized cave beetles, BMC Evol. Biol., 15, 1–9, 2015.

Rohsenow, W. M., Hartnett, J. P., and Cho, Y. I.: Handbook of heat transfer, Mcgraw-hill New York, 1998.

Salmon, F., Lacanette, D., Lharti, H., and Sirieix, C.: Heat transfer in rock masses: Application to the Lascaux Cave (France), Int. J. Heat Mass Transf., 207, 124029, 2023.

Sedaghatkish, A.: Thermal Modelling of caves ventilated by chimney effect. Zenodo, [software], https://doi.org/10.5281/zenodo.14535340, 2024.

Sedaghatkish, A., Pastore, C., Doumenc, F., Jeannin, P., and Luetscher, M.: Modeling heat transfer for assessing the convection length in ventilated caves, J. Geophys. Res. Earth Surf., 129, e2024JF007646, 2024.

Tiwari, R., Boháč, V., Dieška, P., and Götzl, G.: Thermal properties of limestone rock by pulse transient technique using slab model accounting the heat transfer coefficient and heat capacity of heat source, in: AIP Conference Proceedings, 2020.

Tremaine, D. M., Froelich, P. N., and Wang, Y.: Speleothem calcite farmed in situ: Modern calibration of δ18O and δ13C paleoclimate proxies in a continuously-monitored natural cave system, Geochim. Cosmochim. Acta, 75, 4929–4950, 2011.

Waring, C. L., Hankin, S. I., Solomon, S. B., Long, S., Yule, A., Blackley, R., Werczynski, S., and Baker, A. C.: Cave radon exposure, dose, dynamics and mitigation, 2021.

Wassenburg, J. A., Riechelmann, S., Schröder-Ritzrau, A., Riechelmann, D. F. C., Richter, D. K., Immenhauser, A., Terente, M., Constantin, S., Hachenberg, A., and Hansen, M.: Calcite Mg and Sr partition coefficients in cave environments: Implications for interpreting prior calcite precipitation in speleothems, Geochim. Cosmochim. Acta, 269, 581–596, 2020.

Yu, Y.-S., Roh, J.-H., and Kim, J.: A study on thermodynamic natural ventilation analysis by the field survey of underground mines in Korea, Tunn. Undergr. Sp., 23, 288–296, 2013.

Zeng, H. Y., Diao, N. R., and Fang, Z. H.: A finite line-source model for boreholes in geothermal heat exchangers, Heat Transf. Res. Co-sponsored by Soc. Chem. Eng. Japan Heat Transf. Div. ASME, 31, 558–567, 2002.

Chapter 4: Developing an aeraulic-thermal model for ventilated caves with known cave resistance (unpublished)

4.1 Introduction

The thermal models developed in the previous chapters consider the air mass flow rate as an input. In Chapt. 2, a simplified function of mass flow rate was estimated based on the difference between the constant temperature in a vertical conduit in the deep karst and the atmosphere temperature assuming only annual temperature fluctuation. In Chapt. 3, the mass flow rate was measured by installing an anemometer close to the upper entrance of Longeaigue cave.

In this chapter, we further develop an aeraulic-thermal model designed not only to predict the thermal response of a ventilated cave (the main focus of Chapt. 3) but also, to calculate the air mass flow rate. The only inputs for this model are the external temperatures and the cave's aeraulic resistance, a geometric parameter that determines how much airflow passes through a ventilated conduit under a given driving force. In ventilated caves, this driving force is primarily defined by the temperature (density) difference between the interior and exterior of the cave, as well as by the conduit's length and slope. This chapter serves as a complementary section to the thermal model developed in Chapt. 3. A complete understanding of the thermal model analyzed in the previous chapter is a prerequisite for reading this chapter.

4.2 Governing equations

So far, the momentum equation was not considered in the thermal model (Chapt. 3) as the mass flow rate was directly measured inside the cave. In this chapter, the momentum equation must be added besides other governing equations described in Sect. 3.2. The humid air scenario with a finite heat transfer coefficient (**HA**) is investigated as a basis for developing an aeraulic-thermal model.

Recalling all the equations and variables defined in Chapt. 3, the momentum balance for airflow inside a ventilated conduit can be defined as:

$$\frac{d\overline{p}_a}{dx} = -\frac{f_d \dot{m}|\dot{m}| P(x)}{8\rho_a A(x)^3} - \left[\frac{1}{A(x)} \frac{d\dot{m}}{dt} + \frac{\dot{m}^2}{A(x)^2} \frac{\partial\left(1/\rho_a\right)}{\partial x} \right] - \rho_a g \cos(\theta(x)) \quad (1)$$

$\dot{m}$ is the air mass flow rate, f_d is the Darcy friction factor calculated by Haaland correlation (Haaland, 1983). ρ_a is the air density inside the cave. θ is the angle between gravity and the velocity vector in the conduit when the airflow direction is from the upper to the lower entrance (see Fig. 3 in Chapt. 3). $\overline{p}_a$ is the mean air pressure averaged over the conduit cross-section as follows:

$$\overline{p}_a(x) = \frac{1}{A(x)} \iint_{A(x)} p_a(x,r)\, dA \tag{2}$$

Introducing the deviation from the hydrostatic pressure field $\overline{P}_a = \overline{p}_a - p_{atm}$ along with the assumption that the atmosphere is at mechanical equilibrium when $\frac{dp_{atm}}{dx} = -\rho_{atm} g \cos(\theta(x))$, Eq. (1) can be rewritten as:

$$\frac{d\overline{P}_a}{dx} = -\frac{f_d \dot{m}|\dot{m}| P(x)}{8\rho_a A(x)^3} - \left[\frac{1}{A(x)} \frac{d\dot{m}}{dt} + \frac{\dot{m}^2}{A(x)^2} \frac{\partial\left(1/\rho_a\right)}{\partial x} \right] - (\rho_a - \rho_{atm}) g \cos(\theta(x)) \tag{3}$$

The atmosphere density ρ_{atm} is calculated based on the ideal gas law as a function of atmosphere T_{atm} and pressure p_{atm}. Moreover, ρ_a can be estimated from $\overline{p}_a$ and $\overline{T}_a$ assuming that the ideal gas law holds for the section-averaged variables, which is a correct approximation if temperature and pressure variations over a given section are weak. By taking integral over the conduit length between the two entrances, the LHS of Eq. (3) which is the gradient of pressure difference between the atmosphere and the cave, becomes zero because we assume at both entrances $\overline{p}_a = p_{atm}$.

While the first term in RHS of Eq. (3) shows the friction term, the second and third terms correspond to inertia and the last term displays the driving force associated with a chimney effect due to the density difference between the air inside and outside the cave. Equation (3) can be simplified further by neglecting the inertia terms. By taking an integral over the conduit length, the momentum balance can be defined as:

$$-\dot{m}|\dot{m}| \int_0^{L_{cave}} \frac{f_d P(x)}{8\rho_a A(x)^3} dx - \int_0^{L_{cave}} (\rho_a - \rho_{atm}) g \cos(\theta(x))\, dx = 0 \tag{4}$$

The first and second integral in the above equation is called cave aeraulic resistance (***AR***) and the driving force originated by the chimney effect, respectively. ***AR*** can be defined as:

$$AR = \int_0^{L_{cave}} \frac{f_d P(x)}{8\rho_a A(x)^3} dx \tag{5}$$

Theoretically, ***AR*** is a function of the cave geometry as given in Eq. (5). Calculation of ***AR*** using Eq. (5) is not straightforward due to the complicated cave geometry such as the irregularities along the cave passage. Alternatively, it is advised to determine the aeraulic resistance based on the measured mass flow rate and driving force (Lismonde, 2002). More information about calculation of the aeraulic resistance in ventilated caves is found in (Pastore et al., in prep.). Thus, considering a known cave resistance (***AR***) the final form of momentum balance can be defined as:

$$-\dot{m}|\dot{m}|AR - \int_0^{L_{cave}} (\rho_a - \rho_{atm}) g \cos(\theta(x))\, dx = 0 \quad (6)$$

Equation (6) should be solved at the same time with all the equations given in Sect. 3.2 in Chapt. 3. According to (Pastore et al., in prep) the ***AR*** in Longeaigue cave for downward and upward flow is about 72 and 22 ($kg^{-1}.m^{-1}$), respectively. It is necessary to mention that Eq. (6) should be ignored during closure periods assuring the mass flow rate is zero when air circulation is blocked by the lake. More precisely, when the cave closure indicator (see Fig. 4 in Chap. 3) is zero, then the mass flow rate becomes zero otherwise Eq. (6) must be taken into account.

4.2.1 Modification of the external rock temperature

One of the main discrepancies observed between the simulation results and the field data in Chapt. 3 was a difference between the AMTs. In Sect. 5.1 of Chapt. 3, we discussed that the external ground surface temperature may be higher than the atmosphere temperature by a few degrees which diverges from the boundary condition taken in Eqs. (3-4) in the same chapter. Whilst finding the right values of ground temperature is out of scope of this project, they are modified as follows:

$$T_r(0, r, t) = T_{atmU}(t) + 3℃ \quad \text{for } R_p(0) \le r \le R_{dom} \quad (7)$$

$$T_r(L_{cave}, r, t) = T_{atmL}(t) + 3℃ \quad \text{for } R_p(L_{cave}) \le r \le R_{dom} \quad (8)$$

The modifications to Eqs. (7-8) are not based on direct observation or measurement but aim only to demonstrate the effect of rock surface boundary conditions on the AMT of numerical simulations.

The initial condition of the domain is also impacted by this modification as the surface rock temperature was approximated 3 °C higher than the external atmosphere temperature. The determination of the initial condition follows the same procedure as explained in Sect. 3.2.5 of Chapt. 3 considering the modification in Eqs. (7-8).

4.3 Results

Figure 1 shows the mass flow rate computed from the developed aeraulic-thermal model (indicated by green line) considering **HA** scenario and modified ground surface temperatures in Longeaigue cave (see Sect. 4.2.1). Another scenario assumes that there is no lake causing the airflow always circulates in the cave without any restriction (indicated by blue line). When the cave is open the difference between these two cases is negligible.

The uncertainty of water lake measurement for detecting the cave closure periods, the possible presence of a secondary conduit (Fig. 1 in Chapt. 3) as well as the uncertainty on the position of the anemometer (mentioned by Pastore et al., (2024)) described in Appendix 4 in Chapt. 3 causes some discrepancies between the modeled and measured mass flow rate.

Figure 2 displays the wall AMT, ATF and DTF of the aeraulic-thermal model developed in this chapter and the thermal model (based on Chapt. 3) for the **HA** scenario considering the modified ground surface temperature. The effect of the higher surface rock temperature is evident as it raises the AMT of numerical simulations in Fig. 2a compared to Fig. 7a in Chapt. 3. The small difference between the thermal-model results (indicted by the red line) using measured mass flow rate and the aeraulic-thermal model calculating mass flow rate (indicated by green line) in Fig. 2 confirms the efficiency of the developed aeraulic-thermal model for predicting the thermal response of a ventilated cave. This is confirmed by the close values of AMF, AFF and DFF between the aeraulic-thermal model and the measured ones from field data shown in Table 1.

The lack of lake (or cave closure) results in a decreased AMT as can be seen in Fig. 2a. According to Table 1, this is due to the fact that the annual mean flowrate (AMF) value without the lake is more negative (-0.286 kg/s) than the case considering the lake effect (-0.127 kg/s). The more intense upward flow reduces the AMT for about 0.5 °C in average in the middle parts of the cave (see blue line in Fig. 2a). Table 1 shows the amplitude of the main dominant modes of the measured mass flow rate as well as the ones calculated from the aeraulic-thermal model. Moreover, the absence of cave closure increases the ATF and DTF similarly by increasing the AFF and DFF (annual and daily flowrate fluctuations).

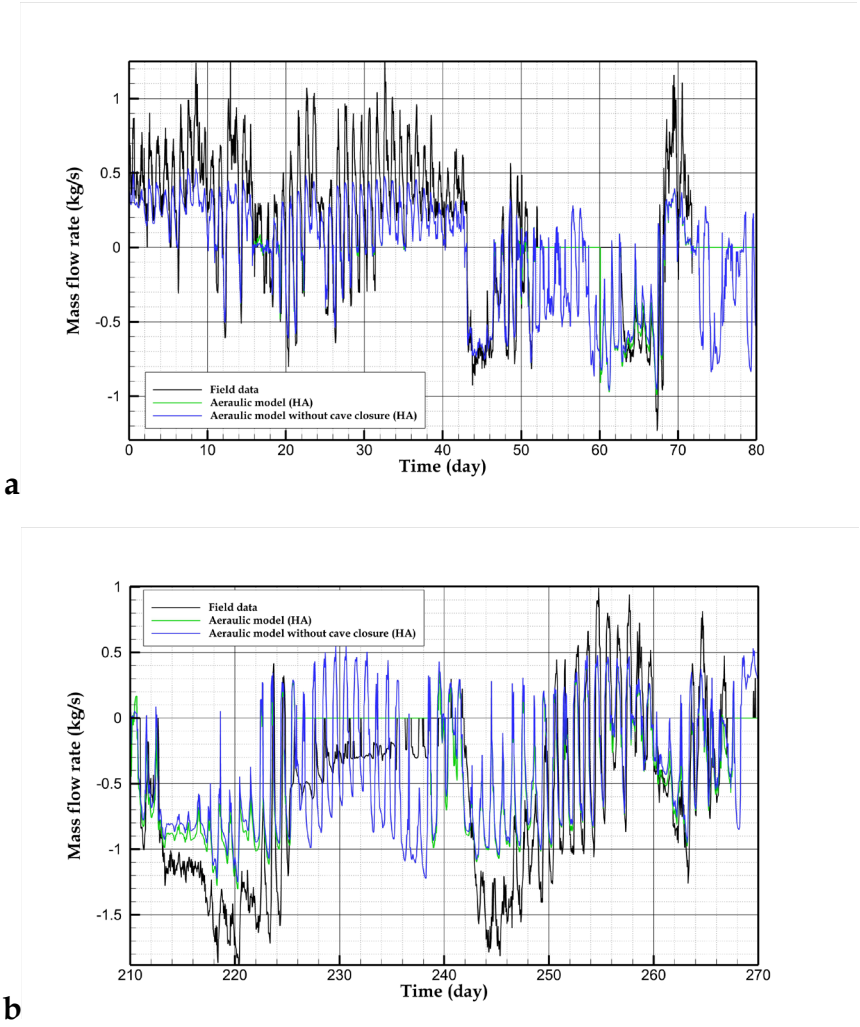

Figure 1. The modelled and measured mass flow rate for different periods (The origin of time series corresponds to 13/08/2020) a) between 0 and 75 days b) between 210 and 270 days

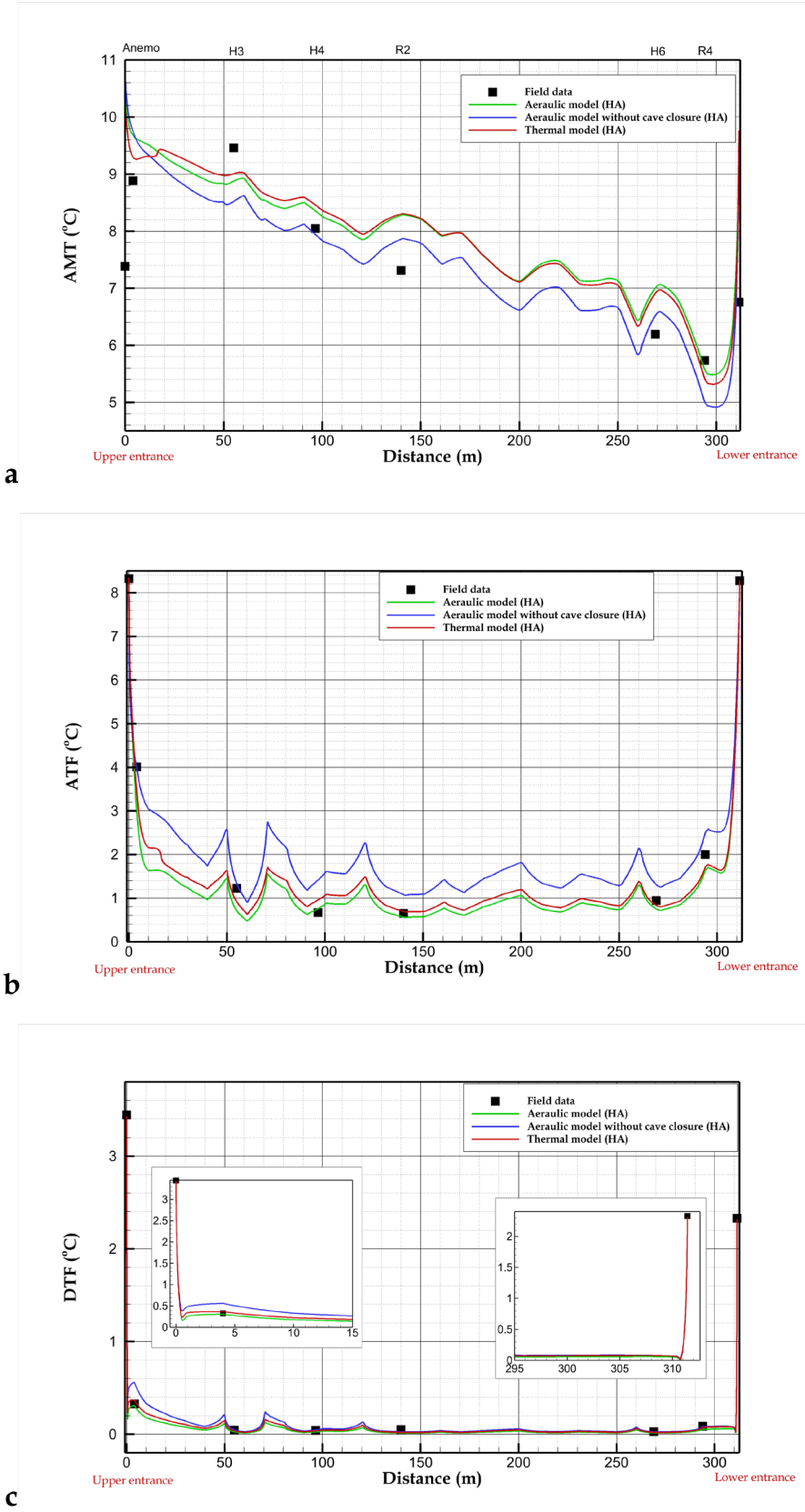

Figure 2. AMT(a), ATF (b) and DTF (c) from the field data and the numerical simulations. Only wall temperatures are shown in simulation results.

Table 1. AMF, AFF and DFF of measured and calculated mass flow rate from aeraulic-thermal model (with and without cave closure)

	AMF (kg/s)	AFF (kg/s)	DFF (kg/s)
Field data	-0.127	0.260	0.117
Aeraulic-thermal model with cave closure (real case)	-0.153	0.244	0.109
Aeraulic-thermal model without cave closure (fictional case)	-0.286	0.513	0.207

4.4 Discussion

The aeraulic-thermal model uses the known and measured cave aeraulic resistance as an input. ***AR*** was derived from the curve fitting between the squared measured mass flow rate and the measured driving force for upward and downward flows (Pastore et al., in prep). In this section, we investigate the difficulties and challenges for calculation of the cave aeraulic resistance based on Eq. (5) and why it cannot be used for the estimation of ***AR.***

Theoretically, in perfect pipe geometries, ***AR*** can be calculated with Eq. (5) using an accurate estimation of the friction factor, area and perimeter along the cave passage. ***AR*** is, however, more sensitive to cross-section area as it is inversely proportional to the area to power of three and directly proportional to the perimeter. It means that smaller and narrower conduits have a big contribution to the aeraulic resistance of ventilated conduits. Figure 2 in Chapt. 3 represents the measured cross-section area and perimeter every 10 m along the Longeaigue cave. Using Eq. (5), the aeraulic resistance based on the distribution of perimeter and area given in this figure and the value of 0.04 for the Darcy friction factor (valid for turbulent flow and a relative roughness of 0.01 (see Fig. 3b)) is estimated 0.9 $kg^{-1}.m^{-1}$ which is much smaller than the reported values of 72 and 22 $kg^{-1}.m^{-1}$ for downward and upward flow (Pastore et al., in prep). However, whilst representing a correct statistical approximation, the narrowest passages may have been omitted. For instance, the cave survey specifies the presence of a tight conduit located slightly above station H3 (see Fig. 1 in Chapt. 3) whose perimeter, area and length are about 1.25 m, 0.125 m^2 and 3 m, respectively. This small conduit has an aeraulic resistance of about 7.5 $kg^{-1}.m^{-1}$ which is much higher than the calculated ***AR*** (0.9 $kg^{-1}.m^{-1}$). Thus, small and local narrow passages can increase ***AR*** extremely demonstrating that a detailed distribution of area and perimeter values all along the cave passage is imperative for finding the total ***AR***.

Although the perimeter and area are essential information for determining ***AR***, they are still not enough. We see that the modified ***AR*** considering the narrow passage

could not compensate the difference with the measured ***AR***. The friction factor (f_d) is another source of uncertainty. Due to many irregularities and obstacles observed along the cave passages, the use of Darcy friction factors for perfect pipes and tubes always underestimates the real friction factor. This can be seen in Fig. 3a. Zhou et al., (2016) proposed a new correlation for finding friction factors inside rock fractures as a function of Reynolds number and relative roughness (ζ is absolute roughness and $2e_h$ is the hydraulic diameter for an aperture size e_h) and they compared it with other models including (Zhang and Nemcik, 2013; Masciopinto, 1999; Nazridoust et al., 2006). It can be seen that the value of the friction factor in turbulent flow at high relative roughness (for instance 5 and 500) is one or two orders of magnitude higher than lower relative roughness (for instance 0.05). The relative roughness much higher than one is not meaningful in standard pipes and this value is considered always less than one as displayed in the Moody diagram (Fig. 2b) resulting in smaller Darcy friction factors. Jeannin, (2001) also investigated different empirical correlations for computing the hydraulic resistance for conduit networks in Hölloch cave in Switzerland. Even though his measured values of hydraulic resistance were in good agreement with the empirical correlation from (Louis, 1968), significant discrepancies were reported in the literature. Care must be taken that some of the empirical correlations which have been examined so far, are designed for hydrodynamic models and friction factors for aeraulic conduits in natural settings are not well understood yet. Nonetheless, there should be a similar analogy for any kind of fluids with the same dimensionless quantities (Reynolds number and relative roughness). Moreover, the effect of an irregular geometry cannot be captured by a certain roughness and a cave is not a succession of straight conduits.

The Longeaigue cave consists of a succession of irregular conduit sections with different dimensions and levels of roughness. As the total aeraulic resistance of a cave is the sum of the ***AR*** in each segment of the cave, a high value of friction factor or a narrow passage of one segment may increase significantly the total value of ***AR***. This effect cannot be too considerable in thermal modeling of ventilated caves as the sudden increase of friction factor (or sudden reduction of cross-section area) causes only a local increase of the heat transfer coefficient. In summary, calculating the ***AR*** in ventilated caves using Eq. (5) is not practical due to many uncertainties about cave dimensions and relative roughness (friction factor). The possible solution for finding the friction factor may be resolved by monitoring the local narrow passages along the conduit by measuring driving force and airflow rate or probably by conducting 3D numerical simulations of turbulent flow within scanned sections of cave passages.

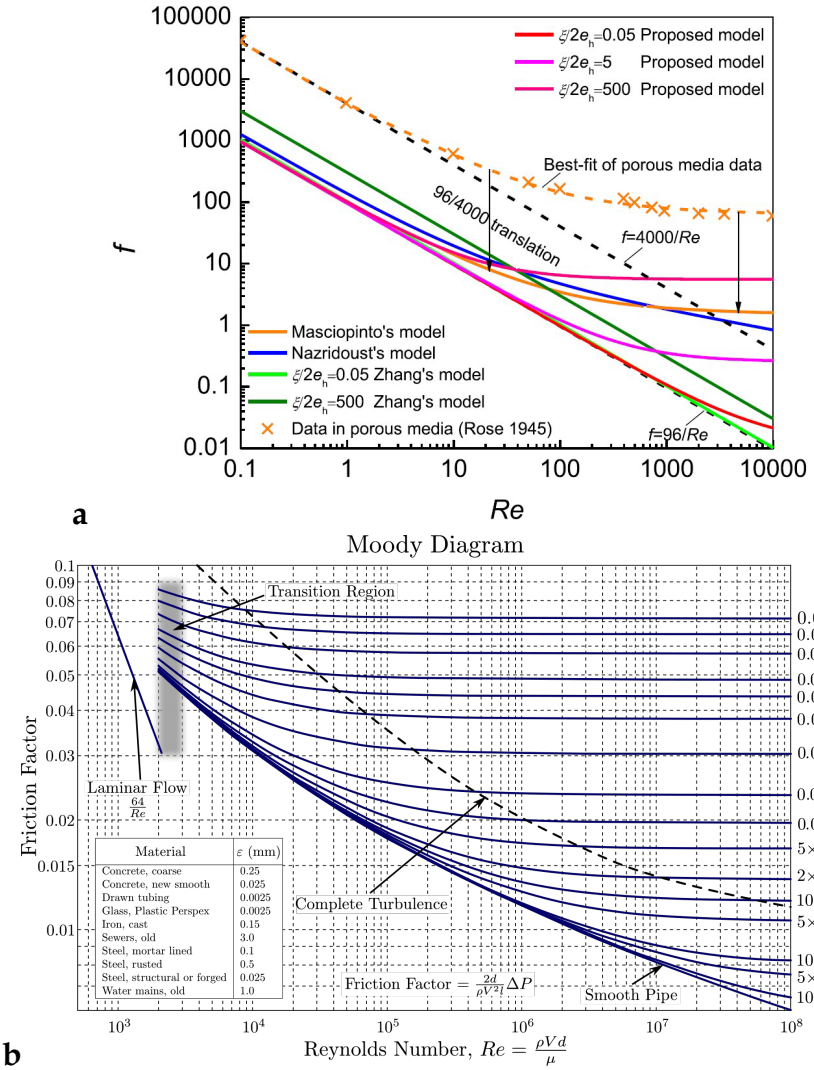

Figure 3. a) Friction factor based on different available correlations in literature for rock fractures (Zhou et al., 2016) and b) Darcy friction factor for standard pipes (Moody, 1944), for different values of Reynolds number and relative roughness

Chapter 5: Modelling the thermal response in epikarst (unpublished)

5.1 Introduction

Epikarst is located at the top of the heterothermic zone in the karst landscape. It can be under soil cover or be in direct contact with atmosphere. Epikarst is considered a fractured medium consisting of a network of connecting fractures distributed in a rock matrix. These fractures have aperture sizes ranging between 0.1 mm and 1 cm leading to contrasting permeability values. The permeability of the porous rock matrix in epikarst is negligible compared to the main fractures. Its value is in the range of 10^{-11} and 10^{-14} m^2 (Dal Soglio et al., 2020a; Dal Soglio et al., 2020b). The absorbed water due to the rain or snow melting (stored in the soil) penetrates mainly through the fracture's opening at the top surface of epikarst. The fractures with higher permeability (higher aperture size) have the most chance for rapid downward infiltration of water. To put it another way, most of the groundwater recharge travels through these high permeable fractures compared to the diffusive flux (or seepage flow) in the matrix, as shown in Fig. 1.

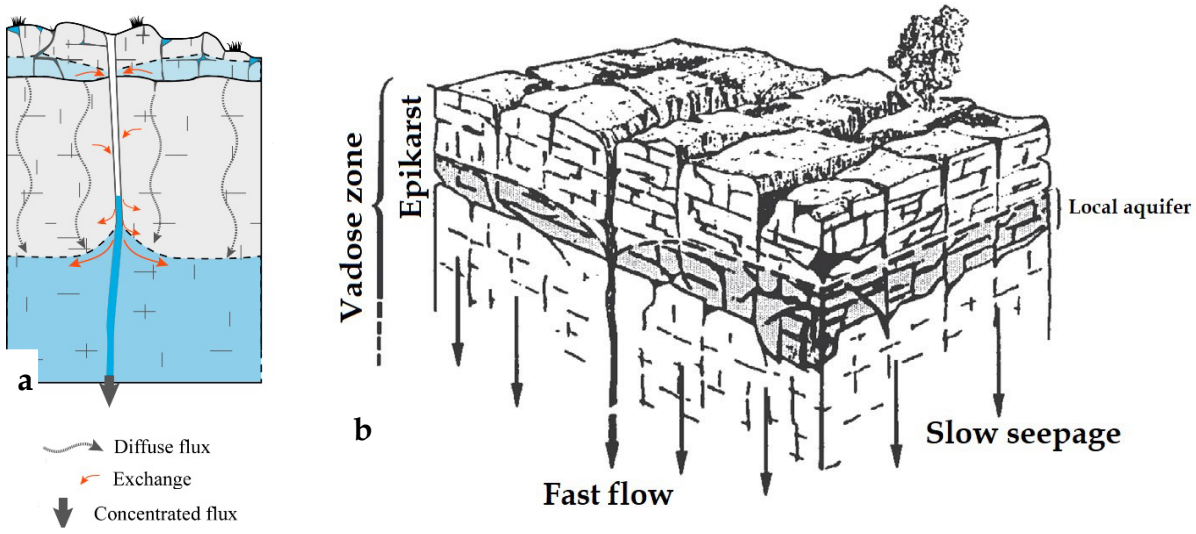

Figure 1. a) The fast (or concentrated) flow in fractures (Dal Soglio et al., 2020a) and b) the diffusive (or slow seepage) flow in matrix (Mangin, 1975)

As mentioned above, the contribution of the fractures in epikarst for infiltration of water is undeniable and these fractures must be taken into account in any hydraulic model for accurate simulation of water flux. Berre et al., (2019) provided a review of conceptual models for characterizing fractured porous media. The suitable model should be selected based on the accuracy expected in the representation of the matrix (background medium) and fractures. Figure 2 briefly shows all the available strategies for modeling fractured porous media. This figure offers a broad overview of the trade-offs involved with different models selected for fractured porous media and how these models might be treated when applied to a specific problem within a given

fractured medium. For instance, if a Discrete Fracture Network model (DFN) accurately represents all main fractures in the original medium, and the permeability of smaller fractures and matrix can be much less than the main fractures, it is considered an ideal model to represent the original medium displayed in Fig. 2 (at top right).

As the fractures can transport the fluid with higher velocity (due to high permeability) than matrix, the effect of convective heat flux is important in a fractured medium. Here, we review some of the main studies considering convective heat flux in fractured media.

Klepikova et al., (2021) developed a numerical model showing that the variation of aperture size is a decisive parameter which leads to the formation, within fracture planes, of preferential flow channels controlling flow and transport processes. They investigated how the statistical parameters determining spatial aperture variations in individual fractures control the convective heat exchange along the fractures. Their findings indicate that the thermal behavior of a rough-walled fracture can be accurately predicted using a parallel plate model, where the aperture is set to the effective hydraulic aperture of the rough fracture.

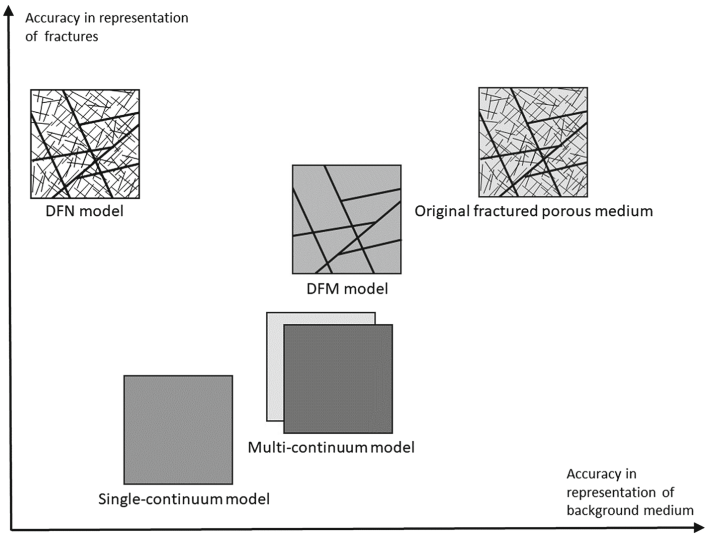

Figure 2. Conceptual models of a fractured porous medium from (Berre et al., 2019)

Exploitation of deep geothermal energy in commercial scale necessitates enhancement of fractures in geothermal reservoirs through hydraulic stimulation. The seismicity induced by such hydraulic stimulation poses significant technical challenges and threatens societal acceptance. Therefore, researchers developed numerical models to quantify permeability enhancement in fractures during hydraulic stimulation and the resulting thermal stress, track its spatial evolution during reservoir development, and analyze the seismic processes associated with fault slip during stimulation (De Simone et al., 2021; Liu et al., 2020; Patterson et al., 2018; Jansen and Miller, 2017).

These thermo-hydro-mechanical numerical investigations are performed on a DFN (Discrete Fracture Network) prepared beforehand. The DFNs are usually produced using probability distribution functions regarding some geometrical information of the fractured aquifer such as the number, size and orientation of fractures. More information about different approaches to produce DFNs can be found in (Huang et al., 2021; Berkowitz, 2002).

The thermal response of epikarst as a fractured medium is worth to be investigated and compared with the results of classical conduction-based models for calculation of temperature in karst underground environment (Domínguez-Villar et al., 2013; Domínguez-Villar et al., 2023) which are extensively utilized for the interpretation of paleoclimate records. The convective heat flux associated with the recharge water infiltrating into the distributed fractures may affect the surrounding rock massif. The main objective of this chapter is to evaluate the thermal response of epikarst to external atmospheric temperature variation and precipitation rates under different hydrodynamic situations assuming a 3D computational domain and a network of 2D fracture planes.

5.2 Computational domain and methodology

5.2.1 Domain geometry

Information about the exact geometry of fractures distributed in the epikarst is not available and, at this stage, we only rely on our conceptual representation for designing the computational domain. We consider a rectangular cube representing a hypothetical epikarst volume comprising impermeable rock and DFNs as displayed in Fig. 3a. The top surface of the domain considers a 30 m × 30 m square catchment area without soil cover. The depth of the epikarst is taken at 10 m. A DFN was produced using add-in feature in Comsol Multiphysics with minimal information based on statistical and geometrical features gathered in Table 1. More detailed information about these parameters can be found in (Comsol Multiphysics, user guide). The produced meshed DFN as the main hydraulic passage of water in epikarst can be observed in Fig. 3b. Moreover, four perfectly horizontal fractures are produced to represent the bedding planes (along the main DFN) with 1 cm aperture size.

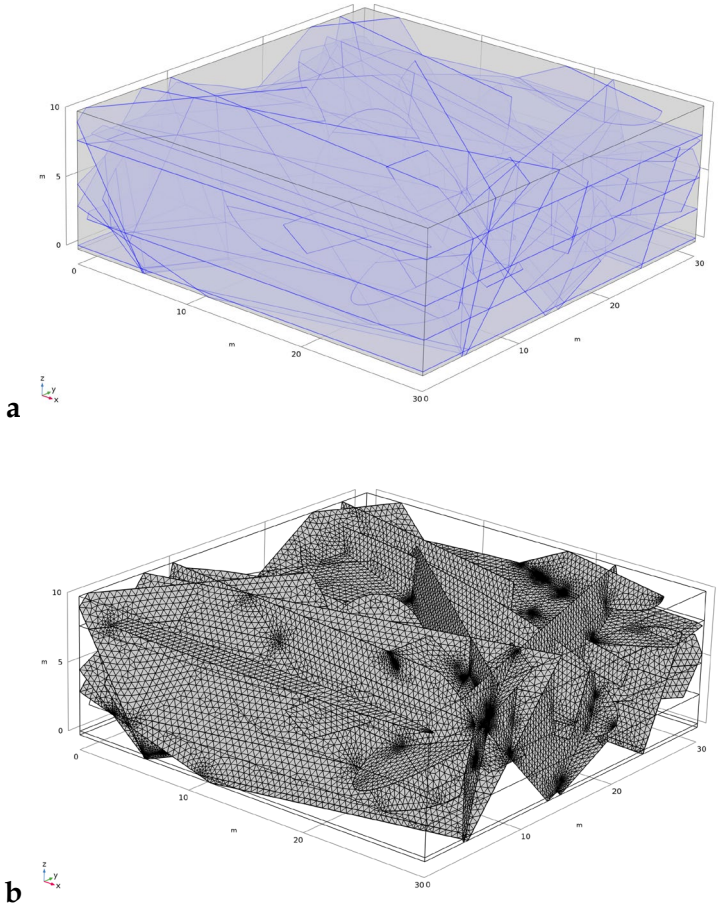

Figure 3. The DFNs and the surrounding impermeable rock of a hypothetical epikarst as the computational domain in this study a) the DFNs (blue planes) and rock massif in transparent mode b) the computational grid used in this study for DFNs

Table 1. the statistical information used for producing the DFN in our hypothetical epikarst (Comsol Multiphysics, user guide.; Berkowitz, 2002).

Number of fractures	30
Aperture size (d_f)	1 mm
Size	
Distribution function	Uniform random
Maximum length of fractures	30 m
Minimum length of fractures	5 m
Orientation	
Distribution function	Fisher
Dip angle	80°
Strike angle	45°
Dispersion coefficient	0.1

5.2.2 Governing equations and boundary conditions

Water flow in epikarst may not saturate the fractures and, depending on the recharge rate (precipitation, snowmelt, …), a water table with variable height may be formed at the bottom of epikarst, dividing the DFN in two zones: a saturated part where the fractures are full of flowing water located under an unsaturated part where the water flow only partially fills the fractures. The distribution of the velocity field is different for these two zones resulting in contrasting convective heat fluxes. Developing a complex model that simultaneously considers both cases demands more comprehensive analysis and will not be examined here. The aim is to define two extreme scenarios as a lower and higher bound for highlighting the effect of convective heat flux on the thermal response of epikarst using a purely qualitative approach. Under this frame, we investigate two scenarios corresponding to fully saturated and fully unsaturated fractures.

5.2.2.1 Hydraulic flow for fully saturated fractures

Flow within a saturated fracture is modeled as a steady-state and incompressible flow where viscous forces dominate inertial effects. The continuity and momentum equation (considered as Darcy law) through 2D fracture planes distributed in 3D impermeable rock massif can be defined as:

$$\nabla . \boldsymbol{u}_f = 0 \tag{1}$$

$$\boldsymbol{u}_f = -\frac{k_f}{\mu_w}(\nabla_t P_f + \rho_w \boldsymbol{g}) \tag{2}$$

$\boldsymbol{u}_f$ is the velocity field of water inside the fractures, P_f is the fluid pressure, $\boldsymbol{g}$ is the gravity acceleration vector, ρ_w and μ_w are the density and dynamic viscosity of water, respectively. The subscript "*f*" indicates fracture. The "∇_t" indicates the tangential derivative along the fracture planes. The k_f is fracture permeability and it can be calculated by cubic law regarding the aperture size:

$$k_f = \frac{{d_f}^2}{12} \tag{3}$$

d_f is the aperture size of the DFN shown in table 1.

5.2.2.2 Hydraulic flow for fully unsaturated fractures

This scenario acts as a lower bound for showing the effect of convective heat flux in epikarst. We assume that the pressure is always zero everywhere in the DFN ($P_f=0$) and the water does not fill the fractures flowing downward with uniform velocity. This velocity (U_{in}) can be calculated by assuming a mass balance between the meteoric precipitation rate and the water flowrate entering the fractures at the top of the epikarst (i.e. no runoff):

$$U_{in} = \frac{A_c U_{rain}}{(d_f L_f)} \tag{4}$$

L_f is the total length of interface lines between the top surface and DFN as displayed in Fig. 4a as blue lines (L_f= 173 m). A_c is the catchment area and U_{rain} is the rainfall rate. It is imposed that there is a uniform velocity (U_{in}) in all the fractures without conserving mass between the inlet and outlet fractures. U_{in} is a function of rainfall rate and it is taken constant throughout the year.

5.2.3 Heat transfer (saturated or unsaturated fractures)

The heat transfer in impermeable rock is considered based on purely conduction:

$$\rho_r c_{p,r} \frac{\partial T_r}{\partial t} = k_r \nabla^2 T_r \tag{5}$$

T_r is rock temperature. Thermal properties of rock are denoted by "r" subscript. Table 2 shows all the thermal properties and parameters defined in this chapter. The energy balance in the fractures considering thin thermal approximation (Klepikova et al., 2021; Liu et al., 2020) can be defined as:

$$d_f \rho_w c_{p,w} \frac{\partial T_f}{\partial t} + d_f \rho_w c_{p,w} \boldsymbol{u}_f . \nabla_t T_f - d_f k_w \nabla_t^2 T_f = -\boldsymbol{n} . (k_r \nabla T_r) \tag{6}$$

T_f is the water temperature inside the fractures and $\boldsymbol{n}$ is the normal vector to fracture planes. The RHS in Eq. (6) represents the contribution of the normal component of the conductive heat flux from the surrounding rock to the fractures. The velocity field in the DFN ($\boldsymbol{u}_f$) can be derived from the two scenarios for fully saturated or fully unsaturated fractures, respectively, described previously by Eqs. (2) and (4). At the interface of rock with fracture planes:

$$T_r = T_f \tag{7}$$

Table-2 the thermophysical properties and parameters defined in the model

Thermophysical properties and parameters	Values and unit
ρ_r	2325 (kg/m^3)
$c_{p,r}$	841.09 (J/(kg.K))
k_r	2.302 (W/(m.K))
ρ_w	1000 (kg/m^3)
$c_{p,w}$	4200 (J/(kg.K))
k_w	0.582 (W/(m.K))
μ_w	0.001 (Pa.s)
T_m	12 ℃
ΔT	8 ℃

5.2.4 Boundary and initial conditions

The intersection of 2D fracture planes with the external domain surfaces results in some lines which are the boundaries of the DFN in epikarst. For hydraulic flow considering fully saturated conditions, the inlet velocity (or zero pressure considering the beginning of transition to unsaturation) is considered for the fractures interface at top of the epikarst (blue lines in Fig. 4a). Only one fracture interface at the bottom of the epikarst is selected as an outlet with zero pressure shown in Fig. 4b. The selection of this boundary is completely arbitrary. Impermeable boundary condition ($\boldsymbol{u}_f=0$) is applied on the rest of the DFN boundaries at the bottom and external surfaces.

For hydraulic flow considering fully unsaturated fractures, Eqs. (1-2) are not solved and, according to Sect. 2.2.2, the velocity field is considered uniform.

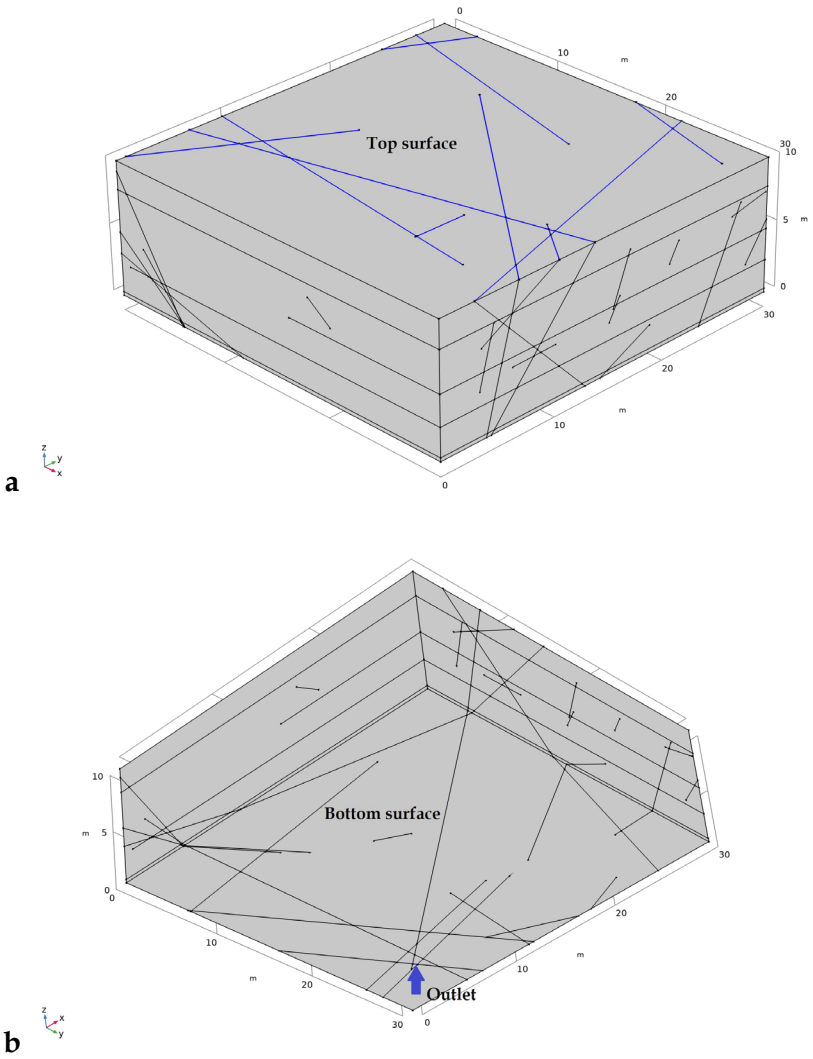

Figure 4. Boundaries of DFN (lines) and the external surfaces of the rock domain a) top surface b) bottom surface

Thermal boundary conditions for the top external surface of epikarst and its fracture interfaces can be defined as:

$$T_f = T_r = T_m + \Delta T \sin(\frac{2\pi}{\tau} t) \quad (8)$$

T_m and ΔT are the yearly average and yearly fluctuations of atmosphere temperature (table-2). τ is the periodicity of temperature variations, taken as one year. In this study, we assume that the inlet water temperature flowing downward into the epikarst DFN has the same temperature as the atmosphere. The remaining boundaries of the DFN and rock surfaces are treated as thermal insulation, assuming a zero-temperature gradient. Thus, the atmosphere is taken as the only source of heat influencing the epikarst by conduction through the impermeable rock or convection through the water flux in fractures.

The uniform temperature T_m is considered as initial condition in all the domain including rock and fractures.

5.3 Results

In order to see when a fully saturated fracture drains towards an unsaturated state, we investigate a transitional case just at the beginning of the unsaturation phase. The transition between these two hydraulic states determines the minimum inlet flow rate to keep the DFN fully saturated. This transition is achieved only when a zero pressure (atmosphere pressure) is applied at the top surface boundaries instead of the inlet velocity mentioned in Sect. 2.2.4. Thus, considering a fully saturated DFN, the modification of boundary conditions results in an inlet recharge rate of approximately 1.5×10^{-2} m^3/s. This value is much higher than a maximum recharge rate of 4×10^{-4} m^3/s (corresponding to 40 mm/d precipitation over a catchment area of 900 m^2). This indicates that the fully saturated fracture scenario is not realistic. However, it can represent an extreme condition of convective heat flux in epikarst.

Figure 5 shows the temperature distribution in different vertical slices across the epikarst considering a fully saturated DFN case with zero pressure at the top surface. The effect of convective heat flux in the epikarst and its propagation into the rock massif is obvious. The density of fractures and their connectivity are important factors for a rapid downward transfer of water allowing for almost uniform temperatures along the fractures and surrounding rock.

Figures 6 and 7 illustrate the effect of convective heat flux in a fully unsaturated DFN with 40 and 4 mm/d precipitation rates, respectively. In the latter, the effect of convective flux is negligible due to smaller velocity but in the former, it is still impacting the impermeable rock.

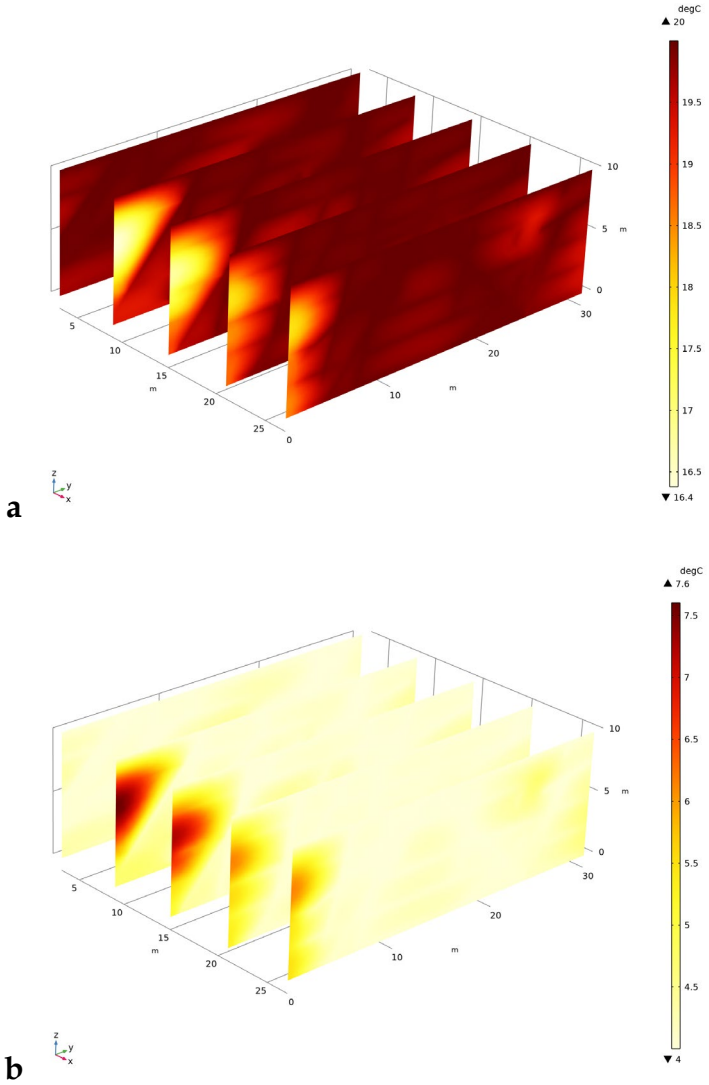

Figure 5. Temperature distribution in the epikarst for fully saturated DFN a) t=0.25 year in the middle of summer b) t=0.75 year in middle of winter

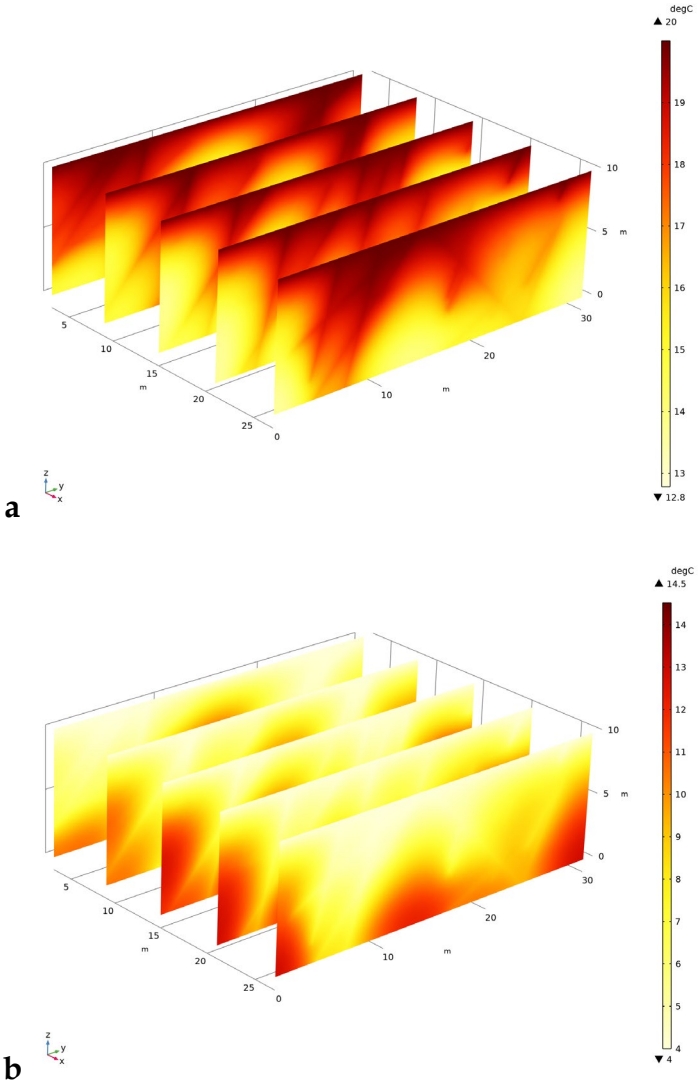

Figure 6. Temperature distribution in the epikarst for fully unsaturated DFN corresponding to Urain=40 mm/d a) t=0.25 year in middle of summer b) t=0.75 year in middle of winter

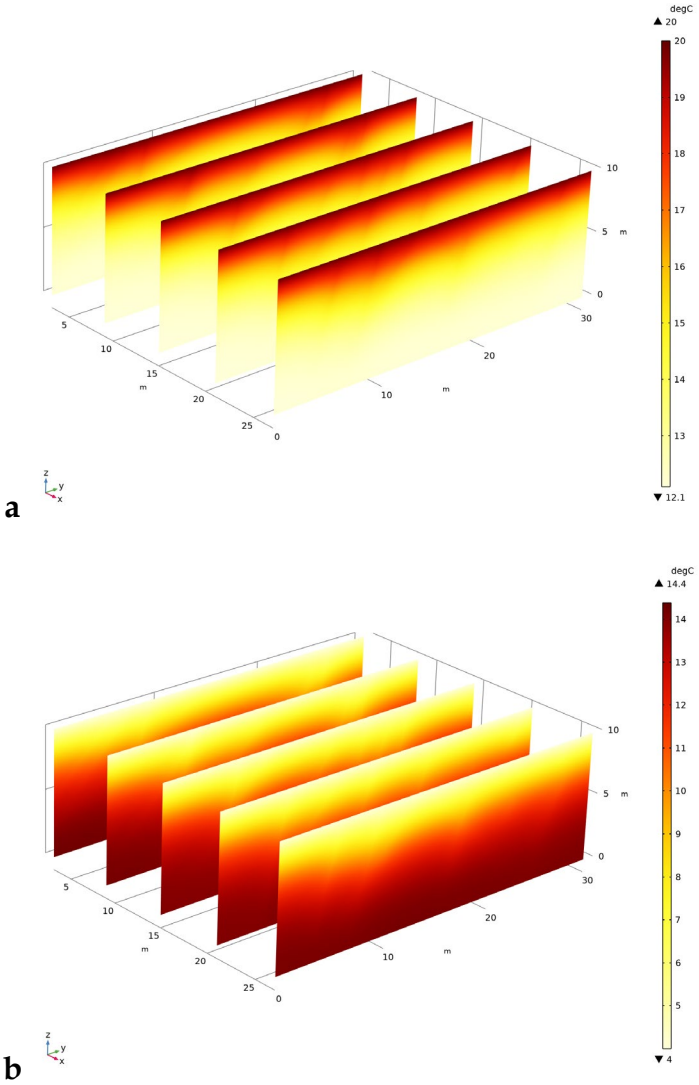

Figure 7. Temperature distribution in the epikarst for fully unsaturated DFN corresponding to Urain=4 mm/d a) t=0.25 year in middle of summer b) t=0.75 year in middle of winter

5.3.1 Comparison with conduction-base thermal models

We have seen in Figs. 5-7 that the convective heat flux of water flow can play an important role for both, fully saturated and unsaturated DFN with 40 mm/d as precipitation rate. Figure 8 shows the temperature profile as a function of depth along a vertical line located exactly in the middle of the 3D computational domain (Fig. 3a) considering fully saturated and fully unsaturated DFN (i.e. with 4 and 40 mm/d precipitation rates) as well as a conduction-based thermal model which ignores the water flux in DFN. The thermal response of unsaturated DFN with a low precipitation rate is closer to the thermal response of conduction-based models but with increasing precipitation rate the thermal attenuation decreases and the deviation from purely conduction behavior is obvious.

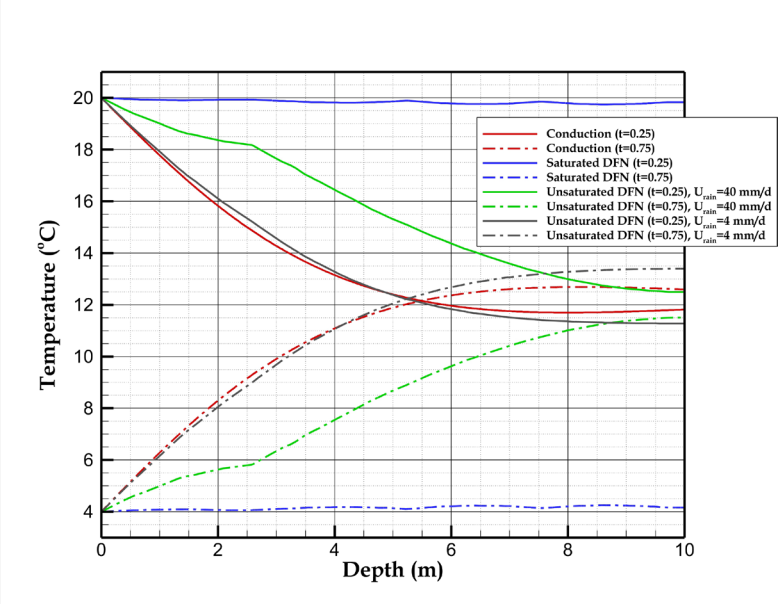

Figure 8. Variation of temperature as a function of depth in the middle of summer and winter (t=0.25 and 0.75 years, respectively) considering DFN (different scenarios) and purely conduction case when the effect of water infiltration is ignored

The time series of outlet temperature at the bottom of the epikarst determines how much the amplitude of inlet water temperature changes through crossing the DFN. Figure 9 displays the outlet temperature time series of the mentioned scenarios as well as atmosphere temperature for 2 years. The fully saturated DFN causes an outlet temperature following almost the atmosphere temperature without any attenuations due to unrealistically high water flux. The unsaturated DFN reduces the amplitude with decreasing precipitations or inlet water flux while purely conduction scenario has the minimum attenuation compared to other scenarios. For instance, the amplitude of the unsaturated DFN scenario with 4 mm/d (denoted by the gray color) is about 1°C higher than the purely conduction scenario. Although considering a constant value of 4 mm/d corresponds to an annual recharge of 1460 mm, which is a high recharge rate for temperate regions, but still within the range of possible conditions. Other hydrodynamic scenarios including the fully saturated and unsaturated (with 40 mm/d for precipitation rate) seem to be unrealistic for this study.

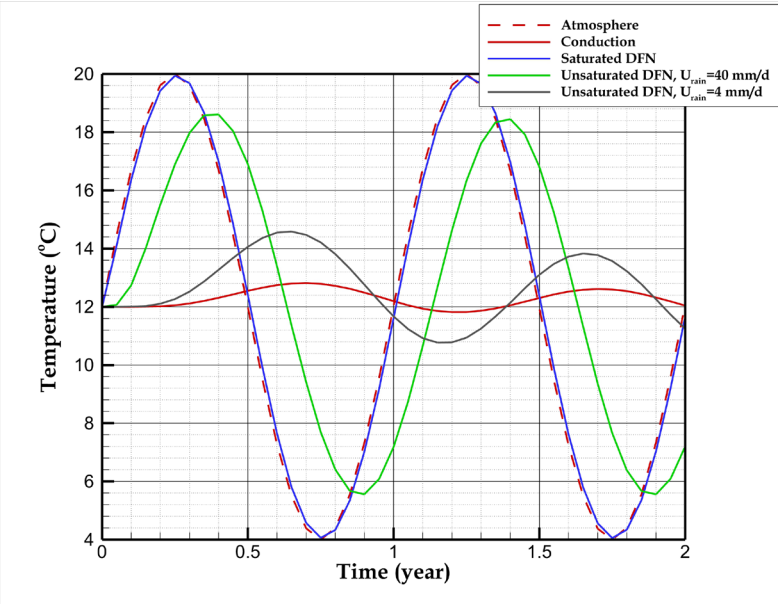

Figure 9. Atmosphere (red dashed line) and outlet temperature (solid lines) as a function of time considering DFN (different scenarios) and purely conduction case

5.4 Discussion

We figured out that the maximum daily average precipitation rate (40 mm/d) cannot make the fractures in epikarst fully saturated. To reach the fully saturated DFN, the minimum flowrate at the inlet of epikarst should be 1.5×10^{-2} m^3/s resulting in 288000 mm/h as rainfall rate which is not realistic at all. Changing geometrical features of epikarst such as fracture densities or aperture sizes may lead to different hydrodynamic response. The production of different configurations for DFN and investigation of the effect of geometrical features on the hydrodynamic response is beyond the scope of this study. The main objective is to emphasize the effect of convective heat transfer within the network of connected fractures in a speculative geometry reasonably representing the epikarst.

5.4.1 The airflow in epikarst

The possibility of airflow due to chimney effect in DFN should be checked. The density difference between inside and outside of DFN may initiate an airflow in dry condition similar to ventilated caves. Figure 10 shows a single vertical fracture with constant wall temperature (T_m). The atmosphere temperature is denoted by T_{atm}. W, H and d_f are width, height and aperture size of the fracture, respectively. For parallel isothermal plates similar to Fig. 10, Rohsenow et al., (1998) reported that the Nusselt number in the fully developed regime is given by:

$$Nu \approx \frac{Ra}{24} \quad for \quad Ra < 10$$
$$Nu = C_1 C_2 Ra^{1/4} \quad for \ 10 < Ra < 10^4 \tag{9}$$

C_1 and C_2 are constant parameters and Ra is the Rayleigh number which is defined as:

$$Ra = \frac{g\beta|T_m - T_{atm}|d_f^3}{\upsilon_a \alpha_a}\left(\frac{d_f}{H}\right) \tag{10}$$

g is gravity acceleration, β is expansion coefficient of air, υ_a is air kinematic viscosity and α_a is air thermal diffusivity. In order to see how much the air convection heat transfer is important within the DFN in epikarst, the maximum Nusselt number is calculated corresponding to an extreme condition based on Eq. (10). Table 1 gathers all the physical properties and parameters for making a maximum Nusselt number. Replacing these values in Eqs. (9-10) results in $Ra \approx 45$ and $Nu \approx 1.6$. We know Nusselt number represents the ratio of total heat flux to conductive heat flux. Thus, the convective heat flux by airflow in epikarst can be neglected with a good approximation.

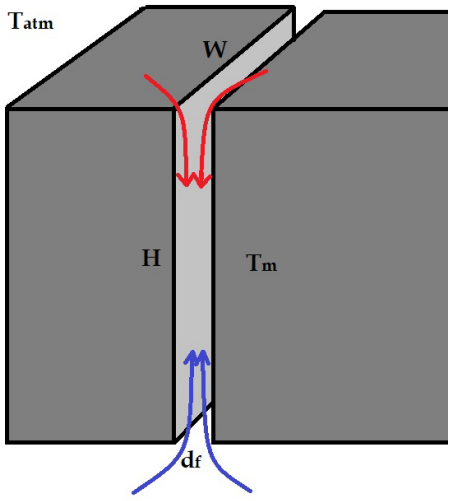

Figure 10. A simplified geometry displaying chimney effect inside a vertical fracture (W,H>>d_f)

Table 1. Thermophysical properties and parameters

Parameter	Value and unit
d_f	2 [cm]
H	5 [m]
T_m	8 [°C]
T_{atm}	20 [°C]
g	9.8 [m/s^2]
β	0.0036 [1/K]
υ_a	1.5e-5 [m^2/s]
α_a	2.1e-5 [m^2/s]
C_1	1.2
C_2	0.515

Chapter 6: Modeling the effect of free convection on permafrost melting-rates in frozen rock-clefts (published paper)

Sedaghatkish, A., Doumenc, F., Jeannin, P.-Y., and Luetscher, M.: Modelling the effect of free convection on permafrost melting rates in frozen rock clefts, *The Cryosphere*, 18, 4531–4546, https://doi.org/10.5194/tc-18-4531-2024 , 2024

Abstract

This research develops a conceptual model of a karst system subject to mountain permafrost. The transient thermal response of a frozen rock-cleft after the rise of the atmosphere temperature above the melting temperature of water is investigated by numerical simulations. Free convection in liquid water (i.e., buoyancy-driven flow) is considered. The density increase of water from 0 to 4°C causes warmer meltwater to flow downwards and colder upwards, resulting in significant enhancement of the heat transferred from the ground surface to the melting front. Free convection increases the melting rate by approximately an order of magnitude compared to a model based on thermal conduction in stagnant water. The model outcomes are compared qualitatively with field data from Monlesi ice cave (Switzerland) and confirm the agreement between real-world observations and the proposed model when free convection is considered.

1. Introduction

With global climate change and rising temperatures, permafrost degradation has become a significant concern (Duvillard et al., 2021; Walvoord and Kurylyk, 2016; Jin et al., 2021). This is particularly true in mountain regions where rapid thawing causes subsidence and rockfalls impacting construction works and tourist facilities (Haeberli et al., 2017). Thawing permafrost poses serious challenges to infrastructures built on frozen ground, including buildings, roads, pipelines, and railways (Larsen et al., 2008; Cheng, 2005; Pham et al., 2008; Zhang et al., 2005; Fortier et al., 2011). Permafrost acts as a natural barrier, preventing water from infiltrating into the ground. As it thaws, drainage patterns are altered, leading to increased erosion and discharge of groundwater to rivers and lakes (Bense et al., 2012; Andresen et al., 2020; Fabre et al., 2017; Painter et al., 2016; Walvoord and Kurylyk, 2016). Permafrost degradation can also disrupt ecosystems adapted to frozen conditions. Trees, plants, and wildlife that rely on permafrost stability may struggle to adapt to climate changes, leading to shifts in species distribution and ecosystem dynamics depending on the permafrost melting rate (Hayward et al., 2018; Krumhansl et al., 2015; Pelletier et al., 2018).

Field measurements in boreholes (e.g. Noetzli et al., 2021; Haberkorn et al., 2021) and caves (Luetscher et al., 2008; Colucci and Guglielmin, 2019; Wind et al., 2022) have shown that heat advected by water and air fluxes may significantly disturb the geothermal field, challenging classical models of heat propagation based on

conductive fluxes. In carbonate environments, in particular, the infiltration of water along well-developed conduits may develop a thermal anomaly deep into the karst system. The discontinuous nature of permafrost in karst environments may lead to the formation of massive cave ice at depth (Bartolomé et al., 2022) but also explain unexpected speleothem formations during glacial times (Luetscher et al., 2015; Fohlmeister et al., 2023; Fohlmeister et al., 2023).

Efforts are being made to study and understand permafrost degradation to mitigate its impacts. So far, most studies considered mainly conductive and latent heat fluxes (Malakhova, 2022; Galushkin, 1997; Ivanov and Rozhin, 2022; Marchenko et al., 2008; Schuster et al., 2018; Jafarov et al., 2012; Cicoira et al., 2019; Hornum et al., 2020). Such models are, however, not applicable to heterogeneous, ice-rich media including debris-slopes, rock glaciers, fractured and/or karst aquifers. But, even though conventional 1D transient models are not suitable to every context, they offer several advantages including lower computational costs than 2 or 3D models and easy implementation. Pruessner et al., (2021) investigated glacier runoff associated with permafrost degradation in high Alpine catchments. They used two different methods GERM (Huss et al., 2008) and SNOWPACK (Bartelt and Lehning, 2002) which are based on 1D transient conduction considering latent heat exchanges, different thermal properties of ground layers constituents and ventilation effects. This distributed model is efficient for calculation of temperature in large domains (catchment scale). Mohammed et al., (2021) developed a hydro-thermal-solutal model for analyzing reactive solute transport in permafrost-affected groundwater system by considering convective flux in the energy balance. Tubini et al., (2021) proposed a numerical approach for modeling heat transfer of permafrost thawing based on conduction and latent heat flux in 1D domain which is capable to deal with high time steps and maintains conservation of energy in long-term simulations. Hasler et al., (2011) built a conceptual model combining numerical modeling and laboratory experiments to investigate the effect of advective heat transport induced by water drainage in frozen rock clefts and fractures at small scales. They built a conceptual model combining numerical modelling and laboratory experiments. These authors find a significant effect of water flow inside the clefts, due to the formation of thermal shortcuts between the atmosphere and the subsurface.

Although, the majority of these studies are designed to address large-scale problems they typically neglect free convection within the liquid water phase. This process could nonetheless play an important role in the total heat transfer particularly in geographically restricted areas subject to mountain permafrost (Haberkorn et al., 2021). Figure 1-a displays the bottom of a frozen cleft hosted in an Alpine karst. Such clefts and fissures are characterized by distinct geometries accommodating contrasted volumes of ice. Our aim is to study the effect of free convection on the melting rate in frozen rock clefts and/or karst conduits at daily scale. Atmospheric warming at the upper boundary melts the ice from top of the fractures, and increases the meltwater temperature. While most fluids expand as temperature increases, liquid water shrinks

when warmed from 0°C to 4°C. Above this temperature, the common behavior is recovered (see the maximum density at 4°C in Fig.2). Therefore, the progressive warming of the meltwater at the top of the cleft results in an unstable situation (heavier fluid above lighter) that triggers free convection (buoyancy-driven flow). To assess the thermal reaction time, and thus hydrological breakthrough associated with the thawing of mountain permafrost we model the heat exchange in a frozen rock cleft. We assess by numerical simulations the temperature field in the meltwater, ice, and surrounding rock, as well as the velocity field within the liquid water to elucidate the main mechanisms driving the thawing of ice. Although a physical monitoring of such processes is hardly possible, our model fits as close as possible to effective field observations. A systematic comparison is conducted under similar thermal settings for two cases: one considers heat conduction in stagnant liquid water (SLW) whereas free convection (FC) is taken into account in the second case. Our study shows how free convection enhances the melting rate of an ice cleft at different aperture sizes.

2. Computational domain and governing equations

2.1 Physical model and simplifying assumptions

We consider the upper part of a single vertical cleft of size aperture A_p filled with pure water whose melting point is $T_m = 0°C$. This cleft is surrounded by a rock mass of width W (see Fig.1-b). In karst massifs, water flow concentrates in well-defined conduits (Ford and Williams, 2007). The micro-porosity of the rock is thus disregarded, and impermeable rock mass is assumed.

The cleft is located at the center of the 2D domain of height H_{dom}. In the initial state, the system (water and surrounding rock) is at the uniform initial temperature T_i =-1°C, and all the water is frozen. At time t=0, the temperature of the ground surface T_s increases at the constant rate 1.77 °C/hour to reach 15°C after 9 hours. This temperature increase is similar to the daily warming between the early morning and the afternoon.

The effect of the cleft aperture size was investigated by varying A_p from 2 cm to 50 cm. We imposed H_{dom}=0.8 m and W =1 m in all simulations. These values are large enough so that the thermal perturbation induced by the presence of the cleft does not reach the domain boundaries at the end of the simulated time (9 hours). The vertical and bottom boundaries of the domain can therefore be considered as adiabatic (see Fig.1-b). It is important to note that the domain height H_{dom} contains only the upper part of the cleft, whose actual depth commonly ranges from 1 to 10 m. The value of H_{dom} used in this study is convenient for the daily time scale considered in the numerical simulations. Simulating larger time scales would require larger values of H_{dom}.

2.2 Governing equations

The temperature T is the only dependent variable in the impermeable rock domain. It satisfies the standard heat equation

$$\rho_r c_{p,r} \frac{\partial T}{\partial t} = k_r \left(\frac{\partial^2 T}{\partial x^2} + \frac{\partial^2 T}{\partial z^2}\right) \quad (1)$$

where ρ_r, $c_{p,r}$ and k_r are the rock density, specific heat and thermal conductivity, respectively. z is the depth and x the horizontal distance from the symmetry plane of the cleft (see Fig. 1-b).

The water domain is more intricate. The velocity field must be calculated in the liquid part of the domain, but reduces to zero in the frozen region. To avoid the difficult task consisting in tracking the moving boundary between ice and liquid water, we adopted a strategy that allows to define the same set of dependent variables and governing equations in the entire water domain. To this end, we do the approximation of smooth phase transition between solid and liquid phases. We assume that ice melting begins at temperature $\mathrm{T_{m1}} = \mathrm{T_m} - \Delta\mathrm{T}$ and ends at $\mathrm{T_{m2}} = \mathrm{T_m} + \Delta\mathrm{T}$ (water is in solid state for $\mathrm{T} < \mathrm{T_{m1}}$, in liquid state for $\mathrm{T} < \mathrm{T_{m2}}$, and both phases coexist for $\mathrm{T_{m1}} \leq \mathrm{T} \leq \mathrm{T_{m2}}$). It is important to note that in this study, $\Delta\mathrm{T}$ is a numerical parameter with no physical meaning. Ideally, the behavior of a pure substance melting at temperature $\mathrm{T_m}$ is recovered for $\Delta\mathrm{T} \to 0$. Decreasing $\Delta\mathrm{T}$ thus improves the model accuracy, but requires more computational resources (see (Michałek and Kowalewski, 2003; Zeneli et al., 2019; Bourdillon et al., 2015; Arosemena, 2018) for more details). Practically, the setting of $\Delta\mathrm{T}$ results from a sensitivity analysis. Its value must be decreased until it does not change the results. This is the purpose of appendix A, where it is shown that the model is a good approximation of a pure substance for $\Delta\mathrm{T} \leq 0.7°\mathrm{C}$.

The dependent variables defined in the water domain are the temperature T, the horizontal and vertical components of the velocity vector u and v, the pressure p and the liquid volume fraction θ. Because of the assumption of smooth phase transition, θ varies continuously from 0 (solid phase) to 1 (liquid phase) throughout the water domain (see Fig.1-b). The corresponding governing equations read:

$$\frac{\partial u}{\partial x} + \frac{\partial v}{\partial z} = 0 \quad (2)$$

$$\rho_0 \frac{\partial u}{\partial t} + \rho_0 \left(u \frac{\partial u}{\partial x} + v \frac{\partial u}{\partial z}\right) = -\frac{\partial p}{\partial x} + \mu\left(\frac{\partial^2 u}{\partial x^2} + \frac{\partial^2 u}{\partial z^2}\right) + A \frac{(1-\theta)^2}{\theta^3 + \varepsilon} u \quad (3)$$

$$\rho_0 \frac{\partial v}{\partial t} + \rho_0 \left(u \frac{\partial v}{\partial x} + v \frac{\partial v}{\partial z}\right) = -\frac{\partial p}{\partial z} + \mu\left(\frac{\partial^2 v}{\partial x^2} + \frac{\partial^2 v}{\partial z^2}\right) - \rho_0 g \beta (T - T_0) + \rho_0 g + A \frac{(1-\theta)^2}{\theta^3 + \varepsilon} v \quad (4)$$

$$\rho c_p \frac{\partial T}{\partial t} + \rho c_p \left(u \frac{\partial T}{\partial x} + v \frac{\partial T}{\partial z}\right) - k\left(\frac{\partial^2 T}{\partial x^2} + \frac{\partial^2 T}{\partial z^2}\right) = 0 \quad (5)$$

$$\theta = \begin{cases} 0 & T < T_{m1}(\text{Solid}) \\ \dfrac{T - T_{m1}}{T_{m2} - T_{m1}} & T_{m1} \leq T \leq T_{m2}(\text{Diphasic}) \\ 1 & T > T_{m2}(\text{Liquid}) \end{cases} \quad (6)$$

This set of equations includes the mass balance Eq.(2), the momentum balance Eqs.(3-4), the energy balance Eq.(5) and the relation between the liquid volume fraction θ and the temperature field Eq.(6). g is the gravity acceleration, ρ_0 is the density of liquid water at the reference temperature T_0, μ and β are the dynamic viscosity and thermal expansion coefficient of liquid water, ρ, c_p and k are the density, specific heat and thermal conductivity of water.

The last term in Eqs.(3-4) is used to impose the velocity transition between the liquid and solid phases. A and ε are numerical parameters imposed by the user. A must be as large as possible provided that solver stability is insured. In contrast, ε is a small parameter used to prevent divisions by zero in numerical calculations (Mousavi Ajarostaghi et al., 2019). It can be demonstrated that for $\theta = 0$ (i.e., in the solid phase), the solution of Eqs.(2-4) turns to $u \simeq v \simeq 0$, which is the solution expected in the solid phase (see Nazzi Ehms et al (2019) and Caggiano et al (2018) for more details). Conversely, the last term in Eqs.(3-4) vanishes for $\theta = 0$ (i.e., in the liquid phase). In this case, Eqs.(3-4) turns to the standard Navier-Stokes equations (momentum balance in an incompressible Newtonian fluid), required to calculate the velocity field in the liquid phase.

The boundary conditions are as follows. At the interface between an impermeable solid and a viscous fluid, the fluid velocity is equal to that of the solid (Guyon et al., 2015). This is the so-called no-slip and impermeability conditions, resulting in $u = v = 0$ at the rock-water interface. The temperature continuity and the heat flux conservation through this interface are also considered (since the water velocity vanishes at the rock-water interface, the heat flux through the interface reduces to conduction). As already mentioned in section 2.1, the bottom and vertical external boundaries are adiabatic, and the temperature evolution of the top boundary T_s increases at a constant rate (see Fig.1-b).

2.3 Material properties

The physical properties used in the simulations are listed in Table_1. Subscripts "r", "s" and "l" refer to rock, ice and liquid water respectively. No subscript indicates the effective physical properties considered in the governing equations of the water domain (solid, liquid and diphasic). They are estimated from the liquid volume fraction θ as follows:

$$\rho = \rho_s(1 - \theta) + \rho_l\theta \quad (7)$$

$$k = k_s(1-\theta) + k_l\theta \tag{8}$$

$$c_p = \frac{\rho_s c_{p,s}(1-\theta)+\rho_l c_{p,l}\theta}{\rho} + L_m \frac{\partial \alpha_m}{\partial T} \quad \text{with} \quad \alpha_m = \frac{1}{2}\frac{\rho_l\theta-\rho_s(1-\theta)}{\rho_l\theta+\rho_s(1-\theta)} \tag{9}$$

$$\mu = \mu_l \tag{10}$$

The effective specific heat c_p defined in Eq.(9) takes into account the latent heat of melting L_m.

The standard Boussinesq approximation is assumed in the liquid phase (Spiegel and Veronis, 1960; Bejan, 2013). This approximation, widely used for free convection modeling, consists in assuming constant liquid density in the governing equations Eqs.(2-4), except in the buoyancy term of the momentum balance equations Eqs.(3-4). The thermal expansion coefficient β at the origin of buoyancy is estimated from the relation

$$\beta = -\frac{1}{\rho_l}\frac{d\rho_l}{dT} \tag{11}$$

where ρ_l is the temperature-dependent liquid water density displayed in Fig.2 (the order of magnitude of β in the unstable temperature range from 0 to 4°C is approximately -3×10^{-5} K^{-1}). In contrast, the constant liquid density ρ_0 estimated at the reference temperature T_0 is considered in the inertia terms of Eqs.(3-4) ($\rho_0 = 999.84$ kg/m^3 at $T_0 = 0$°C). The Boussinesq approximation is valid if the maximum fluid density variation $\Delta\rho_l$ is much lower than the liquid density ρ_l, a condition usually satisfied in liquids ($\Delta\rho_l/\rho_l \sim 10^{-3}$ in our case).

The density of water is greater than that of ice by approximately 10%. This induces a reduction of volume upon melting which is neglected in our model. This is equivalent to assuming that an external water flow replenishes the top layer domain with water at the ground surface temperature T_s. This would result in the additional vertical velocity in the liquid phase (Heitz and Westwater, 1970):

$$v_l = \frac{(\rho_l - \rho_s)}{\rho_l}\frac{dH}{dt} \tag{12}$$

This velocity would be that of the liquid in the absence of free convection, or would be added to the free convection velocity field in the other case. This contraction-induced flow can be neglected if the heat advected in that way is negligible compared to the heat absorbed by the motion of the melting front:

$$\rho_l\, v_l\, c_{pl}(T_s - T_m) \ll L_m \rho_s \frac{dH}{dt} \tag{13}$$

Eqs.(12-13) yield the condition of validity:

$$\frac{(\rho_l - \rho_s)}{\rho_s} \frac{c_{pl}(T_s - T_m)}{L_m} \ll 1 \quad (14)$$

with the physical properties of table 1 and $T_s - T_m$ =15°C, the LHS of Eq.(14) is approximately equal to 0.02, much lower than 1. The volume change induced by melting can thus be safely neglected. Heitz and Westwater (1970) presented a comparison of mathematical solutions with equal and unequal phase densities. In a configuration close to ours, they show that considering equal densities for ice and liquid water resulted in a negligible loss of accuracy.

2.4 Numerical methods

The system of partial differential equations (Eqs. 1-6) was solved by finite elements using the software Comsol Multiphysics version 6.0 (Galerkin method with quadratic Lagrangian elements, time discretization by implicit backward differentiation formula).

The mesh density close to the walls was refined due to the high gradient of velocity and a structured (mapped) mesh type was used for the water-ice domain as shown in Fig. 1-c. The mesh was validated by a sensitivity analysis comparing four different mesh qualities, with 14,000, 24,000, 32,000, and 47,000 elements, respectively. The difference in the results between the latter three cases was found to be insignificant. The mesh with 24,000 elements was thus selected in all simulations.

Regarding the numerical parameters required to model melting, we imposed ΔT=0.5 °C, A =1000 kg.m^{-3}.s^{-1} and $\varepsilon = 10^{-3}$. We checked that imposing ΔT = 0.3 °C or 0.7 °C did not significantly change the results (see Appendix A). The selected values of A and ε produced vanishingly small velocity fields in the ice with no deterioration of the solver stability.

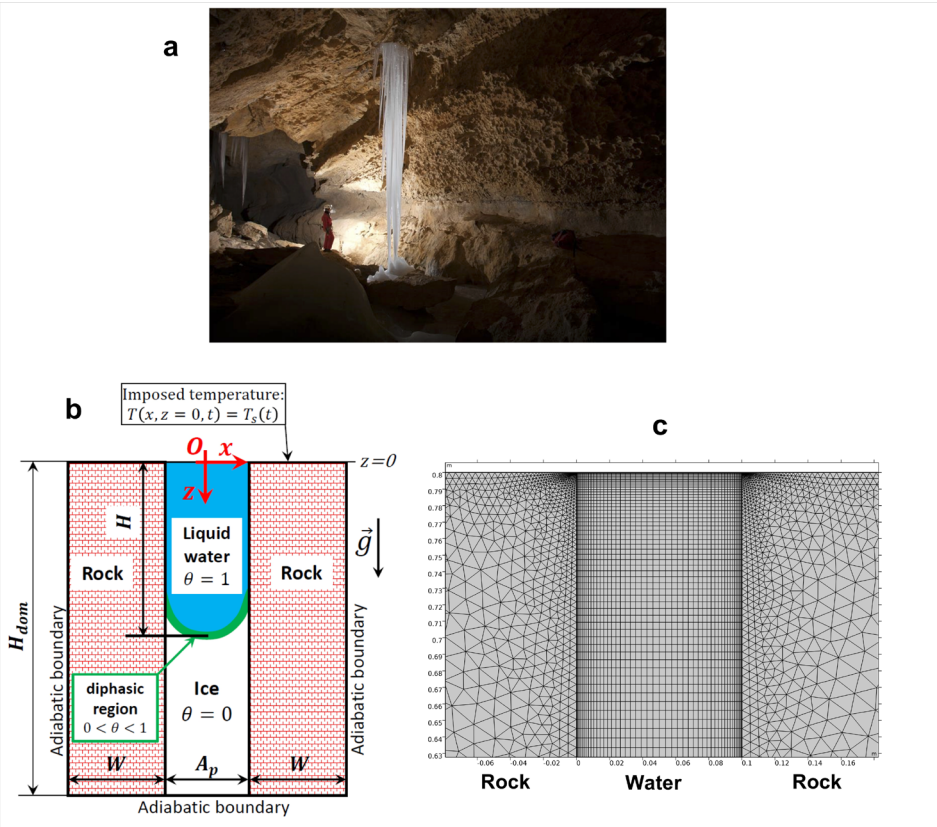

Figure 1. a) Pingouins cave, Switzerland, showing ice-filled clefts exposed on the cave roof (Photo courtesy A. Conne) b) Computational domain with external boundary conditions; 2 cm ≤ A_p ≤ 50 cm, H_{dom}=0.8 m and W_{dom}=1 m (the sketch is not at scale) c) Finite element mesh in the upper part of the computational domain.

Table 1. Thermal properties and numerical parameters. The liquid water properties are temperature dependent. The properties of ice and rock are assumed constant.

Thermal properties	values	Reference
ρ_s (kg/m³)	916.2	-
k_s (W/m/K)	2.22	-
$c_{p,s}$ (J/kg/K)	2050	-
ρ_l (kg/m³)	see Fig.2	(Comsol Multiphysics)
k_l (W/m/K)	0.556 at 0°C, 0.585 at 15°C	(Comsol Multiphysics)
$c_{p,l}$ (J/kg/K)	4216 at 0°C, 4192 at 15°C	(Comsol Multiphysics)
μ_l (mPa.s)	1.79 at 0°C, 1.43 at 7.5°C, 1.15 at 15°C	(Comsol Multiphysics)
ρ_r (kg/m³)	2320	(Covington et al., 2011)
k_r (W/m/K)	1.656	(Guerrier et al., 2019)
$c_{p,r}$ (J/kg/K)	810	(Covington et al., 2011)
L_m (J/kg)	334000	(Weast, 1986)

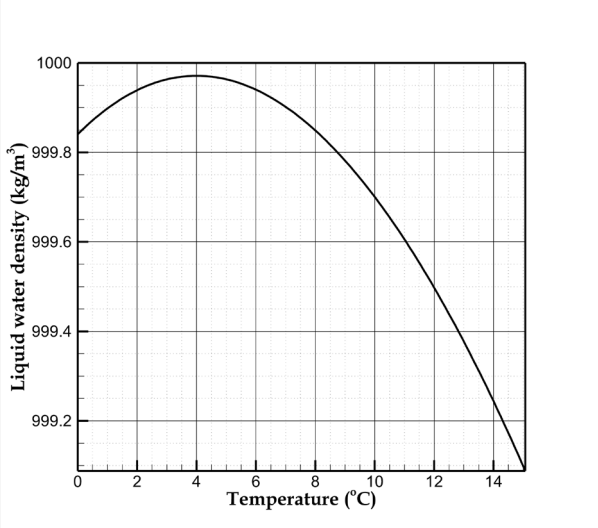

Figure 2. density of liquid water as a function of temperature (Comsol Multiphysics)

3. Model validation

The validity of our model is tested by comparison with two studies from the literature. A simple test case assuming stagnant liquid water (no free convection) was selected as a first step (numerical simulation of ice freezing by Kahraman et al., 1998). In a second step, our model was tested against experimental results including free convection (ice melting experiment by Virag et al., 2006).

3.1 Stagnant liquid water

When free convection is neglected, conduction and latent heat fluxes are the only mechanisms transferring heat in liquid water and ice. We compare our results with the results from (Kahraman et al., 1998). These authors developed a model to examine the heat transfer of ice melting inside a 20 cm×20 cm square assuming stagnant liquid water. A brief description of their conceptual model is given in Fig. 3-a. Ice is at an initial temperature of -30°C and is exposed to a temperature of 20 °C over half of the lower boundary ($0 \leq x \leq 10$ cm, $y = 0$ cm) and 70°C over the other half ($10 \leq x \leq 20$ cm, $y = 0$ cm). The temperature of the solid ice at the top boundary ($y = 20$ cm) is maintained at 0 °C and the other surfaces (left and right sides) are insulated (Fig. 3-a). Figure 3-b shows the temperature distribution after 5 hours modelled in the present work. Temperature profiles at x=4 cm and x=16 cm in different times of melting can be seen in Fig. 3-c and d, respectively. The result of our model is in good agreement with (Kahraman et al., 1998).

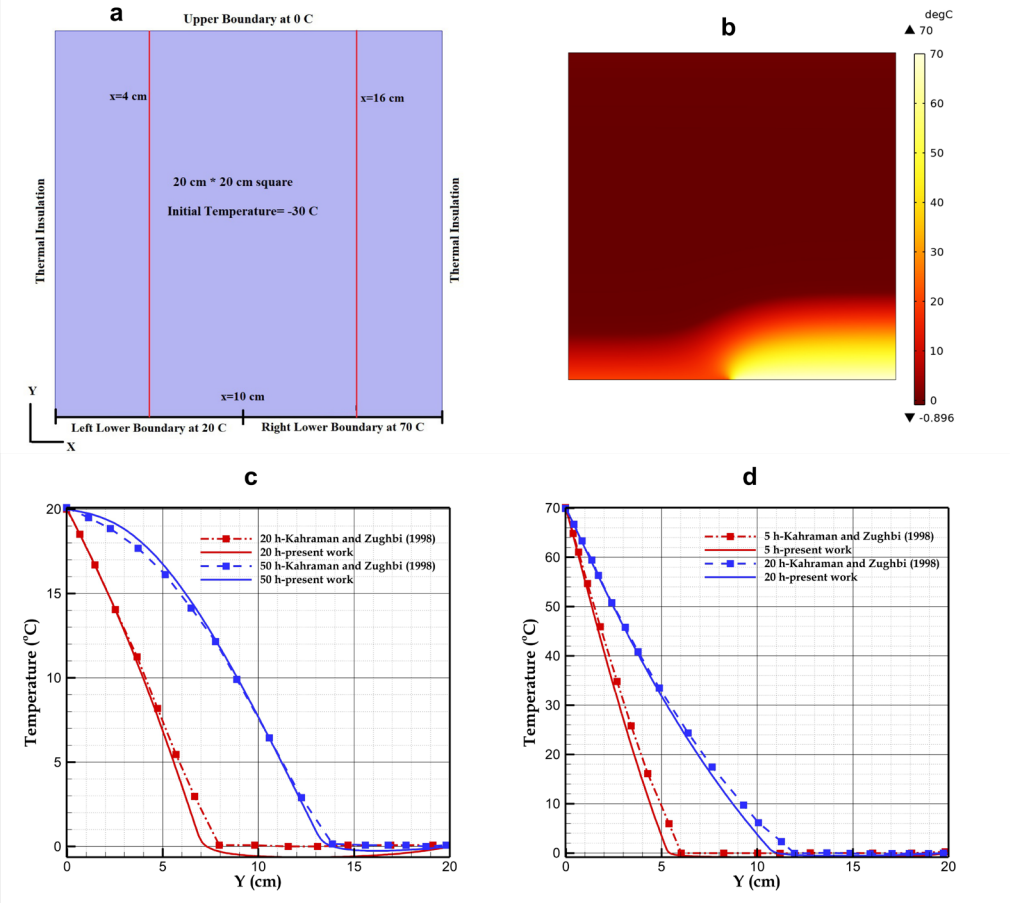

Figure 3. a) model geometry including initial and boundary conditions b) contour of temperature at t=5 hr c) temperature profile of ice and water at different times of ice melting at x=4 cm and d) x=16 cm

3.2 Free convection

Virag et al., (2006) investigated with an experimental approach the effect of free convection on ice melting inside a cavity shown in Fig. 4-a. The lower and top surfaces are thermally insulated. The left and right boundaries are at 0 and 8 °C, respectively. Figure 4-b displays contours of temperature (left) and the velocity field as well as velocity vectors (right) predicted by our model. The black arrows indicate the direction of the water flow. The model predicts the existence of two contra-rotating free convection cells separated by the 4°C isotherm, which corresponds to the maximum liquid water density. In the small cell located in the lower left corner, where temperature is higher than 4°C, the liquid rises upward along the warm wall, as expected when the liquid density is a decreasing function of temperature. In the bigger cell located in the upper part of the liquid region, where the temperature is less than 4°C, the warmer liquid moves downward, as expected when the liquid density increases with temperature. Furthermore, results show that where the temperature gradient is high, the magnitude of the local velocity increases. This is seen next to the left boundary and also close to the ice interface. The convection-induced mixing homogenizes the temperature in the liquid phase.

Our numerical model replicates the melting front positions measured at different times by Virag et al. (2006) (see Fig. 5). Although some discrepancies exist between the experiments and the numerical model, especially at the bottom of the cavity at the beginning of the simulation and in the upper part at later times, the overall performance of our model is suitable to represent the free convection cells and their effect on ice melting despite the simplifying assumptions made in the model (2D geometry, negligible volume contraction upon melting, smooth solid-liquid transition).

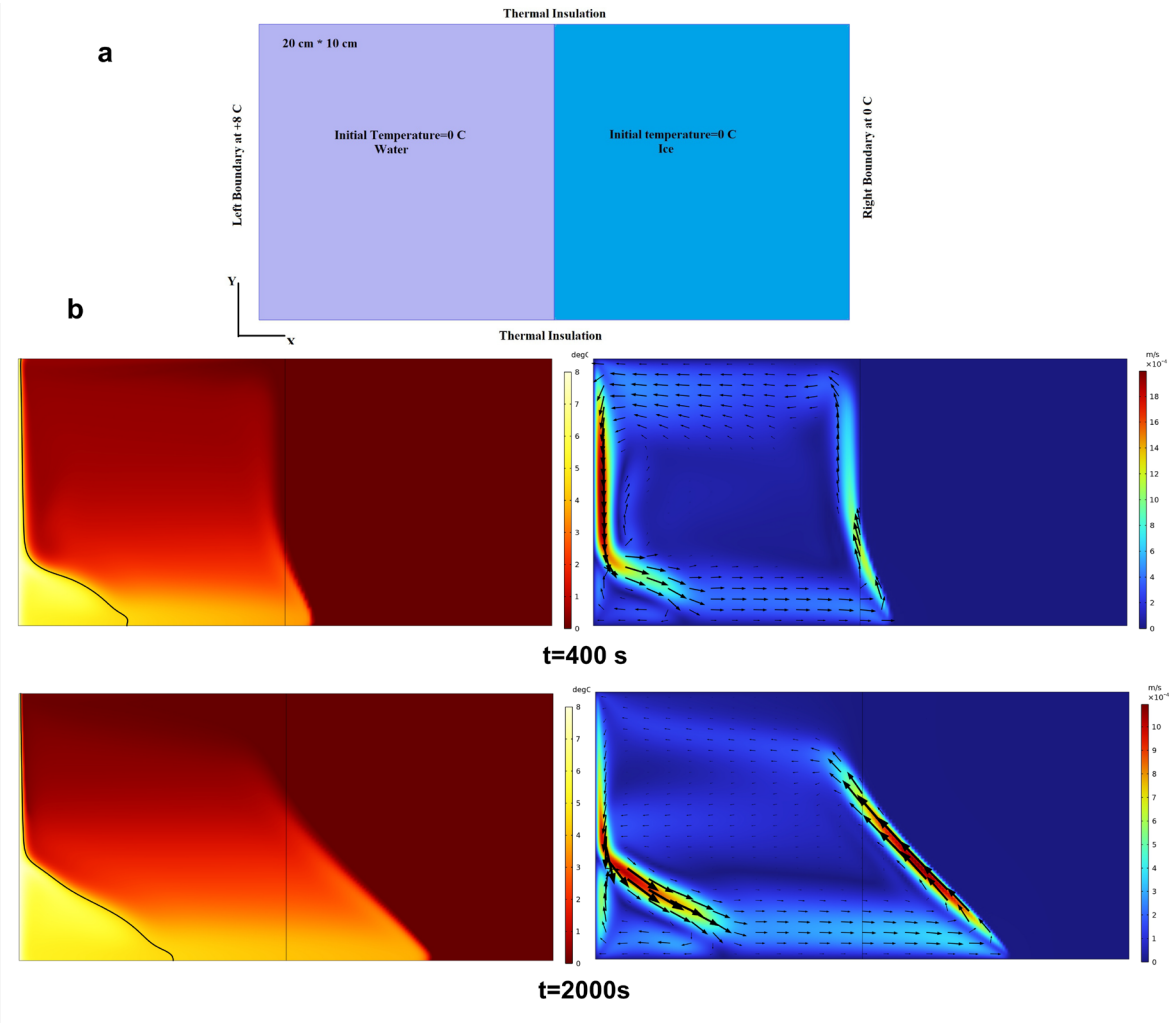

Figure 4. a) Computational domain including boundary and initial conditions in (Virag et al., 2006), b) results at times t=400 and 2000 s; left: temperature (the black line represents the isotherm T=4 °C); right: velocity magnitude.

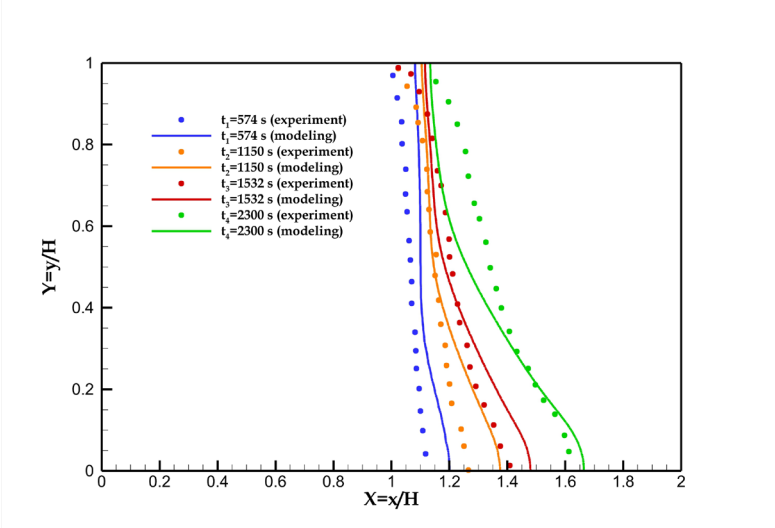

Figure 5. Evolution of the modeled ice-water interface during melting in comparison with experimental data by (Virag et al., 2006)

4. Results

4.1 Stagnant liquid water (SLW) versus free convection (FC)

The effect of free convection in heterogeneous, ice-filled karst environment (cf Fig. 1), where the medium is surrounded by rock and prone to atmospheric warming from the top surface was conceptualized in section-2. Here, we investigate the effect of free convection in more details considering two scenarios under identical thermal settings: 1) stagnant liquid water (SLW) and 2) free convection in liquid water (FC). Figure 6 illustrates the ice volume fraction $(1-\theta)$ for different time steps at 3, 6 and 9 hours for these two scenarios, for an aperture size A_p=10 cm (see Fig. 1-b for a description of the computational domain geometry). For each specified time step, the SLW results are shown on the left and the FC results on the right. The difference between these two scenarios in terms of melting rate is obvious. When convection is disregarded (SLW), the melting front is nearly horizontal except close to the walls, where a steep slope is observed. The higher thermal diffusivity of the rock ($\alpha_r = \frac{k_r}{\rho_r c_{p,r}} = 8.8 \times 10^{-7}\mathrm{m^2/s}$) compared to that of the liquid water ($\alpha_l = \frac{k_l}{\rho_l c_{p,l}} = 1.3 \times 10^{-7}\ \mathrm{m^2/s}$) results in faster heat propagation in the rock, and enhanced melting of the ice closer to the rock. When free convection is considered (FC), the advection of heat by the flow results in faster propagation of the melting front, with an inversion of its curvature (the meting front propagates faster in the center of the cleft than close to the walls).

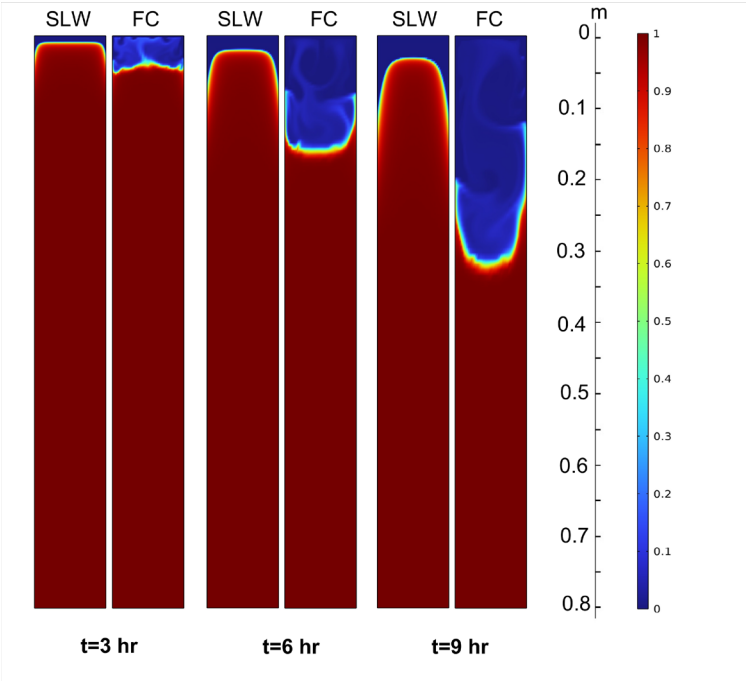

Figure 6. contour of the ice volume fraction $(1-\theta)$ for stagnant liquid water (SLW) and free convection (FC). A_p=10 cm, H_{dom}=0.8 m and W= 1 m.

Figure 7 displays the melting rate for both previous scenarios, SLW and FC. Because the initial temperature was -1 °C, the melting starts with c.1h delay, in both cases. Then the melting rate and the meltwater depth increase with time in response to the temperature increase at the top surface. After 9 hours, the melting rate is nearly an order of magnitude larger for FC (5.1 kg/s) than for SLW (0.6 kg/s). An animation file showing the evolution of the ice fraction can be found in the video supplement of the manuscript (Sedaghatkish and Luetscher, n.d.).

Figure 8 displays the temperature field of ice, water and surrounding rock after 9 hours. In FC case, most of the melted part of the cleft is in the temperature range from 0 to 1°C, with a high temperature gradient localized in a thin layer close to the ground surface (Fig. 8-b). In contrast, the temperature field in SLW case varies more evenly from the ground surface to the melting front (Fig. 8-a). This confirms that the circulation of water inside the cleft results in a thermal bridge between ice interface and top atmosphere. The extent of the mixing zone induced by FC can be much higher than the diffusion length in the case of SLW.

Figure-9 displays the left wall temperature as function of depth at different times for both scenarios. Although the melting rate for FC at t=3 hr is much higher than for SLW at the same time, their corresponding wall temperatures are close from each other. At larger times, the distinction between scenarios becomes more pronounced due to the increasing intensity of free convection.

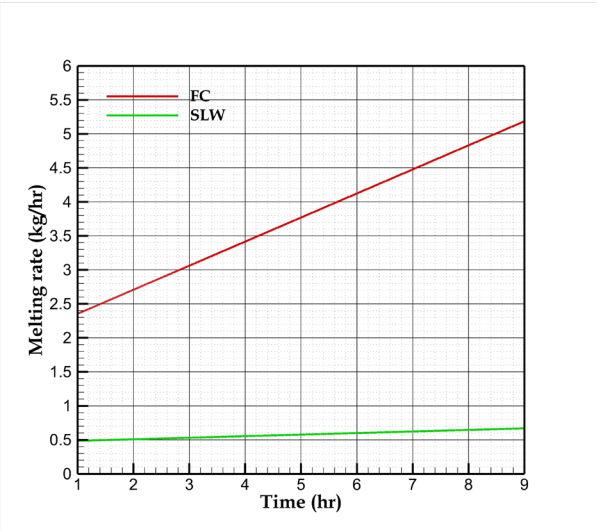

Figure 7. Melting rate versus time considering stagnant liquid water (SLW) and free convection (FC).

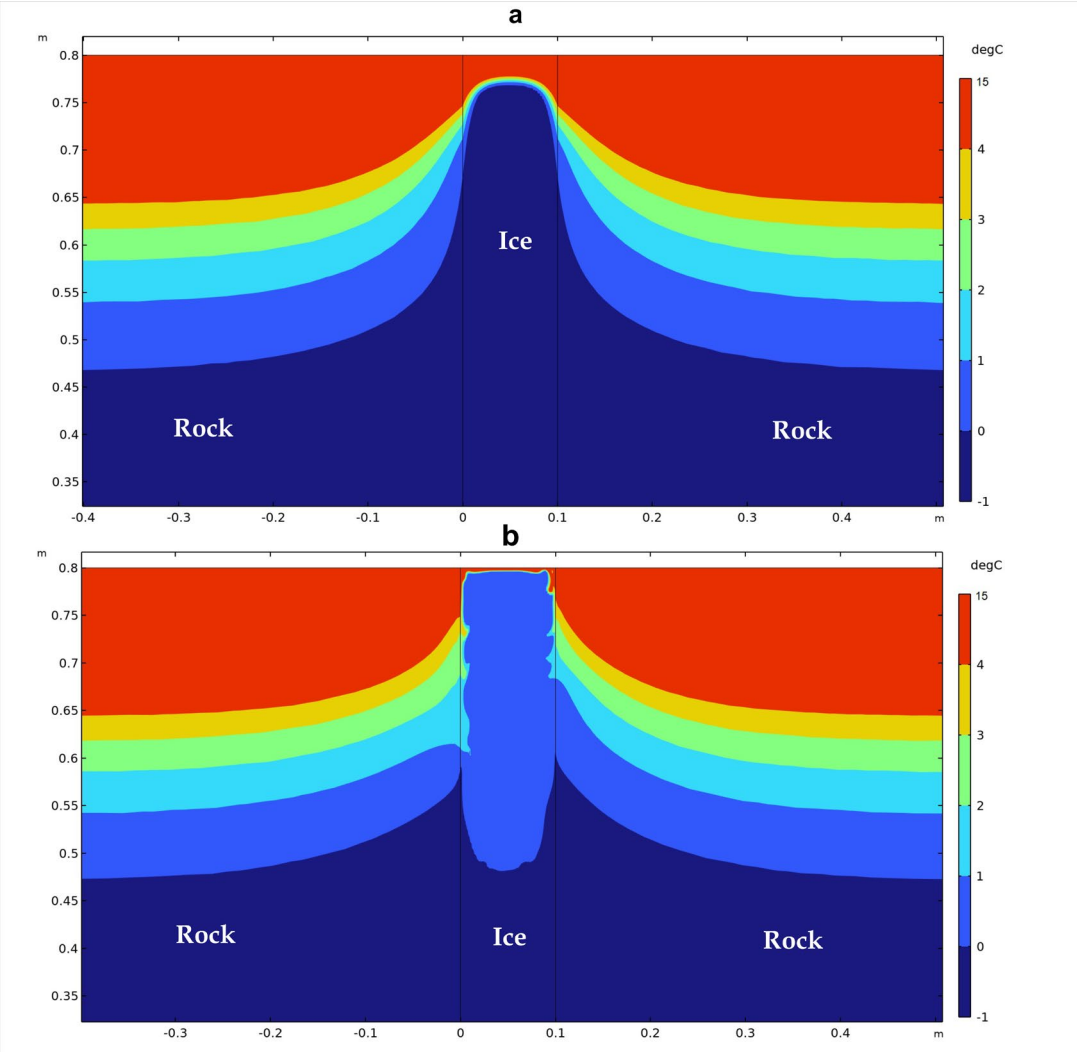

Figure 8. Temperature contour at t=9 hr for a) stagnant liquid water (SLW) and b) free convection (FC).

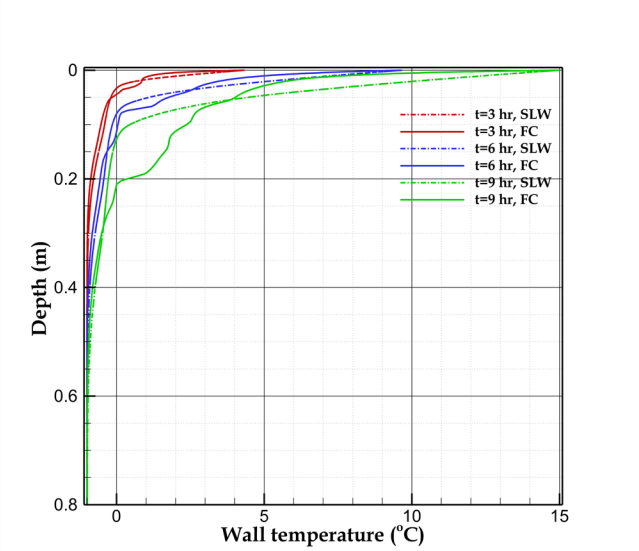

Figure 9. Left wall (rock-water interface) temperature as a function of depth) for stagnant liquid water (SLW) and free convection (FC).

Figure 10 displays the velocity magnitude as well as the flow in the water domain at different times. Vanishingly small velocity is predicted by the model wherever the water fraction is zero. Liquid water circulations generate a range of local velocities mixing the water and homogenizing the water temperature. As the melting of ice advances and the meltwater amount increases the velocity of water within the mixing zone increases, thereby accentuating the significance of free convective flux.

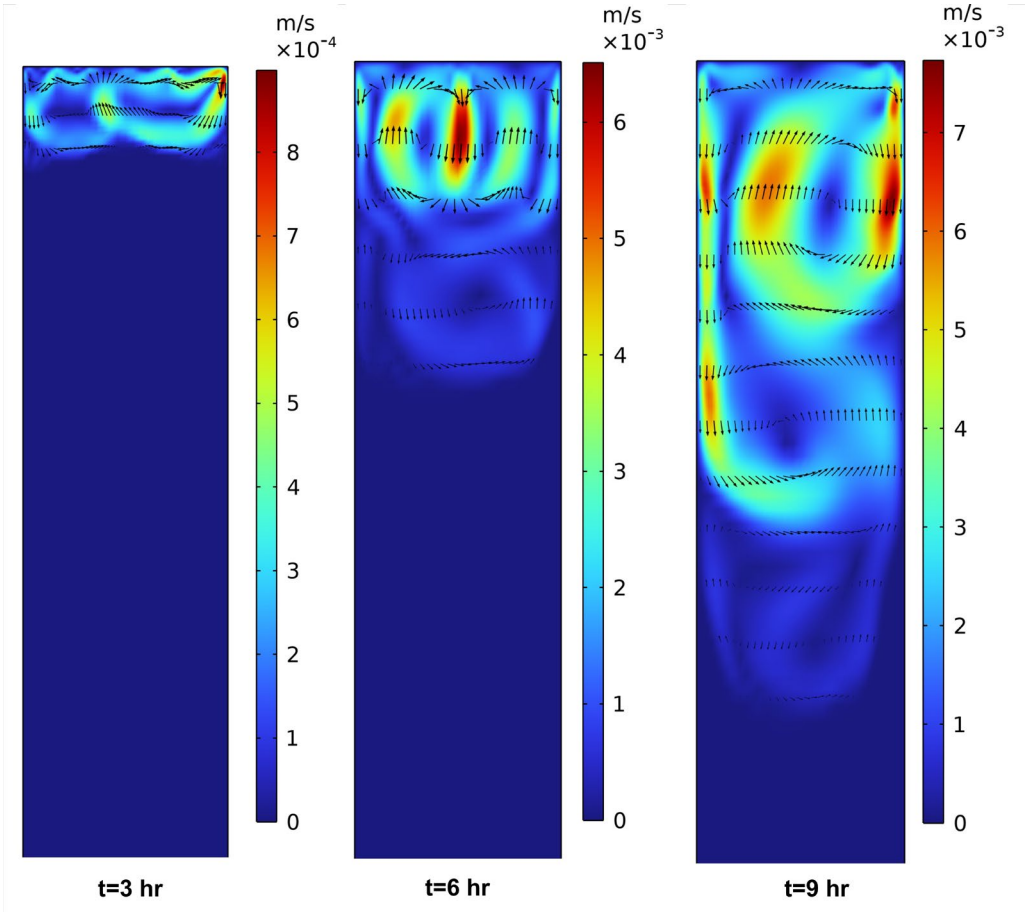

Figure 10. Velocity magnitude field in the upper 40 cm of the ice-cleft at different times. Zero velocity shows solid ice.

4.2 The effect of aperture size on melting rates

The cleft aperture determines the size of the domain and controls the initial ice mass. We considered the aperture sizes 2, 10, 20 and 50 cm in the parametric study. In order to remove the effect of cross-sectional area associated with different aperture sizes, we refer to the melting rate per unit of cross-sectional area (kg/hr/m^2).

Figure 11 illustrates the effect of the aperture size on the melting rate as a function of time. For the SLW case, heat transfer is mainly driven by diffusion in the rock, which has a greater diffusivity than water (see the temperature contour in Fig.8a). At a given depth, the rock is warmer than the water. The ice directly in contact with the rock thus melts faster. This explains the larger specific melting rate obtained with the smallest aperture (Ap=2 cm). In the presence of free convection, the melting rate after 9 hr is almost similar for the aperture sizes 2 and 10 cm (50 kg/hr/m^2). For greater aperture sizes, the effect of free convection becomes more significant, resulting in the increase of the melting rate, which reaches about 110 kg/hr/m^2 for 50 cm aperture size. Figure 11 shows that the melting rate considering free convection with a 2 cm aperture-size (50 kg/hr/m^2) is about twice the rate of the purely conduction case. For higher aperture sizes the difference in melting rates reaches about an order of magnitude.

In the present work, we simulated 9 hours of atmosphere temperature increase. When the aperture size A_p was varied from 2 to 50 cm, the liquid height H at the end of the simulation approximately ranged from 30 to 40 cm, and the convection cell occupied the entire liquid domain. However, the liquid height reached after 9 hours is only a small part of the actual height of the cleft (commonly up to 10 m). H is expected to increase if longer times are considered. The question arises whether the free convection cells always fill the entire liquid domain at longer times, despite the increase of friction due to lower aspect ratio A_p/H. If the convection cell occupies only a part of the cavity, the efficiency of heat transfer between the ground surface and the melting front will be reduced. The significance of free convection can be assessed from the value of the dimensionless Rayleigh number

$$Ra = \frac{g\beta(T_c - T_H)H^3}{\alpha_l \, \nu_l} \tag{15}$$

where $(T_c\text{-}T_H)$ is the temperature difference between bottom and top surfaces, $\alpha_l = k_l/(\rho_l c_{pl})$ and $\nu_l = \mu_l/\rho_l$ are the liquid water diffusivity and kinematic viscosity, respectively. Ra represents the ratio of the diffusion time over the free convection time ($Ra \sim 10^8$ in the numerical experiments presented in this article). In a cavity with infinite lateral dimensions (i.e., for $A_p/H \to \infty$) , free convection is triggered for $Ra \gtrsim 10^3$ (otherwise, the conductive state is stable, see Bergman et al., (2017) for more information about the Rayleigh-Bénard instability). However, in the confined geometry considered in this work, the presence of the vertical walls must be considered. Rohsenow et al (1998) provide the following condition for convection onset, which takes into account the stabilizing effect of the vertical walls for $A_p \ll H$, in the limiting case of perfectly conducting walls:

$$Ra \gtrsim 10^2 \times \left(\frac{H}{A_p}\right)^4 \tag{16}$$

Injecting Eq.(15) in Eq.(16) yields the maximum value of the liquid height H for which the free convection cell extends from the ground surface to the melting front:

$$H \lesssim 10^{-2} \times \frac{g\beta(T_c - T_H){A_p}^4}{\alpha_l \, \nu_l} \tag{17}$$

Considering that the liquid region at temperature T > 4°C is stable and that the isotherm 4°C is close to the top of the cleft when the free convection cell fills the entire cavity (see Fig. 8-b), we get $(T_c\text{-}T_H)$ =-4°C. Using the physical properties from section 2.3 and $A_p = 2$ cm (the minimum aperture size considered in this study) yields $H \lesssim$ 10 m, which is also the order of magnitude of the maximum cleft height. Therefore, free convection cells should always extend throughout the melted region for $A_p \gtrsim$ 2 cm. Note that the assumption of perfectly conducting walls used in Eq.(16) is less favorable to convection than finite conductivity (Rohsenow et al, 1998). Eq.(17) is thus

expected to underestimate the higher bound of *H* corresponding to fully developed free convection cells.

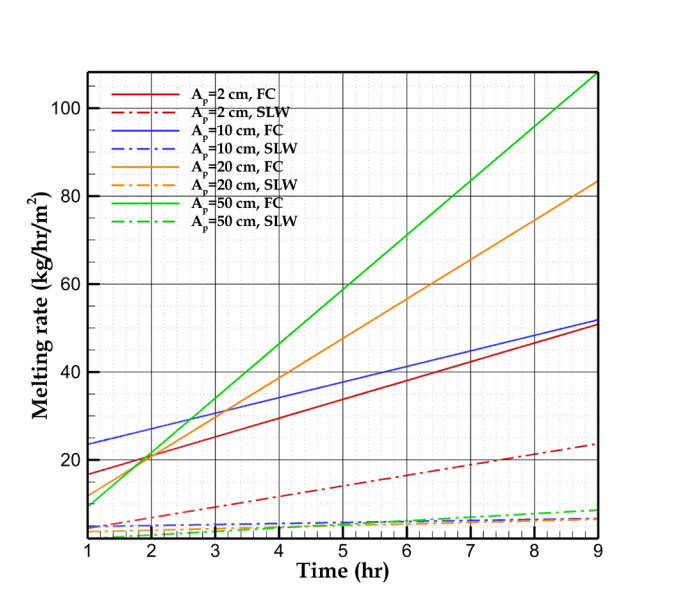

Figure 11. Effect of the aperture size on the melting rate for stagnant liquid water (SLW) and free convection (FC)

4.3 Application to field observations

The model is applied to a case-study from Monlesi ice cave, Switzerland (Luetscher et al., 2008). The main purpose is to qualitatively compare the field data with the model output and test how the pure conduction model can treat these problems.

Monlesi ice cave is a low-elevation sporadic mountain permafrost site controlled by a peculiar ventilation regime associated with multiple cave entrances located at a similar elevation (Luetscher et al., 2008). The c. 600 m^2 cave chamber is partly filled with perennial congelation ice fed by a number of vertical clefts with width ranging from 10^1 to 10^3 mm. Seasonal freezing seals them periodically hindering any further water drainage from the epikarst (Fig. 12-a). The vertical distance between the external ground surface and the cave ceiling reaches c. 20 m. Seasonal and daily outside temperature fluctuations thaw the ice and freeze the meltwater in these rock clefts.

The main cleft (subcutaneous flow) was instrumented to measure discharge rates at 30 min intervals using a pressure probe set at the bottom of a 1 m long perforated PVC tube capturing the inlet. The water height measured in the tube is converted to discharge (Q, in l/min) with an empirically calibrated rating curve checked by nine manual "bucket gauging" between 0 and 13 l/min with an uncertainty of ±10% (Luetscher et al., 2008).

Cave air temperatures were measured using negative temperature coefficient thermistors with a resistance of c.29.5 kOhm at 0°C and a temperature coefficient of about 5% °C-1 (YSI 44006). The thermistors were calibrated in a bath of melting ice to

an accuracy of ±0.1°C. The thermistors were spaced at 2 m intervals in two chains comprising 19 sensors dispatched in the main cave chamber (Luetscher et al., 2008). Air temperatures were recorded at 1 h intervals and logged externally on a Campbell CR10X data logger with two multiplexer logging units.

Figure 12-b displays the atmosphere and the soil temperature at 10 cm depth during 4.5 days (from April 13 to 17). No rainfall is recorded during this time period and the surface is free of snow. The soil temperature increases with a regular trend between 0 and 5 °C and is noticeably attenuated compared to atmosphere temperature fluctuations. The cave temperature is almost constant around -1 °C implying there is no melting from the bottom of the ice cleft. The atmosphere daily temperature variation induces a water flow rate (0-12 l/min) with a trend similar to the surface temperature, supporting an origin associated with melting process of ice-filled clefts surrounding the cave.

To assess the melting rate, we considered the same conceptual model as in Fig. 1. A linear temperature rise from 0 to 5 °C during 4.5 days was assumed at the top boundary (black dash-dotted line in Fig. 12-b). This temperature rise is similar to the temperature evolution measured in the soil (solid black line in Fig.12b). In contrast to our model, meltwater drains deeper into the subsurface. The uncertainty about the cleft geometry is, however, very high and we do not know how many fissures feed this water inlet. While our conceptual model is based on a closed cavity for the ease of simulation, the ice-filled cleft can be connected to a network of partially saturated smaller clefts (as in the epikarst) which drain the meltwater to the main vertical inlet at the top wall of Monlesi cave. Eventually, our simplified 2D geometry only approaches the real 3D-environment since other convection cells emerge along the cavity width which cannot be modeled in 2D.

A rough estimate of the cavity geometry (computational domain) assumes an initial ice-filled cleft with 3 meters depth (H_{dom}=3 m),10 cm aperture size (A_p=10 cm) and a typical length in the order of 1 m. The modelled melting rate is in the same order of magnitude as the water flow rate measured in the cave (red dash-dotted in Fig. 12-b). A purely conduction-based model underestimates the melting rate by >1 order of magnitude as compared to the case considering free convection (dashed in Fig. 12-b).

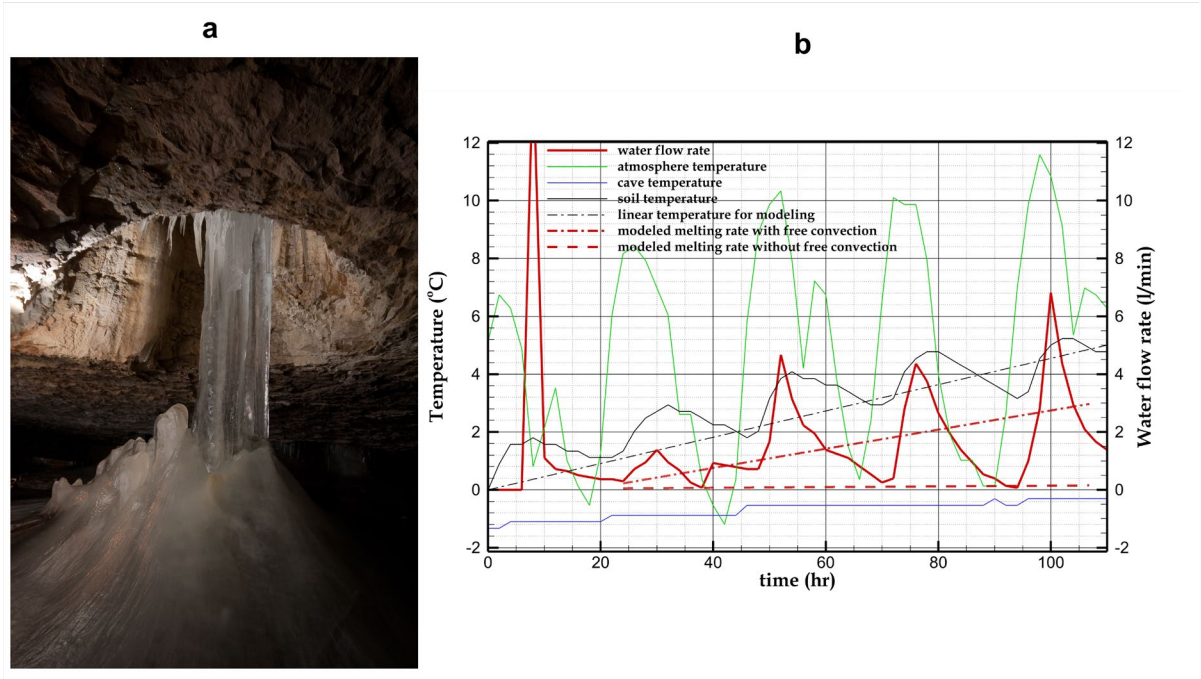

Figure 12. a) ice filled cleft in Monlesi cave b) field data including atmosphere (green), the soil (black) and cave temperature (blue) as well as the water flow rate measured at the fissure outlet (red) in Monlesi cave. The modelled melting rate considering free convection (red dashed dotted line) is compared to a case including only heat conduction (red dashed lines).

5. Discussion

In this study, we assumed a constant aperture size for modeling ice melt at daily time scale, but it should be noted that in the long-term, the repeated freeze-thaw cycles can deteriorate the hostrock clefts due to propagation and coalescence of older ones. Maji and Murton (Maji and Murton, 2021) investigated the mechanism and transition of microcracking and macrocracking during freezing and thawing and developed a statistical modeling of crack propagation dynamics based on tension and shearing.

Our results show that, under similar thermal configurations, conduction may not be the principal heat flux and permafrost degradation in heterogenous and ice-rich media may be much faster than anticipated. This is particularly relevant at high-elevation where a clear relationship is observed between rockfall activity and permafrost thawing (Gruber et al., 2004; Ravanel and Deline, 2011; Savi et al., 2021; Morino et al., 2021). In karst systems and fractured aquifers, where secondary porosity is exceptionally well developed, frozen conduits/fractures may all of a sudden drain water into depth and change the local hydrological regime leading a thermal anomaly within the surrounding permafrost (Phillips et al., 2016). The subsequent freeze-thaw processes may lead to the precipitation of so-called cryogenic cave calcites (Žák et al., 2018), a secondary mineral precipitate increasingly used as proxy for paleo-permafrost conditions (Spötl et al., 2021; Töchterle et al., 2023). In contrast to purely conductive systems, our results support a model where rapid hydrological recharge, e.g. due to extreme rainfall events, may accelerate the thawing of mountain permafrost

(Luetscher et al., 2013) and thus questions classical interpretations for the formation of cryogenic calcites. But also at shallower depth, acknowledging the potential role of convective heat fluxes in ice-rich permafrost degradation may help predicting the rate of greenhouse gas releases, mainly carbon dioxide and methane, due to the decomposition of formerly frozen organic matter (Schaefer et al., 2014; Schuur et al., 2015). The intensity of free convection in soil depends strongly on the Rayleigh number which in turns depends on the permeability and dimensions of soil layer making it negligible, e.g. (Kane et al., 2001) or significant, e.g. (Jazi et al., 2024) with respect to the total heat transfer.

Pure water with a melting point at 0°C was considered in the present study. However, limestone dissolution results in the mineralization of the meltwater. Consequences are twofold: (1) the melting point is shifted to lower temperatures (in the range from -4 °C to 0 °C, see Tubini et al. (2021); McKenzie et al. (2007); Rühaak et al. (2015); (2) the variation of density with salt concentration could impact buoyancy, resulting in different flow patterns (thermo-solutal convection, see for instance Mergui et al., 2002). The significance of the liquid phase composition could be assessed by numerical simulations, and should be considered in future works.

We did not consider any drainage of air or water inside the cleft or in its immediate vicinity. Forced convection induced by drainage could also contribute to the formation of a thermal bridge between the ground surface and the melting front, as suggested by Hasler et al., (2011). More work coupling field observations with numerical simulations including forced and free convection will be necessary to assess their relative significance, and determine the conditions under which one or the other effect dominates heat transfer.

6. Conclusion

A quantification of the melting rate of ice-rich permafrost in heterogeneous media is essential to assess the speed of permafrost degradation. Our model relies on a 2D approach coupling free convection (buoyancy-driven flow) in a vertical cleft with conduction in the surrounded homogeneous rock. Increasing the temperature of the ground surface can generate free convection cells because water-density increases between 0 and 4°C (a property specific to water). The convection cells generate a thermal bridge between the atmosphere and the melting front, resulting in the formation of a mixing zone with quasi-uniform temperature in the water column. This dramatically enhances the melting rate of interstitial ice when compared to models assuming stagnant liquid water (about an order of magnitude after 9 hours for an aperture size of 10 cm). In contrast to scenarios assuming conduction in stagnant liquid water, for which the temperature signal from the atmosphere is fully attenuated beyond a certain distance known as the diffusion length, the presence of free convection extends over greater distances. This thermal penetration also exerts an influence on the surrounding rock. Despite simplifying assumptions in the model and many uncertainties about the cleft geometry and the measured water flow rate,

melting rate predicted by a model including free convection fit the order of magnitude measured in Monlesi cave (Fig. 12).

The significance of free convection should also be estimated in similar thermal configurations with different geometries such as cylindrical conduits or 3D cavities. Furthermore, the effect of free convection is not limited to hourly or daily oscillations and can be studied over much longer timescales, including centennial to millennial fluctuations. Currently, the computational costs are the main barriers for including free convection in long-term simulations. The full coupling of the momentum and energy equations requires the time steps being much smaller compared to simple conduction-based models. Further investigations are thus ongoing to reformulate the governing equations and simplifying them for simulations over longer time-scales. Moreover, refreezing processes have yet to be considered to fully represent the long-term evolution of such a system.

Eventually, the effect of water free convection on ice melting rate is not limited to permafrost regions. For instance, the melting of icebergs can also be impacted by water free convection (Couston et al., 2021; Hester et al., 2021) increasing production of freshwater in oceans with potential impacts on the climate at global scale.

Appendix A. Sensitivity of the model to the melting temperature range ΔT.

The sensitivity of the melting rate to the melting temperature range ΔT is displayed in Fig.A1. Similar results are obtained for $\Delta T \leq \pm 0.7°C$. $\Delta T \leq \pm 0.5°C$ was thus selected in all simulations, as a value giving a good approximation of the pure water melting rate.

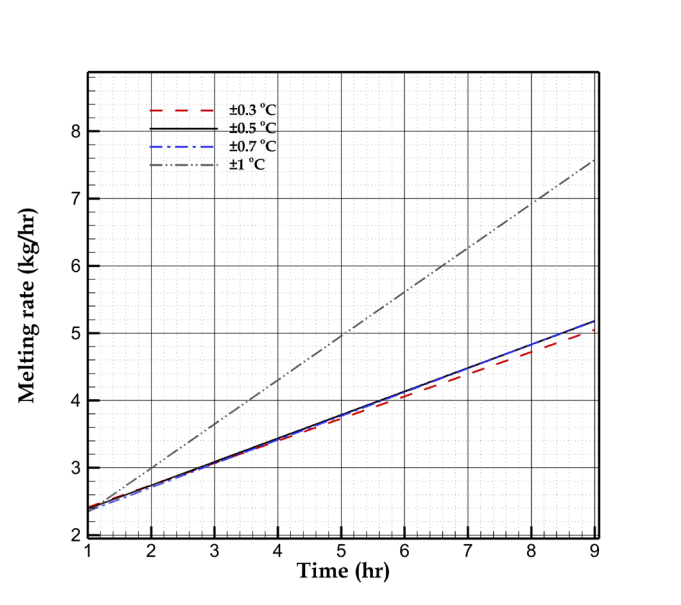

Figure A1. Effect of the melting temperature range ΔT on the melting rate predicted by the model (FC case, A_p=10 cm, H_{dom}=0.8 m, W_{dom}= 1 m .)

Software availability. The Comsol file (closed source software) is available upon request.

Video supplement. The animations of ice fraction evolution are available at https://doi.org/10.5281/zenodo.8435168.

Author contributions. AS completed the modelling work and wrote the original manuscript. ML designed the study together with AS and contributed with field data from Monlesi ice cave. All authors discussed the results and contributed to the final edition of the paper.

Competing interests. The authors declare that they have no competing interests.

Acknowledgements. This project is supported by the Swiss National Science Foundation (project n°200021_188636).

Reference

Andresen, C. G., Lawrence, D. M., Wilson, C. J., McGuire, A. D., Koven, C., Schaefer, K., Jafarov, E., Peng, S., Chen, X., and Gouttevin, I.: Soil moisture and hydrology projections of the permafrost region– a model intercomparison, Cryosph., 14, 445–459, 2020.

Arosemena, A.: Numerical Model of MeltingProblems, 2018.

Bartelt, P. and Lehning, M.: A physical SNOWPACK model for the Swiss avalanche warning: Part I: numerical model, Cold Reg. Sci. Technol., 35, 123–145, 2002.

Bartolomé, M., Cazenave, G., Luetscher, M., Spötl, C., Gázquez, F., Belmonte, Á., Turchyn, A. V., López-Moreno, J. I., and Moreno, A.: Mountain permafrost in the Central Pyrenees: insights from the Devaux ice cave, Cryosph., 17, 477–497, 2022.

Bejan, A.: Convection heat transfer, John wiley & sons, 2013.

Bense, V. F., Kooi, H., Ferguson, G., and Read, T.: Permafrost degradation as a control on hydrogeological regime shifts in a warming climate, J. Geophys. Res. Earth Surf., 117, 2012.

Bergman, T. L., Lavine, A. S., Incropera, F. P., and DeWitt, D. P.: Fundamentals of Heat and Mass Transfer, Wiley, 2017.

Bourdillon, A. C., Verdin, P. G., and Thompson, C. P.: Numerical simulations of water freezing processes in cavities and cylindrical enclosures, Appl. Therm. Eng., 75, 839–855, 2015.

Caggiano, A., Mankel, C., and Koenders, E.: Reviewing theoretical and numerical models for PCM-embedded cementitious composites, Buildings, 9, 3, 2018.

Cheng, G.: A roadbed cooling approach for the construction of Qinghai–Tibet Railway, Cold Reg. Sci. Technol., 42, 169–176, 2005.

Cicoira, A., Beutel, J., Faillettaz, J., Gärtner-Roer, I., and Vieli, A.: Resolving the influence of temperature forcing through heat conduction on rock glacier dynamics: a numerical modelling approach, Cryosph., 13, 927–942, 2019.

Colucci, R. R. and Guglielmin, M.: Climate change and rapid ice melt: Suggestions from abrupt permafrost degradation and ice melting in an alpine ice cave, Prog. Phys. Geogr. Earth Environ., 43, 561–573, 2019.

Comsol Multiphysics: v. 6.1 www. comsol. com COMSOL AB, Stockholm, Sweden.

Couston, L.-A., Hester, E., Favier, B., Taylor, J. R., Holland, P. R., and Jenkins, A.: Topography generation by melting and freezing in a turbulent shear flow, J. Fluid Mech., 911, A44, 2021.

Covington, M. D., Luhmann, A. J., Gabrovšek, F., Saar, M. O., and Wicks, C. M.: Mechanisms of heat exchange between water and rock in karst conduits, Water Resour. Res., 47, 2011.

Duvillard, P.-A., Ravanel, L., Schoeneich, P., Deline, P., Marcer, M., and Magnin, F.: Qualitative risk assessment and strategies for infrastructure on permafrost in the French Alps, Cold Reg. Sci. Technol., 189, 103311, 2021.

Fabre, C., Sauvage, S., Tananaev, N., Srinivasan, R., Teisserenc, R., and Sánchez Pérez, J. M.: Using modeling tools to better understand permafrost hydrology, Water, 9, 418, 2017.

Fohlmeister, J., Luetscher, M., Spötl, C., Schröder-Ritzrau, A., Schröder, B., Frank, N., Eichstädter, R., Trüssel, M., Skiba, V., and Boers, N.: The role of Northern Hemisphere summer insolation for millennial-scale climate variability during the penultimate glacial, Commun. Earth Environ., 4, 245, 2023.

Ford, D. and Williams, P. D.: Karst hydrogeology and geomorphology, John Wiley & Sons, 2007.

Fortier, R., LeBlanc, A.-M., and Yu, W.: Impacts of permafrost degradation on a road embankment at Umiujaq in Nunavik (Quebec), Canada, Can. Geotech. J., 48, 720–740, 2011.

Galushkin, Y.: Numerical simulation of permafrost evolution as a part of sedimentary basin modeling: permafrost in the Pliocene–Holocene climate history of the Urengoy field in the West Siberian basin, Can. J. Earth Sci., 34, 935–948, 1997.

Gruber, S., Hoelzle, M., and Haeberli, W.: Permafrost thaw and destabilization of Alpine rock walls in the hot summer of 2003, Geophys. Res. Lett., 31, 2004.

Guerrier, B., Doumenc, F., Roux, A., Mergui, S., and Jeannin, P.-Y.: Climatology in shallow caves with negligible ventilation: Heat and mass transfer, Int. J. Therm. Sci., 146, 106066, 2019.

Guyon, E., Hulin, J. P., Petit, L., and Mitescu, C. D.: Physical hydrodynamics, Oxford university press, 2015.

Haberkorn, A., Kenner, R., Noetzli, J., and Phillips, M.: Changes in ground temperature and dynamics in mountain permafrost in the Swiss Alps, Front. Earth Sci., 9, 626686, 2021.

Haeberli, W., Schaub, Y., and Huggel, C.: Increasing risks related to landslides from degrading permafrost into new lakes in de-glaciating mountain ranges, Geomorphology, 293, 405–417, 2017.

Hasler, A., Gruber, S., Font, M., and Dubois, A.: Advective heat transport in frozen rock clefts: Conceptual model, laboratory experiments and numerical simulation, Permafr. Periglac. Process., 22, 378–389, 2011.

Hayward, J. L., Jackson, A. J., Yost, C. K., Hansen, L. T., and Jamieson, R. C.: Fate of antibiotic resistance genes in two Arctic tundra wetlands impacted by municipal wastewater, Sci. Total Environ., 642, 1415–1428, 2018.

Heitz, W. L. and Westwater, J. W.: Extension of the numerical method for melting and freezing problems, Int. J. Heat Mass Transf., 13, 1371–1375, 1970.

Hester, E. W., McConnochie, C. D., Cenedese, C., Couston, L.-A., and Vasil, G.: Aspect ratio affects iceberg melting, Phys. Rev. Fluids, 6, 23802, 2021.

Hornum, M. T., Hodson, A. J., Jessen, S., Bense, V., and Senger, K.: Numerical modelling of permafrost spring discharge and open-system pingo formation induced by basal permafrost aggradation, Cryosph., 14, 4627–4651, 2020.

Huss, M., Farinotti, D., Bauder, A., and Funk, M.: Modelling runoff from highly glacierized alpine drainage basins in a changing climate, Hydrol. Process., 22, 3888–3902, 2008.

Ivanov, V. and Rozhin, I.: Numerical simulation of the permafrost thawing near the city of Yakutsk during climate change up to the year 2100, in: AIP Conference Proceedings, 20050, 2022.

Jafarov, E. E., Marchenko, S. S., and Romanovsky, V. E.: Numerical modeling of permafrost dynamics in Alaska using a high spatial resolution dataset, Cryosph., 6, 613–624, 2012.

Jazi, F. N., Ghasemi-Fare, O., and Rockaway, T. D.: Natural convection effect on heat transfer in saturated soils under the influence of confined and unconfined subsurface flow, Appl. Therm. Eng., 237, 121805, 2024.

Jin, X.-Y., Jin, H.-J., Iwahana, G., Marchenko, S. S., Luo, D.-L., Li, X.-Y., and Liang, S.-H.: Impacts of climate-induced permafrost degradation on vegetation: A review, Adv. Clim. Chang. Res., 12, 29–47, 2021.

Kahraman, R., Zughbi, H. D., and Al-Nassar, Y. N.: A numerical simulation of melting of ice heated from above, Math. Comput. Appl., 3, 127–137, 1998.

Kane, D. L., Hinkel, K. M., Goering, D. J., Hinzman, L. D., and Outcalt, S. I.: Non-conductive heat transfer associated with frozen soils, Glob. Planet. Change, 29, 275–292, 2001.

Krumhansl, K. A., Krkosek, W. H., Greenwood, M., Ragush, C., Schmidt, J., Grant, J., Barrell, J., Lu, L., Lam, B., and Gagnon, G. A.: Assessment of Arctic community wastewater impacts on marine benthic invertebrates., Environ. Sci. Technol., 49, 760–766, 2015.

Larsen, P. H., Goldsmith, S., Smith, O., Wilson, M. L., Strzepek, K., Chinowsky, P., and Saylor, B.: Estimating future costs for Alaska public infrastructure at risk from climate change, Glob. Environ. Chang., 18, 442–457, 2008.

Luetscher, M., Lismonde, B., and Jeannin, P.: Heat exchanges in the heterothermic zone of a karst system: Monlesi cave, Swiss Jura Mountains, J. Geophys. Res. Earth Surf., 113, 2008.

Luetscher, M., Borreguero, M., Moseley, G. E., Spötl, C., and Edwards, R. L.: Alpine permafrost thawing during the Medieval Warm Period identified from cryogenic cave carbonates, Cryosph., 7, 1073–1081, 2013.

Luetscher, M., Boch, R., Sodemann, H., Spötl, C., Cheng, H., Edwards, R. L., Frisia, S., Hof, F., and Müller, W.: North Atlantic storm track changes during the Last Glacial Maximum recorded by Alpine speleothems, Nat. Commun., 6, 6344, 2015.

Maji, V. and Murton, J. B.: Experimental observations and statistical modeling of crack propagation dynamics in limestone by acoustic emission analysis during freezing and thawing, J. Geophys. Res. Earth Surf., 126, e2021JF006127, 2021.

Malakhova, V. V: Numerical modeling of methane hydrates dissociation in the submarine permafrost, in: IOP Conference Series: Earth and Environmental Science, 12022, 2022.

Marchenko, S., Romanovsky, V., and Tipenko, G.: Numerical modeling of spatial permafrost dynamics in Alaska, in: Proceedings of the ninth international conference on permafrost, 1125–1130, 2008.

McKenzie, J. M., Voss, C. I., and Siegel, D. I.: Groundwater flow with energy transport and water–ice phase change: numerical simulations, benchmarks, and application to freezing in peat bogs, Adv. Water Resour., 30, 966–983, 2007.

Mergui, S., Geoffroy, S., and Be´ nard, C.: Ice block melting into a binary solution: Coupling of the interfacial equilibrium and the flow structures, J. Heat Transf., 124, 1147–1157, 2002.

Michałek, T. and Kowalewski, T. A.: Simulations of the water freezing process–numerical benchmarks, Task Q., 7, 389–408, 2003.

Mohammed, A. A., Bense, V. F., Kurylyk, B. L., Jamieson, R. C., Johnston, L. H., and Jackson, A. J.: Modeling reactive solute transport in permafrost-affected groundwater systems, Water Resour. Res., 57, e2020WR028771, 2021.

Morino, C., Conway, S. J., Balme, M. R., Helgason, J. K., Sæmundsson, Þ., Jordan, C., Hillier, J., and Argles, T.: The impact of ground-ice thaw on landslide geomorphology and dynamics: two case studies in northern Iceland, Landslides, 18, 2785–2812, 2021.

Mousavi Ajarostaghi, S. S., Poncet, S., Sedighi, K., and Aghajani Delavar, M.: Numerical modeling of the melting process in a shell and coil tube ice storage system for air-conditioning application, Appl. Sci., 9, 2726, 2019.

Nazzi Ehms, J. H., De Césaro Oliveski, R., Oliveira Rocha, L. A., Biserni, C., and Garai, M.: Fixed grid numerical models for solidification and melting of phase change materials (PCMs), Appl. Sci., 9, 4334, 2019.

Noetzli, J., Arenson, L. U., Bast, A., Beutel, J., Delaloye, R., Farinotti, D., Gruber, S., Gubler, H., Haeberli, W., and Hasler, A.: Best practice for measuring permafrost temperature in boreholes based on the experience in the Swiss Alps, Front. Earth Sci., 9, 607875, 2021.

Painter, S. L., Coon, E. T., Atchley, A. L., Berndt, M., Garimella, R., Moulton, J. D., Svyatskiy, D., and Wilson, C. J.: Integrated surface/subsurface permafrost thermal hydrology: Model formulation and proof-of-concept simulations, Water Resour. Res., 52, 6062–6077, 2016.

Pelletier, M., Allard, M., and Levesque, E.: Ecosystem changes across a gradient of permafrost degradation in subarctic Québec (Tasiapik Valley, Nunavik, Canada), Arct. Sci., 5, 1–26, 2018.

Pham, H.-N., Arenson, L. U., and Sego, D. C.: Numerical analysis of forced and natural convection in waste-rock piles in permafrost environments, in: Proceedings of the Ninth International Conference on Permafrost, 2008.

Phillips, M., Haberkorn, A., Draebing, D., Krautblatter, M., Rhyner, H., and Kenner, R.: Seasonally intermittent water flow through deep fractures in an Alpine Rock Ridge: Gemsstock, Central Swiss Alps, Cold Reg. Sci. Technol., 125, 117–127, 2016.

Pruessner, L., Huss, M., Phillips, M., and Farinotti, D.: A framework for modeling rock glaciers and permafrost at the basin-scale in high alpine catchments, J. Adv. Model. Earth Syst., 13, e2020MS002361, 2021.

Ravanel, L. and Deline, P.: Climate influence on rockfalls in high-Alpine steep rockwalls: The north side of the Aiguilles de Chamonix (Mont Blanc massif) since the end of the 'Little Ice Age,' The Holocene, 21, 357–365, 2011.

Rohsenow, W. M., Hartnett, J. P., and Cho, Y. I.: Handbook of heat transfer, Mcgraw-hill New York, 1998.

Rühaak, W., Anbergen, H., Grenier, C., McKenzie, J., Kurylyk, B. L., Molson, J., Roux, N., and Sass, I.: Benchmarking numerical freeze/thaw models, Energy Procedia, 76, 301–310, 2015.

Savi, S., Comiti, F., and Strecker, M. R.: Pronounced increase in slope instability linked to global warming: A case study from the eastern European Alps, Earth Surf. Process. Landforms, 46, 1328–1347, 2021.

Schaefer, K., Lantuit, H., Romanovsky, V. E., Schuur, E. A. G., and Witt, R.: The impact of the permafrost carbon feedback on global climate, Environ. Res. Lett., 9, 85003, 2014.

Schuster, P. F., Schaefer, K. M., Aiken, G. R., Antweiler, R. C., Dewild, J. F., Gryziec, J. D., Gusmeroli, A., Hugelius, G., Jafarov, E., and Krabbenhoft, D. P.: Permafrost stores a globally significant amount of mercury, Geophys. Res. Lett., 45, 1463–1471, 2018.

Schuur, E. A. G., McGuire, A. D., Schädel, C., Grosse, G., Harden, J. W., Hayes, D. J., Hugelius, G., Koven, C. D., Kuhry, P., and Lawrence, D. M.: Climate change and the permafrost carbon feedback, Nature, 520, 171–179, 2015.

Sedaghatkish, A. and Luetscher, M.: Modeling the effect of free convection on permafrost melting-rates in frozen rock-clefts, , https://doi.org/10.5281/zenodo.8435168, n.d.

Spiegel, E. A. and Veronis, G.: On the Boussinesq approximation for a compressible fluid., Astrophys. Journal, vol. 131, p. 442, 131, 442, 1960.

Spötl, C., Koltai, G., Jarosch, A. H., and Cheng, H.: Increased autumn and winter precipitation during the Last Glacial Maximum in the European Alps, Nat. Commun., 12, 1839, 2021.

Töchterle, P., Baldo, A., Murton, J. B., Schenk, F., Edwards, R. L., Koltai, G., and Moseley, G. E.: Reconstructing Younger Dryas Ground Temperature and Snow Thickness from Cave Deposits, Clim. Past Discuss., 2023, 1–21, 2023.

Tubini, N., Gruber, S., and Rigon, R.: A method for solving heat transfer with phase change in ice or soil that allows for large time steps while guaranteeing energy conservation, Cryosph., 15, 2541–2568, 2021.

Virag, Z., Živić, M., and Galović, A.: Influence of natural convection on the melting of ice block surrounded by water on all sides, Int. J. Heat Mass Transf., 49, 4106–4115, 2006.

Walvoord, M. A. and Kurylyk, B. L.: Hydrologic impacts of thawing permafrost—A review, Vadose Zo. J., 15, 2016.

Weast, R. C.: CRC handbook of chemistry and physics., 1986.

Wind, M., Obleitner, F., Racine, T., and Spötl, C.: Multi-annual temperature evolution and implications for cave ice development in a sag-type ice cave in the Austrian Alps, Cryosph., 16, 3163–3179, 2022.

Žák, K., Onac, B. P., Kadebskaya, O. I., Filippi, M., Dublyansky, Y., and Luetscher, M.: Cryogenic mineral formation in caves, in: Ice caves, Elsevier, 123–162, 2018.

Zeneli, M., Malgarinos, I., Nikolopoulos, A., Nikolopoulos, N., Grammelis, P., Karellas, S., and Kakaras, E.: Numerical simulation of a silicon-based latent heat thermal energy storage system operating at ultra-high temperatures, Appl. Energy, 242, 837–853, 2019.

Zhang, M., Lai, Y., Liu, Z., and Gao, Z.: Nonlinear analysis for the cooling effect of Qinghai-Tibetan railway embankment with different structures in permafrost regions, Cold Reg. Sci. Technol., 42, 237–249, 2005.

Chapter 7: General discussion and Conclusion

In this thesis, we aimed to enhance our understanding of heat transfer mechanisms in various settings of the karst environment, including ventilated caves, epikarst, and frozen fractures in ice-rich aquifers. This was achieved by developing innovative thermal models that couple conduction and convection processes in karst media, and by comparing these models with field data obtained from cave monitoring.

In ventilated caves influenced by chimney effect, we observe that external temperature signals penetrate the cave to a distance that depends on the air mass flow rate and the conduit radius (see Eq. (25) in Chapt. 2). This "convection length" is significantly greater than the diffusion length, which is typically only a few meters on a yearly timescale in impermeable rocks. In contrast, the convection length can extend from a few hundred meters to several kilometers from the cave entrances. The temperatures of both the air and the cave walls along the conduit are primarily governed by the interaction between conductive and convective heat exchanges in the rock and airflow, as previously investigated by Gabrovšek, (2023) and Lismonde, (2002). This coupling of conduction and convection accelerates the propagation of external temperature signals into the cave, compared to a purely conductive process that neglects the air flux (Domínguez-Villar et al., 2013; Domínguez-Villar et al., 2023). This interaction must be accounted for as long as the heat transfer coefficient between the air and the cave walls remains significant. The heat transfer coefficient is a function of air velocity. When the airflow rate decreases and approaches laminar regime or there is no airflow (the Nusselt number is approximately 3.6, as shown in Eq. (11) in Chapt. 2), the influence of convection diminishes and heat conduction becomes the dominant process. The extent of the convection length is not confined to the conduits alone but also affects the surrounding rock, referred to as the "thermal width." Figure 6 in Chapt. 2 illustrates how the heat exchange in the surrounding rock mass is influenced by the air flux. The maximum value of this thermal width is approximately one-tenth of the convection length for AMT and ATF and about 5 meters for the diffusion length.

The convection length is not the only important consideration in ventilated caves. Quantifying the rock and air temperature in a real ventilated cave with complex geometries, as well as determining the distribution of water vapor concentration along the cave passage to assess the effects of evaporation and condensation, is essential for evaluating the thermal response of the cave. The four thermal model scenarios developed in Chapt. 3 provides useful upper and lower bounds for uncertainty of the heat and mass transfer coefficients as well as latent heat flux. Furthermore, the uncertainty of measured mass flow rate was determined in Appendix D showing that the location of the anemometer in cave cross-section does not significantly change the results. In the case of Longeaigue Cave, we found that the humid air scenario with a finite heat transfer coefficient (**HA**) provided the best agreement with field data in the main ventilated passage. Although the thermal response under the dry air scenario

(**DA**) is not much different from **HA**, the latter provides additional information about the evaporated and condensed water mass flux along the cave passage.

Predicting the temperature field along the cave passage is essential for the cave ecosystem. Temperature can serve as an indicator of anthropogenic influences, and many aquatic species are highly sensitive to temperature changes (Caissie, 2006). Cave-adapted species may be affected by the amplitude and frequency of these temperature fluctuations (Jegla and Poulson, 1970). Some of these species belong to ancient evolutionary lineages such as Pyrenean beetles, which were studied by Rizzo et al., (2015) in different thermal conditions. It was observed in some tests lasting 7 days and more, the survival rate of several species of the same lineages was almost 100% when the temperature varied between 6 and 20°C. However, all the specimens died when the temperature rose between 23 and 25°C. Caves serve as crucial refuges for many other temperature-sensitive species, including bats, beetles, spiders and various arthropod species (Braack, 1989). Additionally, temperature control is crucial for cave conservation, particularly in preventing the destructive effects of vermiculation on prehistoric cave wall paintings (Freydier et al., 2021).

A quantitative estimate of a cave's thermal response to the outside environment also essential for the interpretation of paleoclimate records from speleothems (Lyu et al., 2024). Evaporation and isotope fractionation in caves are closely related processes that play a significant role in the geochemistry of speleothems (cave formations like stalagmites and stalactites). When water infiltrates into a cave system, it contains isotopes of oxygen (^{16}O and ^{18}O) and hydrogen (^{1}H and ^{2}H or deuterium) in ratios that reflect the conditions of the external environment. As this water drips into the cave and begins to evaporate, lighter isotopes (^{16}O and ^{1}H) preferentially escape into the vapor phase due to their lower mass, while the heavier isotopes (^{18}O and ^{2}H) remain in the liquid. This selective loss of lighter isotopes results in isotopic fractionation, leading to an enrichment of heavier isotopes in the remaining water (Hendy, 1971; Mickler et al., 2004). This fractionation process influences the isotopic composition of the minerals precipitated from this water, such as calcite, which can then be used as a proxy to reconstruct past climate conditions, humidity levels, and evaporation rates (McDermott, 2004).

Although variations in drip water composition predominantly influence proxy partitioning in speleothems (Fairchild and Baker, 2012), trace element concentrations and oxygen isotope fractionation during $CaCO_3$ precipitation are also temperature-dependent (Tremaine et al., 2011; Wassenburg et al., 2020), becoming particularly significant when temperature amplitudes exceed ±0.5°C. The model developed in this study is capable of calculating these amplitudes on both daily and yearly scales at any location within the cave, demonstrating the temperature sensitivity in the convection zone. Additionally, our calculations show that evaporation occurs throughout Longeaigue Cave during the winter at substantial rates, particularly near the lower cave entrance. In this area, the evaporation flux can reach up to 2×10^{-3} $g.m^{-2}.s^{-1}$ during

periods of strong upward airflow. While this rate is lower than the potential evaporation rates typically used in geochemical models (Dreybrodt and Deininger, 2014), it can become locally significant when speleothems are fed by very low drip rates. The results from the highly ventilated Longeaigue Cave suggest that evaporation's impact on isotope proxy records can often be overlooked in hydrologically active caves, but it must be considered in semi-arid environments where drip rates are sporadic.

7.1 A general thermal overview of karst environment

The karst landscape consists of many components which have potentially different thermal and hydrological responses to atmosphere variations. Figure 1 depicts some of the main karst features in the heterothermic and homothermic zones including the soil, epikarst, vadose zone, epiphreatic and (deep) phreatic zones as well as poorly ventilated voids/caves numbered from 1 to 7. Each component may have different thermal configurations and a detailed quantitative/qualitative analysis is only possible based on field observations, monitoring data and the development of thermal models. A general overview of dominant heat fluxes is descriptively presented here to better understand the thermal interactions between the fluid (air or water) circulating within a karst and the surrounding rock massif.

- Usually, the soil covers (number 1 in Fig. 1) the highest layer of karst and lies in direct contact with the atmosphere. The thickness of this layer ranges between 0 (no soil) and ~5 m. Conduction is the main dominant heat transfer in soils (Kane et al., 2001) but under certain conditions, convection plays an important role, controlled by soil permeability and the soil depth (Jazi et al., 2024). The temperature gradient may also trigger free convection in soil (Basok et al., 2022).
- The epikarst (number 2 in Fig. 1) typically consists of a poorly permeable rock mass and a highly permeable fracture network with varying aperture sizes, which allows rapid transfer of rainfall from the surface to deeper layers, as discussed in Chapt. 5. Aperture size and fracture density are critical parameters for generating significant water fluxes coupling thermal convection-conduction processes during periods of high precipitation or extreme flooding. In the absence of such conditions, conduction remains the dominant thermal process in the epikarst.
- At high altitudes and elevations, ice-filled fractures and ice clefts are characteristic features of mountain permafrost (as a frozen epikarst). The active layer of this permafrost is heavily influenced by intermittent melting and freezing cycles. In Chapt. 6, we demonstrated that free convection can accelerate the melting rate by an order of magnitude compared to purely conductive conditions. The intensity of free convection is constrained by the aperture size and the aspect ratio of the fractures/clefts. However, free convection may occur in other dimensions, but its total intensity remains same.

- The vadose zone (number 3 in Fig. 1) can be categorized into two types based on the presence of water or airflow: open channel flow and ventilated flow. The thermal characteristics of open channel flows were extensively studied by Covington et al., (2011) and Luhmann et al., (2015). Their research indicated that the dominant thermal processes controlling water temperature include the coupled convection-conduction processes, as well as radiative heat fluxes between the water and the conduit walls. The effect of ventilation was comprehensively examined in this thesis, where the coupled convection-conduction thermal process was identified as the primary heat transfer mechanism. Additionally, the latent heat flux plays a significant role in humid air conditions within ventilated caves.
- Luhmann et al., (2012) have shown that in the epiphreatic and phreatic zones (see number 4 and 5 in Fig. 1) where conduits are saturated with water, the convection-conduction thermal process is again dominant with the exception that radiation heat flux becomes negligible.
- In the deep phreatic zone as displayed with number 6 in Fig. 1, conduction is the dominant process due to the lack of water and air circulation. This impermeable zone is often called "geothermal layer" and is located below the karst homothermic zone (Badino, 2018) since the geothermal gradient (~3 °C/100 m) is re-established as depth increases.
- Poorly ventilated voids or caves (see number 7 in Fig. 1), such as the Lascaux cave in France (Salmon et al., 2023), can exist at shallow depths. If these caves are situated in shallow depth (<~20 m), where external seasonal temperature variations are still perceptible, a temperature gradient may develop between the cave floor and ceiling. This gradient can lead to the formation of free convection cells and radiative heat fluxes between the cave walls and the air (Guerrier et al., 2019; Qaddah et al., 2022; Qaddah et al., 2023). These thermal processes are interconnected and must be taken into account when predicting the thermal response of these voids to atmospheric signals. Such voids may also occur at greater depths, and any thermal interactions with other zones, such as the vadose zone, phreatic zone, or areas following the geothermal gradient, can create small temperature differences between the cave floor and ceiling, potentially triggering free convection. The thermal behavior of these voids, particularly in response to atmospheric influences, remains insufficiently understood and requires further investigation.

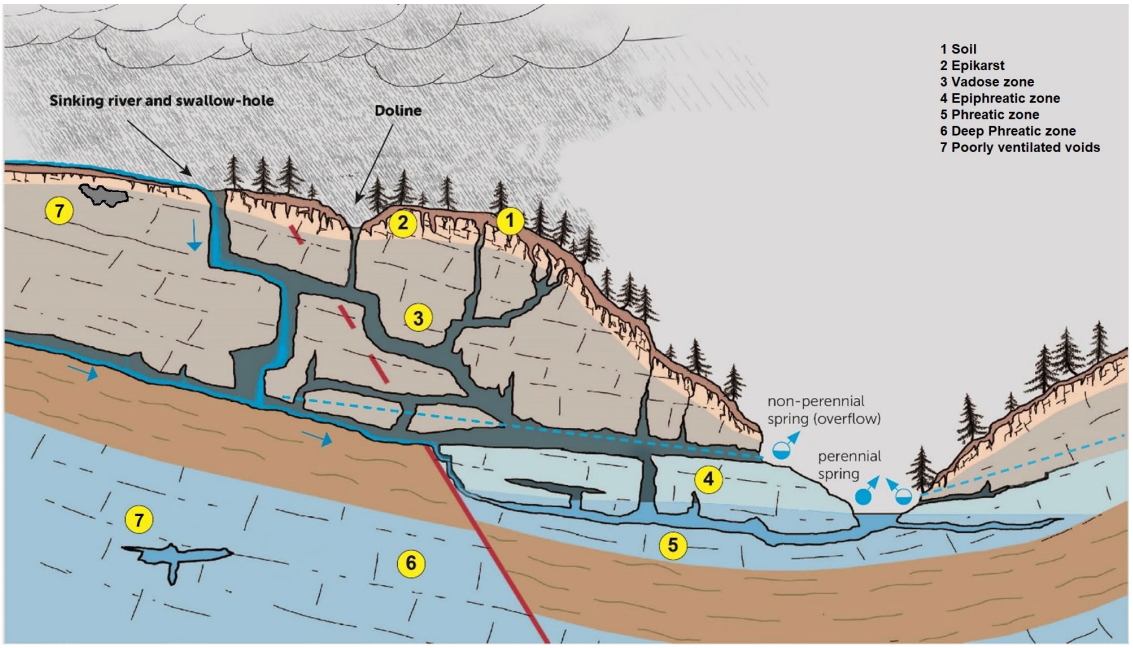

Figure 1. A simplified sketch of the karst landscape (Wenger et al., 2024). The figure was slightly modified.

7.2 Convection length in hydraulic conduits

So far, we focused on the convection length in ventilated conduits but also water-saturated conduits and open channel flows in phreatic and vadose zone transport heat by water flux. Their convection length can be different from that of ventilated conduits considering the contrasting thermal properties and configuration between airflow and waterflow. Luhmann et al., (2015) investigated thermal damping and retardation in karst conduits using analytical and numerical solutions considering convection/conduction coupling. They demonstrated that for a sinusoidal inlet temperature profile, the thermal damping inside a fully saturated channel (two parallel plates) in conduction-limited heat transfer (infinite heat transfer coefficient) can be approximated as:

$$\frac{T_{w,out}}{T_{w,in}} = e^{\left(-\frac{4x}{V\psi D_h}\sqrt{\frac{\pi\alpha_r}{\tau}}\right)} \tag{1}$$

$T_{w,out}$ and $T_{w,in}$ are water temperature peak at the outlet and inlet of the conduit, respectively. V is the constant velocity, D_h is the hydraulic diameter of the pipe and τ is the period of sinusoidal perturbation (here is 1 year). ψ is the ratio of the volumetric heat capacity of rock and water ($\frac{\rho_r c_{p,r}}{\rho_w c_{p,w}}$). If we use the same definition of the convection length given in Chapt. 2 for ventilated caves (based on 90% attenuation of the inlet amplitude) and use a mass flow rate instead of velocity, the hydraulic convection length (L_c) can be defined as:

$$L_c = \frac{2.3\psi\dot{m}}{\pi\rho_w D_h}\sqrt{\frac{\tau}{\pi\alpha_r}} \quad (2)$$

Replacing all the thermophysical properties and parameters in Eq. (2), it can be rewritten with the same notations as Eq. (11) in Chapt. 2:

$$L_c \approx 2300\frac{\dot{m}}{R} \quad (3)$$

R is the average radius of the conduit. We see that the hydraulic convection length (L_c) is much higher than the ventilated convection length. For instance, considering 0.5 m for radius and 1 kg/s mass flow rate for water and yearly amplitude of mass flow rate for air, the convection length for the ventilated and hydraulic conduit is about 565 m and 4600 m, respectively showing that the hydraulic convection length is about 8 times higher than an equivalent ventilated conduit.

It should be noticed that the thermal configurations of a ventilated and hydraulic conduit are inherently different. Firstly, the flow reversals in ventilated caves can change the thermal storage of surrounding rock close to the inlet and outlet compared to the unidirectional flow of water. Secondly, the mass flow rate in ventilated conduits is strongly correlated with the inside and outside temperature of the cave (Eq. (2) in Chapt. 2) while for hydraulic conduits the mass flow rate depends on external factors like precipitation or snowmelt rate. Thus, we should be cautious when we are comparing their convection length with the same input variables.

7.3 A new thermal sketch for the unsaturated zone

This thesis focused mainly on the evaluation of thermal responses in three main domains of the unsaturated zone of karst massifs: 1) ventilated conduits 2) epikarst and 3) ice-clefts in arctic karst or mountain permafrost. Figure 2 shows a simplified sketch of thermal reactions in these areas based on the findings of this project which can alter slightly the global conceptual model displayed in Fig. 2 in Chapt. 1.

The thermal anomaly produced by seasonal asymmetry of chimney-driven airflow can propagate to a few hundreds meter or more from the upper and lower entrances. These areas are shown by red and blue shadows in Fig. 2. The extension of the thermal perturbations, the so-called convection length, depends strongly on the value of the air mass flow rate and the conduit size. It was shown that the narrow passages and singularities can significantly increase cave aeraulic resistance and reduce the mass flow rate (see Sect. 4.4). Subsequently, this can reduce the convection length. According to the Fig. 2 in Chapt. 1 (from Luetscher and Jeannin, 2004; Badino, 2018), the total depth of the heterothermic zone where the yearly external temperature fluctuations are perceptible rarely exceeds 100 m. Our findings show this depth can be larger if conduits openings are large (low aeraulic resistance) inducing high mass flow rates. However, we do not have field data to demonstrate it.

Epikarst, the upper layer of karst consisting of a network of fractures distributed in low permeable rock, has typically a thickness ranging between 1 and 10 m, i.e. close to the thickness of the diffusive region where conduction heat transfer is the dominant process. Thus, the heterothermic zone is limited to depth of epikarst in most cases at yearly scale. Exceptionally, the heterothermic zone can exceed the depth of the epikarst during intense rainfalls and floods.

At high elevations, ice-clefts may form within the epikarst. The climate warming melts the ice from the top surface. The meltwater density increases when water temperature rises from 0 to 4°C triggering free convection cells. This yields a mixing zone between the melting front and top surface of clefts. Since the thaw/refreezing cycles are strongly variables in ice-clefts, finding the limit of heterothermic zone is hard but melting processes can increase this zone locally (indicated by black solid line in Fig. 2). During the freezing period (in solid state), this zone's thickness remains close to the diffusive length. The interface of heterothermic and homothermic zones are indicated by a black solid line in Fig. 2 providing a more detailed distinction of these zones compared to Fig. 2 in Chapt. 1.

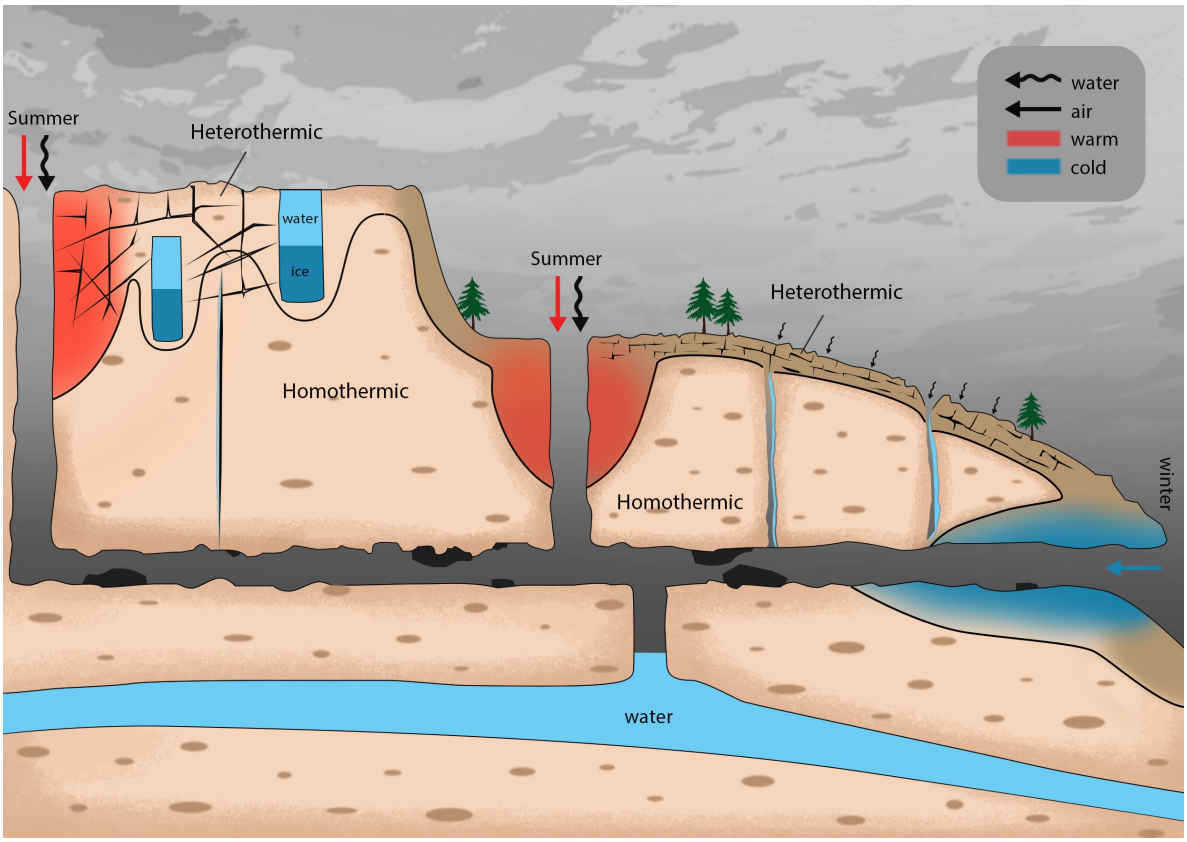

Figure 2. A simplified sketch of the thermal response in the unsaturated zone of karst (particularly in ventilated conduits, epikarst and ice-clefts in mountain permafrost)

7.4 Main conclusions

The main conclusions of this thesis are briefly introduced as follows:

- As shown in Chapt. 2 and 3, atmospheric temperature variations comprise different modes of frequencies including daily and yearly fluctuations. The convective flux of airflow in ventilated caves propagates these signals much faster than conductive flux along the cave passage as well as inside the surrounding rock. The convection length for AMT (annual mean temperature) and ATF (annual temperature fluctuation) have the same order of magnitude.
- Numerical simulations in Chapt. 2 show that the length of the convective region is approximately proportional to the amplitude of the flowrate annual fluctuations divided by the square root of the cave average radius. The maximum value of thermal width in the surrounding rock for AMT and ATF is approximately one-tenth of the convection length and about equivalent to the diffusion length (~5 meters), respectively.
- The complex geometry of caves presents a significant challenge for thermal modeling. A key simplification in Chapt. 3 involved assuming a rectilinear conduit with a circular cross-section of variable diameter. Under this assumption, the conduction problem in the surrounding rock mass becomes a 2D axisymmetric problem, which requires only two independent parameters to define the conduit cross-section: the effective diameter (D_p), based on the conduit perimeter, and the hydraulic diameter (D_h). Utilizing D_p in the conservation equations ensures that the exchange surface area between the air and the rock is accurately preserved, while D_h serves as the relevant geometric parameter for estimating heat and mass transfer coefficients.
- In Chapt. 3, the numerical results underestimate the annual mean temperatures (AMT) observed in the field by 1 to 2°C, which is the model's most significant limitation. This discrepancy is primarily due to the assumption that rock and atmospheric temperatures are equal at the external surface of the massif, highlighting the need for more accurate boundary conditions.
- The thermal model developed in Chapt. 3 effectively predicts temperature fluctuations across daily to yearly timescales, including the specific case of Longeaigue Cave, where temperature variations are influenced by intermittent cave closures. The impact of the initial conditions, estimated from a simplified history, is minimal beyond the first month of the simulation. Additionally, comparisons between field data and simulated temperatures indicate that the influence of water flow from diffuse water recharge is only noticeable in the lower sections of the cave. In contrast, at higher elevations, the temperature field is primarily governed by airflow coupled with heat conduction in the surrounding rock mass. The latent heat effects of evaporation and condensation appear to have a minor influence on the cave's overall climate. Nonetheless, accurately estimating the magnitude of condensation or evaporation rates remains valuable for applications in ecology and paleoclimatology.

- In Chapt. 4, developing an aeraulic-thermal model for ventilated caves can assess the long-term thermal response of a ventilated cave when airflow is not available. However, it requires cave aeraulic resistance (**AR**) as an input to the model. The **AR** can be directly measured from a ventilated cave by measuring the air mass flow rate and driving force for a short period (a few days or preferably a few weeks). Calculation of aeraulic resistance from theory is not recommended due to many uncertainties about cave geometry and friction factor (relative roughness).
- In Longeaigue cave, the results of the aeraulic-thermal model show that if there was no lake (or cave closure) the AMT in the cave would be lower for about 0.5 °C (from 2020 to 2021). So, it is expected that the lake may have favored the warming of the cave for years due to the cave closure. For better confirmation, more investigations are needed to reconstruct the cave closure history in the past.
- The hydrodynamic response of epikarst to recharge rates results in variably saturated DFN along the year. Based on the common values of rainfall intensity observed in temperate countries, water advection through the fractures can be neglected compared to conduction. However, during intense rainfall events, a slight shift towards the depth can be observed (see Chapt. 5). To summarize, attention is required when using conduction-based models which are widely used for the prediction of karst underground temperature in literature (Domínguez-Villar et al., 2013; Domínguez-Villar et al., 2023).
- It has been illustrated in Chapt. 6 that increasing the upper thermal boundary condition can generate free convection cells in melting ice-clefts because the water density increases between 0 and 4°C (a property specific to water). The convection cells generate a thermal bridge between the atmosphere and the melting front, resulting in the formation of a mixing zone with quasi-uniform temperature in the meltwater. This dramatically enhances the melting rate in ice-rich aquifers when compared to models assuming stagnant liquid water. This thermal penetration also exerts an influence on the surrounding rock. The effect of free water convection is limited to the cleft aspect ratio (the ratio between the cleft aperture size and the meltwater depth). Free convection becomes negligible in smaller aperture sizes (less than 2 cm) where conduction is the dominant thermal process.

7.5 Future works

The developed models in this thesis for ventilated conduits can be used efficiently in caves, mines or tunnels dominated by chimney effect (or natural ventilation) for long-term (yearly scale) simulations. The 1D cave passage and 2D axisymmetric surrounding rock massif approximation can reduce the computational cost significantly compared to 3D or 2D cave passage domain making the long-term simulation impractical. Despite developing proper thermal models for ventilated caves, we believe that heat transfer investigations in different settings associated with

the vadose zone in karst are not yet finished and some points need to be addressed in future works. Here we mention a few of them.

The impact of ventilation in parallel conduits on the convection length has not been yet considered in Chapt. 2. If the distance between two parallel ventilated conduits exceeds their thermal width, they can be analyzed independently. However, if the distance is smaller than the thermal width, they will interact thermally, meaning that the thermal response of each conduit affects the other. Our developed model in Chapt. 2 can be a basis for further investigation of this effect.

In Chapt. 3 and 4, we developed (aeraulic) thermal models based on the time scales of daily and yearly fluctuations observed in the external temperature (and resulting mass flow rate). Smaller frequencies related to millennials and centennials climate oscillations may be important based on their associated amplitudes. Using an aeraulic-thermal model will be necessary since the mass flow rate is not available in the past. The primary challenge lies in the high computational costs. Since the amplitudes of different frequencies are comparable, all frequencies must be simultaneously accounted for in the model. Additionally, long-term variations in the cave's aeraulic resistance should be assessed by examining the cave morphology and morphometry. Furthermore, the diffusion length can increase significantly with lower frequencies (longer periodicities), potentially overlapping with the convection length, which calls for the development of new models.

Density difference is not always due to the temperature difference in ventilated caves. Even variations in humidity or carbon dioxide (CO_2) concentrations between inside and outside the cave can possibly contribute to drive airflow (Sánchez-Cañete et al., 2013) which was not investigated in this thesis. During warmer periods, increased CO_2 production in the soil and higher CO_2 levels in the cave air enhance this effect, providing an additional driving force to the downward flow accelerating CO_2 degassing from drip water and enhancing carbon isotopic fractionation and calcite precipitation. A CO_2 pressure variation between 0 and 0.02 atm (Qaddah et al., 2023) results in about 0.01 kg/m^3 density difference in 10 °C generating a driving force of about 10 Pa (for 100 m elevation difference between the upper and lower entrance). Although 0.02 atm for CO_2 pressure seems a high value inside a ventilated cave, the resultant driving force is not much smaller than the typical driving force associated with temperature variations, which is in order of 50 Pa in many ventilated caves (Gabrovšek, 2023), and therefore worth to be assessed.

The thermal model developed for the epikarst in Chapt. 5 offers only an upper and lower bound for the convective heat flux of water and lacks an accurate hydrodynamic response to precipitation rates. Developing a more advanced model for a partially saturated discrete fracture network (DFN) would yield a more realistic distribution of water flux in the epikarst, resulting in a more reliable thermal response to atmospheric variations. Further research is needed to develop such a model.

The impact of free convection on ice melting (Chapt. 6) extends beyond hourly or daily fluctuations and can be examined over much longer timescales, including centennial to millennial variations in deeper ice columns, reaching depths of around 50 meters. However, the primary challenge for incorporating free convection in long-term simulations is the high computational cost. The full coupling of momentum and energy equations demands significantly smaller time steps compared to simpler conduction-based models. Consequently, further research is underway to reformulate and simplify the governing equations, making them more suitable for simulations over extended timescales.

The findings of this thesis lay the groundwork for future research and the development of new models to explore these effects in greater detail. This foundation opens opportunities for refining thermal models, particularly in accounting for complex interactions between conduction, convection, and phase changes within karst systems.

Bibliography

Badino, G.: Geothermal flux and phreatic speleogenesis in gypsum, halite, and quartzite rocks, Int. J. Speleol., 47, 1, 2018.

Baker, A. and Genty, D.: Environmental pressures on conserving cave speleothems: effects of changing surface land use and increased cave tourism, J. Environ. Manage., 53, 165–175, 1998.

Bartelt, P. and Lehning, M.: A physical SNOWPACK model for the Swiss avalanche warning: Part I: numerical model, Cold Reg. Sci. Technol., 35, 123–145, 2002.

Bartolomé, M., Cazenave, G., Luetscher, M., Spötl, C., Gázquez, F., Belmonte, Á., Turchyn, A. V, López-Moreno, J. I., and Moreno, A.: Mountain permafrost in the Central Pyrenees: insights from the Devaux ice cave, Cryosph., 17, 477–497, 2023.

Basok, B., Davydenko, B., Koshlak, H., and Novikov, V.: Free convection and heat transfer in porous ground massif during ground heat exchanger operation, Materials (Basel)., 15, 4843, 2022.

Berkowitz, B.: Characterizing flow and transport in fractured geological media: A review, Adv. Water Resour., 25, 861–884, 2002.

Berre, I., Doster, F., and Keilegavlen, E.: Flow in fractured porous media: A review of conceptual models and discretization approaches, Transp. Porous Media, 130, 215–236, 2019.

Bini, A., Gori, M. C., and Gori, S.: A critical review of hypotheses on the origin of vermiculations, Int. J. Speleol., 10, 2, 1978.

Birk, S., Liedl, R., and Sauter, M.: Karst spring responses examined by process-based modeling, Groundwater, 44, 832–836, 2006.

Braack, L. E. O.: Arthropod inhabitants of a tropical cave 'island'environment provisioned by bats, Biol. Conserv., 48, 77–84, 1989.

Caissie, D.: The thermal regime of rivers: a review, Freshw. Biol., 51, 1389–1406, 2006.

Cheng, G.: A roadbed cooling approach for the construction of Qinghai–Tibet Railway, Cold Reg. Sci. Technol., 42, 169–176, 2005.

Cicoira, A., Beutel, J., Faillettaz, J., Gärtner-Roer, I., and Vieli, A.: Resolving the influence of temperature forcing through heat conduction on rock glacier dynamics: a numerical modelling approach, Cryosph., 13, 927–942, 2019.

Cigna, A. A.: Environmental management of tourist caves: the examples of Grotta di Castellana and Grotta Grande del Vento, Italy, Environ. Geol., 21, 173–180, 1993.

Comsol Multiphysics: v. 6.1 www. comsol. com COMSOL AB, Stockholm, Sweden.

Council, N. R., Geosciences, C. on, Sciences, B. on E., and Sciences, C. on B. R. O. in the E.: Basic research opportunities in earth science, 2001.

Covington, M. D., Luhmann, A. J., Gabrovšek, F., Saar, M. O., and Wicks, C. M.:

Mechanisms of heat exchange between water and rock in karst conduits, Water Resour. Res., 47, 2011.

Crestani, G., Anelli, F., and (Venezia), I. M. dei lavori pubblici. S. idrografico. U. idrografico del R. M. alle acque: Ricerche di Meteorologia Ipogea nelle grotte di Postumia: lavoro eseguito dall'ufficio idrografico del Magistrato alle A con la collaborazione dell'Istituto Italiano di Speleologia, Ist. poligrafico dello stato, Libreria, 1939.

Cropley, J. B.: Influence of surface conditions on temperatures in large cave systems, Bull. Natl. Speleol. Soc., 27, 1–10, 1965.

Dal Soglio, L., Danquigny, C., Mazzilli, N., Emblanch, C., and Massonnat, G.: Modeling the matrix-conduit exchanges in both the epikarst and the transmission zone of karst systems, Water, 12, 3219, 2020a.

Dal Soglio, L., Danquigny, C., Mazzilli, N., Emblanch, C., and Massonnat, G.: Taking into account both explicit conduits and the unsaturated zone in karst reservoir hybrid models: Impact on the outlet hydrograph, Water, 12, 3221, 2020b.

Domínguez-Villar, D., Fairchild, I. J., Baker, A., Carrasco, R. M., and Pedraza, J.: Reconstruction of cave air temperature based on surface atmosphere temperature and vegetation changes: Implications for speleothem palaeoclimate records, Earth Planet. Sci. Lett., 369, 158–168, 2013.

Domínguez-Villar, D., Krklec, K., and Sierro, F. J.: Thermal conduction in karst terrains dominating cave atmosphere temperatures: Quantification of thermal diffusivity, Int. J. Therm. Sci., 189, 108282, 2023.

Dreybrodt, W. and Deininger, M.: The impact of evaporation to the isotope composition of DIC in calcite precipitating water films in equilibrium and kinetic fractionation models, Geochim. Cosmochim. Acta, 125, 433–439, 2014.

Dreybrodt, W., Gabrovšek, F., and Perne, M.: Condensation corrosion: a theoretical approach, Acta carsologica, 34, 2005.

Dublyansky, V. N. and Sockova, L. M.: Microclimate of karst cavities of the Mountain Crimea, in: Proceedings of the 7th International Congress of Speleology, 158–160, 1977.

Dublyansky, Y. V and Spötl, C.: Condensation-corrosion speleogenesis above a carbonate-saturated aquifer: Devils Hole Ridge, Nevada, Geomorphology, 229, 17–29, 2015.

Elias, S.: Encyclopedia of Quaternary science, Newnes, 2013.

Faimon, J., Troppová, D., Baldík, V., and Novotný, R.: Air circulation and its impact on microclimatic variables in the Císařská Cave (Moravian Karst, Czech Republic), Int. J. Climatol., 32, 599–623, 2012.

Fairchild, I. J. and Baker, A.: Speleothem science: from process to past environments, John Wiley & Sons, 2012.

Ford, D. and Williams, P. D.: Karst hydrogeology and geomorphology, John Wiley & Sons, 2007.

Ford, D. C.: Perspectives on karst geomorphology, hydrology, and geochemistry: a tribute volume to Derek C. Ford and William B. White, Geological Society of America, 2006.

De Freitas, C. R. and Littlejohn, R. N.: Cave climate: assessment of heat and moisture exchange, J. Climatol., 7, 553–569, 1987.

De Freitas, C. R. and Schmekal, A.: Condensation as a microclimate process: measurement, numerical simulation and prediction in the Glowworm Cave, New Zealand, Int. J. Climatol. A J. R. Meteorol. Soc., 23, 557–575, 2003.

French, H. M.: The periglacial environment, John Wiley & Sons, 2017.

Freydier, P., Weber, E., Martin, J., Jeannin, P.-Y., Guerrier, B., and Doumenc, F.: Vermiculations in painted caves: new inputs from laboratory experiments and field observations, Int. J. Speleol., 2021.

Gabrovšek, F.: How do caves breathe: The airflow patterns in karst underground, PLoS One, 18, e0283767, 2023.

Goldscheider, N. and Drew, D.: Methods in karst hydrogeology: IAH: International Contributions to Hydrogeology, 26, 2007.

Goldscheider, N., Chen, Z., Auler, A. S., Bakalowicz, M., Broda, S., Drew, D., Hartmann, J., Jiang, G., Moosdorf, N., and Stevanovic, Z.: Global distribution of carbonate rocks and karst water resources, Hydrogeol. J., 28, 1661–1677, 2020.

Gomell, A., Austin, D., Ohms, M., and Pflitsch, A.: Air pressure propagation through Wind Cave and Jewel Cave: How do pressure waves travel through barometric caves?, Int. J. Speleol., 50, 263–273, https://doi.org/10.5038/1827-806x.50.3.2393, 2021.

Groves, C. and Meiman, J.: Weathering, geomorphic work, and karst landscape evolution in the Cave City groundwater basin, Mammoth Cave, Kentucky, Geomorphology, 67, 115–126, 2005.

Guerrier, B., Doumenc, F., Roux, A., Mergui, S., and Jeannin, P.-Y.: Climatology in shallow caves with negligible ventilation: Heat and mass transfer, Int. J. Therm. Sci., 146, 106066, 2019.

Haaland, S. E.: Simple and explicit formulas for the friction factor in turbulent pipe flow, 1983.

Hayward, J. L., Jackson, A. J., Yost, C. K., Hansen, L. T., and Jamieson, R. C.: Fate of antibiotic resistance genes in two Arctic tundra wetlands impacted by municipal wastewater, Sci. Total Environ., 642, 1415–1428, 2018.

Hendy, C. H.: The isotopic geochemistry of speleothems—I. The calculation of the effects of different modes of formation on the isotopic composition of speleothems and their applicability as palaeoclimatic indicators, Geochim. Cosmochim. Acta, 35,

801–824, 1971.

Hill, C. and Forti, P.: Cave minerals of the world, 1997.

Hornum, M. T., Hodson, A. J., Jessen, S., Bense, V., and Senger, K.: Numerical modelling of permafrost spring discharge and open-system pingo formation induced by basal permafrost aggradation, Cryosph., 14, 4627–4651, 2020.

Huang, N., Liu, R., Jiang, Y., and Cheng, Y.: Development and application of three-dimensional discrete fracture network modeling approach for fluid flow in fractured rock masses, J. Nat. Gas Sci. Eng., 91, 103957, 2021.

Huss, M., Farinotti, D., Bauder, A., and Funk, M.: Modelling runoff from highly glacierized alpine drainage basins in a changing climate, Hydrol. Process., 22, 3888–3902, 2008.

Ivanov, V. and Rozhin, I.: Numerical simulation of the permafrost thawing near the city of Yakutsk during climate change up to the year 2100, in: AIP Conference Proceedings, 20050, 2022.

Jansen, G. and Miller, S. A.: On the role of thermal stresses during hydraulic stimulation of geothermal reservoirs, Geofluids, 2017, 4653278, 2017.

Jazi, F. N., Ghasemi-Fare, O., and Rockaway, T. D.: Natural convection effect on heat transfer in saturated soils under the influence of confined and unconfined subsurface flow, Appl. Therm. Eng., 237, 121805, 2024.

Jeannin, P.: Modeling flow in phreatic and epiphreatic karst conduits in the Hölloch cave (Muotatal, Switzerland), Water Resour. Res., 37, 191–200, 2001.

Jegla, T. C. and Poulson, T. L.: Circanian rhythms—I. Reproduction in the cave crayfish, Orconectes pellucidus inermis, Comp. Biochem. Physiol., 33, 347–355, 1970.

Kane, D. L., Hinkel, K. M., Goering, D. J., Hinzman, L. D., and Outcalt, S. I.: Non-conductive heat transfer associated with frozen soils, Glob. Planet. Change, 29, 275–292, 2001.

Klepikova, M., Méheust, Y., Roques, C., and Linde, N.: Heat transport by flow through rough rock fractures: a numerical investigation, Adv. Water Resour., 156, 104042, 2021.

Kukuljan, L., Gabrovsek, F., and Covington, M.: The relative importance of wind-driven and chimney effect cave ventilation: Observations in Postojna Cave (Slovenia), Int. J. Speleol., 50, 275–288, https://doi.org/10.5038/1827-806x.50.3.2392, 2021.

Lario, J. and Soler, V.: MICROCLIMATE MONITORING OF POZALAGUA CAVE(VIZCAYA, SPAIN): APPLICATION TO MANAGEMENT AND PROTECTION OF SHOW CAVES, J. Cave Karst Stud., 72, 169–180, 2010.

Larsen, P. H., Goldsmith, S., Smith, O., Wilson, M. L., Strzepek, K., Chinowsky, P., and Saylor, B.: Estimating future costs for Alaska public infrastructure at risk from climate change, Glob. Environ. Chang., 18, 442–457, 2008.

Lauriol, B. and Clark, I. D.: An approach to determine the origin and age of massive

ice blockages in two arctic caves, Permafr. Periglac. Process., 4, 77–85, 1993.

Liedl, R., Renner, S., and Sauter, M.: Obtaining information about fracture geometry from heat flow data in karst systems, Bull. d'hydrogéologie, 143–153, 1998.

Lismonde, B.: Climatologie du monde souterrain; Tome 2-Aérologie des systèmes karstiques, Persée-Portail des revues scientifiques en SHS, 2002.

Liu, H., Wang, H., Lei, H., Zhang, L., Bai, M., and Zhou, L.: Numerical modeling of thermal breakthrough induced by geothermal production in fractured granite, J. Rock Mech. Geotech. Eng., 12, 900–916, 2020.

Long, A. J. and Gilcrease, P. C.: A one-dimensional heat-transport model for conduit flow in karst aquifers, J. Hydrol., 378, 230–239, 2009.

Louis, C.: Etude des écoulements d'eau dans les roches fissurées et de leurs influences sur la stabilité des massifs rocheux, EDF Bull. la Dir. des Etudes Rech., 3, 5–132, 1968.

Luetscher, M. and Jeannin, P.: Temperature distribution in karst systems: the role of air and water fluxes, Terra Nov., 16, 344–350, 2004.

Luhmann, A. J., Covington, M. D., Alexander, S. C., Chai, S. Y., Schwartz, B. F., Groten, J. T., and Alexander Jr, E. C.: Comparing conservative and nonconservative tracers in karst and using them to estimate flow path geometry, J. Hydrol., 448, 201–211, 2012.

Luhmann, A. J., Covington, M. D., Myre, J. M., Perne, M., Jones, S. W., Alexander Jr, E. C., and Saar, M. O.: Thermal damping and retardation in karst conduits, Hydrol. Earth Syst. Sci., 19, 137–157, 2015.

Luo, M., Wan, L., Liao, C., Jakada, H., and Zhou, H.: Geographic and transport controls of temperature response in karst springs, J. Hydrol., 623, 129850, 2023.

Lyu, Y., Luo, W., Zeng, G., Wang, Y., Chen, J., and Wang, S.: The effect of cave ventilation on carbon and oxygen isotopic fractionation between calcite and drip water, Sci. Total Environ., 915, 169967, 2024.

Malakhova, V. V: Numerical modeling of methane hydrates dissociation in the submarine permafrost, in: IOP Conference Series: Earth and Environmental Science, 12022, 2022.

Mangin, A.: Contribution à l'étude hydrodynamique des aquifères karstiques, 1975.

Masciopinto, C.: Particles' transport in a single fracture under variable flow regimes, Adv. Eng. Softw., 30, 327–337, 1999.

McDermott, F.: Palaeo-climate reconstruction from stable isotope variations in speleothems: a review, Quat. Sci. Rev., 23, 901–918, 2004.

Mickler, P. J., Banner, J. L., Stern, L., Asmerom, Y., Edwards, R. L., and Ito, E.: Stable isotope variations in modern tropical speleothems: evaluating equilibrium vs. kinetic isotope effects, Geochim. Cosmochim. Acta, 68, 4381–4393, 2004.

Moody, L. F.: Friction factors for pipe flow, Trans. Am. Soc. Mech. Eng., 66, 671–678, 1944.

Nazridoust, K., Ahmadi, G., and Smith, D. H.: A new friction factor correlation for laminar, single-phase flows through rock fractures, J. Hydrol., 329, 315–328, 2006.

Palmer, A. N.: Origin and morphology of limestone caves, Geol. Soc. Am. Bull., 103, 1–21, 1991.

Pastore, C., Sedaghatkish, A., Weber, E., Schmid, N., Jeannin, P.-Y., and Luetscher, M.: Monitoring air fluxes in caves using digital flow metres, Int. J. Speleol., 53, 7, 2024.

Pastore, C., Sedaghatkish, A., Jeannin, P.-Y., and Luetscher, M.: Thermal exchanges and conduit resistance in ventilated caves: a model from Longeaigue cave (in preparation), n.d.

Patterson, J. W., Driesner, T., Matthai, S., and Tomlinson, R.: Heat and fluid transport induced by convective fluid circulation within a fracture or fault, J. Geophys. Res. Solid Earth, 123, 2658–2673, 2018.

Pelletier, M., Allard, M., and Levesque, E.: Ecosystem changes across a gradient of permafrost degradation in subarctic Québec (Tasiapik Valley, Nunavik, Canada), Arct. Sci., 5, 1–26, 2018.

Perrier, F., Bourges, F., Girault, F., Le Mouël, J.-L., Genty, D., Lartiges, B., Losno, R., and Bonnet, S.: Temperature variations in caves induced by atmospheric pressure variations—Part 1: Transfer functions and their interpretation, Geosystems and Geoenvironment, 2, 100145, 2023.

Pruessner, L., Huss, M., Phillips, M., and Farinotti, D.: A framework for modeling rock glaciers and permafrost at the basin-scale in high alpine catchments, J. Adv. Model. Earth Syst., 13, e2020MS002361, 2021.

Qaddah, B., Soucasse, L., Doumenc, F., Mergui, S., Rivière, P., and Soufiani, A.: Influence of turbulent natural convection on heat transfer in shallow caves, Int. J. Therm. Sci., 177, 107524, 2022.

Qaddah, B., Soucasse, L., Doumenc, F., Mergui, S., Rivière, P., and Soufiani, A.: Coupled heat and mass transfer in shallow caves: interactions between turbulent convection, gas radiative transfer and moisture transport, Int. J. Therm. Sci., 194, 108556, 2023.

Quindos, L. S., Bonet, A., Diaz-Caneja, N., Fernandez, P. L., Gutierrez, I., Solana, J. R., Soto, J., and Villar, E.: Study of the environmental variables affecting the natural preservation of the Altamira Cave paintings located at Santillana del Mar, Spain, Atmos. Environ., 21, 551–560, 1987.

Radioti, G., Sartor, K., Charlier, R., Dewallef, P., and Nguyen, F.: Effect of undisturbed ground temperature on the design of closed-loop geothermal systems: A case study in a semi-urban environment, Appl. Energy, 200, 89–105, 2017.

Rizzo, V., Sánchez-Fernández, D., Fresneda, J., Cieslak, A., and Ribera, I.: Lack of evolutionary adjustment to ambient temperature in highly specialized cave beetles, BMC Evol. Biol., 15, 1–9, 2015.

Rohsenow, W. M., Hartnett, J. P., and Cho, Y. I.: Handbook of heat transfer, Mcgraw-hill New York, 1998.

Salmon, F., Lacanette, D., Lharti, H., and Sirieix, C.: Heat transfer in rock masses: Application to the Lascaux Cave (France), Int. J. Heat Mass Transf., 207, 124029, 2023.

Sánchez-Cañete, E. P., Serrano-Ortiz, P., Domingo, F., and Kowalski, A. S.: Cave ventilation is influenced by variations in the CO 2-dependent virtual temperature, Int. J. Speleol., 42, 1, 2013.

Schaer, J. P., Stettler, R., Aragno, P. O., Burkhard, M., and Meia, J.: Géologie du Creux du Van et des Gorges de l'Affreuse, Nat. au Creux du Van. Ed. du, 1998.

Schuster, P. F., Schaefer, K. M., Aiken, G. R., Antweiler, R. C., Dewild, J. F., Gryziec, J. D., Gusmeroli, A., Hugelius, G., Jafarov, E., and Krabbenhoft, D. P.: Permafrost stores a globally significant amount of mercury, Geophys. Res. Lett., 45, 1463–1471, 2018.

De Simone, S., Pinier, B., Bour, O., and Davy, P.: A particle-tracking formulation of advective–diffusive heat transport in deformable fracture networks, J. Hydrol., 603, 127157, 2021.

Sinha, D. K., Ramesh, R., Tiwari, M., Chakraborty, S., Managave, S. R., and Yadava, M. G.: Retrieval of south Asian monsoon variation during the Holocene from natural climate archives, Curr. Sci., 1770–1786, 2010.

Tikhomirov, V. V: Hydrogeochemistry fundamentals and advances, mass transfer and mass transport, John Wiley & Sons, 2016.

Tremaine, D. M., Froelich, P. N., and Wang, Y.: Speleothem calcite farmed in situ: Modern calibration of δ18O and δ13C paleoclimate proxies in a continuously-monitored natural cave system, Geochim. Cosmochim. Acta, 75, 4929–4950, 2011.

Veni, G., DuChene, H., Crawford, N. C., Groves, C. G., Huppert, G. N., Kastning, E. H., Olson, R., and Wheeler, B. J.: Living with karst: A fragile foundations, American Geological Institute, 2001.

Villar, E., Fernández, P. L., Quindos, L. S., Solana, J. R., and Soto, J.: Temperature of rock surfaces in Altamira Cave (Spain), Trans. Br. Cave Res. Assoc., 10, 165–170, 1983.

Walvoord, M. A. and Kurylyk, B. L.: Hydrologic impacts of thawing permafrost—A review, Vadose Zo. J., 15, 2016.

Wassenburg, J. A., Riechelmann, S., Schröder-Ritzrau, A., Riechelmann, D. F. C., Richter, D. K., Immenhauser, A., Terente, M., Constantin, S., Hachenberg, A., and Hansen, M.: Calcite Mg and Sr partition coefficients in cave environments: Implications for interpreting prior calcite precipitation in speleothems, Geochim. Cosmochim. Acta, 269, 581–596, 2020.

Wenger, R., Perret, A., and Lalou, J.-C.: Dans les grottes de Suisse, Haupt, 2024.

White, W. B.: Geomorphology and hydrology of karst terrains, 1988.

Wigley, T. M. L. and Brown, C.: Geophysical applications of heat and mass transfer in

turbulent pipe flow, Boundary-layer Meteorol., 1, 300–320, 1971.

Williamas, P. W.: The role of the epikarst in karst and cave hydrogeology: a review, Int. J. Speleol., 37, 1–10, 2008.

Woo, M.: Permafrost hydrology, Springer Science & Business Media, 2012.

Worthington, S. R. H., Ford, D. C., and Beddows, P. A.: Porosity and permeability enhancement in unconfined carbonate aquifers as a result of dissolution, Speleogenes. Evol. Karst Aquifers, Ed. by Klimchouk, AV, Ford, DC, Palmer, AN, Dreybrodt, W., Natl. Speleol. Soc. Am. Huntsville, Alabama, USA, 220–223, 2000.

Zhang, Z. and Nemcik, J.: Friction factor of water flow through rough rock fractures, Rock Mech. Rock Eng., 46, 1125–1134, 2013.

Zhou, J.-Q., Hu, S.-H., Chen, Y.-F., Wang, M., and Zhou, C.-B.: The friction factor in the Forchheimer equation for rock fractures, Rock Mech. Rock Eng., 49, 3055–3068, 2016.